Research & Development

2023

Mechanical Engineering Letters 2023

Contents

Investigate the impacts of generative design on multirotor structures

Ahmad DUGHMI[1], László KÁTAI[2]

[1]*Mechanical Engineering Doctoral School (MTDI), Szent István Campus, Gödöllő, MATE*
[2]*Institute of Technology, Hungarian University of Agriculture and Life Sciences, MATE, Gödöllő*

Abstract

This paper presents a comprehensive overview of the generative design method (GDM) and its impact on the multirotor structure. The GDM is a modern technology that employs software algorithms to explore new designs within a defined design space created by boundary conditions, such as main dimensions, forces, materials, and manufacturing methods.

The First part of the research report shows the effectiveness of GDM. This study uses the GE bracket, which is utilized in jet engines, as an example. A comparison between the traditional design and the GDM-generated design is conducted, focusing on mass, von-misses stress, and displacement.

The second part shows the GDM when applied to the multirotor structure, with a traditional design created by the authors used as a co-design. To apply the GDM, a space design is required, and the authors generated three cases, with the first case resulting in a design that is 40% of the traditional design, the second case 55%, and the third case 80%. The comparison between the traditional design and the three GDM-generated designs is conducted, focusing on mass, von-misses stress, displacement, and factor of safety.

Autodesk Fusion360 is the software used in this study, with Aluminum AISI10Mg being the material used. This study underscores the effectiveness of GDM in generating new designs within specific boundary conditions and its potential to improve the multirotor structure's design.

Keywords

Generative design, traditional design, CAD, GE bracket, multirotor, boundary conditions, Autodesk Fusion360, Aluminum AISI10Mg.

Introduction

Engineering design process or Traditional design method

The process of developing a system, component, or process to meet specified requirements is formally defined as Engineering Design, as per the Accreditation Board for Engineering and Technology (ABET). This decision-making process, which is often iterative, utilizes fundamental science, mathematics, and

engineering to optimize the conversion of resources to accomplish a stated objective. To achieve this objective, the design process requires the establishment of goals and criteria, as well as synthesis, analysis, construction, testing, and evaluation (ABET, n.d.).

Incorporating various features such as student creativity development, the use of open-ended problems, and the development and application of contemporary design theory and methodology, the engineering design component of a curriculum should also involve the formulation of design problem statements and specifications, consideration of alternative solutions, feasibility, manufacturing processes, concurrent engineering design, and detailed system description. Additionally, various realistic constraints such as economic concerns, safety, reliability, aesthetics, ethics, and social impact must be considered(WİNARNO, 2020).

The systematic design process comprises several stages, which are guided by a design model and a collection of design methods, which are tools and techniques that can be applied at various stages of the design process (yousef haik et al., 2018).

In engineering, it is not always necessary to follow a specific order of steps. However, it is common for engineers to describe the problem and brainstorm ideas before developing a prototype, which is then refined and improved until the solution meets the project's requirements. This iterative process is a standard working method (Lee & Ostwald, 2022).

NASA has illustrated the Engineering Design Process as a six-step approach to achieve the design goal, namely asking, imagining, planning, creating, experimenting, and improving (NASA, n.d.).

The first step is to define the problem by asking questions such as who the product is for, the importance of the solution, and how to solve the problem. The next step is to brainstorm potential solutions by conducting archival studies, referring to old experiments, and seeking feedback from individuals with diverse backgrounds.

Once potential designs have been selected, the requirements of each design must be determined, and a plan is created based on factors such as time, cost, and manufacturing methods. After this, a prototype is created using different materials and manufacturing methods, and it is tested to see if it meets the standard requirements.

The next step involves testing the prototype and making any necessary improvements to reach the best design with plans. Finally, after improving the design, the final solution or model is obtained, and the results can be shared in various formats, including reports, presentations, and scientific papers.

Computer-Aided Design (CAD).

Computer-Aided Design (CAD) is a software tool widely used by architects, engineers, interior designers, industrial designers, and manufacturers to assist in the design process. CAD involves any design activity such as initial design, development, analysis, or modification. The system is based on interactive

computer graphics (ICG), where the designer enters data and information into the system, which converts it to create, analyze, or modify the model in 2D or 3D. The benefits of CAD include increased productivity, improved design quality, enhanced communication through documentation, and the creation of a manufacturing database. CAD expedites the process of synthesizing, analyzing, and documenting the design, resulting in lower design costs and shorter design project completion times. Additionally, the system's accuracy minimizes design errors, leading to an increase in the design's quality and accuracy. Using CAD results in enhanced engineering drawings, increased standardization, improved design documentation, fewer drawing errors, and increased drawing legibility. Finally, CAD enables the creation of a manufacturing database that can be used for various computer-integrated manufacturing (CIM) applications such as CNC programming, robot programming, and process planning (K. MALLIKARJUNA RAO et al., 2008; Mikell P.Groover & Emory W.Zimmers, 1984; Zhuming Bi & Xiaoqin Wang, 2020).

Generative design method

Generative design method definition.
Generative Design Method (GDM) is a contemporary approach to exploring new designs using software algorithms. Typically utilized in the preliminary stages of the design process, GDM relies on the designer to provide fundamental parameters such as dimensions, size, force, weight, manufacturing method, a factor of safety, etc. These boundary conditions delineate the design space for the software to generate and evaluate numerous potential designs, enabling the attainment of the design objectives while complying with imposed restrictions. In essence, Generative Design is a feature of CAD engineering software, wherein the designer collaborates with artificial intelligence algorithms to generate and evaluate multiple designs for a given product concept. Thus, the generative design methodology establishes project goals and constraints, enabling the production of optimal designs (Chien & Flemming, n.d.; Junk & Burkart, 2021; Khan & Awan, 2018; Krish, 2011).

Generative design is a design method that uses algorithms and artificial intelligence (AI) to create designs that meet specified constraints and goals. It is an iterative process where a designer inputs design criteria such as materials, manufacturing techniques, and functional requirements, and the algorithm generates numerous design options that meet those criteria. These designs can then be further optimized and refined until a final design is chosen(Krish, 2011). Generative design has been gaining popularity in recent years due to its ability to create complex and efficient designs that would be difficult, if not impossible, to create manually. It can help reduce material waste, increase production efficiency, and improve product performance.

Here diagram (Fig. 1) has been modified to make it more applicable to CAD-based generative design by integrating a generic model in place of algorithms and restrictions in the area of source code change. It is critical to emphasize the

designer's fundamental role in continually updating the generative scheme in response to the results, which is how the solutions space is explored in search of feasible design solutions (Krish 2011).
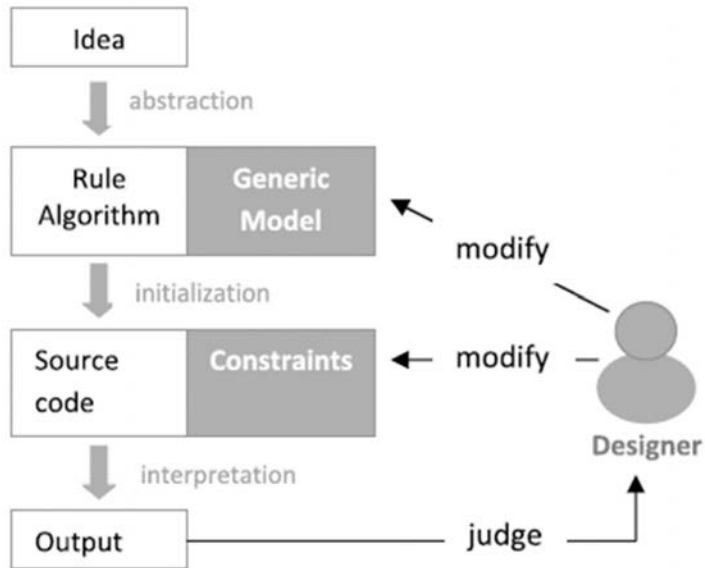

Figure 1. Generative design process (Krish, 2011).

The stages or components of GDM.
Figure 2 illustrates the stages or components of the generative design method:
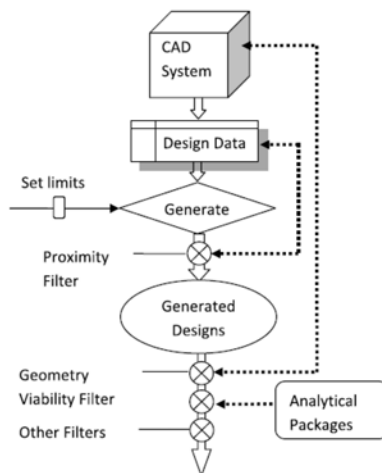

Figure 2. The stages or components of GDM (Krish, 2011).

1. At the first stage need a CAD system to create a co-design or base form to generate the method on it and needs a CAD system that supports generative design methods such as Autodesk fusion 360, and solid edge. Each CAD system has its own generative design algorithms so, in the end, the results will differ from one software to another (Buonamici et al., 2020; Krish, 2011; McKnight, 2017).

2. During this stage, the designer must specify input parameters, or boundary conditions, to create the design space. These parameters include main dimensions, forces, manufacturing methods, materials, and so on. The resulting design, called a genotype, provides the design space and search limits for CAD systems (Buonamici et al., 2020; Krish, 2011; McKnight, 2017).

   For example, suppose the designer wants to create a chair, with one of the parameters being the main dimension. Using this parameter, the system creates the design space, represented by the area within dashed lines in Figure 3. The algorithms then operate within this space, connecting points to generate all possible designs.

   It's important to note that as the number of boundary conditions increases, the design space decreases, which in turn reduces the number of possible results. This is because the solution space becomes more constrained.
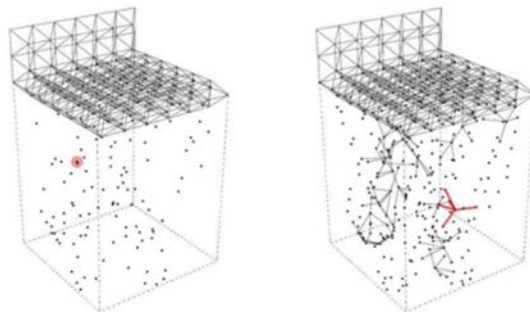
Figure 3. Space design example (Buonamici et al., 2020).

   At this stage, the software will apply algorithms to the space design, creating all possible designs within it. The resulting designs are referred to as phenotypes, which may include building history, building in history, and equations.

3. After applying algorithms to the space design, the results will begin to appear.

   At this stage, the software will provide all possible designs (solutions) within the design space. However, some of these designs (solutions) may not be suitable for the boundary conditions, and therefore the software will need to use filters to eliminate them (Buonamici et al., 2020; Krish, 2011).

Figure 4 illustrates the solution space. As you can observe, the performance envelope region is larger than the viable space. This indicates that the design space may contain unsuitable designs. To address this, filters are used to directly eliminate such designs, thereby retaining only those within the viable space.

Each small grey circle in the figure is referred to as a solution instance, and many more exist beyond what is shown in the figure. These instances can be applied to the established design goals. All designs that fall within the represented region will be integrated from these solution instances. (Krish, 2011).
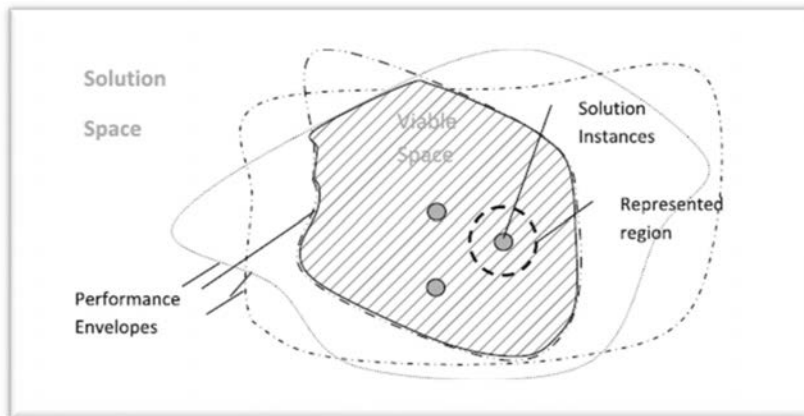
Figure 4. Solution space (Krish, 2011)**.**

4. Upon applying the algorithms to the space design, the software will generate a vast number of new designs, often numbering in the hundreds or even thousands. The number of designs is due to the software's ability to identify and evaluate all possible solutions within the design space.

The designer must then sift through these numerous designs to identify those that align with their goals. Fortunately, the software provides various sorting options to streamline this process. The designer can sort the designs according to specific criteria, such as mass, stiffness, displacements, and factor of safety.

By using these sorting options, the designer can quickly isolate designs that meet their specific requirements. This facilitates a more efficient and targeted approach to design, saving both time and effort in the process. Ultimately, this enables the designer to make informed decisions about which designs to pursue further, leading to improved outcomes and greater success.

Generative design method in mathematics:
Generative design is an approach to design where genetic algorithms generate multiple design options based on a set of input parameters and constraints. This

approach can be used in various fields, including architecture, engineering, product design, and more(Bhoskar et al., 2015; Kalyuzhnaya et al., 2021).

Mathematically, generative design can be formulated as an optimization problem. The goal is to find a design that satisfies a set of constraints while optimizing one or more objectives.

Formally, we can represent generative design as the following optimization problem in three parts (Du et al., 2021):

1. Variable design: input data of the design.

$$f_i(x), (i = 1,2,3, \dots N)$$

2. Constraint condition: boundary conditions or the design space.

$$g_j(x), (j = 1,2,3, \dots N)$$

3. Objective function: The aim function is to maximize the performance of the design.

$$h_k(x), (k = 1,2,3, \dots N)$$

The numerical solution of GDM can describe as (Kalyuzhnaya et al., 2021):

$$Y = H\left(\frac{M}{Z}\right)$$

where H is the operator to simulate data Z with model M.
So, the task of the mathematical model generative design or the mathematical workflow can be expressed as (Kalyuzhnaya et al., 2021; Wang et al., 2021)

$$PR^{max}(M^*) = \max_M f_R(M, T_{gen} \leq T_g), \quad M = \{M_p\}$$

Where PR^{max} is the maximum value of the fitness function, and f_R is a fitness function.

T_{gen} is the time required for model structure optimization with critical threshold T_g.

M_p is the space of the possible model structure.

The optimization problem can be solved using various techniques, such as gradient-based optimization, evolutionary algorithms, or other metaheuristic methods. The result is a set of optimal design solutions that satisfy the given constraints.

One example of generative design is in architectural design, where the goal is to optimize the layout of a building while satisfying various constraints such as maximum occupancy, structural stability, and energy efficiency. The design variables can include the location of walls, windows, and doors, as well as the

orientation and shape of the building. The objective function can be expressed as the energy consumption of the building, while the constraints can include structural stability and maximum occupancy.

Another example of generative design is in product design, where the goal is to optimize the shape and size of a product while satisfying various constraints such as manufacturability and cost. The design variables can include the dimensions and shape of the product, while the objective function can be expressed as the product's performance or cost. The constraints can include manufacturing constraints, such as maximum curvature or draft angle.

In conclusion, generative design is a powerful approach to design that uses mathematical optimization to generate multiple design options based on a set of input parameters and constraints. The approach can be used in various fields, including architecture, engineering, and product design, to optimize the design while satisfying various constraints.

Advantages of Generative Design Methodology (GDM) for Engineering and Design Applications.
Generative Design Methodology (GDM) has been widely adopted in various industries, including aerospace, product design, art, interior and exterior design, and industrial design. This is primarily due to the numerous advantages it offers over traditional design methods. In this paper, we highlight the benefits of GDM.

1. Reduced Development Time and Cost

GDM employs an iterative design approach, allowing designers to explore numerous design options concurrently while minimizing computational requirements. This approach significantly reduces the time and cost required for traditional design methods(Li & Lachmayer, 2018).

2. Customizable Product Development

GDM enables the creation of complex geometries that can be optimized to meet specific design requirements. By utilizing advanced algorithms, GDM can create designs with optimal performance characteristics that are often difficult to achieve through traditional design methods. Additionally, GDM can consider multiple constraints simultaneously, making it a powerful tool for product development(Li & Lachmayer, 2018).

3. Effective in Early-Stage Design

GDM is particularly effective in early-stage design, where incomplete assessment criteria and early-stage design models are frequently encountered. This is because GDM can operate with incomplete design specifications and provide designers with numerous design options, which they can evaluate and refine. Early-stage design is critical because it sets the foundation for subsequent design phases(Buonamici et al., 2020; Krish, 2011).

4. Embedded Design Intent and Intelligence

GDM incorporates design intent and intelligence directly into the generative model. This means that designers can input their design specifications, and the generative model can create designs that meet these specifications. Furthermore, GDM has basic CAD functions and dimensioning capabilities, enabling

geometric logic and connections to be included in the generated designs. This ensures that the designs created by GDM are not only optimal but also functional and manufacturable(Ahmed & Gupta, 2022; Wang et al., 2021).

5. Increased Creativity

GDM generates thousands of design options that designers and engineers can evaluate and refine. This leads to increased creativity as designers and engineers are exposed to designs that they may not have considered otherwise. Additionally, GDM allows designers to explore design spaces that are not possible with traditional methods, leading to the creation of unique designs(Li & Lachmayer, 2018).

2. Method and materials

The generative design method is a modern technique that uses algorithms and artificial intelligence to explore novel designs. This approach offers numerous advantages over traditional design methods. To successfully implement the generative design method in a design project, it is essential to follow the stages outlined in the introduction section of this paper.

For this study, we use Autodesk Fusion 360, which is a cloud-based 3D CAD, CAM, and CAE software tool designed for product design and development. The software comes equipped with a generative design feature that enables users to generate multiple design solutions based on specific criteria such as materials, manufacturing processes, and performance requirements.

This section is divided into two parts. The first part will focus on a GE bracket to illustrate how the generative design method works. We will provide a comparison between the traditional and generative designs, with a particular focus on mass, von-mises stress, and displacement.

In the second part, we will design a multirotor structure using the traditional design approach. Then, we will apply the generative design method to this structure as a percentage. We will provide detailed explanations of how the generative design method was applied in this part.

Aluminum is widely used in aerospace because it is lightweight and has good mechanical and strength properties, and the Aluminum AISI10Mg is used in complex geometry and can use in additive manufacturing, which is a boundary condition in GDM, so the Aluminum AISI10Mg will be the material for the whole designs (traditional and GDM).

The first boundary condition is material, the material chosen is Aluminum AISI10Mg, table 1 shows the important mechanical properties of the Aluminum AISI10Mg which will use to calculate the factor of safety for both parts.

The second boundary condition is the manufacturing method, the traditional design will be applied to manufacturing by additive manufacturing method or any other method, and the generative design method will use additive manufacturing method and be unrestricted about the manufacturing method in the study for the comparison. For both parts.

Note: all the boundary conditions used will be the same for the traditional design and generated designs.

Table 1. Aluminum AISI10Mg mechanical properties.

Material	Young modulus (GPa)	Poisson's ratio	Shear modulus (MPa)	Density (g/cm^3)	Yield strength (MPa)	Tensile strength (MPa)
Aluminum AISI10Mg	71	033	26690	2.670	240	460

GE bracket.

The GE bracket is a critical component in ensuring the safe and efficient operation of an airplane engine. Its primary function is to provide support for the cowling, which covers and protects the engine.

Since the engine is always running, the bracket must be able to withstand the constant vibration and stress generated by the engine. Any cracking or distortion of the bracket could result in catastrophic failure of the engine or other components, which could lead to a serious accident.

While the bracket may only be utilized occasionally during maintenance, its importance cannot be overstated. It is a vital part of ensuring the overall safety and reliability of the aircraft, and any issues with the bracket could have significant consequences.

Overall, the GE bracket is a crucial component of airplane engine maintenance and must be carefully designed and maintained to ensure the safe and efficient operation of the aircraft.

the third boundary condition is the forces, the forces applied in the bracket are 5000N in the Y and Z axes.

Traditional design.

To design a GE bracket in a traditional way, one must adhere to the engineering design stages outlined in the introduction section. However, in this first part, we have chosen to use a standard or straightforward design of the bracket to make a fair comparison. We obtained the design from the GrabCAD site.
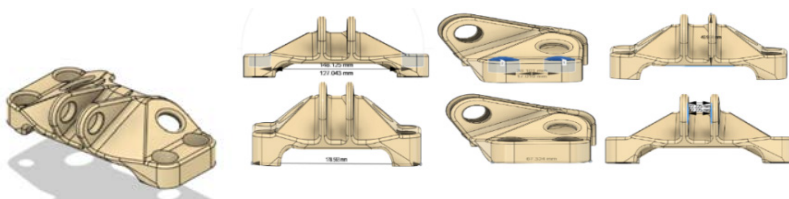
Figure 5. GE bracket designed in a traditional way. By GrabCAD.

Figures 5 and 6 illustrate the main dimensions of the design and the location where forces are applied.
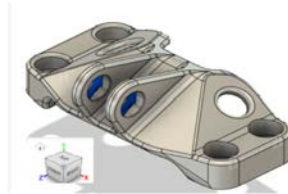
Figure 6. Forces applied in GE bracket.

The forces applied to it for analysis, to get the stresses and displacement distribution on it.

Generative design.
As mentioned earlier, to use the GDM, we must follow a set of steps. The first step involves selecting the Autodesk Fusion 360 student version software to apply the GDM.

The second step entails designing the space or genotype. In our case, we retrieved the base form of the GE bracket from the software library. This base form has the same main dimensions as the traditional design. The space design includes setting boundary conditions. There are three boundary conditions to consider. The first is the material, which in our case was Aluminum AISI10Mg. The second condition is the manufacturing method, which can be additive or unrestricted. The third boundary condition concerns the forces applied to the bracket. In our design, the forces applied in the Y and Z axes were 5000N. Detailed illustrations of the methodology are presented in the figures below.

Figure 7 shows the generated base form with the main dimensions.
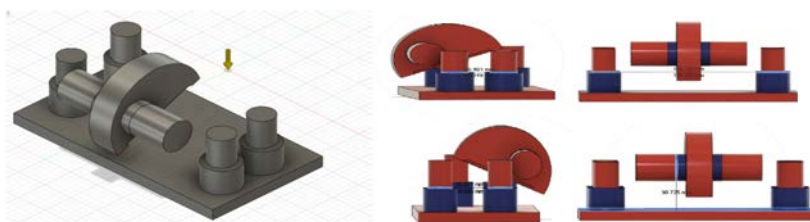
Figure 7. Generated base form.

Figure 8 shows the initial shape of the GE bracket, which we obtained from the generated base form. This shape is merely intended to facilitate understanding of how to construct the bracket from this form. It is not a step in

the GDM methodology, but rather a visualization of the bracket derived from this form.

Figure 8 also shows the primary dimensions of the starting shape of the bracket.
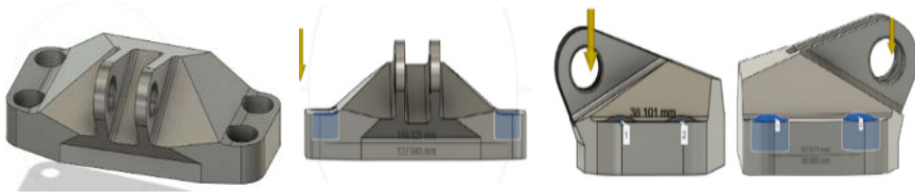
Figure 8. Starting the shape of the GE bracket with
the main dimensions.

Figure 9 illustrates how to set up the GDM on the base form. In Figure 9A, the blue parts are converted to green parts in 9C. These green parts are called reserved areas, meaning that the geometry of these areas should not be modified during the generation of outcomes. In contrast, the red parts in 9C are called obstacle parts, which refer to empty spaces where materials should not be added. The rows in 9C represent the forces that were previously applied to the base form, as discussed earlier.
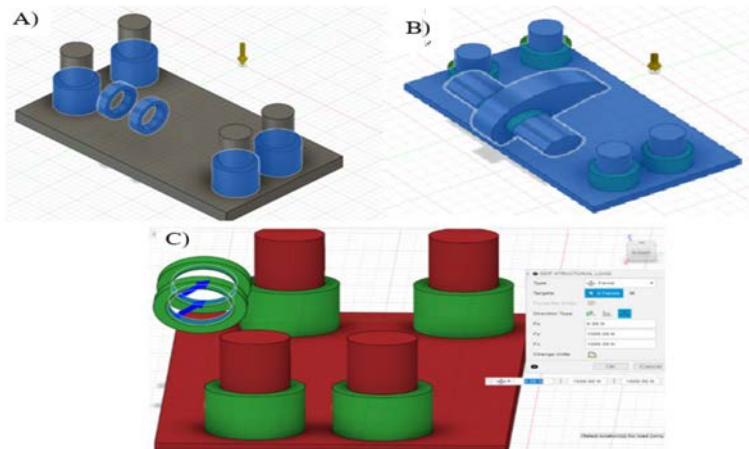
Figure 9. A- reserved area, B- main dimensions of generation space,
C- forces applied.

The final boundary condition pertains to the factor of safety, which is a critical measure of the reliability of the design. Upon analysis of the boundary

conditions, the traditional design yielded a factor of safety of 2.36. In order to ensure a fair comparison, any generated designs should possess a factor of safety that is not less than 2.36. Moreover, the Federal Aviation Regulation mandates that the factor of safety should not fall below 1.5. Given that the traditional design satisfies the regulatory requirements, we will utilize it as the basis for our example. The software is employed in calculating the factor of safety based on the yield strength of the material, as indicated in Table 1.

The other boundary condition is the manufacturing method we decided to choose from the software additive manufacturing and unrestricted, the manufacturing method is important because it affects the type of used material and the other properties such as mass.

Multirotor structure

This section will use the same methodology as the first part, with the exception that a multirotor structure (quadcopter) will be designed and the traditional design will serve as the basis for generative design. There will be three cases in generative design: the first case will use 60% of the traditional design as the base form, leaving 40% of the design subject to generative design; the second case will generate 55% of the traditional design and keep 45% as the base form for generative design; the third case will generate 80% of the traditional design and keep 20% as the base form. The specific cases will be illustrated in more detail in the figures below (in the section on **multirotor structure - generative design**). Autodesk Fusion 360 will be used for the traditional design in this section as well.

As previously stated, the material for this design is Aluminum AISI10Mg, and the main dimensions will be consistent between both the traditional and generated designs, which will be demonstrated in the figures to follow.

Forces of 50 N will be applied to each arm as a motor, resulting in a total thrust of 200 N. Therefore, the combined weight of the multirotor, electronic components and motors must not exceed half of the total thrust (100 N or 10 kg) to maintain optimal flight performance.

The minimum factor of safety is 1.5 based on federal aviation regulations, we decided to set it to 2.

The traditional design will be able to manufacture by any method, for generative design will use additive manufacturing as a method and is unrestricted about the method also.

Traditional design.

The frame design was initially developed through the traditional design process and created using Fusion 360, as depicted in figures 10 and 11. The design is relatively complex, as it will serve as a co-design in the generative design process, which will be discussed in further detail later on.
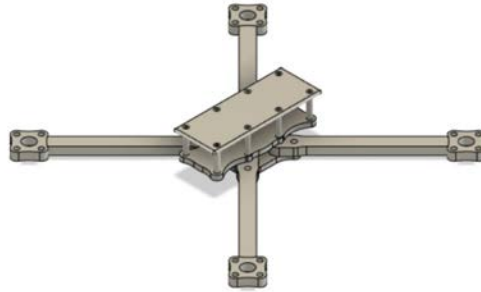
Figure 10. Traditional design.
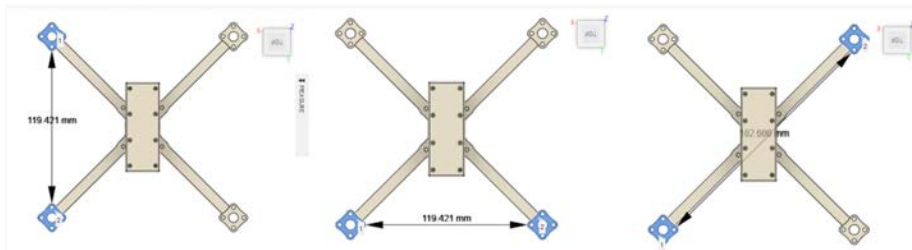
Figure 11. Main dimensions of traditional design.

Generative design.

The GDM will take the traditional design as a starting point or base form to apply his algorithms on it, the goal is to explore and study the different base forms for the same traditional design can impact in mass, stress, displacement, and factor of safety when the space design is more restricted.

This part will illustrate three cases:

Case 1: In the first case, we will generate a design that represents 40% of the traditional design, as shown in Figure 12. Specifically, we will apply the design methodology to the arms of the frame, such that the arms account for 40% of the overall mass of the design.
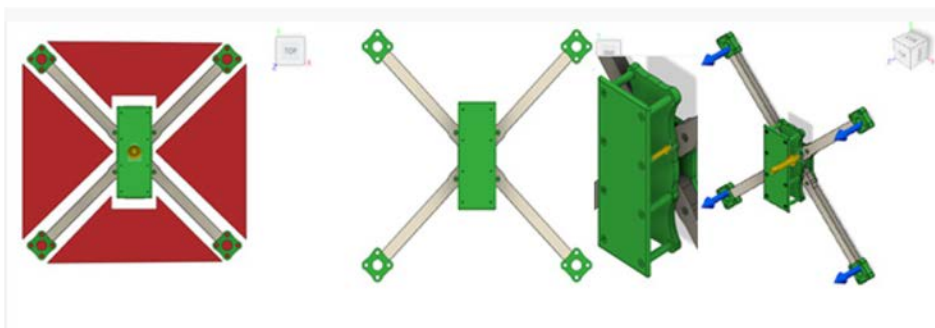
Figure 12. Case 1 generates 40% of traditional design.

To help guide the design process, we will use color coding. The green parts represent geometry that we will preserve during the optimization process. Meanwhile, the red parts represent areas where we will not add any materials. These red parts are designed to accelerate the optimization process and help us arrive at a quadcopter shape more quickly, rather than starting with a rectangular shape.

Finally, the blue rows indicate the forces that will be applied to the design.

Note: Zooming on the center of the quadcopter (figure 12). To enable you to visualize the difference between figures 12 & 13 more clearly. Specifically, the main difference is noted in the columns connecting the upper and lower lids.

Case 2: To generate the design for this case, we will use 55% of the traditional design and apply the GDM to both the arms and a portion of the center, as shown in Figure 13.
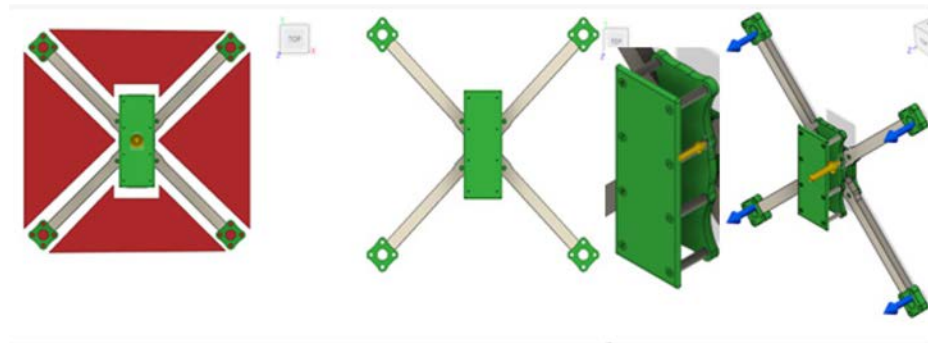
Figure 13. Case 2 generates 55% of traditional design.

Case 3: we will generate a design that represents 80% of the traditional design. To do this, we will save the geometry of the motor base only and then apply the GDM to the entire design, as shown in Figure 14.
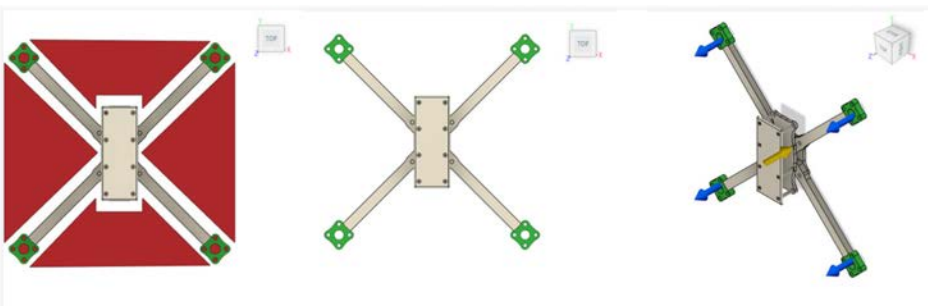
Figure 14. Case 3 generates 80% of traditional design.

3. Results and discussion.

GE bracket
Traditional design

As previously mentioned, the traditional design used in this study was obtained from the GrabCAD site. To ensure consistency in our results, we applied the same boundary conditions to the traditional design as we did to the optimized designs. Specifically, we applied a force of 5000 N in the Y and Z axes and fixed the design in four locations on the bracket.

The mass of the traditional design was measured to be 494.253g, with a maximum displacement (total) of 0.2299mm and a maximum von Mises stress of 101.7MPa. These results were obtained through simulation analysis, and are presented in Figure 15, which displays the distribution of displacement and stress on the traditional design.

These findings serve as a baseline for comparing the performance of the optimized designs generated using the GDM. By comparing the results of the traditional design to those of the optimized designs, we can evaluate the effectiveness of the GDM in reducing weight while maintaining structural integrity.
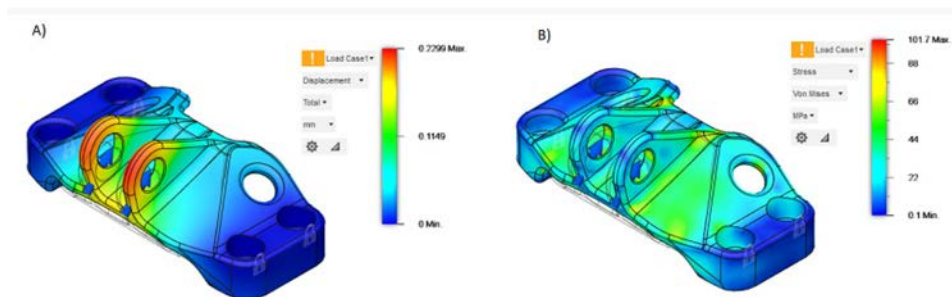
Figure 15. Traditional design analysis, A) displacement,
B) von mises stress.

Generative design

The generative design method offers a wide range of possible designs within the defined space constraints (space design). As the number of possible designs can be extensive, with hundreds or thousands of variations, this study focused on identifying the lowest mass design for comparison with the traditional design. To ensure that the optimization process was centered on minimizing mass.

Figure 16 provides an overview of the generative design process and demonstrates how the method iteratively explores possible designs by integrating insights from previous iterations. While it is not practical to include all possible designs in this paper, the figure provides an illustrative example of the generative design method in action.

By the GDM, this study aims to identify an optimized design that balances mass reduction with structural integrity. The generative design approach provides a valuable means of exploring the design space and can help to identify new solutions that may not have been possible through traditional design methods.

Figure 16. Progress in GDM.

As a result of using additive manufacturing and the unrestricted manufacturing method in this study, the results of the generative design method will be presented in two parts. The first part will showcase the designs generated using the additive manufacturing approach, while the second part will present the designs generated using the unrestricted manufacturing method.

This approach is necessary to understand the impact of the different manufacturing methods on the final design and to identify any potential trade-offs or limitations associated with each approach. By examining the results of both methods, this study aims to provide a comprehensive overview of the potential benefits and drawbacks of each manufacturing method, as well as any design insights that can be gleaned from the generative design process.

Generated design with additive manufacturing method.
From the hundreds of designs generated through the GDM, we selected the lowest mass design (shown in Figure 17) that is manufacturable using additive manufacturing.

Figure 17. Generated design with additive manufacturing.

After analyzing the design using additive manufacturing as the boundary condition, we obtained a design with a mass of 287.921g. The design was then

exported to the simulation section of Fusion 360 software for analysis. The analysis revealed a maximum displacement (total) of 0.179mm and a maximum von Mises stress of 101.65 MPa, as illustrated in Figure 18 which shows the distribution of displacement and stress on the design.
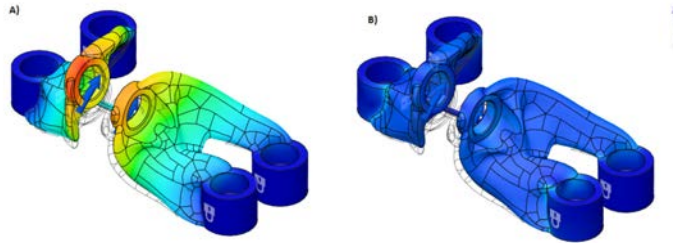
Figure 18. Generated design additive manufacturing analysis, A) displacement, B) von mises stress.

Generated design with unrestricted manufacturing method:
Similar to the generative design with additive manufacturing, we followed the same steps to analyze the design using the unrestricted manufacturing method, as shown in Figure 19. The design was then analyzed using the simulation section of Fusion 360 software.

Figure 19. Generated design unrestricted manufacturing method.
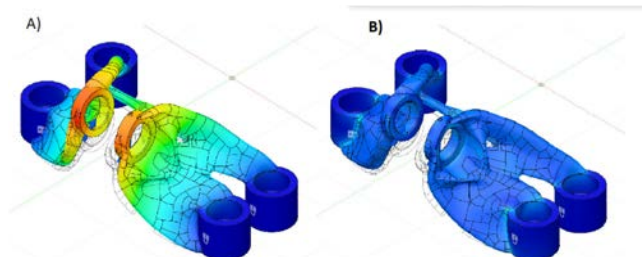
Figure 20. Generated design unrestricted manufacturing analysis, A) displacement, B) von mises stress.

Following the analysis of the second generated design using the unrestricted manufacturing method (shown in Figure 20), the mass was found to be 279g, with a maximum displacement (total) of 0.181mm and a maximum von Mises stress of 101.7MPa. The distribution of displacement and stress is shown in Figure 20.

Comparison of the generated designs to traditional design:
Table 2 displays the mass, maximum displacement (total), and maximum von Mises stress of each design. The mass is presented as a percentage of the traditional design to highlight the impact of GDM on weight reduction. A negative value indicates a reduction in weight compared to the traditional design.

Table 2. Comparison between traditional design and generated designs

Design method	Mass [g]	Mass [%]	Maximum displacement (total) [mm]	Maximum von mises stress [MPa]
Traditional method	494.253	100%	0.2299	101.7
Generated with additive manufacturing	288.14	-41.7%	0.179	101.6
Generated with an unrestricted manufacturing method	279.252	-43.5%	0.181	101.7

The three charts presented in Figure 13 provide a comparison between the three designs with respect to various parameters. Each chart focuses on a different parameter, allowing for a comprehensive evaluation of the designs.
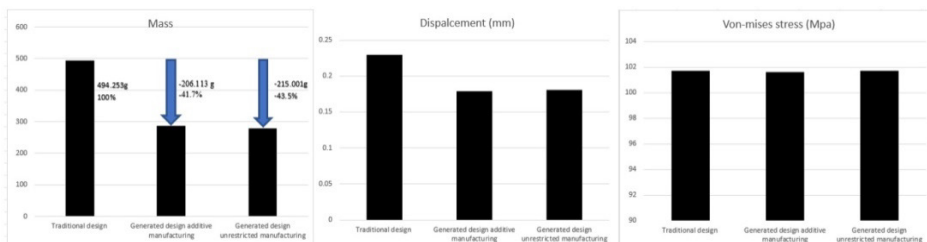
Figure 21. Comparison in mass, displacement, and von mises stress between the designs.

The Generative Design Method (GDM) employs software algorithms to explore all possible design options that refine boundary conditions and goals. The results of GDM in our previous example are more complex than traditional design methods, which may affect production time. However, on the other hand,

the GDM provides a design that is lighter than the traditional one, leading to savings on raw materials since they are lighter. Depending on the purpose of the design, whether for commercial or personal use, the designer or producer can decide on the appropriate method.

The generated design using additive manufacturing was lighter than the traditional design by 41.7%, and the unrestricted manufacturing method yielded a design that was 43.5% lighter than the traditional design. The manufacturing method is one of the boundary conditions that affect the mass of the GDM results.

Therefore, it is essential to consider the trade-offs between complexity, production time, and raw material usage when selecting the appropriate design method. The GDM offers an advantage in reducing the mass of the design, which can lead to a decrease in material usage and cost savings.

Multirotor structure

Traditional design

Table 3 shows the results obtained after applying the boundary conditions to the traditional design. The mass of the design was measured to be 105.557 g, with a maximum displacement (total) of 0.806 mm and a maximum von Mises stress of 80MPa, and a minimum factor of safety of 3.7. These results serve as a baseline for comparing the performance of the optimized designs generated using the generative design method.

Table 3. properties of traditional design.

Mass	105.557 g
Max Von misses stress	80 MPa
Max Displacement	0.806 mm
Min factor of safety	3.7

Generative designs

This section presents the results of applying the GDM to generate hundreds of new designs for each case. As an example, we will introduce the first case with unrestricted manufacturing method results. Figure 22 shows a selection of designs obtained during the iterative optimization process.

The methodology employed in this study generated hundreds of new designs for each of the three cases. Due to a large number of results, it is not feasible to present all of them in this paper. However, the software used in this study includes filters that can assist the designer in selecting designs that meet specific

criteria. For the purpose of comparison, we sorted each case by mass and selected the lowest mass design for each case. In addition, the software provided information about the mass, maximum von Mises stress, maximum displacement, and a minimum factor of safety for each design.

Figure 22. Case 1 unrestricted manufacturing method results.

This approach demonstrates the potential of the generative design method to produce complex designs that may not have been achievable using traditional design methods. The use of filters allows the designer to quickly and efficiently identify designs that meet specific requirements, saving time and resources in the design process. This method can potentially revolutionize the way designers approach design problems, allowing them to explore a wider range of design options and achieve optimal results.

Table 4 provides mass (g), Max von misses stress (MPa), Max displacement (mm), and Min factor of safety for each case with different manufacturing methods.

The next shows the properties of each design with different manufacturing methods as we mentioned above in the method and material section, in the sub-section of multirotor.

Table 4. The properties of each case.

Case/ manufacturing method	Mass (g)	Max von misses stress (MPa)	Max displacement (mm)	Min factor of safety
case 1 unrestricted manufacturing	92	8.487	0.041	28.279
case 1 additive manufacturing	92	11.809	0.067	20.323
case 2 unrestricted manufacturing	89	8.773	0.042	27.357
case 2 additive manufacturing	90	11.98	0.069	20.003
case 3 unrestricted manufacturing	32	67.519	0.882	3.5
case 3 additive manufacturing	33	96.963	1.487	2.47

Comparison between generated designs to traditional design.
The comparison focuses on mass because when it comes to design, the mass of an object plays a crucial role in determining its overall shape, limitations, and functionality. The mass of an object is a measure of the amount of matter it contains, and it has a direct impact on the object's physical properties.

When comparing designs, it's important to consider the mass of each object in order to accurately assess its strengths and limitations. A design with a lower mass may be more agile and efficient but may also be less stable or sturdy. A design with a higher mass may be stronger and more stable but may be slower or less energy efficient.

In conclusion, the mass of an object is a critical factor in design, affecting everything from its shape and size to its functionality and limitations. When comparing designs, it's essential to consider the mass of each object to determine which design will best meet your needs.

But here the generative design method demonstrates how designs can achieve lower mass while maintaining or even improving physical properties compared to designs with fewer mechanical properties.

Table 5. Comparison between traditional design and generated designs.

Case/ manufacturing method	Mass (g)	Mass [%]	Max von misses stress (MPa)	Max displacement (mm)	Min factor of safety
Traditional design	105.557	100%	80	0.806	3.7
case 1 unrestricted manufacturing	92	-12.8433%	8.487	0.041	28.279
case 1 additive manufacturing	92	-12.8433%	11.809	0.067	20.323
case 2 unrestricted manufacturing	89	-15.6854%	8.773	0.042	27.357
case 2 additive manufacturing	90	-14.738%	11.98	0.069	20.003
case 3 unrestricted manufacturing	32	-69.6846%	67.519	0.882	3.5
case 3 additive manufacturing	33	-68.7373%	96.963	1.487	2.47

The upcoming figure will display four charts, with each chart representing a different property. Each bar in the chart corresponds to a distinct case or

traditional design. under each bar, a number will be displayed which can be found in the table below the figure to determine which design it represents.

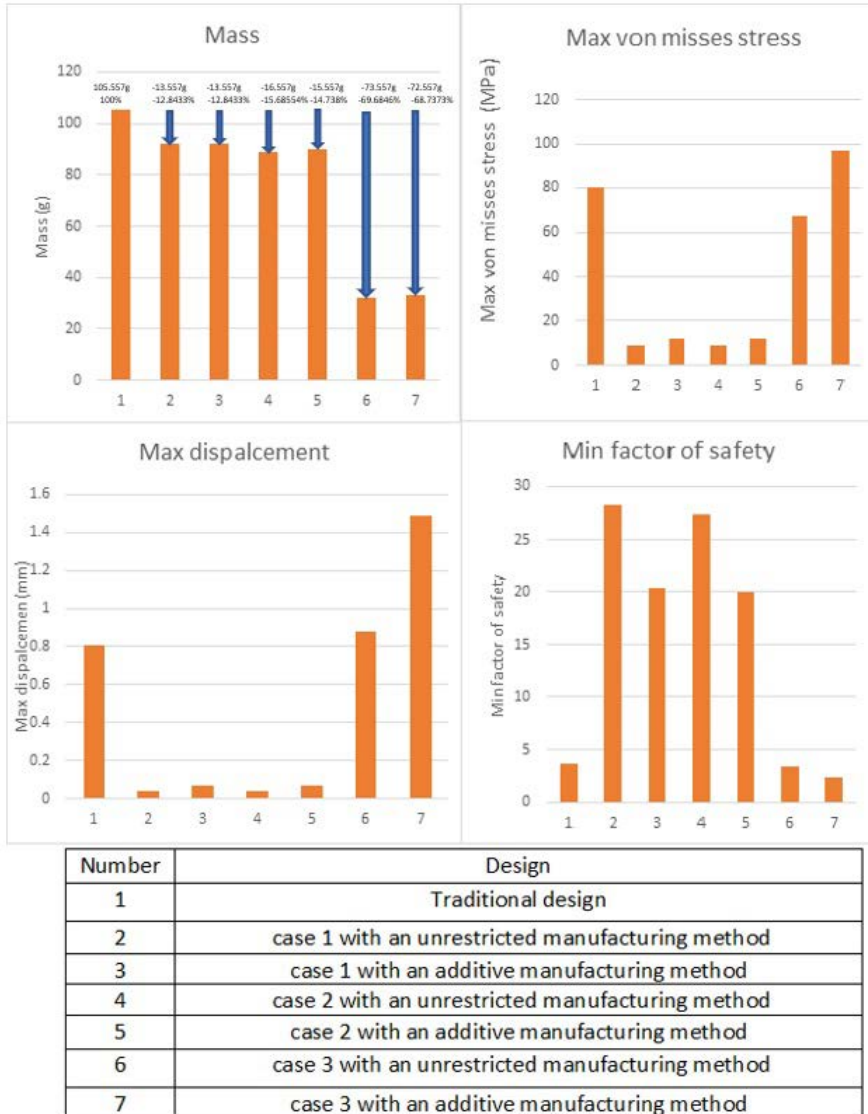| Number	Design
1	Traditional design
2	case 1 with an unrestricted manufacturing method
3	case 1 with an additive manufacturing method
4	case 2 with an unrestricted manufacturing method
5	case 2 with an additive manufacturing method
6	case 3 with an unrestricted manufacturing method
7	case 3 with an additive manufacturing method

Figure 23. Comparison between traditional design and generated designs.

The comparison between traditional design and the other three case designs reveals that all generated designs have less mass than the traditional design. The percentage of decrease for each case is displayed above the corresponding column, with case 3 exhibiting a significant decrease in mass compared to the

other cases. This reduction indicates that reducing the restricted part of the design during the process, thereby increasing space design leads to a greater reduction in mass.

Regarding maximum von mises stress, case 3 with additive manufacturing shows the highest value, although significant decreases are observed in cases 1 and 2 when compared to the traditional design. This suggests that the GDM helps reduce the mass of the design while keeping or improving its rigidity, as observed in cases 1 and 2.

The maximum displacement also shows a significant decrease in cases 1 and 2 when compared to traditional design, with case 3 with additive manufacturing exhibiting the highest value.

In terms of the minimum factor of safety, which represents the lowest factor of safety found in the design after applying all boundary conditions, cases 1 and 2 exhibits a significant increase compared to the traditional design, whereas case 3 is closer to the traditional design.

Overall, the GDM can generate a design with a lower mass than the traditional design, reduce stress and displacement, and increase the factor of safety.

In conclusion, Generative Design Methodology (GDM) is a powerful tool for engineering and design applications. It offers numerous advantages, including reduced development time and cost, customizable product development, effectiveness in early-stage design, embedded design intent and intelligence, and increased creativity. As demonstrated in this paper, these advantages have been scientifically documented and validated, making GDM a valuable tool for designers and engineers.

Future plans for optimization multirotor structure by the generative design method:

There are several studies on generative design methods, illustrating the method with examples in architecture or other fields, in this example the researcher creates a comparison between generative design, topology optimization, and common designs (traditional) for Joints for the treelike column (Wang et al., 2021), one of the biggest problems of multirotor is flight duration which has an inverse relation with weight and positive relation with batteries capacities, The objective of this research is to optimize the design of a multirotor structure using generative design methods and additive manufacturing, in order to improve flight duration and reduce weight while maintaining structural strength and stability, the generative design method it is applied on the multirotor structure and get a lower mass than traditional one in static behavior in our study, to create a multirotor should to take in your consideration the flight principle (Yaw, Roll, Pitch) and the stabilization of the multirotor each these requirements can be determined b specific equations also the flight duration (Modelling and Control of Quadcopter) , based on that we thinking to apply these equations to the generative design method equations, after this stage will reflect the new equations and the specific multirotor equations to the algorithms, An algorithm is a set of instructions or procedures that are followed to solve a particular problem or to perform a specific task. Algorithms are commonly used in computer programming, where they serve as the foundation for designing

software and computer systems (David Berthelot & Luke Metz, 2017; Khan & Awan, 2018), so these equations will be as a restrictions or boundary conditions for the algorithms to create new designs based on those equations. Will use FEA to analyze the results and will determine a filter for the results to sort by the flight duration with the flight principles working smoothly and correctly. The algorithms used are genetic algorithms are a type of optimization algorithm inspired by the principles of natural selection and genetics. They are used to solve complex problems (Bhoskar et al., 2015), Afterwards, we seek to validate the findings and their relevance to reality and determine if the results obtained from this method are truly valid and valuable.

Conclusion

- The generative design method is used to explore new designs by using software algorithms, these designs can't be created by using the traditional design method.
- All generative design results meet the required goals and get lower mass than traditional design.
- The process of generative design produces a large number of new designs, numbering in the hundreds or even thousands. Each design is unique and may be more complex than traditional designs. While this complexity may impact the ease of production, it also allows for greater material savings. In the end, the designer or client must select the design that balances material conservation with ease of production from among the many options generated.
- By allowing more space for the application of our algorithms in the generative design method, we can obtain a greater number of results. Similarly, if we reduce the restrictions on the area where the method is applied, we can observe varied outcomes. For example, in the case of the multirotor structure, we utilized the same base form but with differing percentages.
- The generated designs with unrestricted manufacturing methods got a lower mass than the generated designs used additive manufacturing.

Acknowledgment

References

[1] ABET. (n.d.). Criteria for Accrediting Engineering Programs, 2019 – 2020.
[2] Ahmed, S., & Gupta, M. K. (2022). Investigations on motorbike frame material and comparative analysis using generative design and topology

optimization. Materials Today: Proceedings, 1440–1446. https://doi.org/10.1016/j.matpr.2021.12.040

[3] Bhoskar, T., Kulkarni, O. K., Kulkarni, N. K., Patekar, S. L., Kakandikar, G. M., & Nandedkar, V. M. (2015). Genetic Algorithm and its Applications to Mechanical Engineering: A Review. Materials Today: Proceedings, 2(4–5), 2624–2630. https://doi.org/10.1016/j.matpr.2015.07.219

[4] Buonamici, F., Carfagni, M., Furferi, R., Volpe, Y., & Governi, L. (2020). Generative design: An explorative study. Computer-Aided Design and Applications, 18(1), 144–155. https://doi.org/10.14733/cadaps.2021.144-155

[5] Chien, S.-F., & Flemming, U. (n.d.). Design space navigation in generative design systems. In Automation in Construction (Vol. 11). www.elsevier.comrlocaterautcon

[6] David Berthelot, & Luke Metz. (2017). BEGAN: Boundary Equilibrium Generative Adversarial Networks.

[7] Du, W., Wang, H., Zhu, L., Zhao, Y., Wang, Y., Hao, R., & Yang, M. (2021). Innovative joint for cable dome structure based on topology optimization and additive manufacturing. Materials, 14(18). https://doi.org/10.3390/ma14185158

[8] Junk, S., & Burkart, L. (2021). Comparison of CAD systems for generative design for use with additive manufacturing. Procedia CIRP, 100, 577–582. https://doi.org/10.1016/j.procir.2021.05.126

K. MALLIKARJUNA RAO, K. LALIT NARAYAN, & MMM SARCAR. (2008). Computer Aided Design and Manufacturing.

[9] Kalyuzhnaya, A. V., Nikitin, N. O., Hvatov, A., Maslyaev, M., Yachmenkov, M., & Boukhanovsky, A. (2021). Towards generative design of computationally efficient mathematical models with evolutionary learning. Entropy, 23(1), 1–26. https://doi.org/10.3390/e23010028

[10] Khan, S., & Awan, M. J. (2018). A generative design technique for exploring shape variations. Advanced Engineering Informatics, 38, 712–724. https://doi.org/10.1016/j.aei.2018.10.005

[12] Krish, S. (2011). A practical generative design method. CAD Computer Aided Design, 43(1), 88–100. https://doi.org/10.1016/j.cad.2010.09.009

[13] Lee, J. H., & Ostwald, M. J. (2022). The relationship between divergent thinking and ideation in the conceptual design process. Design Studies, 79. https://doi.org/10.1016/j.destud.2022.101089

[14] Li, H., & Lachmayer, R. (2018). Generative Design Approach for Modeling Creative Designs. IOP Conference Series: Materials Science and Engineering, 408(1). https://doi.org/10.1088/1757-899X/408/1/012035

[15] McKnight, M. (2017). Generative Design: What it is? How is it being used? Why it's a game changer. KnE Engineering, 2(2), 176. https://doi.org/10.18502/keg.v2i2.612

[16] mikell p.groover, & emory w.zimmers. (1984). CAD/CAM: computer aided design and manufacturing .

[17] Modelling and control of quadcopter A? (n.d.).

[18] NASA. (n.d.). engineering design process .

[19] Wang, H., Du, W., Zhao, Y., Wang, Y., Hao, R., & Yang, M. (2021). Joints for treelike column structures based on generative design and additive manufacturing. Journal of Constructional Steel Research, 184. https://doi.org/10.1016/j.jcsr.2021.106794

[20] WİNARNO, N. (2020). The Steps of the Engineering Design Process (EDP) in Science Education: A Meta-Analysis. Journal for the Education of Gifted Young Scientists. https://doi.org/10.17478/jegys.766201

[21] yousef haik, sangarappillai sivaloganathan, & tamer shahin. (2018). engineering design process (third edition). Zhuming Bi, & Xiaoqin Wang. (2020). Computer Aided Design and Manufacturing.

Visible range spectrophotometric colour results and shear strength data of sandy loam soil

Alaa El HARIRI[1] , Péter KISS[2]

[1] Mechanical Engineering Doctoral School –
Hungarian University of Agriculture and Life Sciences,
2100 Gödöllő, Páter K. u. 1., Hungary

[2] Institute of Technology, Department of Vehicle Technology –
Hungarian University of Agriculture and Life Sciences,
2100 Gödöllő, Páter K. u. 1., Hungary

Abstract

The soil shear strength and its parameters - the shear cohesion and the internal friction angle - are important values needed for studying the performance of a vehicle on soil terrain. This article contains strength results (shear strength and its parameters) of a soil type. The tested soil is the sandy loam soil, where the shear strength results were measured using the direct shear test and the shear strength parameters were obtained relying on drawing the Mohr-Coulomb line. In addition to the strength results, the article contains colour results of the tested soil at different moisture contents, measured using the visible band spectrophotometric technology (spectrum; 400-700 nm). Linking the soil shear strength values to its colour through the moisture content, achieved by laboratory work, might be a solution for identifying the shear strength of the soil and its parameters in the field. The process of correlating the soil colour and the strength values (cohesion, internal friction angle, and the shear strength) at different moisture contents is presented in the article. The measurements were carried out at the Hungarian University of Agriculture and Life Sciences (MATE - Department of Vehicle Technology Laboratory).

Keywords

Soil shear strength; Sandy loam soil; Direct shear test; Mohr-Coulomb diagram; Shear cohesion; Internal friction angle; Soil spectral behaviour; Visible range Spectrophotometer; Soil colour.

1. Introduction

Ending up with the shear strength and the shear strength parameters of soil is a step that is important in studying the shearing failure of the soil under a shearing load having simultaneously a consolidation normal load applied on the soil. The cohesion of the soil shows its consistency and has two connotations: In physics,

soil cohesion reflects the cohesive bonding between the soil particles, but in soil mechanics, the shear cohesion is the shear strength of the soil when the applied normal stress on the surface is equal to zero [36]. The internal friction angle is a parameter reflecting the internal resistance of the soil to shearing resulting from the friction on the particle's level (interparticle sliding friction and geometrical interface). The cohesion strength parameter is stress independent parameter, while the internal friction angle depends on the applied stress. The shear strength parameters serve in finding the shear strength of the soil by the usage of the Coulomb criterion that is of a similar idea to the Mohr failure criterion (the soil shear strength is as function of the applied consolidation stress), but combines the shear strength parameters and the applied normal stress in a linear function to calculate the shear strength [12] [18].

The soil thrust which results from the shearing of the terrain by the tractive element (wheel/track) is calculated using the shear strength of the soil. In soil mechanics, the soil thrust is a property that contributes to the propelling of a vehicle [16].

The change in the soil moisture content influences its behaviour by affecting its physical and mechanical properties (load-bearing capacity and shear strength). Ahmed has shown experimentally in his article the change in load-bearing capacity of the sandy loam soil with the change in the moisture content [6]. In the case of clayey soils, the increase in the moisture content weakens the bonding between the soil particles resulting in decreasing its cohesion, and the decrease in the moisture increases the internal friction [25]. The soil's physical composition, dampness (water content), density, and initial compression state affect the soil deformation resulting from the passage of a vehicle [20]. The moisture content is the most influencing soil condition on the soil strength [26].

There are different methods used for measuring the shear strength of soil, but none of these methods is standardized, so choosing the suitable method for measuring the shear strength is decided based on the case of study. For studying land locomotion cases it is important to choose the shear test that closely emulates the interaction between the tractive element (wheel/track) and the terrain. Direct shear test resembles most closely the failure mechanism of soil beneath a tire, thus the soil shear strength results obtained using this test can be used for studying a vehicle's performance on the soil [26]. In the direct shear test the soil is shearing along a predetermined plane [24], thus simplifying the case of the soil shear failure for measuring the displacement as a function of the applied shear stress, which is hard to be studied in the field where the failure plane is unidentified or difficult to be obtained.

Soils might reflect a wide range of colours, the grey, black, white, reds, browns, yellows, and greens [11]. The resulting colour of a soil is due to different processes and conditions influencing the soil, the minerals present in the soil, and the content of the organic matter [31]. The organic matter is what mostly influences the soil colour [4], that is why scientists worked on relating the darkness of the soil colour to its organic matter content [34] [11] [30] [17].

Different methods are used for measuring or identifying the colour of the soil such as the Munsell charts and the spectrophotometric technology. The

spectrophotometer is a precise quantitative technology that works based on tangible results (spectral reflectance). The reflected wavelength of the sent light wave (its wavelength is in the visible spectrum range; 400-700 nm) is the value that describes the colour of the soil at a specific moisture content.

The direct shear test machine will be used for measuring the soil shear strength parameters at different moisture contents, then upon ending up with the curves fitting (cohesion and internal friction angle) the resulting shear strength parameters at different moisture contents, these parameters can be predicted from the resulting curves at any input moisture value. The soil moisture value in the field is predicted using the curve fitting the colour reflectance of the soil at different moisture contents (curve obtained from laboratory work), having a given soil colour reflectance as an input (measured by the spectrophotometer).

Finally, the shear strength and its parameters will help in studying the land locomotion of a vehicle, and if not serving in adjusting the design of the vehicle's tractive element or its power system, at least taking the right decision (Go/no Go) before moving on a soil zone (high moisture), so the vehicle doesn't get immobilized. Having the strength parameters connected to the colour of the soil at different moisture contents will facilitate knowing the soil terrain strength parameters in the field (real-time terramechanics case).

2. Research significance

The main target from the prepared article is to show the ability of predicting the shear strength parameters from the colour of the soil. The process of linking the colour to the shear cohesion and the internal friction angle is mentioned in details. This idea is new and pioneer in terramechanics field. Reaching convincing results (after validating field measurements) will help in predicting the performance of a vehicle on soil terrain based on the colour of the soil. This work is a tremendous step in terramechanics science (land locomotion), especially that many fields have interest in off-road engineering projects (agriculture, military…). Better vehicle performance on soil terrain leads to less fuel consumption and safe drive.

There is a gap in our work that is divided into two parts. The first part is that the measurement is restricted to the usage of a spectrophotometer measuring the colour in the visible band (spectrum; 400-700 nm), which might not be useful in measuring the colour of the soil at high moisture content. The second part is that even though the shear strength parameters are obtained using the direct shear test, but there aren't cohesion and internal friction angle standardized results in the field's database (terramechanics or soil mechanics field) to compare the obtained results to. Confirming the obtained results requires field measurement for measuring a performance parameter (such as vehicle drawbar pull) using a sensor, and the measured value is compared to the calculated result using a terramechanics model (the shear strength parameters substituted in it).

3. Measuring the shear cohesion and the internal friction angle of sandy loam soil

The measurements were carried out at the Hungarian University of Agricultural and Life Sciences using soil from the university area. The soil used is sandy loam soil (shown in Figure 1), composed of 90.50 % sand (0.05-2 mm), 3.20 % silt (0.002-0.05 mm), and 6.30 % clay (<0.002 mm). The method used for measuring the shear strength results at different moisture contents is the direct shear test machine that is available in the laboratory (ELE 26-2112/01). The direct shear test machine is shown in Figure 2.

Figure 1. Sandy loam soil

Figure 2. Direct shear test machine (ELE 26-2112/01)

The soil samples were prepared in boxes and were moistured by adding water and then stirred till becoming uniform. The moisture of each of the samples was measured using the moisture analyzer (HE53 230 V; shown in Figure 3) that works based on the drying principle. An amount of soil is placed in it (on a tray) and dried by the analyzer's heating plates. For calculating the moisture percentage, the remaining mass is deducted from the initial wet mass and then divided by the initial wet mass (wet base moisture content calculation). The samples were placed and covered in plastic boxes to avoid the decrease in the moisture content. Starting with the first sample, the soil was placed in the direct shear box of the machine - approximately the soil amount was placed symmetrically in the two frames (upper and lower frame of the shearing box) - and then the upper frame was covered by the plate (cover plate). The screw pressing on the plate (used for applying the consolidation load by masses) was tightened, but not with a high torque (smooth tight just for anchoring the plate and levelling the soil surface). A 30 kg consolidation load was applied on the plate to compact the soil, since the soil used in the test is disturbed (taken from field), while the soil in the field is undisturbed. The soil was compacted by the 30 kg mass for 5 minutes as a chosen compaction period (compacting the soil for a longer period influences the shear strength result). After compacting the soil for 5 minutes, the 30 kg mass was removed and a 10 kg mass was applied as measuring consolidation stress (applied when shearing the soil), then the machine was operated. The shearing speed was set to be 9 mm/min (maximum speed in the machine). New soil amounts from the same sample (same moisture) were tested with the same compaction load applied for five minutes (except for the 15.03 % moisture), but having 20, 30, 50 and 70 kg as measuring consolidation masses (normal stress if the load is divided by the area of the shear box).

Figure 3. Moisture analyzer HE53 230 V

The soil samples of moisture content above 15 % were not compacted for 5 minutes to avoid water drainage, because the moisture is high. The tested soil saturation level (approximately liquid limit level) is around 27 %, and that was obtained by adding water to dry soil (at ambient conditions) prepared in a box, till it stops the absorption of water and a small water layer appears on the surface. The surface water (additional small amount) was removed carefully and the moisture was measured by the analyzer. For checking the saturation level in another way the hygroscopic effect of the soil was checked by filling dry soil in a tube and then inverted on a box, water was added into the box (small amount) till the soil (in the tube) stops absorbing water, and the moisture was measured by the anaylzer showing a value close 27 %.

Unsaturated soil is of a shape that is more complicated when compared to satured soil. This complex structure has impact on the strength, deformation, and the seepage of the soil [37] [38].

A 30 kg (approximately 1.1 bar; equal to real tyre pressure applied on the terrain) consolidation load is applied on the 115 grams soil sample in the direct shear box, and after 5 minutes, the consolidation load is discharged, then the pressing plate is removed where the consolidation load was applied, and using a caliper measure the depth (distance between the upper surface of the direct shear box and the upper surface of the soil). Having the depth measured and also measuring the total height in the direct shear box, the soil sample thickness will be calculated by subtracting the depth from the total height. The thickness of the soil sample multiplied by the area of the direct in the shear box will result in the volume of the soil sample. Having the soil volume obtained, the density is calculated by dividing the mass over the volume of the soil sample.

Figure 4 shows the obtained density of the tested loam sand soil at different moisture contents.
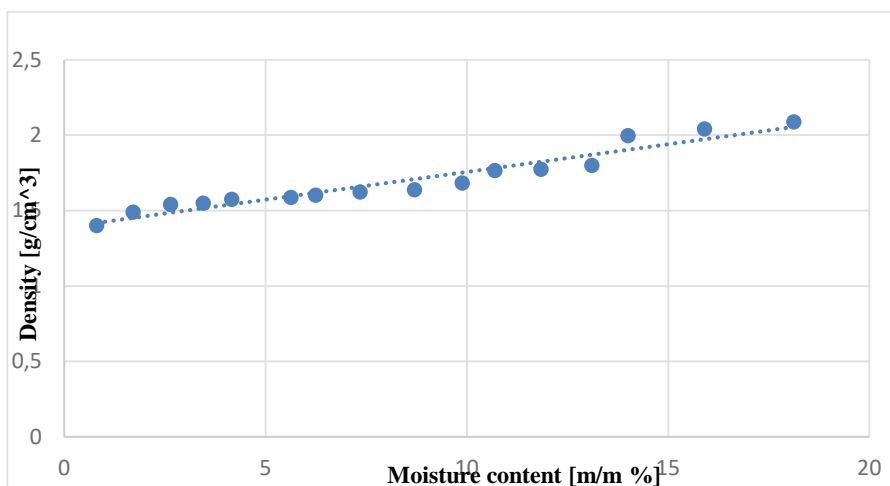
Figure 4. Loam sand soil density as function of moisture content

The shear strength results of the tested sandy loam soil at the gradually incremented moisture values are shown in Figure 5.
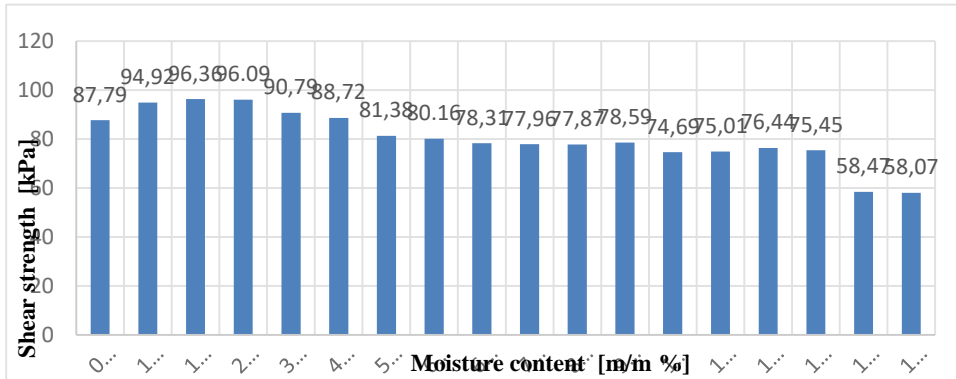
Figure 5. The shear strength of loam sand soil at different moisture contents
(shearing speed 9 mm/min)

For reaching the shear cohesion and the internal friction angle of the tetsed soil at different moisture contents, the obtained shear strength result at each of the applied loads was recorded (maximum stress value in the stress-displacement diagram). The same test was repeated on the same soil type with different moisture contents.

The shear strength was plotted as a function of the consolidation stress (at the loads 10, 20, 30, 50, and 70 kg), thus ending up with a linear Mohr-Coulomb failure criterion for finding the shear cohesion and the internal friction angle of the soil at each moisture content.

The shear cohesion is the intercept of the Mohr-Coulomb line with the shear strength results axis (y-axis) and the internal friction angle is the angle the line is making with the horizontal (acute angle).

The obtained Mohr-Coulomb diagrams are shown below (Figure 6);
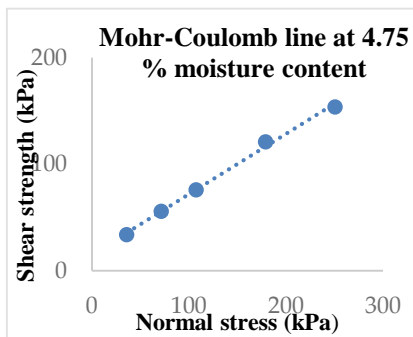
(a)
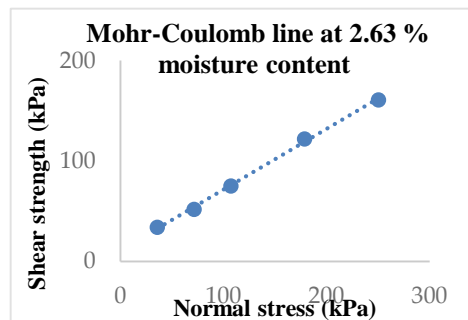
(b)
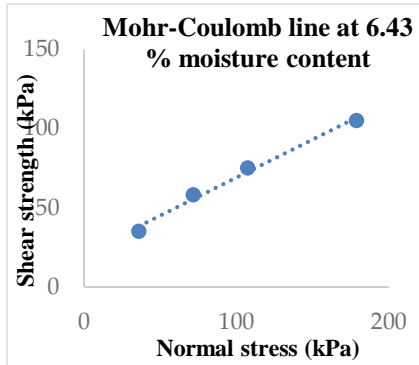
(c)
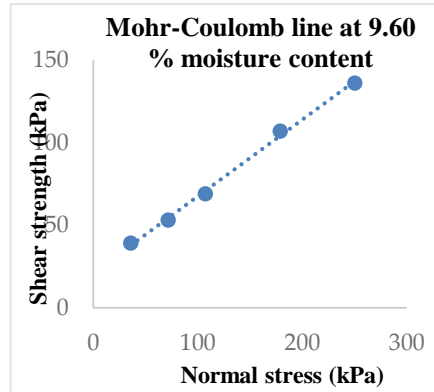
(d)
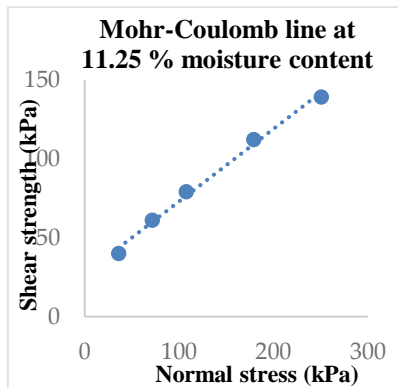
(e)
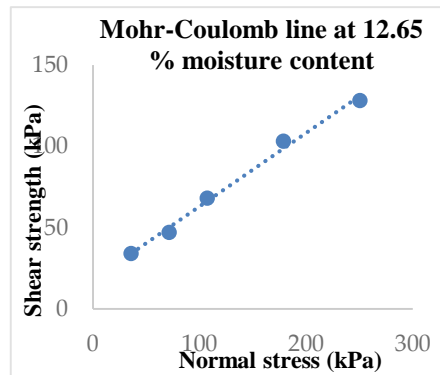
(f)
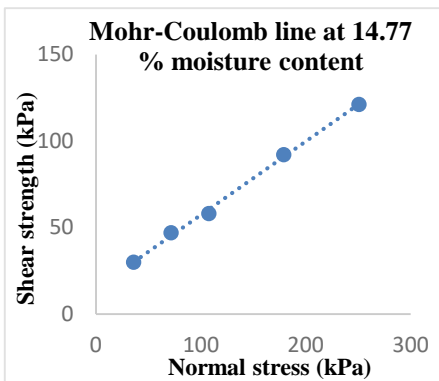
(g)
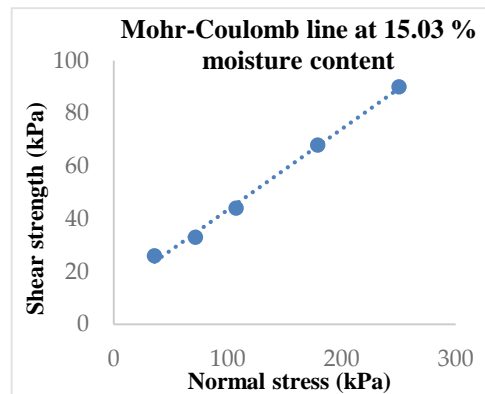
(h)

Figure 6. (a) to (h), Sandy loam soil Mohr-coulomb diagrams at different moisture contents

4. Results analysis

The change in the soil density
The results show that the density of the loam sand soil upon being compacted with same load increases with the increase in the moisture content. Connecting the density points ends with straight line of a regression analysis value 0.9329. The density is approximately increasing linearly upon having the same compaction load for the same compaction time (except for the last two moisture value; there was no compaction to avoid the drainage of water), and having the moisture (soil in boxes) increasing gradually in an increment way. The moisture values in percent (%) are 0.8, 1.71, 1.93, 2.64, 3.45, 4.16, 5.63, 6.24, 6.8, 7.35, 8.7, 9.88, 10.69, 11.84, 13.1, 14, 15.9, 18.12. The increase in the density reflects the increase in the compressibility of the tested soil type (tested soil characteristic) with the increase in the moisture content.

Shear strength of the tested sandy loam soil
Starting with the shear strength 87.79 kPa soil at 0.8 % moisture content, the shear strength increases with increasing the moisture content to 1.93 %, and beyond this moisture value the shear strength decreases up till reaching a stable point where the shear strength remains approximately equal with the increase in the moisture content (from 7 to 14 %), and then starts to decrease beyond 14 % moisture content as at the values 14, 15.9 and 18.12 %.

Upon repeating the measurement on the same type of soil containing moisture close to the above values and having the same consolidation load applied, the results obtained are not similar to the results in Figure 5 (the absolute difference of the shear strength results is ≤ 12 kPa). It is recognized that the soil shear strength results are changing as function of moisture content in a similar trajectory. The shear strength increases, then decreases and afterwards remains constant in a moisture content range, and beyond a high moisture content value it starts decreasing. The measurements done confirm what Osman (1964) mentioned, that the lack in the shear strength results published might be due to the difficulty in obtaining reliable set of values from a single method [40].

Shear cohesion and internal friction angle of the tested sandy loam soil
The cohesion (physical cohesion) resulting from the bonding between similar atoms reflects how these particles are bonded to each other, thus a step for understanding the behaviour of the soil.

As mentioned in the introduction, even though shear cohesion is different from soil physical cohesion, these two terms are related. The soil cohesion forms initial stress acting as compressive stress to the shear cohesion [36].

Based on the obtained results of the tested soil type, as the moisture content increases the shear cohesion increases to a value around 21 kPa and remains approximately constant in the moisture content range from 6 % to 9 %, and beyond this point, the shear cohesion increases with the increase in the moisture

content reaching a maximum point (breaking point) of a value 27.17 kPa at 11.25 % moisture content. Beyond the breaking point as the moisture increases, the shear cohesion decreases to a low value reaching 12.72 kPa at 15.25 %. The shear cohesion results are shown in Figure (7).

For loam soils, cohesion decreases with the increase in the moisture content (this can be recognized in Figure 7 at the high moisture values), and inversely the cohesion in sandy and clayey soils increases with increasing the moisture [39].
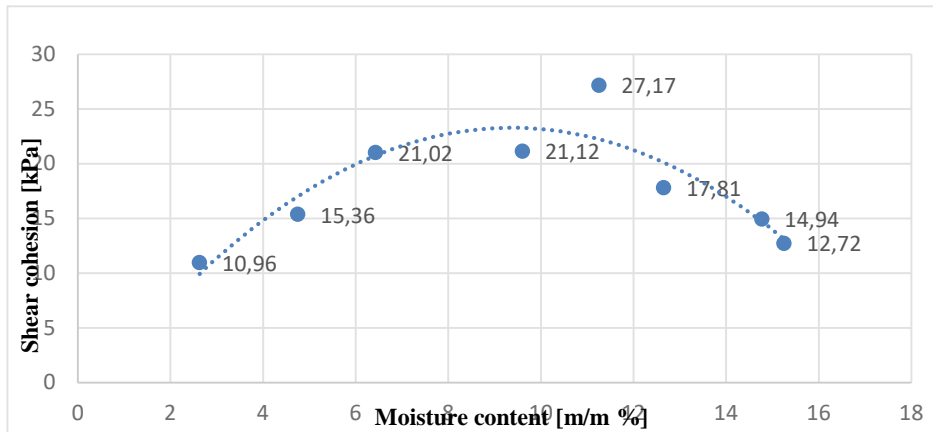
Figure 7. Sandy loam soil shear cohesion at different moisture contents

The interaction between the soil particles leads to friction between them, and this friction acts as a resistance to the shearing load. The shear strength based on the Coulomb equation consists of two values, the first which is the shear cohesion (C) and the second value resulting from the product of the internal friction coefficient (μ) and the applied normal stress.

$$\tau = C + \sigma tan\Phi \tag{1}$$

Having,
C (kPa) the shear cohesion,
σ (kPa) The normal stress applied on the soil (consolidation load divided by the area),
ɸ (degree) The internal friction angle (tan(ɸ) which is equal to μ; it is the friction coefficient and it indicates the slope of the line).

The increase in the applied normal load increases the compaction of the soil, thus increasing the density (density increases to a limit due to the decrease in the voids), which leads to the increase in the particle's interaction. When there isn't normal stress applied to the soil, the internal friction will not influence the shear strength of the soil (its influence is neglected).

The internal friction angle results of the sandy loam soil show that at ambient conditions (no water added; moisture in the soil is due to humidity) the internal friction angle of the soil is the highest, of a value 31.15 degrees, and with the increase in the moisture content the internal friction decreases to a value 24.87 at 9.6 %. Beyond the 9.6 % moisture, the results remain approximately constant with the increase in the moisture content till reaching 12.65 % (the results are decreasing, but at a slow rate, thus considered constant). Beyond 12.65 % moisture content, with the increase in the moisture, the internal friction angle continues to decrease reaching 17.04 degrees at 15.25 %. The internal friction angle results are shown in Figure (8). Low moisture content means high soil friction, and the high moisture content decreases the soil friction [39].
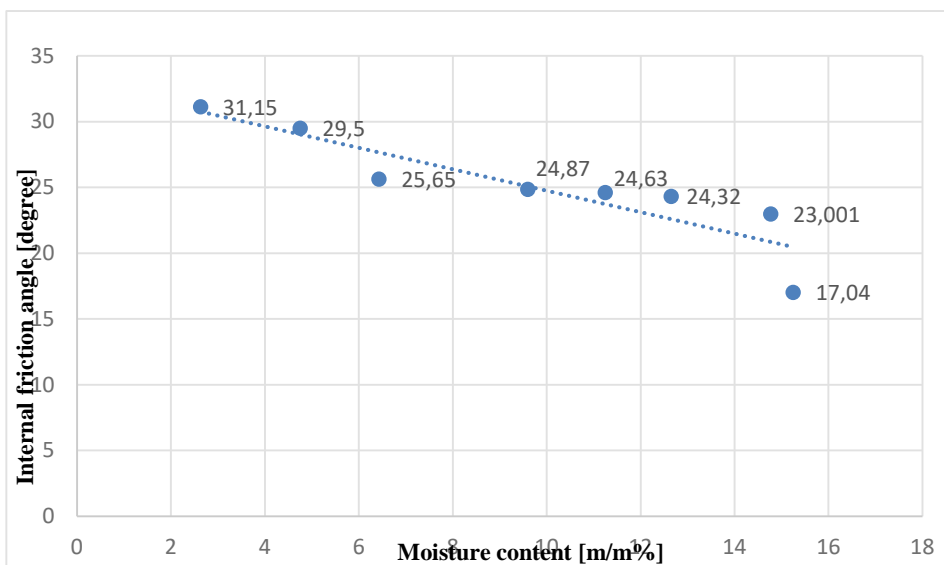
Figure 8. Sandy loam soil internal friction angle at different moisture contents.

5. Spectral behaviour of the tested sandy loam soil at different moisture contents (soil colour)

The description of the soil colour has been used by soil scientists in field to classify the soil and in mapping [28] [32].

The pedologists relied on the Munsell soil colour charts (1975) for more than 60 years in describing the normal range of soil colours, which is a qualitative colour estimate method [5] [23]. This method relies on determining the colour visually, and then comparing it to standard chips that are arranged systematically based on their Munsell's notations.

Many scientists replaced this method by fast instrumental technologies and methods to rely on in specifying the soil colour, such as UV-VIS

spectrophotometry (ultraviolet visible), leading to precise and quantitative approach in specifying the colour (quality control) [32] [4] [7]. The spectrophotometer removed some of Munsell's method limitations by using standard values and removing the human 'judgement' (observer viewing angle and the lighting conditions) [34] [32] [23] [13] [35] [29].

The colour of the tested soil was measured using a spectrophotometer (CM-700d; shown in Figure 9). The spectrophotometer is a modern technology used for measuring the colour of a body (material), the working principle of the used type is by sending light waves in the visible band, spectrum (400-700 nm), and based on the reflected wavelength the colour of the soil is identified. The colour of the soil is described by the reflected wavelength, which is a digital value (quantitative). It is difficult to specify the colour of the soil based on the vision as in Munsell charts, since it is a qualitative method. Despite the errors that might result from the traditional Munsell charts method, such as human errors (vision), using this method in the case of moistured soil becomes complicated. In most soil types, the increase in the moisture content of the soil makes the soil darker, but even though not being able to see the change in the colour by the eye's vision, the spectrophotometer is able to decode the colour of the soil to a digital value.

Figure 9. Spectrophotometer CM-700d.

The sandy loam soil was moistured to be at different moisture contents. Each soil moisture value was measured using the moisture analyzer (gravimetric measurement). At each moisture content value three soil colour records were taken by the spectrophotometer, and the average of these records was taken into account. The reflected wavelength results of the soil at the same moisture content are not precisely the same (but close results), and the reason behind the difference is that the soil is a particle material. There are factors that influence

the reflectance such as the pores and the density. The reflected wavelength results of the sandy loam soil at different moisture contents in the visible band (spectrum; 400-700 nm) are shown in Figure 10.
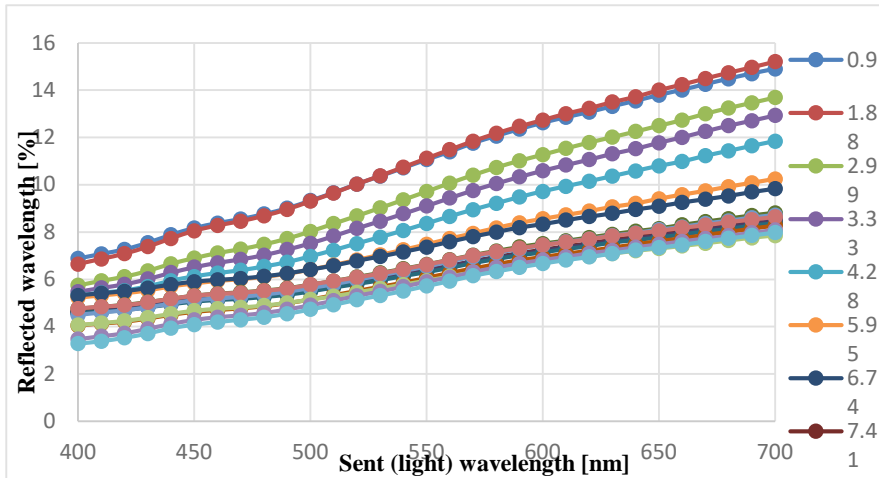
Figure 10. Sandy loam soil colour reflected wavelength at different moisture contents

The soil reflectance increases with the increase in the moisture content from 0.9 to 1.88 % indicating a slight brightening in the colour. Beyond the moisture 1.88 (or a value close to it), with the increase in the moisture amount the reflected wavelength decreases, showing that with the increase in the moisture the soil colour becomes darker. The soil reflectance decreases with the increase in the moisture content till reaching 6.74 % moisture value, and that can be recognized clearly in Figure 10 (at 700 nm). At values above 6.74 % moisture, the reflectance points (clear at 700 nm) start to overlap in a reflectance range.

6. Sandy loam soil colour reflectance at 700nm

For simplifying reading the above curve (reflectance of the spectrophotometer), the reflectance results at 700 nm (points are dispersed) were plotted as function of the moisture content values (each at its moisture content; shown in Figure 11).

Analyzing the curve in figure 11 shows that the moisture values used in the measurement are divided into two ranges, the first section ranging from 0.9 % to approximately 7.41 %. Fitting a curve into the plotted points (for an accurate curve with a good regression analysis, measurement repetitions are required) will end up with a useful equation for calculating the moisture based on the colour reflected wavelength at 700 nm. In this range the reflectance is changing in a clear curve path without having overlapping in the results, the case that makes calculating the moisture possible, and thus ending with a single moisture

44

result in the mentioned range upon substituting a reflectance into the curve equation (equation is not given here; measurement repetitions and equation validation are required before confirming an equation).
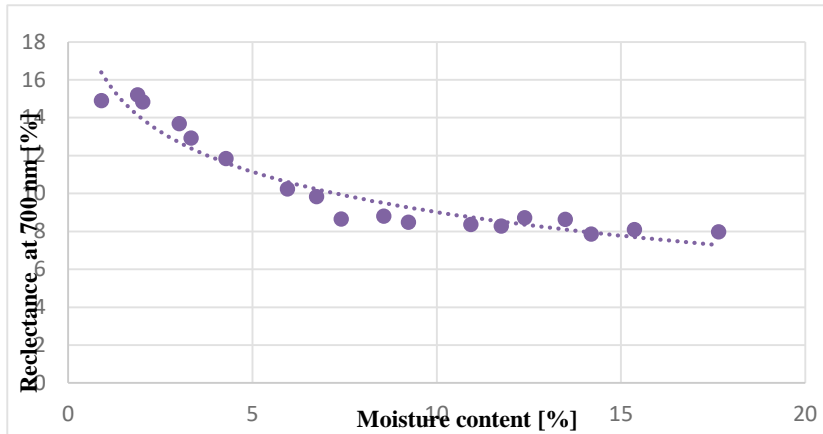
Figure 11. Colour reflectance of the tested sandy loam soil (700 nm)
at different moisture contents

Even though the moisture result will not be precisely similar to the moisture value calculated (gravimetric or volumetric calculation), but it should be of a value close to the precise value. The main reason behind the difference in the moisture values (colour equation calculation and gravimetric/volumetric calculation) is the reflected wavelength. Upon repeating the soil colour measurement at the same moisture content, the resulting reflected wavelength will not be precisely the same, since the material that is being studied is a particulate material. The density of the soil has influence on the wave reflectance, also the technical usage of the spectrophotometer (the front measuring part of the instrument should be normal to the soil surface and its pressing level should be accounted, since pressing leads to soil compaction) has influence on the reflectance result.

The second moisture section is ranging from a moisture value approximately beyond 7.41 % till the maximum moisture value, which is 17.65 % (shown in Figures 10 and 11). In this range the reflectance is approximately constant, thus a horizontal straight-line fit into the points. Having the soil at any moisture value in the mentioned range, and upon measuring its colour, the colour reflectance will be the same (constant value on the horizontal line). The same reflectance indicates that either: (1) beyond the moisture approximately equal to 7.41 % the soil colour is no more changing, thus the soil absorbed an amount of water, and the additional amount of water in the soil is water film occupying the space between the particles and leading to the same reflectance (water influencing the measurement).

The other reason which is (2) the used spectrophotometer measurement ability. The used spectrophotometer measures the colour based on sending light waves in the visible band (spectrum 400-700), and maybe by sending waves in this band the spectrophotometer is unable to receive precise reflectance at high moisture values, thus the usage of a spectrophotometer that sends waves in other ranges (such as infrared) might end up with good results at this stage.

7. Sandy loam soil shear strength parameters obtained using its colour

As mentioned in the introduction, that linking the mechanical properties of the soil to its colour facilitates knowing the infield mechanical properties of the soil from its colour. This work achieved through laboratory work, and the results should be validated by field measurements. In case of studying the mobility of a vehicle on a soil terrain, especially for calculating the traction (drawbar pull), some of the shear stress - displacement models require the shear strength and/or its parameters as input data for predicting the traction of the vehicle, as in Ageikin model (shear strength parameters required) shown in Equation 2 [1] [2] [3] [22].

The shear strength of the soil is calculated using the Mohr-Coulomb model, having its parameters both the shear cohesion and the internal friction angle. This Mohr-Coulomb model is the mostly used in terramechanics community (Equation 1). Some scientists worked on modifying this model to fit specific soil types such as clay soil [27], unsaturated soil [14], and partially saturated soil [8].

The three pioneer scientists that have settled the basics for the development of the shear stress-displacement models are Bekker, Pokrovski, and Janosi [9] [10] [15] [21].

Oida (1975) proposed a model based on Pokrovski's model that is only applicable on soils that are of shear stress-displacement profile with a hump and residual stress [19]. Certain types of loams are of shear stress-displacement profile having the mentioned characteristic [33].

$$\tau = \frac{1}{\frac{1}{\varsigma C + p tan(\Phi)} + \frac{t_{gr}}{E' \downarrow j}} \tag{2}$$

Where:

τ is the shear stress,
j is the shear displacement,
t_{gr} is the grouser pitch,
C is the soil shear cohesion,
P is the average ground pressure,
Φ is the internal friction angle,
m' and E' are soil shear parameters,
ς is a model parameter.

Having the equation of the curve fitting the colour reflectance points at 700 nm (Figure 11) will help in finding the moisture content of the soil upon substituting the reflectance value (at 700 nm) in it, thus the moisture value is obtained.

With the equation of the curve passing through the plotted shear cohesion points, the shear cohesion can be calculated at the moisture content (calculated from the colour). By using the equation of the internal friction angle curve fitting the plotted points, the internal friction angle is obtained at the moisture content calculated from the colour. Also, the way is applicable to find the shear strength of the soil from curve fitting the shear strength results at different moisture contents (in case the results are plotted, as points). The equations of the curves fitting the plotted points of both the shear cohesion and the internal friction angle are not provided in the article, considering that confirming these equations require measurements repetitions and validation (validation through field measurement).

Conclusion

The main target behind the article is fulfilled, and it shows the ability of relating the shear strength parameters of the tested sandy loam soil to its colour. The shear strength parameters were measured using the direct shear test. The tendency of the cohesion and the internal friction angle plotted points as function of moisture content is changing in a specified trajectory (curve can be obtained using a trendline fitting the points). With the increase in the moisture content, the colour reflectance of the soil has also shown a clear tendency (curve of specified path fitting the plotted point). By analyzing the obtained results, the following tangible results about the soil behaviour (mechanical and colour) can be concluded:
- When measuring the shear strength of the soil using the direct shear test it is important to take into consideration the effect of the consolidation load on the result, and that is recognized not just experimentally by comparing obtained results, but also in Coulomb's equation (Equation 1).
- The shear cohesion and the internal friction angle of soil are influenced by the moisture content and that can be recognized in the obtained results and in the soil physical behaviour.
- For the tested sandy loam soil, the shear cohesion increases with the increase in the moisture content reaching a maximum breaking point, and beyond this point, the shear cohesion tends to a low value. The internal friction angle of the sandy loam soil decreases with the increase in the moisture showing the maximum value at ambient conditions (no water added) and low values at high moisture content.
- At high moisture contents the water films existing between the particles act as lubrication breaking the cohesive bonds between the particles and decreasing the friction resulting from the contact of the particles.

- The decrease in the shear cohesion and the internal friction angle at high moisture content results in decreasing the shear strength (can be deduced from coulomb equation).
- The colour reflectance of sandy loam soil decreases with the increase in moisture till reaching a level (at a moisture value), and beyond this moisture value the reflectance results are approximately constant.
- Plotting the reflectance at 700 nm will result in a curve equation which is beneficial in finding the moisture if having a given colour reflectance value at 700 nm. Using the obtained moisture value, the shear cohesion and the internal friction angle (also the shear strength if plotted) can be calculated using the curves fitting the plotted points (Figures 7 and 8).

Acknowledgement

References

[1] Ageikin, J.S. Physical and mathematical soil parameters for evaluation of wheeled vehicle–terrain interaction, in: Proceedings of the International Symposium "Optimal Interaction", Russian Terramechanics Committee, Syzdal, Russia, 1992, pp. 3–9.

[2] Ageikin, J.S. Off-the-road wheeled and combined traction devices: theory and calculation, New Delhi: Amerind Pub. Co., New Delhi, 1987a.

[3] Ageikin, J.S. Off-the-road mobility of automobiles, New Delhi: Amerind Pub. Co., New Delhi, 1987b.

[4] Aitkenhead, M.; Coull, M.; Towers, w.; Hudson, G.; Black, H. Prediction of soil characteristics and colour using data from the national soils inventory of Scotland, Geoderma, 2013, 200–201, 99–107.
DOI:10.1016/j.geoderma.2013.02.013

[5] Albert Henry Munsell, Munsell soil color charts, Baltimore, 1975.

[6] Ahmed, A. E. E.; El Hariri, A.; Kiss, P. Soil strength and load bearing capacity measurement techniques, HAE, 2021, 40, pp. 16-27.
https://doi.org/10.17676/HAE.2021.40.16.

[7] Bloch, I.; Hosen, J.; Kracht, E.; Lefebvre, M.; Jazmine-Lopez, C.; Woodcock, R.; Keegan, W. Is it better to be objectively wrong or subjectively right? testing the accuracy and consistency of the Munsell capsure spectrocolorimeter for Archaeological applications, adv. Archaeol. pract,2021, 9, 132–144. DOI:10.1017/aap.2020.53

[8] Bishop, A.W.; Alpan, I.; Blight, G.E. Donald, I.B., Factors controlling the strength of partly saturated cohesive soils, in: Research Conference on Shear Strength of Cohesive Soils, Boulder, CO, 1960, pp. 503–532.

[9] Bekker, M.G. Introduction to Terrain-Vehicle Systems. Part I: The Terrain. Part II: The Vehicle. University of Michigan, Ann Arbor, Michigan, 1969.

[10] Bekker, M.G. Theory of land locomotion: the mechanics of vehicle mobility, The University of Michigan Press, Ann Arbor, Michigan, 1956. DOI: 10.3998/mpub.9690401

[11] Brady, N.; Weil, R. Elements of the nature and properties of soils, Pearson Prentice Hall: Boston, Ma, USA, 2008.

[12] Coulomb, C.A. Essai sur une application des regles de maximis et minimis quelques problemes de statique, relatits a l'architecture. Memoires de Mathematique de l'Academie Royale de Science, Paris, 1776, 7.

[13] Doi, R.; Wachrinrat, C.; Teejuntuk, S.; Sakurai, K.; Sahunalu, P. Semiquantitative color profiling of soils over a land degradation gradient in Sakaerat, Thailand. Environ. Monit. Assess, 2010, 170, 301–309. DOI: 10.1007/s10661-009-1233-x

[14] Hilf, J.F. An investigation of pore water pressure in compacted cohesive soils, Denver, CO., 1956.

[15] Janosi, Z. The analytical determination of drawbar-pull as a function of slip for tracked vehicles in deformation soils, in: Proc. of the 1st Int. Conf. of Terrain-Vehicle Systems. Torino, Italy, 1961.

[16] Kogure, K.; Sugiyama, N. A Study of Soil Thrust Exerted by a Tracked Vehicle, Journal of Terramechanics 1975, 12, (3-4), pp. 225 to 238, Pergamon Press Printed in Great Britain, https://doi.org/10.1016/0022-4898(75)90032-4

[17] Konen, M.; Burras, C.; Sandor, J. Organic carbon, texture, and quantitative color measurement relationships for cultivated soils in north central Iowa, Soil Sci. Soc. Am. J., 2003, 67. https://doi.org/10.2136/sssaj2003.1823

[18] Mohr, O. Welche Umstände bedingen die Elastizitätsgrenze und den Bruch eines Materials? Zeitschrift des Vereines deutscher Ingenieure, 1900, 44(45), pp. 1524-1530.

[19] Oida, A. Study on equation of shear stress-displacement curves. J. JAPANESE Soc. Agric. Mach, 1975, 37, 20–25.

[20] Pillinger, G., Kiss, P., Géczy, A., Hudoba, Z., Determination of soil density by cone index data, Journal of Terramechanics, 2018, 77, pp. 69-74 https://doi.org/10.1016/j.jterra.2018.03.003.

[21] Pokrovski, G.I. Issledovanie no fizike gruntov, 1937.

[22] He R.; Sandu C.; Khan A.K.; Glenn Guthrie A.; Schalk Els P.; Hamersma H.A. Review of terramechanics models and their applicability to real-time applications, Journal of Terramechanics, Volume 81, 2019, Pages 3-22, ISSN 0022-4898, https://doi.org/10.1016/j.jterra.2018.04.003.

[23] Rabenhorst, M.; Schmehling, A.; Thompson, J.; Hirmas, D.; Graham, R.; Rossi, A. Reliability of soil color standards, Soil Sci. Soc. Am. J, 2015, 79, 193–199. https://doi.org/10.2136/sssaj2014.10.0401.

[24] Sallberg, R.J. Shear strength, U.S Department of Transportation, Bureau of Public Roads Washington, D.C., 1965. https://doi.org/10.2134/agronmonogr9.1.c34

[25] Salman, N.D.; Kiss, P. Survey: Effect of bulk density and moisture content of soil on the penetration resistance and penetration depth, MEL, 2018, 17, pp. 109-118.

[26] Shoop, S.A. Thawing soil strength measurements for predicting vehicle performance, J. Terramechanics 1993, 30 (6), pp. 405-418. https://doi.org/10.1016/0022-4898(93)90034-U

[27] Sun, D., Yao, Y.P., Matsuoka, H., Modification of critical state models by Mohr-Coulomb criterion, Mech. Res, Commun, 33, 217-232, 2006.

[28] Soil survey staff, Soil Taxonomy: a basic system of soil classification for making and interpreting soil surveys, 2nd ed., U.S. dept. of agriculture, natural resources conservation service: Washington, DC, USA, 1999.

[29] Turk, J.; Rebecca, Y. Field conditions and the accuracy of visually determined Munsell soil color, Soil Sci. Soc. Am. J, 2020, 84, 163–169. https://doi.org/10.1002/saj2.20023

[30] Torrent, J.; Barrón, V. Laboratory measurements of soil color: theory and, Soil Sci. Soc. Am, 1993, 31, 21–33. https://doi.org/10.2136/sssaspecpub31.c2

[31] United States Department of Agriculture (USDA). soil color. USDA. 2020. available online: https://www.nrcs.usda.gov/wps/, Portal/nrcs/detail/wi/soils/?cid=nrcseprd1370419 (accessed on 10 april 2021).

[32] Viscarra-rossel, R.; Minasny, B.; Roudier, P.; Mcbratney, A. Colour space models for soil science, Geoderma, 2006, 133, 320–337. DOI:10.1016/j.geoderma.2005.07.017

[33] Wong, J.Y. Terramechanics and off-road vehicle engineering: terrain behaviour, off-road vehicle performance and design, 2nd ed. Butterworth-Heinemann, Oxford, 2009.

[34] Wills, S.; Sandor, J.; Burras, L. Prediction of soil organic carbon content using field and laboratory measurements of soil color, Soil Sci. Soc. Am. J, 2007, 71, 380–388. https://doi.org/10.2136/sssaj2005.0384

[35] Warr, B. Soil Colour; INSEAD: Fontainebleau, Singapore, 2015. [Google Scholar]

[36] Yokoi, H. Relationship between soil cohesion and shear strength, Soil Science and Plant Nutrition, 1968,14:3, pp.89-93 https://doi.org/10.1080/00380768.1968.10432750

[37] Duan, X.; Zeng, L.; Sun, X. Generalized stress framework for unsaturated soil: Demonstration and discussion. Acta Geotech. 2019, 14, 1459–1481 https://doi.org/10.3390/app13042502

[38] Li, J.; Bi, W.; Yao, Y.; Liu, Z. State-of-the-Art Review of Utilization of Microbial-Induced Calcite Precipitation for Improving Moisture-Dependent Properties of Unsaturated Soils. *Appl. Sci.* **2023**, *13*, 2502. https://doi.org/10.3390/app13042502

[39] Komandi, G. On the mechanical properties of soil as they affect traction, J. Terramechanics, 1992, vol. 29, no. 4/5, pp. 373-380.

[40] Osman, M.S., The measurement of soil shear strength, J. Terramechanics, 1964, volume 1, issue 3, pages 54-60.

Airflow optimization of solar drying unit using computational fluid dynamics approach

Halefom KIDANE[1,2], János BUZÁS[3], István FARKAS[3]

[1]Mechanical Engineering Doctoral School (MTDI), Szent István Campus, Gödöllő, MATE
[2]Hawassa University Institute of Technology, Hawassa, Ethiopia
[3]Institute of Technology, Hungarian University of Agriculture and Life Sciences, MATE, Gödöllő

Abstract

Solar drying is one of the most environmentally friendly and cheap sources of energy which can be applied to dry different products. Drying reduces the growth of microorganisms inside being dried. It is helpful for preserving the products for a long time. However, drying products using solar dryers has some bottlenecks. The main problem of most solar drying chambers is the unequal distribution of warm airflow inside the drying unit. In this work, different approaches to shape optimization using computational fluid dynamics have been presented. Computational fluid dynamics is a tool that provides the numerical solutions of the partial differential equations which govern airflow and heat transfer in a discretized form. The result of computational fluid dynamics analyses is relevant engineering data used in conceptual studies of new designs, detailed product development, troubleshooting, and redesign. The computational fluid dynamic analysis complements testing and experimentation which reduces the total effort required in the laboratory. In this study, two modified designs of solar drying were investigated and shows better airflow distribution compared to the existing solar drying chamber based on the computational fluid dynamics results. Finally, it can be drawn conclusion, that the current optimization and the proposed design give clear clues for further investigation of the existing drying chamber and development efficient dryer.

Keywords

computational fluid dynamics, drying, drying chamber, heat transfer, optimization, thermal circuit networking, solar dryers

1. Introduction

Sun drying is one of the ancient, customary techniques for drying agricultural products. People still use the sun to dry and preserve modest amounts of food in different parts of the world. In this method, the crops or fruits that need to be dried are placed on a flat surface or the ground and exposed to direct sunlight. So, such type of mechanism has many drawbacks a long time, labour intensive,

and enormous amounts of these goods decomposed as a result of a variety of factors including weather, insect attack, and other contaminants it needs a large area to spread the fruit out to dry and have drying control mechanism, etc. Hence to overcome the negative side of open sun dryers (Sharma et al., 2009) artificial or controlled drying methods called solar dryers are used in recent times to improve quality control, eliminate spoilage, and minimize losses.

Drying refers to the removal of moisture to a safe moisture level and it is used to maintain grain quality (Bala, 2017). Drying is the process of removing moisture from a biological product through evaporation induced by heat and mass transfer between the biological product and the drying air and is primarily driven by temperature and air convection force (Keneni et al., 2019). From a physical perspective, drying is a heat and mass transfer process that results in a reduction in a material's liquid content (Kolesnikov and Gavrilov, 2020).

The general approach of the simultaneous heat and mass transfer process on a food surface can be seen in Fig. 1 (Singh, 2015).
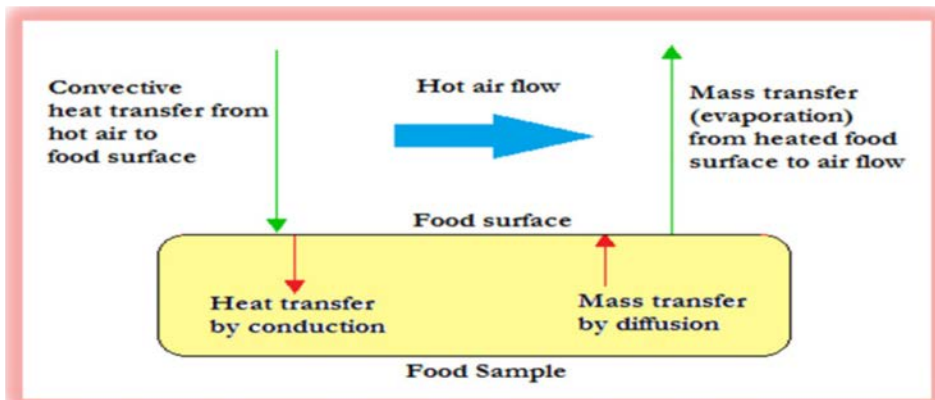
Figure 1. Simultaneous heat and mass transfer process on a food surface

Drying is an important process to preserve agricultural products It is used to improve food stability because it lowers the water activity of the substance, inhibits microbial activity, and reduces physical and chemical changes during storage. When properly packaged, dried products have a nearly infinite shelf life and far cheaper transportation, handling, and storage costs than those preserved by other methods (Rafiee, 2009). The basic goal of drying is to lower the moisture content to a level that allows the products to be stored for longer periods of time without deterioration. Low moisture content in agricultural products inhibits the growth of microorganisms such as molds, bacteria, and yeasts, as well as chemical processes that degrade product quality (Rabha and Muthukumar, 2017).

The post-harvest and preservation conditions for perishable products are represented in Fig. 2 (Ramkishore, 2020).
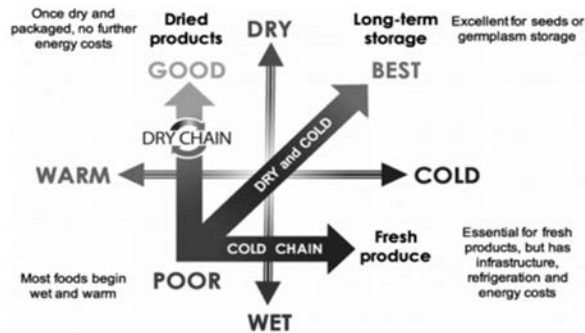
Figure 2. Representation of post-harvest and preservation conditions for perishable products

2. Modelling approach

Computational fluid dynamics (CFD)

As briefly explained by Zhai (2020) the field of computational fluid dynamics (CFD) is the numerical simulation of flow-related issues using a computer. CFD solves the flow governing equations (i.e., the fundamental conservation equations in mass, momentum, and energy) with the help of computers and numerical algorithms to anticipate what will happen quantitatively when fluids move, frequently with the complications of simultaneous flow of heat and mass transfer phase change chemical reaction mechanical movement and displacement of immersed or surrounding solids.

Computational fluid dynamics is used extensively because of its capability to solve equations for the conservation of mass, momentum, and energy using numerical methods to predict the temperature, velocity, and pressure profiles (Singh et al., 2015). Bakker and Marshal (2006) also compared the difference between experimental and CFD in terms of results as criteria. The study showed that CFD provides detailed results than traditional analysis Traditional methods, such as design based on experimental data correlations. As reported by Dutta et al. (2020) CFD has gained popularity in recent years as an alternative to the traditional branch of fluid dynamics, particularly experimental fluid dynamics, for analysing fluid flow. This is because it has several advantages over experimental methods.

The partial differential equations which are mostly solved by CFD are the following.

Governing equations

The main governed equation solved here are continuity, momentum and energy equations (Anand et al., 2020):

continuity equation:

$$\partial/\partial(\rho u i) = 0, \tag{1}$$

momentum equation:

$$\partial/\partial x_i\,(\rho u_i u_j) = -\partial p/\partial x_i + \partial/\partial x_j\,[\mu\,(\partial u_i/\partial x_j + \partial u_j/\partial x_i)] + \partial/\partial x_j\,(\overline{-\rho\acute{u_i}\acute{u_j}}), \quad (2)$$

energy equation:

$$\partial/\partial(\rho u_i T) = \partial/\partial x_j((\Gamma+\Gamma_t)\,\partial T/\partial x_j), \tag{3}$$

$$\frac{P}{\rho} = RT, \tag{4}$$

where: Γ and Γ_t are molecular thermal diffusivity and turbulent thermal diffusivity, respectively and are given by

$$\Gamma = \mu/Pr,\text{ and }\Gamma t = \mu t/Prt,$$

where *Pr* is the Prandtl number, and *Prt* is the turbulent Prandtl number, *R* is the characteristic gas constant = 0.287 kJ/kg-energy and ρ (density) is a function of temperature.

Several studies were carried out to optimize, evaluate its performance, design, develop etc of direct solar drying chamber using CFD by different researchers. For example, Chaudhari et al. (2021) examined cabinet-type solar dryer with auxiliaries of heaters and blowers using computational fluid dynamics. The simulations are carried out at 318 K drying temperature. The findings revealed that the region of average temperature increases as the day passes (radiation intensity increases). Jain et al. (2019) worked on computational investigation, validation of design, and energy analysis of domestic direct-type multi-shelf solar dryer. The ANSYS Fluent 14.0 software was used to design and simulate the household direct-type multi-shelf dryer at no load conditions.

A case study was conducted on the numerical method to predict the thermal performance of longitudinal solar dryer in a semi-arid area, using the finite element method (Kherrour et al., 2019). The simulation results of the case study revealed that the achieved outcomes are generally satisfactory. Ambesange and Kusekar (2017) applied CFD with help of the fluent version 14.5 CFD tool to design, test, and optimize the flow through solar dryer duct. The CFD approach solves the conservation equations of mass, momentum and energy which are used to model the convective heat transfer. Ghaffari and Mehdipour (2015) have used computational fluid dynamics to model and improve the performance of cabinet solar dryer and a new numerically modelling approach was proposed. The numerical results are consistent with experimental results.

Authors such as Amanlou and Zomorodian (2010) used CFD for designing a new fruit cabinet dryer. Seven various shapes of cabinet dryers were imagined theoretically utilizing fluent software and empirically to achieve a uniform distribution of drying air flow and temperature taking into account the overall operating parameters. Babu et al. (2020) utilised CFD to study different configurations of drying chamber used for thin-layer drying of leaves. The main

role of the CFD in the research was to select the optimal design from the four alternative of the air flow drying chamber layouts.

Using a computational fluid dynamics (CFD) technique, the airflow, temperature, radiative heat flux, and other parameters inside the simulation of hot-air supplemented solar dryer (HSSD) system were simulated. The calculated and predicted parameter values for the HSSD were compared to the simulated result (Aduewa and Solomon, 2022). Rosli et al. (2021) simulated five different tray layouts (i. e. Design A to Design E) of drying chamber to find out their uniformity using CFD used to dry marine products. Based on the findings, it was determined that designs (A) and (D) are the best for uniformity since there is less disagreement for each point provided and the distribution was more uniform.

Computational fluid dynamics approach was used to study the effect of weather on temperature variation within a solar dryer in Ahvaz, Iran. The CFD model's accuracy, which was tested against physical testing, was promising for CFD-based drying process optimization study (Sajadiye and Saberian, 2021). Güler et al. (2020) employed CFD analysis for both solar air collectors and drying chamber. The analysis indicated that the use of mesh modification has a positive impact on the collector performance, according to numerical modelling and experimental results. Aladeniyi et al. (2012) used ray tracing CFD technique for temperature distribution of solar dryer box was analysed. The results are consistent with the experiment.

Modes of heat transfer conducted in the drying chamber
During drying, heat transfer is one of the dominant phenomena. The heat is transferred in all directions between the air and products in the racks and throughout the walls of the drying boxes up to the ambient air and the sky.

The heat conduction is observed in the solid medium making the dryer. It's the transfer case in the walls of the dryer and inside the solar collector layers. This heat transfer is a very important factor in the design and optimization of a dryer, it determines the quantity of heat drained outwards which in turn influences the thermal losses of the dryer and its performance (Simo-Tagne et al., 2020).

Heat transfer by conduction
According to Fourier law heat conduction the heat flow rate through a body per unit time (Q_{cond}) in Watts (W), is given by Eq. 5:

$$Q_{cond} = -\, k\, A\, \frac{dt}{dx}, \qquad\qquad (5)$$

where:
K - Thermal conductivity of the body, W/mK,
A – Surface area of the flow (perpendicular to the direction of flow), m^2,
dt - Temperature difference of the face of the wall or block in K or ℃ and
dx - Thick of the body in the direction of the flow, m.
Thermal conduction resistance (Rth):

$$(R_{th})_{cond} = \frac{dx}{kA}, \tag{6}$$

Heat transfer by convection

Inside the dryer, heat transfer between air and product, air and walls, air and racks, is done by convection. This is the most interesting mode of heat transfer in which the drying air moves around the dried product. Heat transfer by convection is also noticeable outside the dryer, between the walls external and ambient air. The convective rate of heat transfer between a solid surface and a fluid with a convective heat transfer coefficient hc and temperature difference *ΔT* may be described as (Simo-Tagne et al., 2020). The rate of heat transfer by convection (h)is given by newton's law of cooling as follows:

$$Q = h \, A \, (T_s - T_f), \tag{7}$$

$$h = \frac{Q}{A \, (T_s - T_f)}, \tag{8}$$

where:
Q - Rate of conductive heat transfer,
A - Area exposed to heat transfer,
h - Coefficient of convective heat transfer,
T_s - Surface temperature,
T_f - Fluid tempretature.
   Convection thermal resistance [$(R_{th})_{conv}$]:

$$(R_{th})_{conv} = \frac{1}{hA}. \tag{9}$$

Heat transfer by radiation

The most dominant heat transfer mode in the case of solar dryers is radiant heat transfer. It takes into account the exchange between the outer wall of the dryer and the sky, and the exchange between the upper part of the collector and the sky. The radiation heat exchange rate between two surfaces of temperature *T1* and *T2* with the radiative heat transfer coefficient *Qr* is expressed by Eq. 10 (Simo-Tagne et al., 2020).
   Heat transfer by radiation(Q) is given by the stefan-boltzmann law as follows.

$$Qr = F \, \sigma \, A \, (T_1^4 - T_2^4), \tag{10}$$

where:
F - a factor depending on the geometry and surface properties,
σ - Stefan-Boltzmann constant $= 5.67 \times 10^{-8}$ W/m^{2}K^4,
A - surface area, m^2
T_1, T_2 - Tempereture in degree Kelvin scale (K).
   The thermal analysis of the solar drying chamber can be done step by step based on Fig. 3 and Fig. 4.
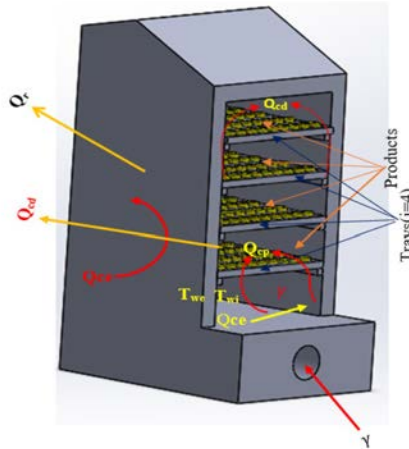
Figure 3. Main heat and mass transfer modes conducted in the drying chamber
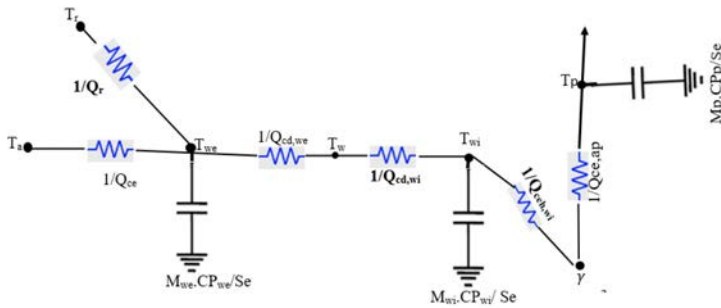
Figure 4. Thermal circuit networking of drying chamber

The notations in the figure are the following:

Cp: Heat capacity of air (J/Kg K),
Cp_p: Heat capacity of products,
Cpw_s: Heat capacity of wall face,
dt: Time step,
hceach,wi: Convection heat coefficient between the air and the internal wall face,
hcep,ach: Convection heat coefficient between the air and the product,
m_p: Mass of the product,
m_{hp}:   Half of the wall mass,
Pev: Evaporation power,
γ: Heated air temperature comes from the solar collector,
Q: Flow rate,
Qce: Convection heat coefficient between the chamber wall external face and the ambient air,
Qcd, we: Conduction heat coefficient between the through-the-wall faces,

Qr: Radiation heat coefficient between the wall external face and the sky,

Se: Exchange surface between product and air for one tray,

Ta: Ambient temperature,

Tp: Product temperature,

 Tw: Temperature between two faces of the wall,

Twi Internal wall face temperature,

Twe: External wall face temperature,

Tr: Temperature of the solar radiation or temperature of the sun,

we: External wall face or simply wall face,

wi: Internal wall face,

W_s: Wall face surface for one tray section.

Thermal circuit analysis of drying chamber

The thermal network method is based on the discovery that the comparable values for electrical engineering and thermal engineering's diffusion equations are voltage temperature and current-heat flow, respectively (Ishizuka et al., 2011). The Thermal Network Method (TNM) is based on the substitution of a circuit made up of thermal resistances, capacitances, and heat sources for an arbitrary 3D geometry. The nodal potentials and currents in such a network represent temperatures and heat flow, respectively. The mathematical formulations of electrical circuit programming are similar enough that a solution can be found using them. The primary benefit of thermal network analysis is its quick computing time, which enables huge models' steady-state calculations to be completed in a matter of seconds (Gramsch et al., 2007).

Figure 5. Thermal network method analogy between electrical
and thermal problems

The thermal analysis of the solar drying chamber can be done step by step based on Fig. 3 and Fig 4 following the first law of thermodynamics or 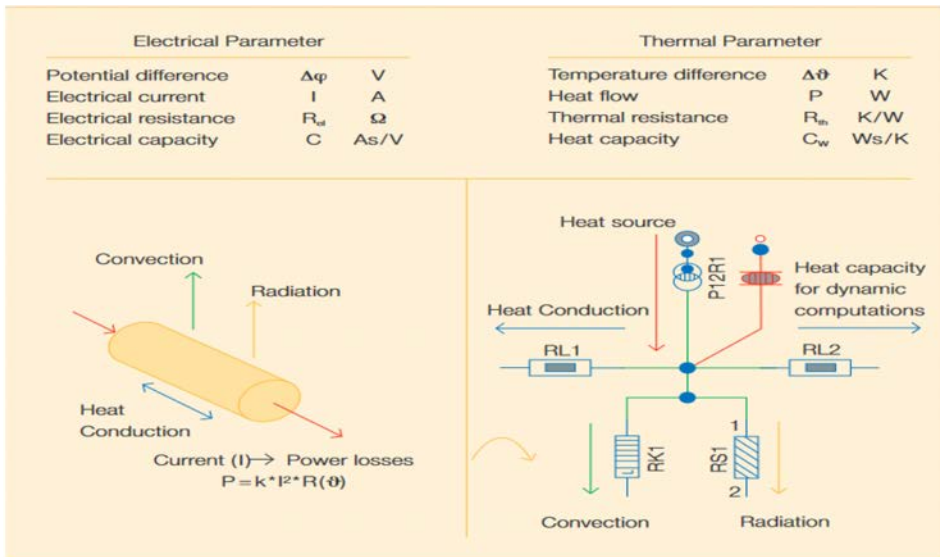energy conversion principle. The thermal network method analogy between electrical and thermal problems is shown in Fig. 5 (Grossmann et al., 1990).

The first law of thermodynamics states that energy stored in an element or substance is equal to the energy it acquired by conduction, radiation, and convection minus the energy it lost by conduction, convection, and radiation. This applies to both mass rate and energy.

1) At the external surface of the drying chamber wall:
In this surface all modes of heat transfers are carried out:

$$M_{wi} Cp_{we} \left(\frac{dTwe}{dt}\right) = Q_{ce} W_s (T_a - T_{we}) + Q_r$$
$$W_s (T_r - T_{we}) + Q_{cd,\ we} W_s (T_w - T_{we}). \tag{11}$$

2) At the internal wall surface of the drying chamber:

$$m_{wi} Cp_{wi} \left(\frac{dTwi}{dt}\right) = Q_{cd,wi.} W_s (T_w - T_{wi}) + h_{cash,wf} W_s (\gamma_{(j-1)} - T_{wi}). \tag{12}$$

3) Between the product, internal wall face and the drying air exchange:

$$Q\ C_p (\gamma_{(j)} - \gamma_{(j-1)}) = h_{cash,we} S_e (Twi - \gamma_{(j-1)}) + h_{cep,\ cash} S_e (T_p - \gamma_{(j-1)}). \tag{13}$$

4) Exchange between the product and the drying air:

$$M_p Cp_p \left(\frac{dTp}{dt}\right) = h_{cep,}\ ach\ S_e (\gamma (j-1) - T_p) - P_{ev}. \tag{14}$$

5) Exchange through the wall between internal and external faces:

$$M_{we} Cp_{we} \left(\frac{dTp}{dt}\right) = h_{cd,we} W_s (Tp - Te) = m_{wi} C p_{wi} \left(\frac{dTp}{dt}\right) = h_{cd} W_s (T_{pi} - T_p). \tag{15}$$

Next, these equations are discretized for the numerical study as follows using the finite-difference method with help of the energy balance method.

1) At the external surface of the drying chamber wall:

$$mwe\ Cpwe \left[\frac{T_{we}^{t+\Delta t}(j) - T_{we}^t(j)}{\Delta t}\right] = Qce\ Ws\ (Ta - T_{we}^{t+\Delta t}(j))$$
$$+ Qre\ Ws\ (Tc - T_{we}^{t+\Delta t}(j)) +$$
$$Qcd,wf\ Ws\ (T_w^{t+\Delta t}(j)) - T_{we}^{t+\Delta t}(j)) \tag{16}$$

2) At the internal wall surface of the drying chamber:

$$mwi\ Cp \left[\frac{T_{wi}^{t+\Delta t}(j) - T_{wi}^t(j)}{\Delta t}\right] = hcd,pi\ Ws\ (T_{wi}^{t+\Delta t}(j) - T_{we}^{t+\Delta t}) +$$
$$hcash\ Ws\ (\gamma^{t+\Delta t}(j-1) - T_{wi}^{t+\Delta t}(j)) \tag{17}$$

3) Exchange between the product, internal wall face, and the drying air:

$$Q.Cp(\gamma^{t+\Delta t}(j) - \gamma^{t+\Delta t}(j_1)) = \text{hcep, ach.Ws } (T_{wi}^{t+\Delta t}(j) - \gamma^{t+\Delta t}(j-1) +$$

$$\text{hcep, ach. Se } (T_p^{t+\Delta t}(j) - \gamma^{t+\Delta t}(j-1) \tag{18}$$

4) Exchange between the product and the drying air:

$$Mp\ Cp_p \left[\frac{T_p^{t+\Delta t}(j) - T_w^t(j)}{\Delta t}\right] = h_{cep,ach}\ S_e\ (\gamma^{t+\Delta t}(j-1) - T_p^{t+\Delta t}(j)) - Pev \tag{19}$$

5) Exchange through the wall between internal and external faces:

$$M_{we}\ Cp_{we}\left[\frac{T_p^{t+\Delta t}(j) - T_w^t(j)}{\Delta t}\right] = h_{cd,we}\ W_s\ (T_w^{t+\Delta t}(j) - T_{we}^{t+\Delta t}(j)) = m_{wi}$$
$$Cp_{wi}\left[\frac{T_p^{t+\Delta t}(j) - T_P^t(j)}{\Delta t}\right] +$$
$$h_{cd,wi}\ W_s\ (T_{wi}^{t+\Delta t}(j) - T_w^{t+\Delta t}(j)) \tag{20}$$

where:

$$W_s = 2\ (\text{width+depth})\ \Delta x \tag{21}$$

and *Δx* is the length of the section.

Solving the above equations by hand is time consuming and tedious. So, solving using CFD the best option and recommend method.

3. Experimental

Description of CFD model
The computational fluid dynamic (CFD) is a powerful method to study heat and mass transfer from many years. CFD codes are structured around numerical algorithms that can tackle fluid flow problems. CFD provides the numerical solutions of partial differential equations which governing airflow and heat transfer in a discretised form. The complicated fluid flow and the heat transfer processes involved in any drying system can be examined by CFD software. The programming concept is based around numerical algorithms that are able to tackle complex fluid flow problems. In order to provide this solution commercially their the CFD packages includes sophisticated user interfaces for input and setup parameters as well as results analysis. The main CFD tool used here in this article was ANSYS fluent software. The 3D geometric model was prepared in solid work 2022. Any CFD tool contains three main components namely pre-processor, solver and post-processor. Generally, in order to run simulation using the CFD codes the steps which shown in (Fig. 6) are followed.
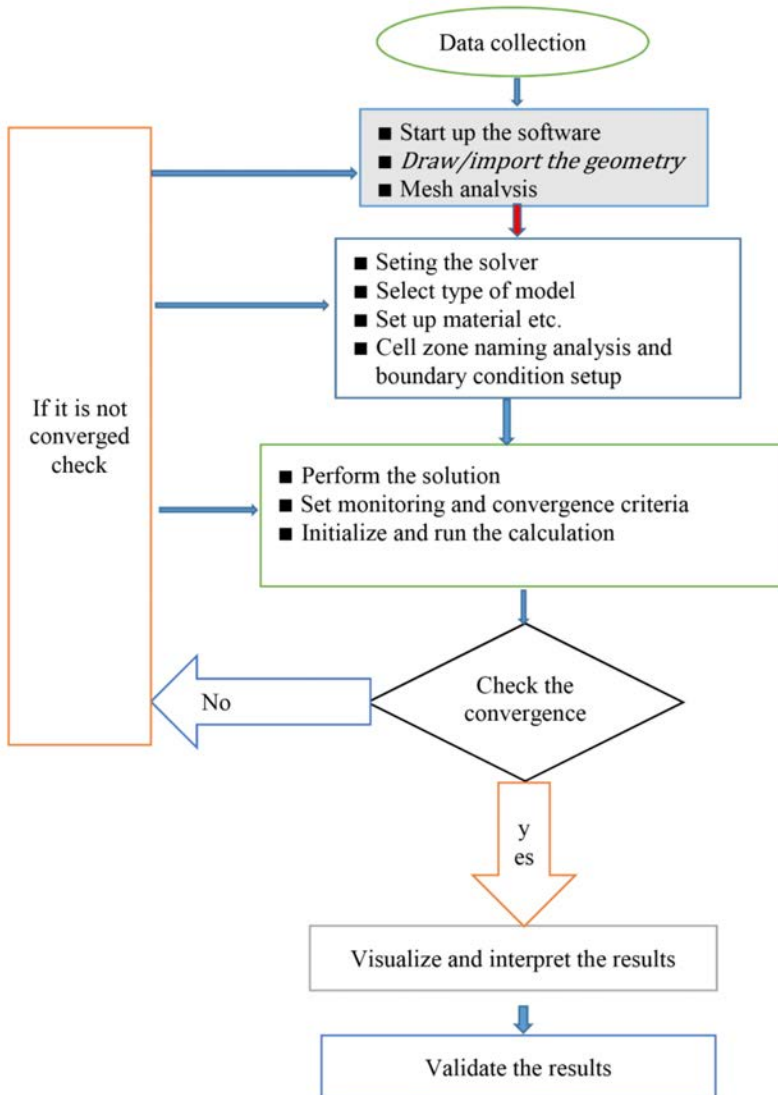
Figure 6. General flow work of computational fluid dynamics process

Specification of the drying chamber

The drying chamber is made up polystyrene blocks with 5 cm thickness. The chamber is integrated with the solar collector by a small duct (indirect drying), then the exit heated air from the collector enters the chamber with high temperature and low humidity. The moist and hot air rises and escapes from the upper vent of drying chamber. Inlet and outlet of drying chamber have a diameter 10 cm with a small slop angle for the upper side of the chamber to keep the smooth movement of the air. Steady state calculations were carried on by

default calculation settings until convergence is reached or temperature monitors show steady state condition has been reached. The boundary conditions for the simulation were derived the previous experimental works. The detailed information of the drying chamber and boundary condition used for CFD are described in Table 1 (Al-Neama and I. Farkas, 2018).

Table 1. The existing solar drying chamber system specification and boundary conditions

Parameter	Value
Density of air (kg/m^3)	1.2
Specific heat capacity of air (J/kg K)	1007
Walls	Adiabatic /insulated
Outlet	Assumed gauge pressure
Type of solar collector used	Double-pass solar air collector
Inlet, outlet temperature (K)	294.45, 312.65 respectively
Inlet velocity (m/s)	2.3
Overall dimension (H× W ×L)	100 cm × 50 cm × 50 cm
Number of trays used for current analysis	4
Dried product	Apple/banana

4. Results and discussions

Flow optimization of the existing prototype using CFD
The existing laboratory prototype Fig. 7 (Al-Neama and Farkas, 2019) has some limitations. The main problem of the dryer is there no uniform air flow inside drying chamber. Thus, the products are drying irregular manner or at dry at different hours and moisture content. The irregular drying occurs due to non-uniform air flow means that inside of the drying chamber, the fresh air cannot be distributed equally. The air is high in first the lower tray and decrease when it goes up and finished before it reaches the upper ones. So, solve existing limitation of the solar drying chamber optimization was done using CFD techniques. Thus, more than ten 10 designs were drawn. However, for the current study two designs were chosen.

Initial three-dimensional (3D) model of the drying chamber was created in solid work 2022 version. Solid work is among the common modelling software in current times which is easily integrated with ANSYS software.

To improve the air flow and to minimize the described problems, several approaches are possible. Here in this study the main modification was done by adding another air passes in different locations of the dryer and shuffling the tray configuration (Fig. 7). Another optimizing methods is changing the process parameters such as temperature, humidity, air flow or modifying physical parameters of the dryer like length, height, tray configuration, number holes or

passes etc. Another method is also by adding baffles to reduce or increase the air flow, however reduction of the air flow has drawn back like causes to lower velocities and this would reduce problems like the distribution of the air and lower the efficiency of the dryer.

Figure 7. Existing drying chamber in found the laboratory

Simulation results

The modified versions of Fig.7, the 3D model and its meshed parts are shown in Fig. 8 and Fig. 9, respectively.

A   B
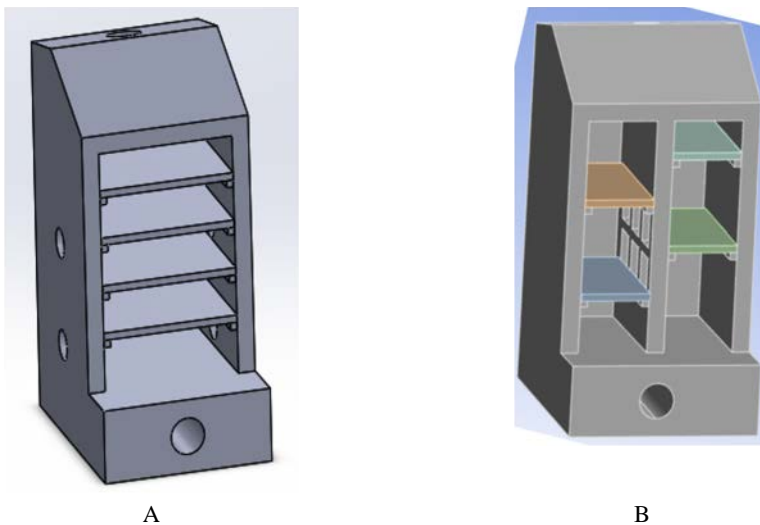
Figure 8. 3D models of selected designs ready for simulation
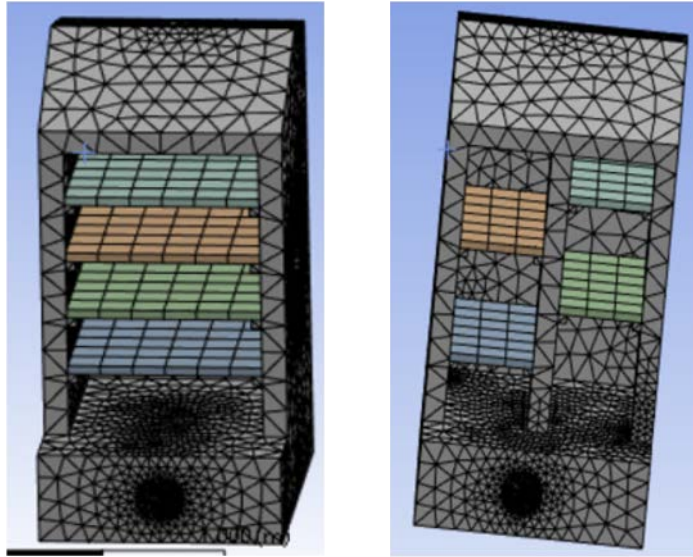
Figure 9. Meshed parts of the selected designs ready for simulation

Simulation result proposed of the first design

The first-order upwind scheme was chosen for energy and momentum equations. The simple algorithm is chosen as a scheme to couple pressure and velocity; it is more economically efficient and stable than the other algorithms. After setting all necessary input conditions starting modelling, meshing, model selection, material, cell zone specification boundary condition and so on the problem was iterated to solve the governing of continuity, momentum and energy partial differential equations. The solution is converged (minimum values reached), when the residuals equation reaches less than 1×10^{-2} for *x, y, z* velocity components and 1×10^{-4} for (k–ε).

The following CFD simulation results show the initial prototype and optimized by adding some new feature like add number of inlets of warm on the different part of drying chamber. In order to perform the simulation, the following solver setting were used:

- solver: Pressure based,
- Time: Steady,
- Model: k-epslon(2equ),standard with standar wall functions and defualt values of model constants,
- Solution methods: Second Order up wind discretization for momentum and energy, first order up wind for turbulence equations (i.e turbulence knetic energy and turbulence dissipation rate),
- Under-relaxation factors for pressure, density, body forces, momentum, turbulent kinetic energy, turbulent dissipation rate, turbulent viscosity and energy were default valuesare of the software,

–   Solution initialization: Hybrid itialization method,

Convergence criteria of 0.0001. The simulation results shown on Fig 10A indicates uneven distribution of air flow, and so give us some hints of where the initial optimization will be done. So, based on the rough clue of exiting solar dryer simulation results the right and left walls of the dryers needs to optimise. Thus, in the case of the CFD analysis (Fig. 10B) an additional hot air one entrance on the left side was added. Thus, the flow velocity is increased, and it is a little bit better than the existing.

(a)   (b)
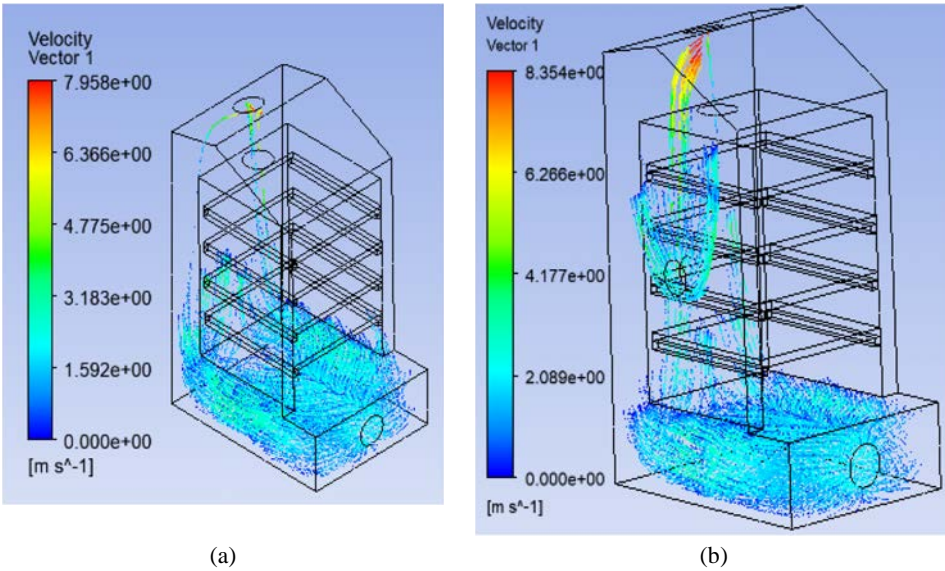
Figure 10. CFD analysis of the drying chambers: a) existing design, b) proposed design
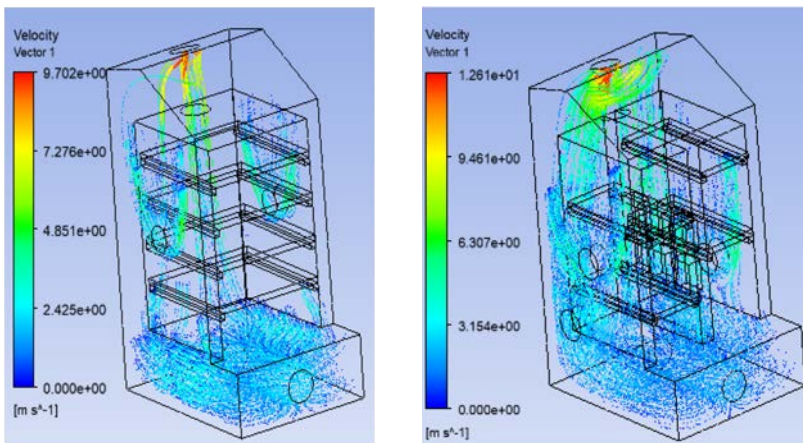
Figure 11. Optimized simulation results of first design (Fig. 8A)

As it can be observed in Fig. 10 the flow hot air is limited in the lower part of the first tray and somehow in the left side of the drying chamber. However, there is air flow on the right side and back side of the drying. So, let's add another hole on the first right side then back side. As show in Fig. 11 the dryer still needs some modification.

The Fig. 12 shows better air flow inside the drying chamber, so it can be optimized in a higher extent.
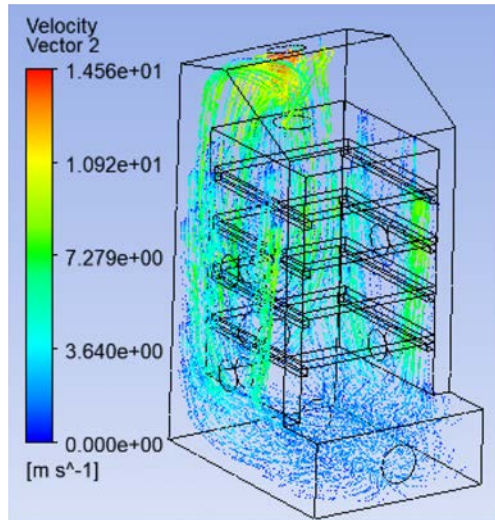
Figure 12. Better optimized simulation results of (Fig. 8B)

Simulation result proposed of the first design
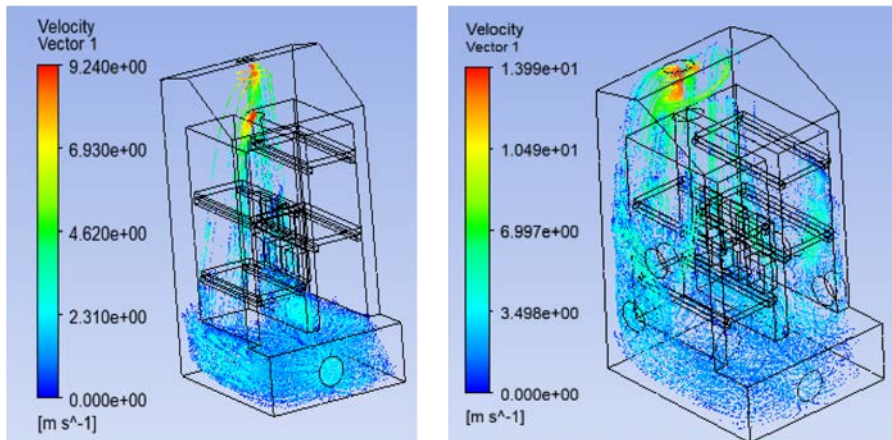
Figure 13. More optimized simulation results of (Fig. 8B)

The snapshot on Fig. 13 shows that the air enters the device with a speed of 2.3 m/s for both devices. However, the flow of the air in the left side is concentrated on the bottom tray and small amount of the flow partly reached in top tray. So, to solve the problem of the left side figure some modification was made like add addition inlet holes on external walls of left, right and back side and in the internal walls of the drying chamber.

Conclusions

- Solar dryer is the best alternative technology to avoid disadvantages of conventional drying methods.
- Improving solar dryer performance has been concern of many academicians and researchers for long period of time and still undergoing research interest.
- In this context, the computational fluid dynamics (CFD) analysis was applied to analyse the flow distribution of existing drying chamber and different optimization measures was taken.
- The detailed energy analysis and the types of heat transfer modes in the solar drying chamber were formulated.
- Two optimized designs were presented for optimization purpose. The main optimization tasks done here was adding additional inlet warm air on the selected parts of the drying chamber.
- The simulation was conducted with the use of a commercial computational fluid dynamics program, ANSYS Fluent version 2022 R_2 which solves the Reynolds-averaged Naiver-Stokes (RANS) with two-equation models k–ε turbulence standard model.
- The solutions obtained from simulation of the computational fluid dynamics is with the acceptable range. Thus, the solution was converged (minimum values were reached), when the residuals of the continuity equation and the conservation of momentum equation reach 10^{-2}, for *x, y, z* velocity components: 10^{-4} for (k –ε).
- The modified designs results reveal that they have better flow distribution than existing design of the solar drying chamber.

Acknowledgements

References

[1] Aduewa, T. and Ajiboye Solomon (2022), Analysis of hot-air supplemented solar drying using computational fluid dynamics technique. Journal of applied science, engineering, technology, and education, 4(1), 2685–059.

[2] Al-Neama, M.A. and Farkas, I. (2018), Evaluation of temperature and relative humidity stratifications in a solar drying chamber, Journal of Scientific and Engineering Research, 5(10), 59-65.

[3] Al-Neama, M. A. and Farkas, I. (2019), Thermal efficiency of vertical and horizontal-finned solar collector integrated with forced air circulation dryer for apple as a sample. Drying technology, 37(5), 546–558.

[4] Aladeniyi, K., Adeniy and Mohammed, A. (2012), Analysis of a solar dryer box with ray tracing CFD technique radon monitoring in homes, 3(10).

[5] Amanlou, Y. and Zomorodian, A. (2010), Applying CFD for designing a new fruit cabinet dryer. journal of food engineering, 101(1), 8–15.

[6] Ambesange, A.I. and Kusekar, P. (2017), Analysis of flow through solar dryer duct using CFD, 5(1).

[7] Anand, S., Mishra, D.P. and Sarangi, S.K. (2020), CFD supported performance analysis of an innovative biomass dryer, 159, 860–872.

[8] Andre´ Bakker and Elizabeth Marden Marshal (2006), Computational fluid dynamics, 505–515.

[9] Babu, A.K., Kumaresan, G., Antony Aroul Raj, V. and Velraj, R. (2020), CFD studies on different configurations of drying chamber for thin-layer drying of leaves, 42(18), 2227–2239.

[10] Chaudhari, V.D., Kulkarni, G.N. and Sewatkar, C.M (2021), Computational fluid dynamics analysis of cabinet-type solar dryer. Journal of Food Process Engineering, 44(8).

[11] Dutta, A., Erdogdu, F. and Sarghini, F. (2020), Computational fluid dynamics simulation in food processing, 244–261.

[12] Ghaffari, A. and Mehdipour, R. (2015), Modeling and improving the performance of cabinet solar dryer using computational fluid dynamics. International Journal of Food Engineering, 11(2), 157–172.

[13] Gramsch, C., Blaszczyk, A., Löbl, H. and Grossmann, S. (2007), Thermal network method in the design of power equipment. 213–219.

[14] Grossmann, S., Löbl, H. and Kaltenborn, U. (1990), Hot stuff. 55–58.

[15] Güler, H.Ö., Sözen, A., Tuncer, A. D., Afshari, F., Khanlari, A., Şirin, C. and Gungor, A. (2020), Experimental and CFD survey of indirect solar dryer modified with low-cost iron mesh. Solar Energy, 197, 371–384.

[16] Ishizuka, M., Hatakeyama, T., Funawatashi, Y. and Koizumi, K. (2011), Application of thermal network model to transient thermal analysis of power electronic package substrate. Active and Passive Electronic Components, 2011

[17] Jain, A., Sharma, M., Kumar, A., Sharma, A. and Palamanit, A. (2019), Computational fluid dynamics simulation and energy analysis of domestic direct-type multi-shelf solar dryer. Journal of Thermal Analysis and Calorimetry, 136(1), 173–184.

[18] Keneni, Y.G., Hvoslef-Eide, A. K. (Trine) and Marchetti, J. M. (2019), Mathematical modelling of the drying kinetics of Jatropha curcas L. seeds. Industrial Crops and Products, 132, 12–20.

[19] Kherrour, S., Bouhdjar, A., Hanini, S., Boualit, A., D.Lalmi (2019), Numerical study of a longitudinal solar dryer in semi-arid area; case study. Instrumentation Mesure Metrologie, 18(2), 95–103.

[20] Kolesnikov, G. and Gavrilov, T. (2020), Modeling the drying of capillary-porous materials in a thin layer: Application to the estimation of moisture content in thin-walled building blocks. Applied Sciences.

[21] Rabha, D.K., and Muthukumar, P. (2017),Performance studies on a forced convection solar dryer integrated with a paraffin wax–based latent heat storage system. Solar Energy, 149, 214–226.

[22] Rafiee, E. (2009), Mathematical modeling of kinetics of thin-layer drying of apple (var. Golab)". Agricultural Engineering International: the CIGR Ejournal, 1-10.

[23] Rosli, M.A.M., Jing, H.S., Azhar, N.I.M., Saputra, M. and Ali, S. (2021), A simulation study of drying chamber for marine product. international journal of integrated engineering, 13(6), 62–69.

[24] Sajadiye, S.M. and Saberian, A. (2021), The effect of weather on temperature variation inside a solar dryer in Ahvaz-Iran using computational fluid dynamics method. Journal of Food Process Engineering, 44(12).

[25] Sharma, A., Chen, C.R. and Vu Lan, N. (2009),Solar-energy drying systems: A review. In Renewable and Sustainable Energy Reviews (Vol. 13, Issues 6–7, pp. 1185–1210).

[26] Simo-Tagne, M., Ndukwu, M.C., Zoulalian, A., Bennamoun, L., Kifani-Sahban, F. and Rogaume, Y. (2020), Numerical analysis and validation of a natural convection mix-mode solar dryer for drying red chilli under variable conditions. Renewable Energy, 151, 659–673.

[27] Singh, J. (2015), Review paper of study on solar dryer. Journal of Mechanical and Mechanics Engineering, 1(1), 1-11.

[28] Singh, S., Singh, B., Hans, V.S. and Gill, R.S. (2015), Computational fluid dynamics investigation on Nusselt number and friction factor of solar air heater duct roughened with non-uniform cross-section transverse rib. Energy, 84, 509–517.

[29] Zhiqiang (John) Zhai (2020), Computational fluid dynamics for built and natural environments. Springer Nature Singapore Pte Ltd.

Machine learning in cattle breeding

Bence TARR[1,2], István SZABÓ[2], János TŐZSÉR[3]

[1]Mechanical Engineering Doctoral School (MTDI), Szent István Campus, Gödöllő, MATE
[2]Institute of Technology, Hungarian University of Agriculture and Life Sciences, MATE, Gödöllő
[3]Department of Animal Science, Albert Kázmér Faculty, Széchenyi István
University, Mosonmagyaróvár

Abstract

Artificial intelligence became a key technology in precision agriculture. Cattle breeding is facing ever growing problems as it must increase its productivity while has to fulfill the always growing animal health needs. Food industry also needs better quality raw materials which puts stress on farmers as well. Our research areas are focusing on implementing the power of machine learning to help cattle breeding. In one of our research we examined the possibilities of data based prediction of the linear traits on the Limousin young breeding bulls using machine learning algorithms. In another research we used previously collected milk data to predict somatic cell count numbers in milk samples. We also examined the possibilities of using image recognition in animal cattle health monitoring. Since image recognition based solutions are widespread across several industry and agriculture implementations we did not make new research in this field of AI usage. However to give a broad picture of possibilities and the power of image recognition in animal husbandry we show two use-cases of animal identification. Animal identification can form a basis of many other AI assisted animal healthcare solutions that is why we consider these examples important.

The other two data driven research are new experiments for predicting vital parameters in cattle breeding.

Keywords

cattle breeding, machine learning, somatic cell count, artificial intelligence

1. Introduction

Artificial intelligence (AI) has been increasingly used in cattle breeding to improve genetic selection and increase the efficiency of breeding programs. There are already many applications of AI in cattle breeding for e.g.:

Genetic evaluation: AI algorithms can be used to analyze large amounts of data on an animal's genetic makeup and performance, including pedigree data, genomic data, and phenotypic data. This information can be used to make more accurate predictions about an animal's potential for growth, milk production, and other traits that are important for breeding. (Berglund 2008)

Predictive modeling: Machine learning algorithms can be used to build models that predict an animal's genetic potential based on a variety of factors, including its genetic makeup, environment, and performance data. (Becker et al., 2021). Not just genetic models can be predicted, but also data based prediction models can help in many stages of animal farming. Early selection of young bulls, prediction of weight gain based on breeding data any many other solution exists.

Automated data collection: AI can be used to automate the collection of data on animal performance, such as weight, milk yield, and reproductive performance, which can be used to inform breeding decisions (Micle et al., 2021).

Precision breeding: AI can help breeders identify the best combinations of animals to produce offspring with specific traits, such as disease resistance or meat quality (Nogoy et al., 2021)

Overall, AI has the potential to significantly improve the efficiency and effectiveness of cattle breeding programs, leading to healthier, more productive animals and more sustainable agricultural practices.

Most of the AI solution used in cattle breeding focuses on utilizing image recognition in favor of helping breeders. That is why we made a survey on cattle identification solutions used in animal health. This part of our research focus on mainly reviewing the existing solutions for the role of image recognition in animal husbandry. We found the identification to be the most interesting part, and research area that can serve as the basis for several animal health solutions.

Our other researches focuses on data based prediction methods. First we used previously collected data to predict linear traits in young breeding Limousin cattle. And then in our other solution we used milk analysis database to predict somatic cell count in milk samples. In both cases our aim was to utilize historical collected data. This makes our solutions very cost-effective as for creating the models we do not need new investments for data collection.

In the following we will show our results in those fields.

2. Animal identification using AI

Identification of bovine animals based on nose print
Animal biometrics is an emerging field of research based on the representation of the visual appearance of animals based on general characteristics and primary biometric features. The identification of individual cattle is an important issue worldwide for the classification, registration, traceability and health management of different breeds (Kühl HS, Burghardt T, 2013). Classical animal identification methods usually based on manual identification systems. Classical animal identification methods can be easily falsified by changing the unique numbers on the labelled ear tags. These main problems can be solved by using dot images of cattle noses.

One possible approach to using dot images of cattle noses to identify individual animals in a herd is through a process called "nose printing." To create a nose print, a cow's nose is coated with a non-toxic ink, and then pressed onto a piece of paper or a digital scanner. This creates a unique pattern of dots that can be used to identify the individual animal. Once the nose prints are created, they can be stored in a database along with information about each animal, such as its breed, age, and health history. Then, when a particular cow needs to be identified, its nose can be scanned and compared to the database of nose prints to find a match. Nose printing is a relatively low-tech and inexpensive way to identify individual animals, and it can be useful for tracking things like health records, breeding history, and ownership information. However, it does require some initial training to learn how to correctly identify and record the unique patterns of each cow's nose.
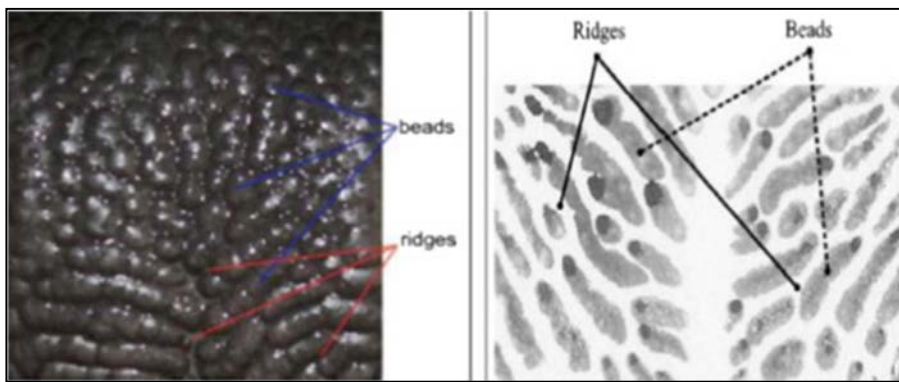

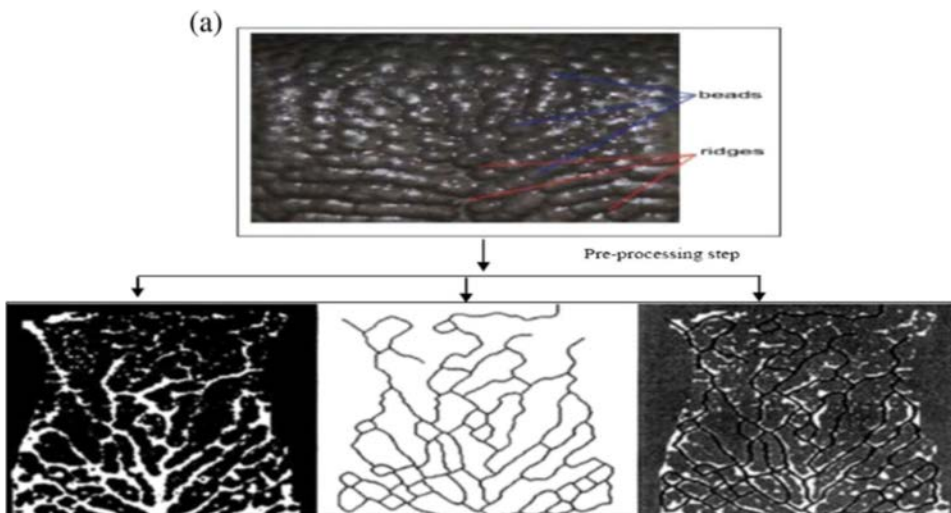*Figure 1.* The two main characteristics

Figure 2. Models after processing

After we have created the database identification by nose dots (muzzle print) is similar to the recognition of minutiae dots in human fingerprints. In the study, 500 cattle were examined, each with 10 20-megapixel images. The images were then used to identify the animals by two main characteristic stamps (beads, ridges) (Figure 1).

The images were then edited to reduce noise, improve image quality and make key features more visible. The resulting models could then be recognised and worked with by an artificial intelligence (Figure 2).

The research involved working with 5,000 images, at the end of which the software was able to identify cattle with 96.74% accuracy. High accuracy of this solution proves the usage of this method can be implemented for solving real life problems.

Identification of cattle by appearance

Modern solutions such as the unique identification of cattle are needed to properly run a precision farming system. Currently, cattle are identified visually, using unique radio frequencies or ear tags. Artificial intelligence can again be used to replace these systems. In one study, this is precisely what has been attempted using deep learning algorithms. Deep learning algorithms use multi-level neural networks for learning (Yongliang at al., 2019). In this case, they combined CNN (Convolutional Neural Network) and LSTM (Long Short-Term Memory) networks to achieve outstanding results in animal identification.

A convolutional neural network (CNN) is a type of artificial neural network commonly used in image and video recognition, natural language processing, and other tasks involving structured inputs.

The key feature of a CNN is its use of convolutional layers, which are designed to recognize spatial patterns in the input data. Each convolutional layer consists of multiple filters that scan the input data and extract features that are relevant for the given task. These features are then passed to one or more fully connected layers, which perform the actual classification or prediction. One advantage of CNNs is that they can learn to recognize patterns in the input data that are invariant to translation, rotation, and other types of transformations. This makes them well-suited for tasks such as object recognition in images and speech recognition in audio.

LSTMs are often used for sequence modeling tasks, where the input data has a temporal structure and the order of the elements matters, such as predicting the next word in a sentence or the next stock price in a time series. In some cases, it is beneficial to combine CNNs and LSTMs to leverage their respective strengths. Tipically, in video classification tasks, a CNN can be used to extract spatial features from each frame of the video, and then an LSTM can be used to model the temporal relationships between the frames and make a prediction for the entire sequence (Ahsan et al.,2020).

Overall, combining CNNs and LSTMs can lead to improved performance on tasks that require both spatial/temporal feature extraction and sequence modeling.

A total of 516 video recordings were made of 41 cattle once a month for three months. First, the recorded footage was analysed frame by frame by the CNN network and then a dataset of each cattle, including their visual characteristics and individual movements, was created. The resulting CNN sets are then fed into the LSTM network, which is able to learn and recognise the cattle (Figure 3).
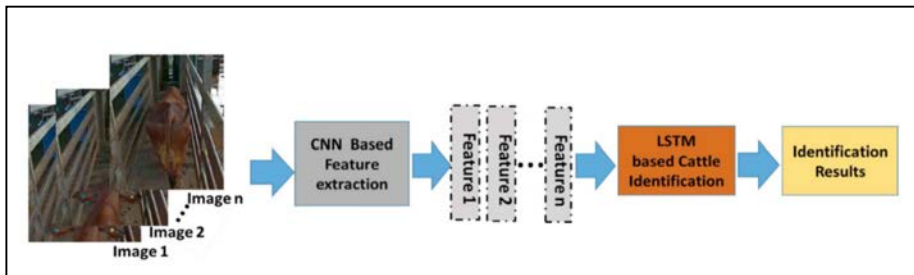
Figure 3. The process image identification

The experimental results show that our method achieved 88% and 91% accuracy for 15 and 20 frame videos, respectively, so the experiment can be considered a success. In addition, when only the CNN system was used without the LSTM network, the accuracy was only 57% instead of nearly 90%. This also shows that combining several AI-based models improves the achievable accuracy.

3. Predicting linear traits in young breeding Limousin cattle

The objective of our research was to prove that machine learning can be used for prediction of different phenotype parameters with satisfactory results.

Conformation scores of 325 animals were collected in one Limousin seedstock herd. The animals were the progenies of 18 sires, born between 1990 and 1996. Sire candidates of 12 months old were officially qualified at the end of the performance test. Four trait groups were formed, including four traits in each.

Group I: height at withers, chest depth, shoulder stability, strength of back and rump

Group II: length of the body, length of the back, length of the loin, length of the rump

Group III: width at withers, chest width, loin width, rump width I

Group IV: muscularity of breast, muscularity of shoulder, muscularity of back, muscularity of rump.

The bulls were scored on the 1-9 point scale according to Balika and Bíró (1993). In this modified classification system 1-3 points mean the undesirable and ≥ 4 points the excellent stature. The present scoring system described in the

Breeding Programme of the Breeding Association of Limousin Breeders (Balika and Tőzsér, 2001).

Recorded data were used to train linear regression based AI algorithm.

In this study we used Microsoft Azure provided algorithms. Using the Linear regression AI learning algorithm, we have separated our database in two parts. First, we used 70% of our data to train the algorithm. The remaining 30% of data were used to test and verify the algorithm after training.

To decided how good our prediction absolute error and coefficient of determination were used as metrics. Since a regression model approximates the relationship between the variables, by adding irreducible error term we get:

$$Y \approx \beta_0 + \beta_1 X_1 + \beta_2 X_2 + \cdots + \beta_n X_n + \epsilon$$

Where ϵ is a mean zero random error.

Linear regression is a type of supervised machine learning model used to predict a continuous output variable based on one or more input variables. In other words, it is a method of modelling the relationship between a dependent variable (output) and one or more independent variables (inputs). The goal of linear regression is to find the best-fit line that describes the relationship between the input variables and the output variable. The following steps were made to build our trained model (Jamal et al., 2018):

Data Collection: The first step is to collect a dataset with input variables (also known as features or predictors) and the corresponding output variable. We used previously collected data.

Data Preparation: The next step is to clean and pre-process the data. We removed missing data and zero values. After that normalization were used to prepare data for training our model.

Splitting the Data: The dataset is then split into a training set and a testing set. The training set is used to train the model, and the testing set is used to evaluate its performance. For training our machine learning algorithms we have separated our database in two parts. First, we used 70% of our data to train the algorithm. The remaining 30% of data were used to test and verify the algorithm after training.

Model Training: The linear regression model is trained on the training set by finding the best-fit line that describes the relationship between the input variables and the output variable. The line is determined by finding the coefficients that minimize the difference between the predicted output and the actual output.

Model Evaluation: The performance of the model is then evaluated using the testing set. This is done by comparing the predicted output from the model with the actual output for each input in the testing set.

In Table .1 we can see which dependent variables were used for prediction. We also show the input variables that were used to train the model. The range of the possible given scores are also shown.

Table 1. Characteristics of estimation

Dependent variables	Independent variables
Score for muscularity (0-60 score)	Score for utility value, Score of length, Score for with (0-40 score, or 0-60 score)
Length of the rump (1-9 score)	Length of the body, Length of the back, Length of the loin (1-9 score)
Muscularity of breast (1-9 score)	Muscularity of shoulder, Muscularity of back, Muscularity of the round of rump, Muscularity of the width of rump (1-9 score)
Muscularity of the width of rump (1-9 score)	Muscularity of breast, Muscularity of shoulder, Muscularity of back, Muscularity of the round of rump (1-9 score)

A web-based interface was developed to the trained algorithm, so later new real-life data can easily be used to predict scoring of the chosen quantity or body condition scores. This web-based interface uses api to connect to

Results

Although in our experiment we used a little different phenotype parameter to predict the correlation between the parameters, former studies gave as a firm guess which machine learning model to use for our AI prediction (regression models).

Testing our trained algorithms, the following results were received which are summarized in *Table 2*.

Table 2. Results of prediction (n=325)

Methods of AI	Dependent variables	Mean absolute error, score	Coefficient of determination, R^2
	Score for muscularity (0-60 score)	3.38	0.86
Linear regression based algorithm	Length of the rump (1-9 score)	0.42	0.80
	Muscularity of breast (1-9 score)	0.35	0.86
	Muscularity of the width of rump (1-9 score)	0.41	0.77

Results shows us that machine learning prediction using trained models can be used successfully for predicting the scores for our chosen traits: Score for muscularity, Length of the rump, Muscularity of breast, Muscularity of the width of rump.

Analysing the measurement results it can be interesting that by building and using more data from the past even better models can be trained to help real life trait selection on farms.

Our proposed method for using ML for estimating linear traits on Limousin breeding bulls well fits the line of new technology solutions in helping precision livestock farming. As several ML solutions have been made for diary energy, animal health, animal monitoring and many others (Garcia et al., 2020), our solution can be used for prediction of several different phenotype parameters using ML.

4. Predicting Somatic Cell Count (SCC) in milk samples

In Hungary milk production is the main driving power for cattle breeding. Milk quality is important for several aspects: animal health, milk quantity, milk and dairy food production. That is why it is of great importance to find new ways to help farmers to predict anomalies in milk production process.

Milk samples are regularly collected and analyzed in accredited laboratories. That is why milk data are available for many years with standardized laboratory measurements.

Milk is a good source of quality fats, proteins, carbohydrates, minerals, and vitamins. Determining milk constituents is very important in dairy production and is usually conducted by means of physical or chemical processes in laboratories.

Our partner provided us anonymized milk data from 3 different farms. The main aim for milk data analysis is to select possible infected milk samples and to predict mammary health. In case infected milk sample is found, then the corresponding cow must be ruled out from milk production and needs medicaments for healing.

Somatic cell count (SCC) is a measurement of the number of somatic cells, mainly white blood cells and epithelial cells, that are present in a sample of milk. In dairy cattle, an elevated SCC can indicate the presence of an udder infection or mastitis, which can impact milk production and quality.

The SCC in cattle milk is typically measured in thousands of cells per milliliter (thousands/ml) and is used as an indicator of milk quality. In many countries, the legal limit for SCC in milk is 300,000 cells/ml, although some regions may have stricter or more lenient regulations (Alhussien et al., 2018).

Milk with a high SCC may also have a shorter shelf life and may not be suitable for certain dairy products, such as cheese. Therefore, dairy farmers aim to keep SCC as low as possible through proper animal husbandry, such as maintaining a clean and dry environment, proper milking techniques, and promptly treating any udder infections. Factors which influence somatic cell counts in bovine milk are reviewed and guidelines for their interpretation are presented. It is suggested that the thresholds of 300 000 and 250 000 cells/mL be used to identify infected cows. However, it is stressed that somatic cell counts are general indicators of udder health which are subject to the influence of many factors. Therefore, the evaluation of several successive counts is preferable to the interpretation of an individual count.

Predicting SCC based on other measured parameters of milk samples yields a great economical gain. As mastitis can be much easier treated when realized in time. Both the cost of medication will be lower and the cow can get back to milking process earlier. That is why it is vital to find new solutions for prediction of SCCC in milk.

Dataset

Data collected from 3 different herds were used in this study. All together 3 years of measurement (2019-2021) data were used in the initial dataset. Milk samples were collected every month, so all together we had 36 months of data from each herd. The full dataset had 18000 entries with 14 parameters analyzed from each sample. The main milk parameters that were used in this study: casein, lactoferrin, somatic cell count (SCC), proteins and milk fat.

Since our main goal was to predict somatic cell count, we have to examine the SCC variable at first step.

Table 3. Description of somatic cell count values
in our dataset

	SCC Value
Count	186686
Mean	575000
Std	1245000
Min	2000
25%	50000
50%	150000
75%	401000
Max	800000

Somatic cell count

Milk somatic cells (SCC) are a mixture of milk-producing cells and immune cells. These cells are secreted in milk during milking and are used as an index for estimating mammary health and milk quality (Burvenich at al., 2000). The main role of SCC is to fight infection and repair tissue damage. All the developed countries are using milk somatic cell counts (SCCs) as a marker to monitor the prevalence of mastitis in dairy herds.

The SCC is quantified as the number of cells per ml of milk.
- SCC of 100,000 or less indicates an 'uninfected' cow,
- SCC of 200,000 would determine whether a cow is infected with mastitis
- SCC of 300,000 or greater Cows infected with significant pathogens

The variance of the somatic cell count is rather large and therefore the so-called linearized somatic cell count is commonly used in the literature (Dégen, Monostori). Logarithmic somatic cell count (LogSCC) is a transformed

measurement of somatic cell count that expresses the count on a logarithmic scale. The LogSCC is calculated by taking the logarithm of the somatic cell count and then multiplying by 100. For example, a somatic cell count of 400,000 cells/ml would have a LogSCC of 5.6. LogSCC is used as a tool to compare the level of somatic cell count between different milk samples, herds, or regions. This method of expressing somatic cell count is useful because it magnifies differences between samples and allows for more accurate statistical analysis. LogSCC is also used to evaluate the effectiveness of somatic cell count reduction programs in dairy herds. (Dabdoub et al. 1984).

After logarithmic transformation of SCC values we get the following linearized results. Which gives us a 9 grade scale for different SCC value ranges (Table 4).

Table 4. Linear scores after SCC logaritmization

Linear Score	Somatic cell count	Linear score	Somatic cell count
1	25 000	6	800 000
2	50 000	7	1 600 000
3	100 000	8	3 200 000
4	200 000	9	6 400 000
5	400 000		

Lactoferrin

For creating good prediction, we need to decide which other parameters will have an effect on SCC? This is the main question. Biological experiments showed a great influence of lactoferrin and SCC (O'Halloran at al., 2010)

Lactoferrin is a protein that is present in the milk of many mammals, including cattle. It is a glycoprotein with a molecular weight of approximately 80 kDa and is highly conserved across species. Lactoferrin is a multifunctional protein that plays a crucial role in the innate immune system and provides several benefits to the calf and the cow.

In cattle, lactoferrin is synthesized and secreted by epithelial cells of the mammary gland during lactation. It is present in the milk of healthy cows in relatively high concentrations, ranging from 0.1 to 2.5 g/L, and is essential for the health and development of the calf. Lactoferrin provides several benefits, including:

Immune defense: Lactoferrin has antimicrobial properties and can bind to and sequester iron, which limits bacterial growth in the mammary gland and prevents the spread of infection to the calf.

Anti-inflammatory properties: Lactoferrin has been shown to have anti-inflammatory effects, which may help to reduce inflammation and promote healing in the mammary gland.

Nutrition: Lactoferrin is a source of iron for the calf and is also thought to have other nutritional benefits, such as promoting the growth and development of the gastrointestinal tract.

Antioxidant activity: Lactoferrin has antioxidant properties and can help to protect cells from oxidative damage.

Overall, lactoferrin plays an essential role in the health and well-being of the cow and her calf and is an important component of cattle milk.

Lactoferrin and somatic cell count (SCC) are related to each other in several ways. Lactoferrin is synthesized and secreted by the same epithelial cells of the mammary gland that produce somatic cells. Thus, changes in SCC in cattle milk can affect the amount of lactoferrin present in the milk.

Lactoferrin has been shown to have antimicrobial properties, which can help to reduce bacterial growth in the mammary gland and prevent mastitis. Since mastitis is a common cause of high SCC in cattle milk, and lactoferrin has been suggested as a potential biomarker for mastitis detection.

Lactoferrin has been shown to have anti-inflammatory effects, which can help to reduce inflammation in the mammary gland that is associated with mastitis. Elevated SCC in cattle milk is also indicative of inflammation in the mammary gland, and lactoferrin may help to alleviate the inflammation and reduce SCC.

Lactoferrin plays a crucial role in the innate immune system of cattle and may be a useful biomarker for mastitis detection and management. However lactoferrin alone is not enough to create good prediction for elevated SCC values.

5. Methods

Our aim was to build a machine learning based model to predict somatic cell count using some mixture of Lactoferrin and other milk parameters.

Logaritmic SCC were divided into 3 groups not the original 9. As 3 group is enough for everyday classification (not infected = 0, possible infection=1 and infected=2) we created 3 SCC categories from our linear scores.

For data cleaning we first deleted all zero values and all records where any missing values were found. The whole software was written in Python using Pandas and sickit-learn. We needed no normalization as we were planning to use tree-based models that are much more robust to outliers than linear models. As our output variable (linearized SCC) was divided into 3 categories we were using tree-based algorithms that are good for multiclass classification.

After creating the three linear SCC groups we examined our output dataset. For distribution of categorical outcomes, we received the following values (Table 5).

It is clearly seen the we have much more 0 output values (low SCC means healthy milk) than 1 and 2 values. So we were facing the so-called unbalanced output dataset problem. Where one of the output categories are very overrepresented than others.

Table 5. Occurrence of output variable values in our dataset.

SCC score	Number of occurrences in dataset
0	15500
1	2200
2	2100

We had to find workarounds to balance categories. There are two possible solutions:

An unbalanced dataset will present high accuracy on majority classes and poor results on minority class, while the minority class may be more important (usually that is the case). The problem is even worse in the case of multi-class imbalanced datasets. For handling this circumstance, there are several methods that can be classified into two major groups: data-level methods and algorithm-level methods.

Data-level methods for balancing a dataset
Data level methods for balancing a dataset in a multi-class classification problem involve modifying the training data to create a more balanced distribution of classes. There are several techniques that can be used for this purpose:

These solutions are categorized into three techniques: under-sampling, over-sampling, and hybrid-sampling. All these techniques operate similar way, they re-sample data. There are several solutions for this such as random under-sampling (samples are randomly removed from the database), directed under-sampling (samples to be deleted are not random), random over-sampling (creates new samples randomly), directed over-sampling (new samples are not created), and combinations of the above techniques. So basically, under-sampling methods remove samples from majority classes until the two classes become balanced. Random under-sampling (RUS) when we remove samples from majority classes randomly is the most used technique.

Over-sampling is when we create new entries for the minority class (Liu et al., 2007). Usually we increase the number of minority class samples by randomly adding new entries from existing entries, but this solution often causes overfitting (Ramentol et al., 2012).

We can also use a hybrid solution when both under and over sampling is used together to reach a balanced dataset.

Algorithm-level methods
In case of algorithm-level method, the algorithm itself is modified to solve the problem of being biased towards the overrepresented classes. One of the solutions is the so-called cost-sensitive learning. In that method we give penalty points when the result from the minority set is not predicted correctly. We will look for the most cost-effective solution which will help the algorithm to tend towards prediction good results in the minority set and not just focusing on the majority classes (Ling et al., 2008).

Hybrid methods

In the hybrid method we try to combine the data-level and the algorithmic level solution together.

The problem with this solution is that it is the most complex to implement ant the most time consuming to train.

One of the most often used method for combining the two solutions is ensemble learning. Ensemble learning is a technique in machine learning where multiple models are combined to improve the overall performance and accuracy of a predictive model. By combining several weak learners, a strong learner can be created that is more accurate than any individual model. A weak learner is a model that performs slightly better than random guessing. In other words, a weak learner is a model that has an error rate that is only slightly lower than 50%, which is the error rate of random guessing for a binary classification problem. A weak learner can be thought of as a model that is not very good at making accurate predictions on its own but can still contribute to an ensemble model by providing some useful information.

A strong learner is a model that is able to make accurate predictions with high confidence. A strong learner is typically a model that is able to capture the underlying patterns and relationships in the data and make accurate predictions on new, unseen data. In ensemble learning, a strong learner is created by combining multiple weak learners in a way that maximizes the overall accuracy.

The idea behind ensemble learning is that by combining multiple weak learners, we can create a strong learner that is better at making predictions than any individual model. This is because each weak learner may capture a different aspect of the underlying patterns in the data, and by combining them, we can build a more comprehensive and robust model.

Ensemble learning can be used with a variety of machine learning algorithms, such as decision trees, random forests, and neural networks.

In our experiment we used two data level solutions. As a first step we did up-sampling of minority data when we duplicate the underrepresented values and at the same time, we alter a little bit the input variables. In our case a random multiplying factor were used to alter the input variables (*a factor of 0.98-1.02).*

After this data balancing, we had a very balanced dataset which is eligible for multiclass machine learning algorithms. After our initial benchmarking which included 4 ML methods and were benchmarked on the untreated database for quick overview, we choose to do our first experiment using Extra Trees Classifier.

In all cases dataset and training sets were divided on a 70% (training) and 30% (testing) basis. The division of the database happened after the balancing and data cleaning of the input database.

We ran several trial predictions to find the best suited input variables. The input variables were chosen based on the correlation matrix.

6. Verification

Since we had only three categories, we decided to calculate the accuracy separately for all three categories and then calculate an average accuracy as well to describe our results (Ben-David et al., 2012).

The accuracy score function we utilized computes the accuracy as the count of correct predictions.

In multilabel classification, the function returns the subset accuracy. If the entire set of predicted labels for a sample strictly match with the true set of labels, then the subset accuracy is 1.0; otherwise it is 0.0.

If y_i is the predicted value of the *i*-th sample and y_i is the corresponding true value, then the fraction of correct predictions over $n_{samples}$ is defined as

$$\text{accuracy}(y, \hat{y}) = \frac{1}{n_{samples}} \sum_{i=0}^{n_{samples}-1} 1(\hat{y}_i = y_i)$$

So accuracy were checked independently for all three variables, and we assumed that the average accuracy is calculated as the average of the three subclass.
We considered good result if the prediction is over 80% and an over 90% success rate would be considered as excellent.

Results

We run 15 different combination of input variables using the chosen algorithm.

The best result came using the following input variables: 'Z', 'KARBAMID','CUK_SZ', 'LF', 'ZSIR_SZ','FEH_SZ'.

We calculated the average accuracy, and the accuracy for each category (positive TRUE values).

Table 6. Results for the demo algorithm

ML algorithm accuracy score	For LSCC value=0	For LSCC value=1	For LSCC value=2	average
Extra Trees Classifier	0.89	0.88	0.86	0.88

The Extra Trees Classifier gave well over 80% results in all classification categories. Our results proved to be consistent, and the accuracy checking for each output categories separately made it sure that our algorithm is not biased. So it will not tend to predict the most likely outcome, as it gave similar good prediction values for less represented cases in our testing database.

Conclusion

The role of AI in many aspects of agriculture industry is gaining more and more importance. In our research we previewed many cases when image recognition was used to help cattle breeding. Then we experimented with existing farming data. At first, we predicted linear traits in young breeding Limousin cattle. Our prediction reached an accuracy level of 83%. Then we analyzed collected milk data to predict somatic cell count as the best marker for mastitis in cows.

In this case we reached an average of 88% prediction accuracy with using 6 input variables. All these experiments proves that AI can significantly improve the effectiveness of animal husbandry. Both image recognition and data analysis using machine learning tools give us great results in predicting useful outcomes of information.

Further research needs to be made by gathering more data to broaden our database. Also, we need to find new output variables that would be helpful for farmers or food producers and use machine learning for those cases.

In the case of somatic cell count prediction our results show us that it is possible to predict the change in SCC values. To make it even more useful and accurate prediction we must find a database with daily milking data. This is possible since in the last years robot milking machines make on the fly analysis during milking. So our first results give a firm bases that future research using daily milking data with machine learning built models can be even more beneficial in predicting mastitis.

Our initial results prove that using already existing data from animal husbandry can be a great help in creating a more efficient farm management.

References

[1] B Berglund, Genetic Improvement of Dairy Cow Reproductive Performance 09 July 2008 https://doi.org/10.1111/j.1439-0531.2008.01147.x

[2] C.A. Becker, A. Aghalari, M. Marufuzzaman, A.E. Stone, Predicting dairy cattle heat stress using machine learning techniques, Journal of Dairy Science, Volume 104, Issue 1, 2021, Pages 501-524, ISSN 0022-0302, https://doi.org/10.3168/jds.2020-18653.

[3] Micle, D.E.; Deiac, F.; Olar, A.; Drența, R.F.; Florean, C.; Coman, I.G.; Arion, F.H. Research on Innovative Business Plan. Smart Cattle Farming Using Artificial Intelligent Robotic Process Automation. Agriculture 2021, 11, 430. https://doi.org/10.3390/agriculture11050430

[4] Nogoy, K.M.C.; Park, J.; Chon, S.-i.; Sivamani, S.; Park, M.-J.; Cho, J.-P.; Hong, H.K.; Lee, D.-H.; Choi, S.H. Precision Detection of Real-Time Conditions of Dairy Cows Using an Advanced Artificial Intelligence Hub. Appl. Sci. 2021, 11, 12043. https://doi.org/10.3390/app112412043

[5] Kühl HS, Burghardt T (2013) Animal biometrics: quantifying and detecting phenotypic appearance. Trends Ecol Evol 28(7):432-441
DOI: 10.1016/j.tree.2013.02.013

[6] Yongliang Qiao, Daobilige Su, HeKong, Salah Sukkarieh, Sabrina Lomax, Cameron Clark (2019) Individual Cattle Identification Using a Deep Learning Based Framewor, IFAC-PapersOnLine, Volume 52, Issue 30, Pages 318-323 https://doi.org/10.1016/j.ifacol.2019.12.558

[7] Ahsan, M., & Nygard, K. E. (2020, March). Convolutional Neural Networks with LSTM for Intrusion Detection. In CATA (Vol. 69, pp. 69-79).

[8] Balika, S., I. Bíró. The order of type classification system in Limousin breed in Hungary (in Hungarian). Association of Limousin Breeders, 1993, Budapest, 1-7.

[9] Balika, S., Tőzsér J. Breeding Programme of the Breeding Association of Limousin Breeders, Budapest, 2001, 1-35.

[10] Jamal, S., Goyal, S., Grover, A., Shanker, A. (2018). Machine Learning: What, Why, and How?. In: Shanker, A. (eds) Bioinformatics: Sequences, Structures, Phylogeny . Springer, Singapore. https://doi.org/10.1007/978-981-13-1562-6_16

[11] Rodrigo García, Jose Aguilar, Mauricio Toro, Angel Pinto, Paul Rodríguez, A systematic literature review on the use of machine learning in precision livestock farming, Computers and Electronics in Agriculture, Volume 179, 2020, 105826, ISSN 0168-1699,
https://doi.org/10.1016/j.compag.2020.105826.

[12] Alhussien MN, Dang AK. Milk somatic cells, factors influencing their release, future prospects, and practical utility in dairy animals: An overview. Vet World. 2018 May;11(5):562-577. doi: 10.14202/vetworld.2018.562-577. Epub 2018 May 2. PMID: 29915493; PMCID: PMC5993762.

[13] Burvenich, Christian, et al. "Physiological and Genetic Factors That Influence the Cows Resistance to Mastitis, Especially during Early Lactation." Proceedings of the 5th IDF Mastitis Congress, Symposium on Immunology of Ruminant Mammary Gland, 11-14 June 2000, Stresa, Italy, 9-20, 2000.

[14] Dr. Dégen László, Dr. Monostori Attila, Az új tőgyegészségügyi rendszer bemutatása, Állattenyésztési Teljesítményvizsgáló Kft.

[15] Dabdoub, S.A.M., Shook, G.E., Phenotypic relations among milk yield, somatic cell count and clinical mastitis, Journal of Dairy Science, 1984, Volume 67, Issue SUPPL. 1, Pages 163-164

[16] F. O'Halloran, D.P. Berry, B. Bahar, D.J. Howard, T. Sweeney, L. Giblin, Polymorphisms in the bovine lactoferrin promoter are associated with reproductive performance and somatic cell count, Journal of Dairy Science, Volume 93, Issue 3, 2010, Pages 1253-1259, ISSN 0022-0302, https://doi.org/10.3168/jds.2009-2699.

[17] Liu A, Ghosh J, Martin CE. Generative oversampling for mining imbalanced datasets. In: DMIN; 2007. p. 66–72.

[18] Ramentol E, Caballero Y, Bello R, Herrera F. SMOTE-RSB*: a hybrid preprocessing approach based on oversampling and undersampling for high imbalanced data-sets using SMOTE and rough sets theory. Knowl Inf Syst. 2012;33(2):245–65.

[19] Ling CX, Sheng VS. Cost-sensitive learning and the class imbalance problem. Encyclopedia Mach Learn. 2008;2011:231–5.

[20] Arie Ben-David, Eibe Frank, Accuracy of machine learning models versus "hand crafted" expert systems – A credit scoring case study, Expert Systems with Applications, Volume 36, Issue 3, Part 1, 2009, Pages 5264-5271, ISSN 0957-4174, https://doi.org/10.1016/j.eswa.2008.06.071.

Thermal vacuum testing method and test results of the experimental packages of radnano dosimeters

Gábor GÉCZY[1], István SERES[2]

[1]Mechanical Engineering Doctoral School (MTDI), Szent István Campus, Gödöllő, MATE
[2]Institute of Mathematics and Basic Science, Hungarian University of Agriculture and Life Sciences, MATE, Gödöllő

Abstract

This paper presents the evaluated test method and the test result of the outgassing qualification results of the experimental plastic packages of the RadNano dosimeters manufactured by 27G-Technology Ltd. The RadNano dosimeters are tiny next-generation integrated circuit devices that use semiconductor-based technology to sense and measure the ionizing radiation that reaches the electronics, including gamma, X-ray and high-energy proton radiations. A unique test method was evaluated for this qualification which took the ECSS-Q-ST-70-02C standard as basis, that is commonly used by the European Space Agency (ESA) and the results are compatible and comparable with the NASA low outgassing recommendations. Several different package constructions were tested, all of them passed the low outgassing recommendations and the test results made it possible to select the best construction from outgassing point of view.

Keywords

RadNano, dosimeter, package, 27G-Technology, TVAC, thermal, vacuum, testing, outgassing, TML, CVCM, ECSS-Q-ST-70-02C

1. Introduction

Polymer plastic packages are used with preference in the electronics industry in order to increase environmental resistance, as a massive protective coating can be formed from it. These coatings can be used to waterproof and insulate electronic devices, such as space devices, but also prevent contamination of sensitive electronic sensors. In addition, it can also protect devices from mechanical impacts and damage.

In addition to the general industrial requirements, the packages and housings of space equipment must also meet special requirements, such as low outgassing in vacuum, they must withstand extreme mechanical loads and accelerations, they must withstand extremely extreme temperature conditions, as well as extreme UV radiation (Shimmin, 2015).

Plastic packaged parts on spacecraft or satellites are often placed close to electronic or optical devices, where contamination can lead to serious problems. For example, many adhesives emit gases, possibly volatiles, that condense and contaminate electronic, optical, and other precision instruments. Outgassed compounds can cloud or vaporize optical and electro-optical components and disrupt circuit operation. Even small amounts of condensed organic matter can alter the reflectivity or absorption of optical components. Accurate control of gas emission levels is critical in preventing pollutant build-up and the resulting loss of performance in critical subsystems (Pastore, 2020), (Sang, 2012).

This paper presents the evaluated test method and the test result of the outgassing qualification tests of the packages of the RadNano dosimeters. The RadNano dosimeters are tiny next-generation integrated circuit devices that use semiconductor-based technology to sense and measure the ionizing radiation that reaches the electronics, including gamma, X-ray and high-energy proton radiations (RadNano Technical Datasheet). The test was performed according to the ECSS-Q-ST-70-02C standard of the European Space Agency. The definitions and glossary of terms from ECSS-S-ST-00-01C apply to this document.

2. Experimental

Test method

The test procedure was evaluated based on the recommendations of the ECSS-Q-ST-70-02C standard, that is using the ASTM E595 test method. This method is widely used by NASA and other research institutions and industrial companies to measure the outgassing properties of the materials and samples to qualify (NASA Reference Publication, 1997).

At least 12 g of the material sample must be prepared for the tests (10 g for the first test and 2 g for the subsequent repeat test).

The temperature must be set between 10 °C and 130 °C with an accuracy of ± 1 °C. The relative humidity should be between 40% and 80% relative humidity with an accuracy of ± 1% relative humidity. The vacuum required for the measurement must be set at a pressure of 10^{-4} Pa with an accuracy of ± 10%.

This procedure also measures the volatile content of adhesives in a heated vacuum chamber. The samples are kept at 25 °C, 50% humidity and standard atmospheric pressure for 24 hours prior to testing so that all samples are prepared in the same way. The samples are then weighed and placed in separate compartments in a solid copper heating rod, with separate lids for each compartment.

The heating rod shall be placed in a test chamber with a pressure of no more than 5×10^{-5} torr. Both the samples and the copper rod are heated to 125 °C for 24 h and the volatile gases are vented through the outlet. With the collector plate set to a temperature of 25 °C, a significant part of the volatile substances condenses on the plate. The total mass loss (TML) of each sample shall be calculated as a percentage

by comparing the mass of the sample before and after the test. The amount of volatile condensable material (CVCM) collected for each sample should be calculated as a percentage by comparing the mass of the clean collection plate with the mass of the collection plate after the test. The ECSS-Q-ST-70-02C standard describes the detailed procedure (see Fig. 1), and the sample mass vs. time (see Fig. 2) and the collector plate related diagram (see Fig. 3).
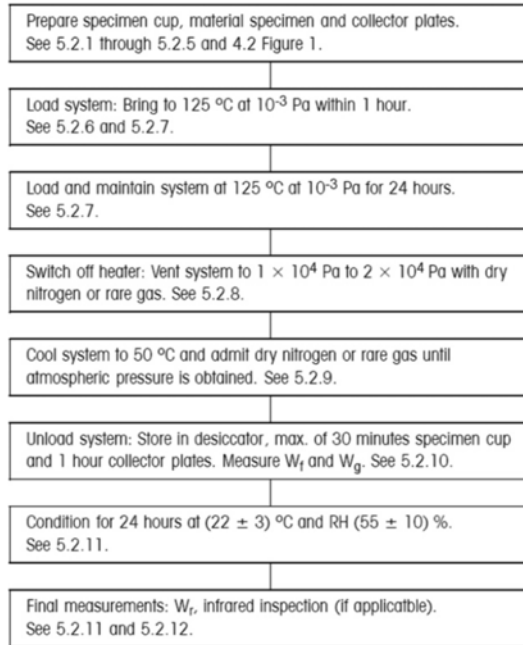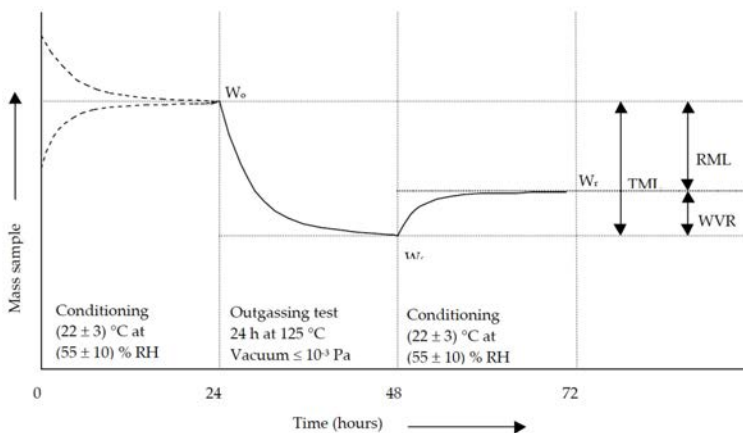

Figure 1. Test flow chart (ECSS-Q-ST-70-02C)
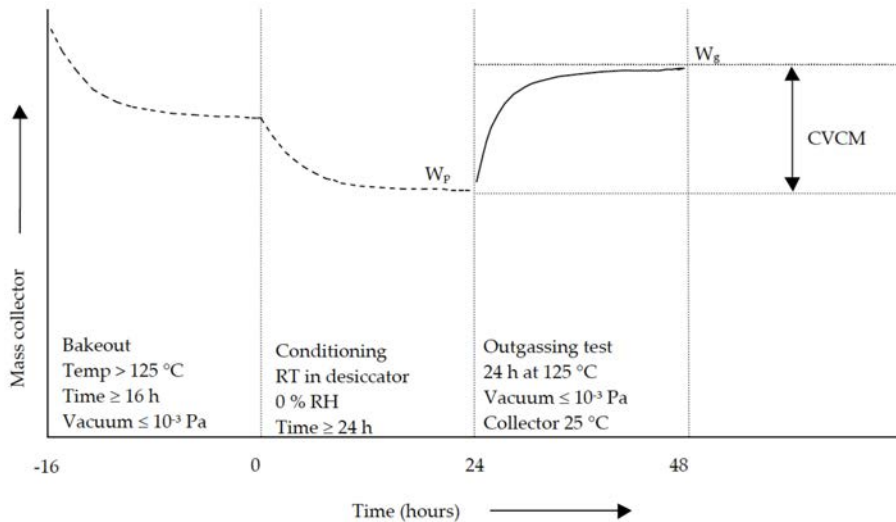

Figure 2. Parameters for sample

Figure 3. Parameters for collector plate

Test criteria

In practice, the NASA low outgassing recommendation placed a limit that requires that the total mass loss (TML) of a polymer-based sample under vacuum and high temperature should not exceed 1% of its original weight, and the collected volatile condensables (CVCM) should not exceed 0.10% of the original sample weight. An addendum states that the total mass loss may exceed 1.0% if it can be shown that the mass loss in excess of 1.0% was water vapour. Low-emission adhesives and polymers for use in space are screened using the standard ASTM E595 test method.

If the CVCM does not exceed 0.10% and the TML does not exceed 1.0%, the material passes the test. If the CVCM exceeds 0.10% - regardless of the TML - the material fails the test. However, if the CVCM is less than 0.10% but the TML is greater than 1.0%, an additional measurement must be made to determine how much water vapor the sample can reabsorb after conditioning, which is a 50% RH takes place in a chamber at 25 °C for another 24 hours. Water vapor recovered (WVR) is the mass of recovered water vapor relative to the mass of the original sample, expressed as a percentage. If the difference between TML and WVR does not exceed 1.0% (and CVCM does not exceed 0.10%), the material passes the test.

To summarize the results of ASTM E595:
- If CVCM ≤ 0.10% and TML ≤ 1.0%, the material meets expectations.
- If CVCM ≤ 0.10% and TML > 1.0%, the material may meet expectations if TML – WVR ≤ 1.0%.
- If CVCM > 0.10%, the material does not meet the requirements.
- If TML – WVR > 1.0%, the material does not meet expectations.

Test facility and equipment

The TVAC test facility of the Centre for Energy Research, Hungarian Academy of Sciences was used for the tests (see Fig. 4). This laboratory is located in the Radiation Protection Department at the Central Physical Research Institute of the Hungarian Academy of Sciences (abbreviated as: KFKI), operated by Remred Space Technologies Ltd. This is the only one laboratory in Hungary that is currently able to carry out the aimed measurements according to the ECSS-Q-ST-70-02C standard, however, this chamber also does not have a cooled collection tray, so the tests were limited to TML measurements, it was not possible to measure CVCM.

The following Table 1. contains the applicable equipment used for the tests.

Table 1. Test Equipment List

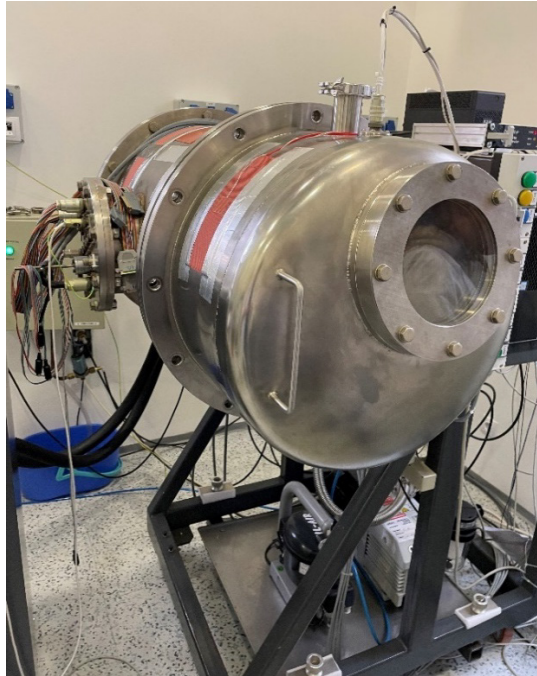| #	Name	Model	S/N	Due Date
1	Space Simulator	-	-	-
2	Space Simulator PLC Controller Unit	PLC-PC	CR5239837	According to NI documentation
3	Network distributor for the TVAC system	TL-SF1008D	2169132016817	-
4	Compressor	SILAIR 30/6	001002256	-
5	Rotary Pump	Trivac B D16B	31001456387	2023.11.03
6	Turbomolecular pump	Turbovac 450i	31001460367	2023.11.03
7	Turbo Pump Controller Unit	Turbo Control 300	-	2023.11.03
8	Turbomolecular pump interface	-	-	2023.11.03
9	Vacuummeter Data-acquisition Unit	Graphix Two	400	2023.11.22
10	Electronic/Automated Air Valve	-	-	2023.11.03
11	High vacuum angle valve BAV 1	Leycon 215325	2021129012766	2023.11.03
12	High vacuum angle valve BAV 2	Leycon 215324	2057384012173	2023.11.03
13	Thermostat (for the T-VAC system)	Presto A80	-	-
15	Uninterruptible Power Supply	NIKY S 1.5 kVA	R40GN00068	-

Figure 4. The TVAC chamber used for the tests

The following table lists the instruments used for the measurements.

Table 2. Instrumentation List

#	Name	Model	S/N	Due Date
1	Temperature Sensor #7	PT-103-14H	P35353	-
2	Residual Gas Analyzer	Transpector MP-H20P	70146167	2024.03.01
3	TQCM Contamination Monitoring System	66TR	66TR289	2024.03.01
4	Vacuummeter (at the turbo pump)	Penningvac PTR 90N	1630573014	-
5	Vacuummeter (inside the chamber)	Ionivac ITR90	13030	2023.11.22
6	Moisture Analyzer	Sartorius AG MA30-000V3	80702496	2023.08.20.
7	Precision Scale	Agimpex HA-50	CT-33-1027	2023.11.07.

The following tables show the applicable test activity related tolerances and accuracies. Note that tolerances and accuracies were identified based on ECSS-E-ST-10-03C section 4.4.2 and section 4.4.3.

Table 3. Test Tolerances

#	Name	Parameters	Tolerances
1	Temperature	above 80 K	T_{min} +0/-4 K; T_{max} -0/+4 K
		T<80 K	Tolerance to be defined case by case
2	Pressure (in vacuum chamber)	>1.3 hPa	± 15%
		$1.3 \cdot 10^{-3}$ hPa to 1.3 hPa	± 30%
		<1.3 hPa	± 80%
3	Test duration		-0/+10%

Table 4. Test Accuracies

#	Name	Parameters	Tolerances
1	Temperature	above 80 K	± 2 K
		T<80 K	Accuracy to be defined case by case
2	Pressure (in vacuum chamber)	>1.3 hPa	± 15%
		$1.3 \cdot 10^{-3}$ hPa to 1.3 hPa	± 30%
		<1.3 hPa	± 80%

Sample preparation and sample holder

The RadNano samples were prepared by 27G-Technology for the qualification. Since the RadNanos are quite small (12.7×12.7×2.5 mm, see Fig. 5) and light (~ 0.9 g/pc), 16 samples were prepared (14 for the test and 2 spare pieces) from 3 different batch groups to give a representative qualification and to reach the necessary 10 g mass for the test. Each sample had their own electrical acceptance test and unique laser marked serial number in the factory.
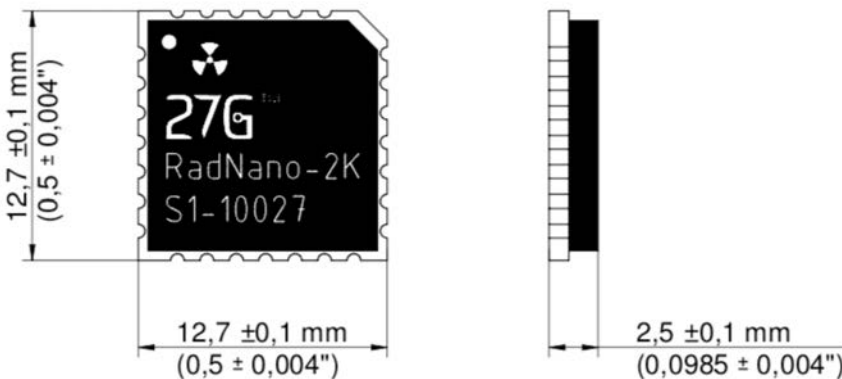

Figure 5. RadNano size and serial number marking example

The following figure shows the samples selected to perform the outgassing qualification test.
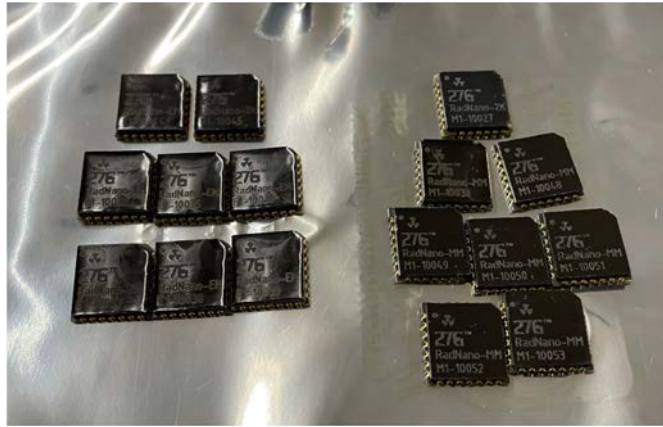

Figure 6. RadNano samples before TVAC test

A sample holder was designed and manufactured for this test to act as an adaptor between the heated plate of the vacuum chamber and the samples during the tests (see Fig. 7). This sample holder was manufactured by anodized aluminum and needed no further elements or materials to keep the samples fixed during the test, this way the holder had no influence on the test results. Since the used vacuum chamber has a vertically positioned heater plate, the gravitational force could be used to hold the samples in their place. The following cross-section shows the arrangement of the test setup. The holder has an open structure at both ends that allows gases to escape from the samples.
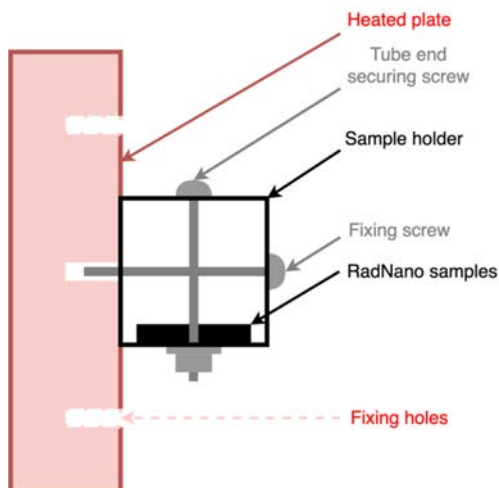

Figure 7. Sample holder/adaptor structure cross-section view

Test procedure

The test procedure started on the 22nd of November 2022. Based on the ECSS-Q-ST-70-02C standard, before the vacuum test, the samples were preconditioned for 24 hours, i.e. they were stored at a controlled temperature of 22 ± 3°C and a relative humidity of 55 ± 10% RH. Each unit has a factory marking and a unique serial number, so there was no need to apply additional distinguishing markings.

The test laboratory cleanliness was checked before the test procedure as per "Absence of Contamination when examined with a specific light source, angle of incidence and viewing distance using normal or magnified vision." defined in ECSS-Q-ST-70-01C.

After preconditioning, the weight of the samples was measured individually at the test site, using a Sartorius AG MA30-000V3 precision scale (see Fig. 8). Before each mass measurement procedure, the precise operation of the instrument was checked with a calibration weight of 1 and 20 g. In addition, all samples were weighed with a second Agimpex HA-50 precision scale for control purposes.

The weight of individual samples was determined from the average of three parallel measurements on the two scales. After measuring and recording the individual weight of the samples, the total weight of all the samples was weighed. The results are listed in the results and discussion section.

Figure 8. Samples prepared for weight measurement

After the measurements, the test samples were placed in the sample holder and fixed in the vacuum chamber. A total of 14 samples were placed in the

console in order to meet the minimum quantity requirement of 10 g of the material to be tested as prescribed by the ECSS-Q-ST-70-02C standard. The sample holder is made of anodized aluminum, which, due to its good thermal conductivity, was able to adequately transfer the heat of the heated plate to the tested samples. In addition, thanks to its open structure, the emitted gases were able to escape from the samples.
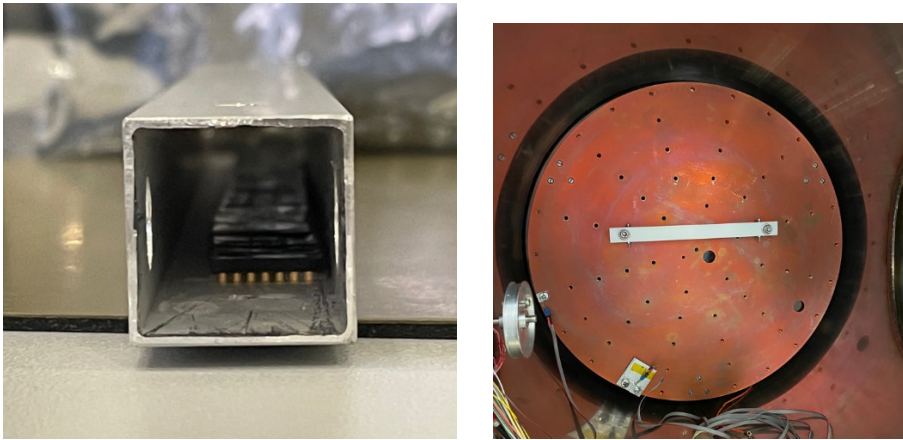

Figure 9. Sample holder loaded with samples (left), and fixed in the vacuum chamber (right)
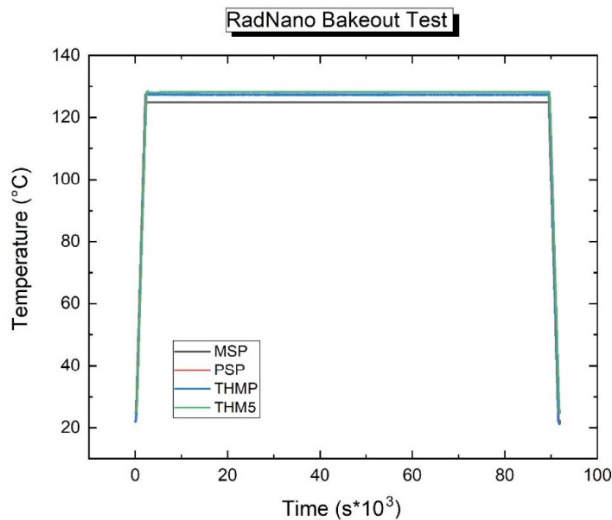

Figure 10. TVAC test profile

The TVAC chamber's temperature profile was set using the SpaceSim software. First, the chamber got depressurized until 10^{-3} mbar was reached. After

a short dwell on room temperature (+22 °C), the chamber was heated up to +125 °C, with a 3 °C/minute heating rate. The measured items were kept at the target temperature for 24 hours, then the cooldown process was started with a -3 °C/minute cooling rate. The temperature profile is shown in Fig. 10 (MSP is the master setpoint from the applied test profile, PSP is the setpoint of the thermostat, THMP is the measured temperature of the cooling liquid of the thermostat, and THM5 is the temperature measured by the sensor placed on the chamber base plate).

After the vacuum test, the sample holder was removed from the vacuum chamber, and the samples were collected. No visual changes could be detected on the samples (see Fig. 11).

Then, following the recommendations of the ECSS-Q-ST-70-02C standard, the weight of the samples was again measured and recorded, and then post-conditioning took place for 24 hours. During the post-conditioning, the units were stored at a controlled temperature of $22 \pm 3°C$ and a relative humidity of $55 \pm 10\%$ RH. After another 24 hours, the samples were subjected to a final mass measurement, thereby allowing the measurement of the mass of any moisture absorbed by the samples from their environment.

Figure 11. RadNano samples after the test procedure, no visible changes occurred on the samples

3. Results and discussion

Calculations

For Total Mass Loss (TML) calculation the weights of the tested items were measured before and after thermal bakeout. For TML calculation the following equation was used:

$$TML\% = \frac{(M_1 - M_2)}{M_1} * 100\%$$

Water Vapor Regain (WVR) was also calculated, with the following equation:

$$WVR = M_3 - M_2$$

Where M_1 = mass before bakeout, M_2 = mass after bakeout, and M_3 = mass after incubation at room temperature and humidity.

TML values were calculated individually for each RadNano device, and a total TML for all 14 units as well. Regained Mass Loss (RML) refers to the mass deficit which persists even after rehydration. The values result from the following equation:

$$RML\% = \frac{(M_1 - M_3)}{M_1} * 100\%$$

Table 5. TML and WVR Results

#	Name	S/N	M1 23/11/22 [g]	M2 24.11.22 [g]	M3 24.11.22 [g]	Unit TML Result [%]	Unit WVR [g]	Unit RML Result [%]	Electrical test
1	TVAC-TS-1	E1-10034	0.750	0.747	0.748	0.40	0.001	0.27	OK
2	TVAC-TS-2	E1-10035	0.763	0.760	0.760	0.46	0.0005	0.39	OK
3	TVAC-TS-3	E1-10036	0.775	0.772	0.773	0.39	0.001	0.26	OK
4	TVAC-TS-4	E1-10037	0.771	0.768	0.768	0.39	0	0.39	OK
5	TVAC-TS-5	E1-10038	0.778	0.775	0.776	0.39	0.001	0.26	OK
6	TVAC-TS-6	E1-10039	0.768	0.765	0.765	0.39	0	0.39	OK
7	TVAC-TS-7	E1-10044	0.885	0.883	0.883	0.23	0	0.23	OK
8	TVAC-TS-8	G1-10045	0.926	0.923	0.924	0.32	0.001	0.22	OK
9	TVAC-TS-9	M1-10048	0.861	0.861	0.861	0.00	0	0.00	OK
10	TVAC-TS-10	M1-10049	0.843	0.842	0.842	0.12	0	0.12	OK
11	TVAC-TS-11	M1-10050	0.819	0.817	0.817	0.24	0	0.24	OK
12	TVAC-TS-12	M1-10051	0.883	0.882	0.883	0.11	0.0005	0.06	OK
13	TVAC-TS-13	M1-10052	0.864	0.863	0.863	0.12	0	0.12	OK
14	TVAC-TS-14	M1-10053	0.860	0.859	0.859	0.12	0	0.12	OK
RadNano series total mass (14 units, measured by scale) [g]*			11.547		11.516		11.520		
Results summarized by calculator [g]*			11.546		11.517		11.522		

*Differences between the values measured by scale and the calculated summaries result from scale inaccuracies.

Table 6. Summarized TML Results

TML all measured [%]	0.26847
WVR all measured [%]	0.03464
RML all measured [g]	0.23383

Residual Gas Analyser Results

From the residual gas mass spectra, a peak at 18 amu can be seen which probably refers to water vapour (M=18 g/mol). The smaller peaks may refer to N_2 (M=28 g/mol) remaining from atmospheric air, and NH_3 (M=17 g/mol).

Fig. 12 shows the results of the mass spectrometry analysis performed by FabGuard Residual Gas Analyzer software. The upper graph shows one sweep through the sensor's whole sensitivity range, which was done at the beginning of the incubation. Each peak represents one type of molecule that was captured by the sensor. The lower graph depicts the decrease of the peaks' amplitudes between 12:30 and 14:20 on 2022.11.23. Red line refers to the 18 amu peaks.
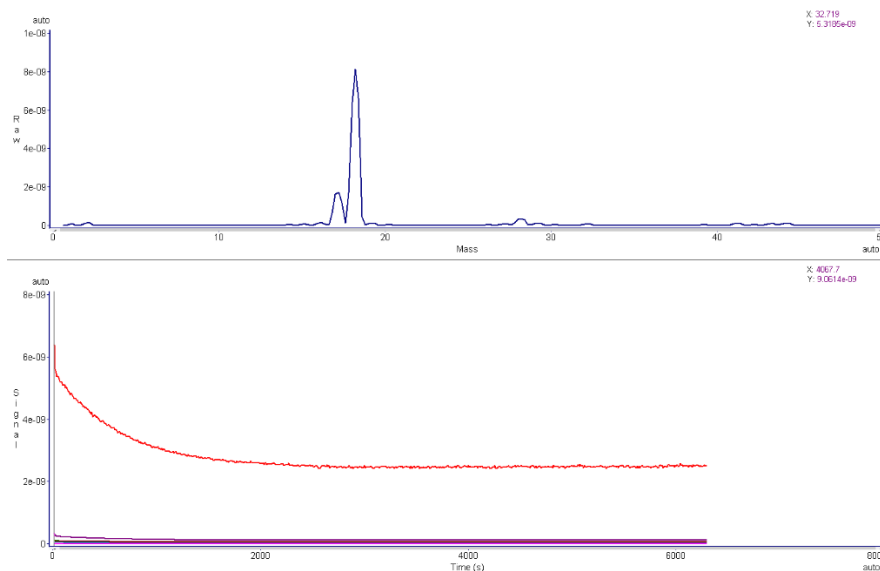

Figure 12. Results of RGA by FabGuard

In Fig. 13, eight specific sweeps are shown in the same frame. Each line refers to a sweep from a different time. There is an inverse correlation between the time of bakeout and the amount of residual gas measured by the sensor.
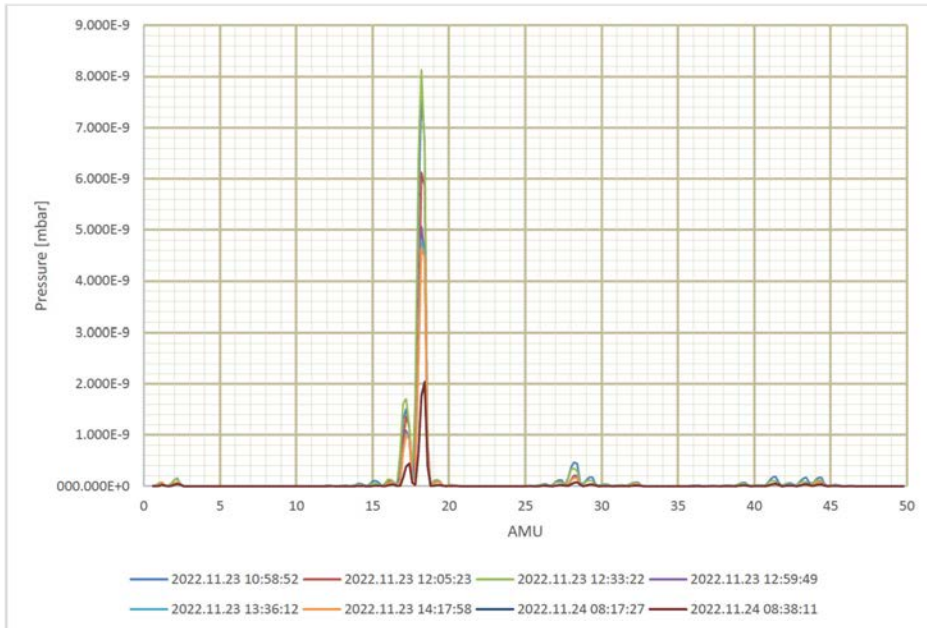
Figure 13. Analysis of RGA DataTemperature
and Humidity

Fig. 14 shows the registration of the environmental conditions (humidity and temperature) in the TVAC test facility during the course of the test program.
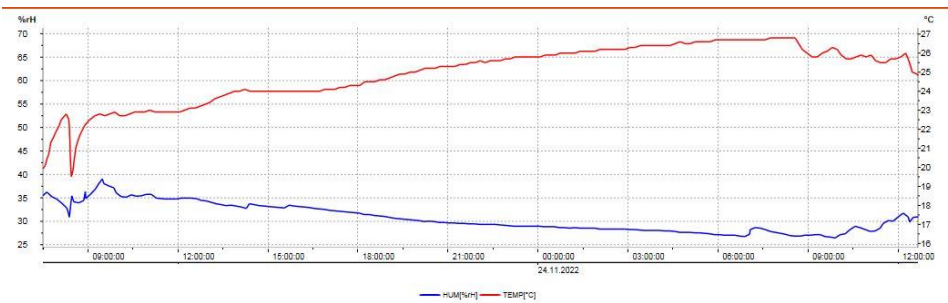

Figure 14. Environmental Parameters During the Test

Table 7. Minimum and Maximum Environmental
Parameter Values

Parameter	Min.	Max.
Temperature (°C)	19.50	26.80
Humidity (rH%)	26.50	39.10

Results Discussion

Table 5. presents the detailed results of the individual samples. As it is listed in the Unit TML Result [%] row, all samples are well below the 1.0% total mass loss limit regardless of its sample group. Items with ID TVAC-TS-1…8 were selected from the first manufactured RadNano batch, this group have the highest outgassing of 0.22 to 0.46%, that is still well below the limit. Items with ID TVAC-TS-10…14 were selected from the second manufactured RadNano batch, where the processes and materials are improved from an outgassing point of view that is also visible from the results (0.06 to 0.24% TML).

TVAC-TS-9 test item was an experimental unit, forming the third group, manufactured with a unique process focusing on the minimization of the outgassing. The experimental process seems successful, since no detectable mass loss occurred in this unit during the outgassing test (0.00% TML).

In Fig. 13, eight specific sweeps are shown in the same frame. Each line refers to a sweep from a different time. There is an inverse correlation between the time of bakeout and the amount of residual gas measured by the sensor. The residual is decreasing with time.

From the residual gas mass spectra, a peak at 18 amu can be seen which probably refers to water vapour (M=18 g/mol). The smaller peaks may refer to N_2 (M=28 g/mol) remaining from atmospheric air, and NH_3 (M=17 g/mol).

Conclusions

- The above described test method made it possible to test and measure the outgassing of the selected samples based on the ECSS-Q-ST-70-02C standard.
- From the above detailed investigations, the following conclusions can be drawn:
- The tested RadNano samples were all compliant with the total mass loss requirements of the low outgassing requirements, the worst sample has 0.46% TML that has still adequate margin from the 1.0 % maximal TML limit.
- The second and third sample groups show reduced outgassing parameters therefore, the development of the RadNano package seems to be effective in this respect. It would be worthwhile to carry out new tests on a higher number of samples from the latest package construction to confirm the near-zero outgassing with higher initial mass.
- Even if it was not possible to analyze the CVCM of the samples, the low TML values indicate a strong likelihood that the latest package construction is compliant with the CVCM requirements as well.
- From the residual gas mass spectra, a peak at 18 amu can be seen which probably refers to water vapour. The smaller peaks may refer to N2 remaining from atmospheric air, and NH_3.

Acknowledgements

References

[1] ASTM E595-15(2021) Standard Test Method for Total Mass Loss and Collected Volatile Condensable Materials from Outgassing in a Vacuum Environment https://www.astm.org/e0595-15r21.html

[2] ECSS-Q-ST-70-02C European Cooperation for Space Standardization (ECSS) Standards System – Spacecraft Product Assurance: Thermal Vacuum Outgassing Test for the Screening of Space Materials (15-NOV-2008) https://ecss.nl/standard/ecss-q-st-70-02c-thermal-vacuum-outgassing-test-for-the-screening-of-space-materials/

[3] ECSS-S-ST-00-01C European Cooperation for Space Standardization (ECSS) Standards System - Glossary of terms (1 October 2012) https://ecss.nl/standard/ecss-s-st-00-01c-glossary-of-terms-1-october-2012/

[4] NASA Reference Publication 1124 Revision 4 June 1997 Outgassing Data for Selecting Spacecraft Materials https://ntrs.nasa.gov/api/citations/19970027853/downloads/19970027853.pdf

[5] R. Pastore, A. D. (2020). Outgassing effect in polymeric composites exposed to space environment thermal-vacuum conditions. Acta Astronautica, Volume 170, 466-471.

[6] Sang Yoon Park, H. S. (2012). Effect of vacuum thermal cyclic exposures on unidirectional carbon fiber/epoxy composites for low earth orbit space applications. Composites Part B: Engineering, Volume 43(2), 726-738.

[7] Shimmin, R. A. (2015). Small spacecraft technology state of the art. NASA Ames Research Center, Mission Design Division, NASA/TP-2015-216648/REV1.

[8] RadNano Technical Datasheet - 27G-Technology https://27g.space/wp-content/uploads/RadNano_Datasheet.pdf

Integrating system dynamics stella and plantCV to analyze the growth process of indoor precision vegetable production system

Nezha KHARRAZ[1], Dr. István SZABÓ[2]

[1]Mechanical Engineering Doctoral School (MTDI), Szent István Campus, Gödöllő, MATE
[2]Institute of Technology, Hungarian University of Agriculture and Life Sciences, MATE, Gödöllő

Abstract

The use of image-based approaches for plant phenotyping provides a great potential for automated analysis of various plant cultivars, which can be utilized as variables or parameters for mathematical and computational models. The interplay between models and data could help identify plant traits and metadata necessary for model calibration and parameterization, leading to the discovery of new traits or environmental data relevant to the plant phenotyping community. In this paper, we demonstrate the integration of PlantCV for image analysis and Stella software for system dynamics modeling to analyze the growth process of a plant phenotyping system, specifically a green salad. Our results highlight the potential for plant phenotyping and system dynamics modeling to evaluate connections and identify compatible ways to communicate between these communities, ultimately leading to more sustainable and efficient agricultural technologies.

Keywords

System dynamics, Reinforcing loop, Phenotyping systel, PlantCV, Plant growth.

1. Introduction

Automation and computer assisted production systems are key areas of developing modern sustainable agricultural technologies and it can be essential for environmental aspects as well as for efficiency approaches. Since powerful IT solutions are becoming accessible, economical rationality also supports these trends, and the possibilities of using IoT solutions makes these solutions practically available.

   Over the past ten years, platforms for studying plant characteristics have produced vast amounts of detailed data on various genotypes, collected under specific conditions or in the field (Tardieu et al. 2017). Precision agriculture is advancing more and more with the use of modern computation and engineering solutions that are data-intensive. With increasing computational power and the availability of robust mathematical algorithms, it is advantageous to incorporate

them into precision agriculture. By using image-based approaches for plant phenotyping, there is a great potential for automated analysis of various plant cultivars. (Dmitrii et al.2020). This data can then be utilized as variables or parameters for mathematical and computational models, which increases the potential usefulness of phenomics data (Muller and Martre 2019; Louarn and Song 2020). By incorporating this data into process-based crop models or individual-based models, we could predict integrated or functional traits across different environments and management practices. This interplay between models and data could also help identify the plant traits and metadata necessary for model calibration and parameterization, potentially leading to the discovery of new traits or environmental data relevant to the plant phenotyping community. (Parent and Tardieu 2014; Casadebaig et al.2020).

One critical question is the extent to which phenomics and modeling communities share datasets and use them together. System dynamics can provide insight into specific research disciplines' historical evolution and emerging topics, as well as visualize the main research areas of a community. We conducted a causal loop analysis on a green salad, to see how phenotyping helps in growing the plant in better conditions and faster. Plant phenotyping and System dynamics modeling can help in evaluating the connections and identify compatible was to communicate between these communities. (Nardi et al. 2016). In this paper we used PlantCV for image analysis and Stell software for System Dynamics.

2. Experimental

As we explained in the beginning, this research is a continuity of the prototype realized for the BSC and MSC studies. The growing chamber consists of a box with 4 faces of plexiglass plates, the back plate is covered. The top and bottom plates are supplied by thin wood plates. The aim of the wood plate in the top side is to hold the 4 bulbs while in the bottom plate is to hold the reservoir, all together with the remaining components. In the beginning, the parts were designed independently using part design section.
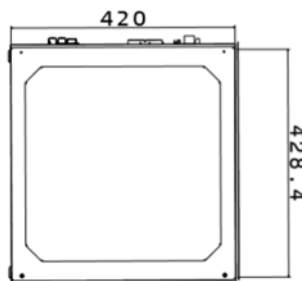

Figure 24. Back view of the hydroponic prototype wireframe

The parts were assembled together using assembly design section. We have used multiple type of constraints to connect the parts together. For connecting the light bulbs to wood plate, we have used coincidence constraint, and the same for the bolts. As for the other parts, we have simply used contact surface constraint, by defining the multiple surfaces where contact takes place. For positioning some parts to others, we have used the offset constraint, by defining the distance at which one part is located from another. The figures show the front view wireframe and back view wire frame respectively.
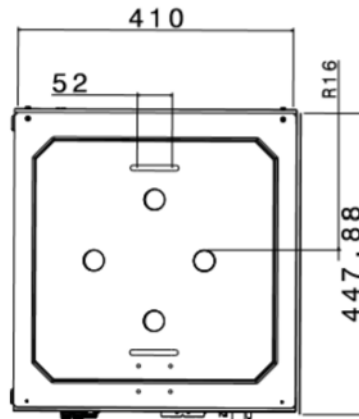

Figure 25. Up view of the hydroponic prototype wireframe
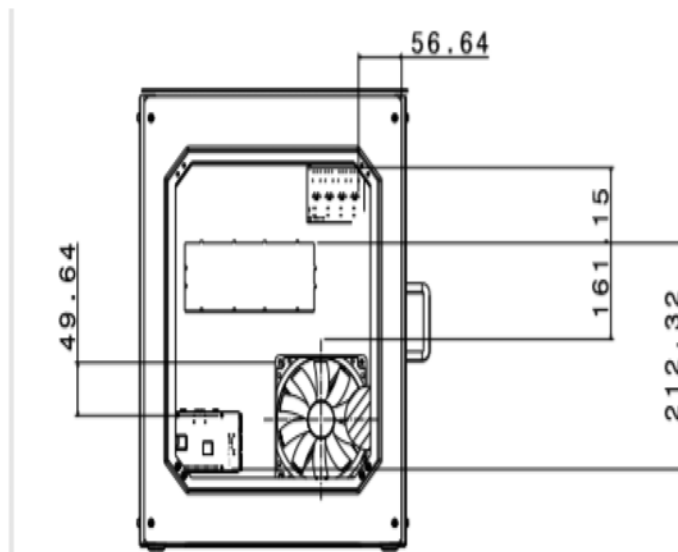
Figure 26. Electronic design of the hydroponic system wireframe

Figure 27. Plant Reservoir placed inside the hydroponic system

Figure 28. Rockwool placed in the reservoir
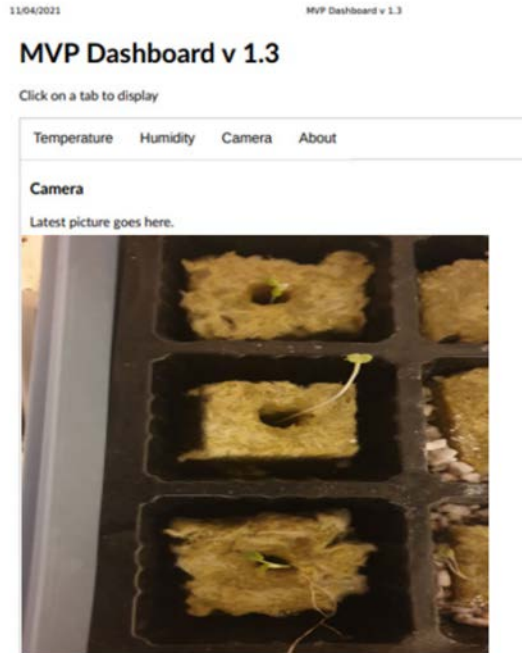
Figure 29. Image capturing the first growing leaves

PlantCV

PlantCV is an open-source image analysis software with an aimed package for plant phenotyping using computer vision. The software is built based on modular functions, it is applicable to a wide range of plant types and different imaging systems, it has multiple functions where the use of each one is centered on the context of an overall image-processing workflow. Nonetheless, the software is new and under continuous development where new functionalities are added on a regular Basis. PlantCV currently supports the analysis of standard

RGB color images, standard grayscale images, thermal infrared images, grayscale images from chlorophyll fluorescence imaging systems, and hyperspectral images. Support for additional image types is under development.

PlantCV is composed of modular functions that can be rearranged and adjusted quickly and easily. Workflows do not need to be linear. Please see workflow example below for more details. A global variable "debug" allows the user to print out the resulting image. The debug has three modes: either None, 'plot', or 'print'. If set to 'print' then the function prints the image out to a file, or if using a Jupyter notebook we could set debug to 'plot' to have the images plot to the screen. Debug mode allows users to visualize and optimize each step on individual test images and small test sets before workflows are deployed over whole datasets.

Images can be proceeded in any case, with any type of camera used (In this paper, we will user later, Raspberry PI camera). Image processing works with adjustments if images are somehow lit and free of background which is similar in color to plant material.

This particular image was captured by a digital camera, this proves that PlantCV works on images not necessarily captured on a high-throughput phenotyping system with idealized VIS image capture conditions.

In order to run the pant CV code, we need to previously have two required inputs:

1. **Image:** Plant CV process the Images regardless of what type of camera was used, particularly in our project, we used Raspberry PI. The processing work better if the images are of good lighting and the background's color is different to the plant's material.

2. **Output directory:** We need to select and name an output directory where the output images from each step will be saved.

In the input, we have the input image. As we mentioned before, our particular image was captured by Raspberry PI, this means that Plant CV works on images not captured with specialized VIS image capture conditions. In our project, we used Plant CV to decompose the contours that constitute each plant. Our main challenge was to use plant processing for a single plant that can be composed of several contours, therefore we needed to sort out contours and cluster them together in some way. In order to be able to arrive to the final result, which is color values. There are several steps that we need to follow until color values for each plant pixel is processed.

If the background is foreseeable, the program starts with defining the background. For our particular image, the program did some pre-masking of the background, in order to keep all plant's information while removing the background. Thresholding is the simplest method of segmenting images, as it can be used for creating binary images. Generally, we need to select one of the color channels before performing a binary threshold on any image. The plant CV code as shown fully in appendices convert the RGB image to HSV color space then extract the 's' or saturation channel, but if some of the plant's information is missed or disappeared then the resulted channels may be combined in more steps.

Figure 30. Input image

```python
#!/usr/bin/env python
import os
import argparse
from plantcv import plantcv as pcv


### Parse command-line arguments
def options():
    parser = argparse.ArgumentParser(description="Imaging processing with opencv")
    parser.add_argument("-i", "--image", help="Input image file.", required=True)
    parser.add_argument("-o", "--outdir", help="Output directory for image files.", required=False)
    parser.add_argument("-r", "--result", help="result file.", required=False)
    parser.add_argument("-w", "--writeimg", help="write out images.", default=False, action="store_true")
```

The code starts by importing necessary packages of libraries, and by defining the inputs. One importing thing before running the program is to make sure that plant CV is installed. We easily installed it from PyPI, by running the following command in the terminal as an administrator:
<pip install plantcv>.

```python
def main():
    # Get options
    args = options()

    pcv.params.debug = args.debug  # set debug mode
    pcv.params.debug_outdir = args.outdir  # set output directory

    # Read image
    img, path, filename = pcv.readimage(filename=args.image)
```

```
# Read image
img, path, filename = pcv.readimage(filename=args.image)

# Convert RGB to HSV and extract the saturation channel
s = pcv.rgb2gray_hsv(rgb_img=img, channel='s')
```

Stella

STELLA, an acronym for Systems Thinking, Experimental Learning Laboratory with Animation, and also marketed under the brand iThink, is a graphical language for modeling dynamic systems. It was created by Barry Richmond in 1985 and is distributed by iSee Systems, formerly known as High Performance Systems. Using just four fundamental elements, this software allows for the graphical modeling and simulation of complex systems. STELLA has been employed in academia as both a learning tool and for a diverse range of research and industrial applications.

STELLA has been used in agriculture for modeling and simulating various aspects of agricultural systems, including crop growth and development, irrigation management, and agricultural supply chains. For example, STELLA has been used to model the impact of climate change on crop yields, to optimize crop management strategies, and to simulate the effects of different irrigation management techniques on crop water use and productivity.

To predict the growth height of a plant using STELLA, we need to construct a model that captures the key factors that influence plant growth. For our hydroponic system, we know in advance that the amount and timing of water and nutrient inputs, the ambient temperature and humidity, and the genetic traits of the plant are the main factors.

Once we have identified these factors, we can represent them in a graphical model using the building blocks provided by STELLA. We can use stock-and-flow diagrams to represent the accumulation and depletion of water and nutrients in the soil and plant tissues and use feedback loops to capture the dynamic interactions between these variables.

To calibrate the model and predict the growth height of a green salad plant, we will use the collected data on the environmental conditions and management practices that are relevant to our system. This includes data on temperature, precipitation, soil moisture, and fertilizer applications, as well as measurements of plant growth and development that we did over time.

Using this data, we can estimate the parameters of our model and use it to simulate the growth of the plant under different scenarios. By varying the inputs to the model and observing the outputs, we can explore how different factors influence plant growth and predict how the plant will grow under different conditions.

The first thing we suspected is the relationship between harvested biomass and plant biomass. In a causal loop diagram, the relationship between harvested biomass and plant biomass can be depicted as a reinforcing loop (positive

feedback loop). This is because the more biomass that is harvested, the less biomass is left in the plant. This reduction in biomass can result in slower growth and lower yields in subsequent harvests, which in turn leads to a decrease in the amount of biomass that can be harvested. On the other hand, if the plant biomass increases, there will be more biomass available for harvesting, leading to higher yields and a greater amount of biomass being harvested. This positive feedback loop can continue as long as the plant biomass is able to sustain the level of harvesting. However, it is important to note that there are other factors that can impact the relationship between harvested biomass and plant biomass, such as environmental conditions, nutrient availability, water and oxygen. These factors can also be represented in a causal loop diagram to provide a more comprehensive understanding of the system.

Figure 31. Reinforcing loop of Biomass

In order to include water, oxygen, and nutrients in a causal loop diagram that studies the relationship between harvested biomass and plant biomass, we can add additional feedback loops that account for the effects of these factors.

Therefore, we added a feedback loop that includes the effects of water availability on plant growth. This loop shows that as water becomes scarce, plant growth decreases, which in turn leads to lower plant biomass and reduced yields of harvested biomass.

Similarly, we added a feedback loop that includes the effects of oxygen availability on plant growth. This loop shows that as oxygen becomes limited, plant growth slows down, which reduces plant biomass and ultimately the amount of biomass available for harvest.

Lastly, we added a feedback loop that includes the effects of nutrient availability on plant growth. This loop shows that as nutrient levels become insufficient, plant growth slows down, which again reduces plant biomass and ultimately the amount of biomass available for harvest.

By including these feedback loops in our causal loop diagram, we can create a more comprehensive understanding of the relationships between harvested biomass and plant biomass, and the impact that water, oxygen, and nutrient availability can have on the overall system.

a. Stella Model

In the context of Stella, which is a software tool for modeling and simulation of systems, these concepts refer to the following:

Stocks: Stocks represent the quantity or amount of a particular variable or entity that exists within the system at a given time. In Stella, stocks can be represented by a "stock" module, which allows you to specify the initial value of the stock, as well as any inflows or outflows.

In our research, we examined five types of stocks:

- – Water
- – Nutrient
- – Plant Biomass which is the central stock.
- – Plant height
- – Carbon dioxide

Inflows: Inflows represent the rate at which a particular variable or entity is added to the system over time. In Stella, inflows can be represented by a "flow" module, which allows you to specify the rate at which the inflow occurs.

Outflows: Outflows represent the rate at which a particular variable or entity is removed from the system over time. In Stella, outflows can also be represented by a "flow" module, which allows you to specify the rate at which the outflow occurs.
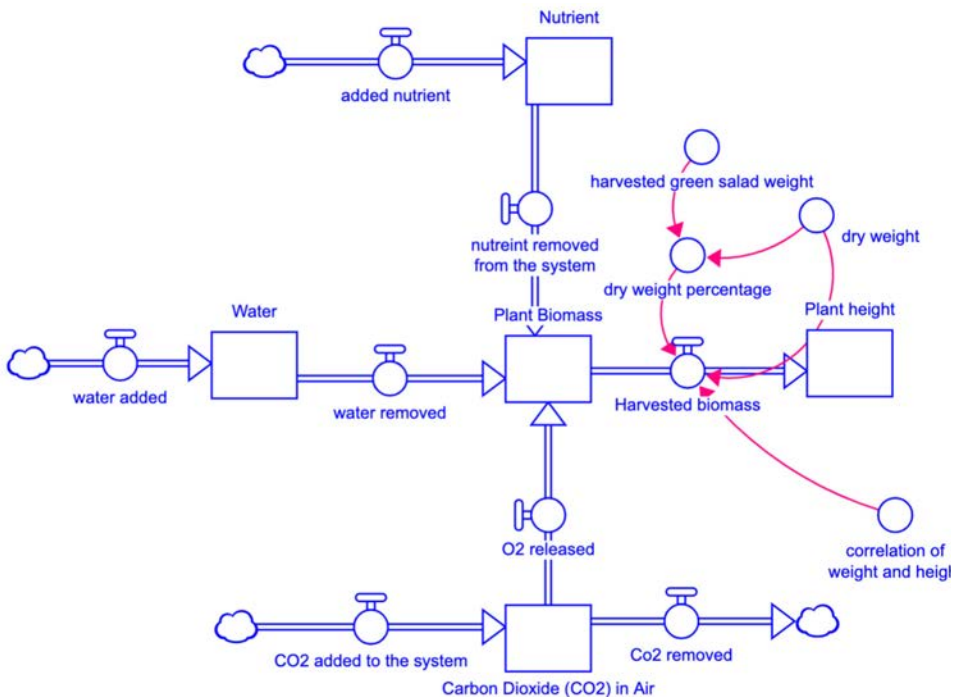

Figure 32. Plant height model on Stella

Together, stocks, inflows, and outflows can be used to model complex systems and analyze how different variables or entities within the system interact with each other over time. Therefore, we used stella model to see if under proffered conditions of our phototyping system, how much time will it take for the plant to reach a height of 30 cm.

In the model below we calculate the harvested biomass from the factor of the plant weight using the following formula:

$$\text{Dry weight percentage} = \frac{Dry\ weight}{Harvested\ weight}$$

$$\text{Harvested Biomass} = \frac{Dry\ weight}{Dry\ weight\ percentage}$$

3. Results and discussion

PlantCV
PlantCV is designed to work with a wide range of plant images, including visible light, fluorescence, and infrared, and it can analyze images of many different plant organs, such as leaves, stems, and roots.
Threshold saturation images are used in plant phenotyping to extract specific features of interest, such as individual leaves, from plant images. By thresholding the saturation channel of the image, the pixels representing the plant or leaves can be separated from the background, allowing for accurate and efficient analysis of plant growth and development.

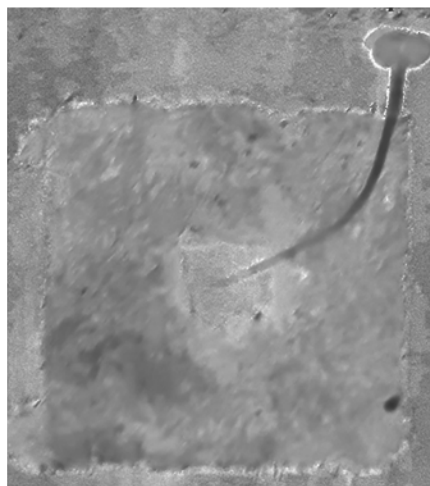*Figure 33.* Threshold the saturation image

Figure 34. Saturation channel from original RGB image converted to HSV color space.

The saturation channel is thresholded, which means the code created a binary image from a gray image based on the threshold values. Our object in this project was the plant which is light.

The threshold creates a binary image from a gray image based on the threshold values than can be adjusted depending on the quality of our image, in our case used 85 for threshold and 255 pixels as a maximum value.

Figure 35. Thresholded saturation channel image. Remaining objects are in white.

In the next step, again depending on the level of lighting, the code can be modified to bettermanipulate the background. The image is then again thresholded and there is an optional fill step that the code runs or not depending on the image, in our case it was not needed.

```
# Convert RGB to LAB and extract the Blue channel
b = pcv.rgb2gray_lab(rgb_img=img, channel='b')

# Threshold the blue image
b_thresh = pcv.threshold.binary(gray_img=b, threshold=160, max_value=255, object_type='light')
b_cnt = pcv.threshold.binary(gray_img=b, threshold=160, max_value=255, object_type='light')
```

Figure 36. Converting and threshold

Figure 37. Blue-yellow channel from LAB color space from original image.

Figure 38. Binary Threshold blue-yellow channel image.

After this step, the resulted the binary image was applied as an image mask over the original image, in order to remove as much background with simple thresholding without missing out any plant material.

```
# Apply Mask (for VIS images, mask_color=white)
masked = pcv.apply_mask(img=img, mask=bs, mask_color='white')
```

Figure 39. Masked image with background removed.

Figure 40. Masked image with background removed

After getting the masked image wit background slightly removed. The next step of the code is capturing the plant in the masked image from the last figure. The masked green-magenta and blue-yellow channels are taken out. The two channels are thresholded after to show different sections of the plant. The small objects are filled. The image taken has very green leaves, but often (especially with stress treatments) there are yellowing leaves, red leaves, or regions of necrosis. The different thresholding channels capture different regions of the plant, then are combined into a mask for the image that was previously masked.

```
# Convert RGB to LAB and extract the Green-Magenta and Blue-Yellow channels
masked_a = pcv.rgb2gray_lab(rgb_img=masked, channel='a')
masked_b = pcv.rgb2gray_lab(rgb_img=masked, channel='b')

# Threshold the green-magenta and blue images
maskeda_thresh = pcv.threshold.binary(gray_img=masked_a, threshold=115, max_value=255, object_type='dark')
maskeda_thresh1 = pcv.threshold.binary(gray_img=masked_a, threshold=135, max_value=255, object_type='light')
maskedb_thresh = pcv.threshold.binary(gray_img=masked_b, threshold=128, max_value=255, object_type='light')

# Join the thresholded saturation and blue-yellow images (OR)
ab1 = pcv.logical_or(bin_img1=maskeda_thresh, bin_img2=maskedb_thresh)
ab = pcv.logical_or(bin_img1=maskeda_thresh1, bin_img2=ab1)

# Fill small objects
ab_fill = pcv.fill(bin_img=ab, size=200)

# Apply mask (for VIS images, mask_color=white)
masked2 = pcv.apply_mask(img=masked, mask=ab_fill, mask_color='white')
```

Figure 41. RGB to LAB conversion code

Figure 42. RGB to LAB conversion. (Top) The green-magenta "a" channel image. (Bottom) The blue yellow "b" channel image.
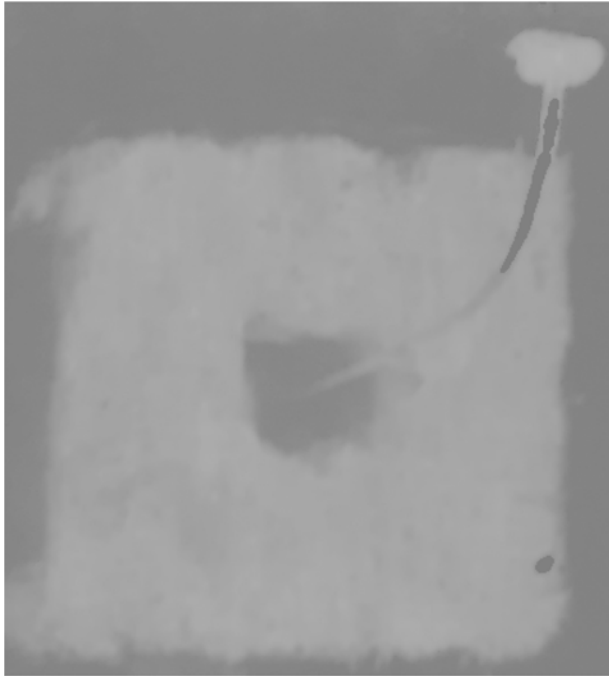
Figure 43. Thresholded LAB channel images

Figure 44. Fill in small objects.

For the identification process within the image, Plant CV is based on contours in OpenCV. A rectangular region on interest is determined.

Figure 45 Defining region of interest
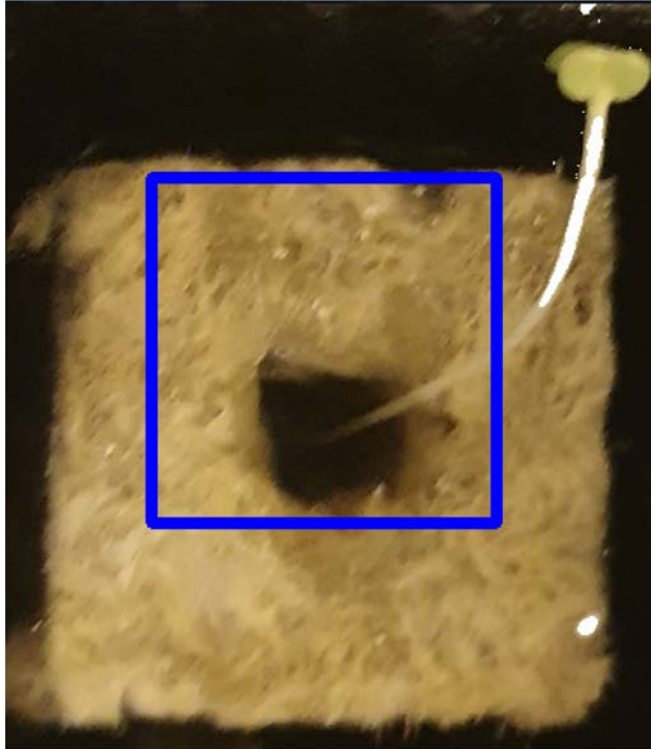
Figure 46. Region of interest drawn
onto image.

Once the region of interest is resulted, the code keeps then the rest of the image overlapping with the region inside the rectangle or cut the objects to the shape of the region of interest. In our particular case, as seen in the following image. The isolated items now should all be plant material that we are interested about. There can be more than one object that makes up the material of plant, sometimes leaves appear in the images as separate objects.

```
# Object combine kept objects
obj, mask = pcv.object_composition(img=img, contours=roi_objects, hierarchy=hierarchy3)
```

Figure 47. Command for object combine
kept objects
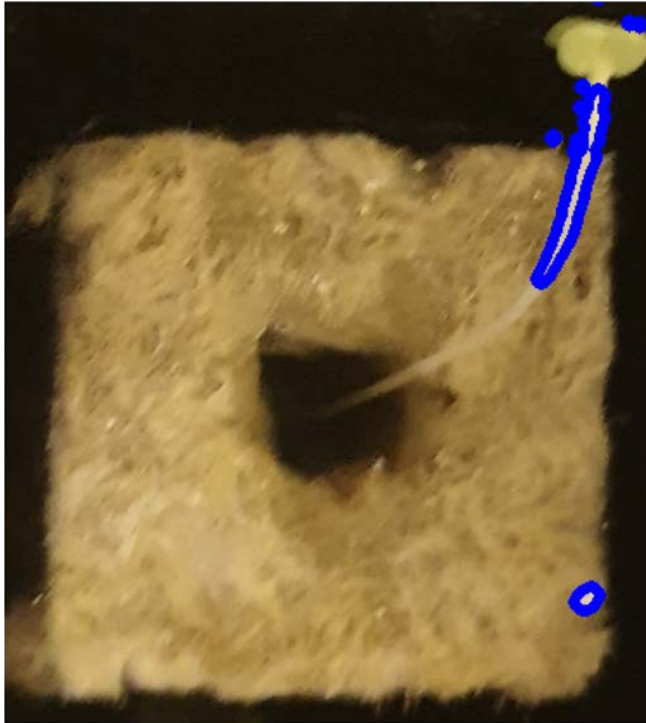
Figure 48. Outline (blue) of combined objects
on the image.

The final step of the image analysis is to examine the plant material such as horizontal height, shape, or color.


```
############## Analysis ################

outfile = False
if args.writeimg == True:
    outfile = os.path.join(args.outdir, filename)

# Find shape properties, output shape image (optional)
shape_imgs = pcv.analyze_object(img=img, obj=obj, mask=mask, label="default")

# Shape properties relative to user boundary line (optional)
boundary_img1 = pcv.analyze_bound_horizontal(img=img, obj=obj, mask=mask, line_position=1680, label="default")

# Determine color properties: Histograms, Color Slices, output color analyzed histogram (optional)
color_histogram = pcv.analyze_color(rgb_img=img, mask=mask, hist_plot_type='all', label="default")

# Pseudocolor the grayscale image
pseudocolored_img = pcv.visualize.pseudocolor(gray_img=s, mask=mask, cmap='jet')

# Write shape and color data to results file
pcv.print_results(filename=args.result)

if __name__ == '__main__':
    main()
```

Figure 49. Analysis section

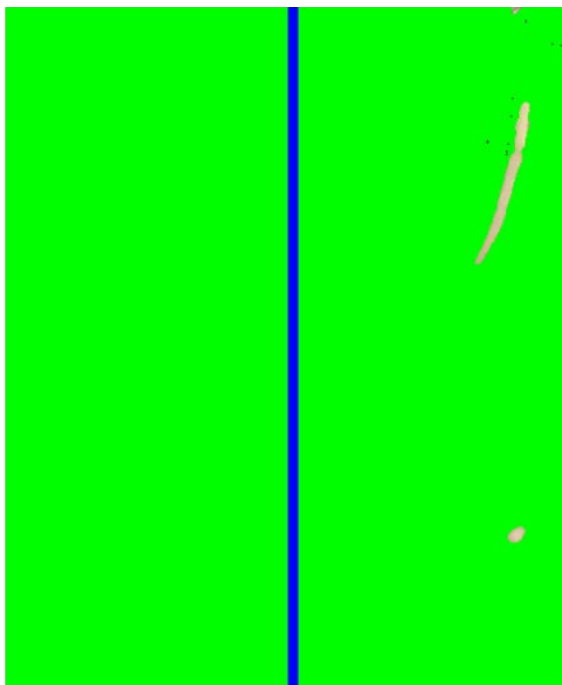*Figure 50.* Shape analysis output image.

Figure 51. Boundary line output image.

The "Boundary line output image" refers to the image that highlights the boundary line in the input image. This output image is generated by the plantcv.morphology.obj_boundary function, which takes the input binary image and returns a binary image of the same size where the boundary of the objects is highlighted in blue pixels as shown in the picture.

The boundary line output image is useful in plant phenotyping and image analysis applications. In later stage, it will be used to identify the shape and size of objects in an image, or if needed we can use it to calculate the plant perimeter or area. Additionally, the boundary line output image is overlaid on the original input image to provide visual context and aid in the interpretation of the results.
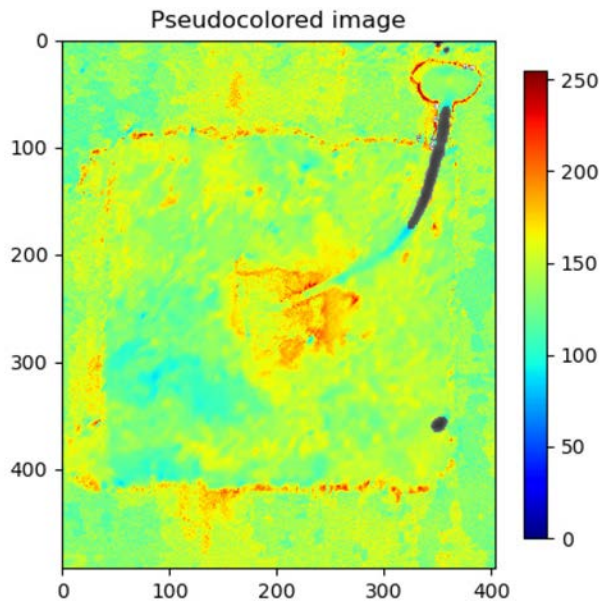
Figure 52. Pseudocolored image

The pseudocolored image refers to the image where the grayscale intensity values have been mapped to a color scale for visualization purposes. This is done to highlight different features in the image that may not be easily visible in the original grayscale image.

The process of pseudocoloring involves assigning a color to each grayscale value in an image, creating a false-color image that can make it easier to distinguish between different features or areas of interest in the image. In plant phenotyping, pseudocolored images may be used to highlight specific plant structures, such as leaves or roots, or to distinguish between healthy and diseased areas of a plant.

PlantCV provides several functions for generating pseudocolored images, such as plantcv.visualize.pseudocolor, which maps grayscale intensity values to a specified color map and returns a color image. The resulting image can then be saved or displayed for visualization and further analysis.

Figure 53. Histogram of color values for each plant pixel.

A histogram of color values for each plant pixel is a graphical representation of the distribution of color values in an image. In PlantCV , this histogram can be generated to provide insight into the color composition of an image and help identify any potential issues or inconsistencies.
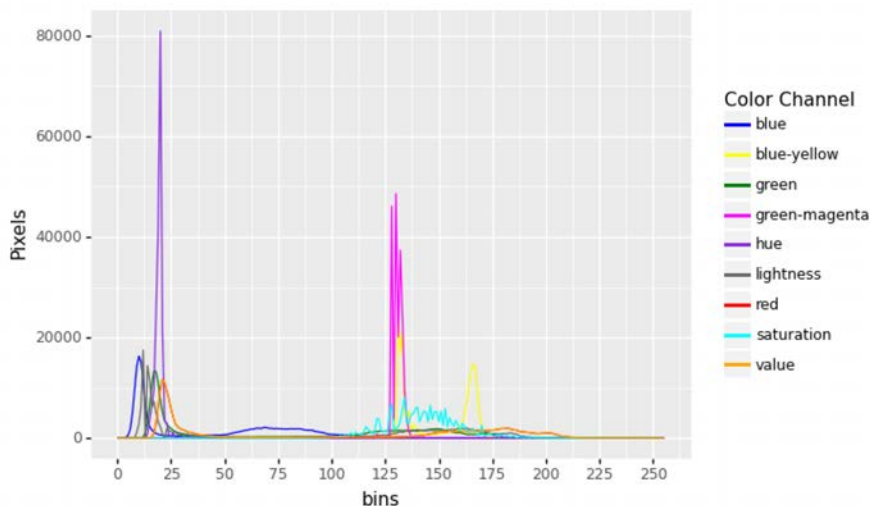
To create a histogram of color values for each plant pixel, PlantCV uses the plantcv.visualize.color_histogram function, which takes an input color image and returns a histogram for each color channel (red, green, and blue) in the image. The histogram displays the frequency of each color value on the x-axis and the number of pixels with that color value on the y-axis.

The histogram of color values for each plant pixel is used to identify any color biases or issues in an image, such as lighting or camera calibration problems. Additionally, the histogram can help identify differences in color composition between different plant genotypes or treatments, which is useful for plant phenotyping and analysis.

Stella model

Plant phenotyping using rockwool has reduced the growth period by half for green salad compared to traditional soil-based methods. Rockwool is an inert growing medium made from melted rock that provides a stable and consistent environment for plant growth. It is commonly used in hydroponic systems, which are systems that grow plants in a nutrient-rich water solution instead of soil.
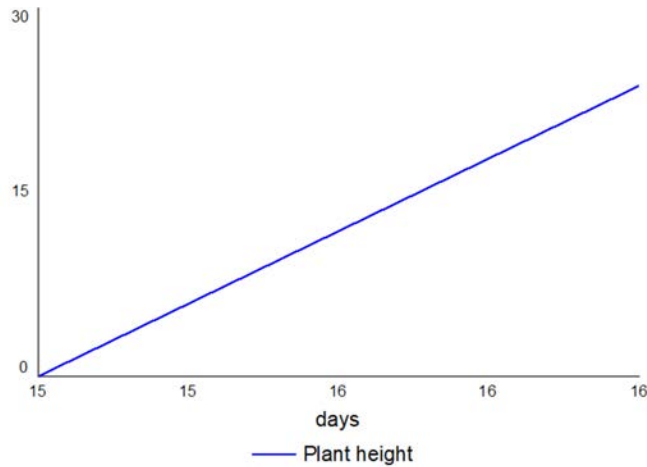
Figure 54. Plant heigth of green salad using Rockwool for 16 days

One of the advantages of using rockwool for plant phenotyping is that it allows for precise control of nutrient and water availability to the plants. This resulted in faster growth and higher yields compared to traditional soil-based methods, as the plants have access to optimal growing conditions throughout the growth period.

In addition, rockwool-based systems can reduce the risk of soil-borne diseases and pests, which can be a significant problem in traditional soil-based methods. This has further enhanced plant growth and reduced the time needed for growth and development.

However, it is important to note that the specific growth period reduction achieved by using rockwool for plant phenotyping may depend on various factors, such as the specific variety of green salad being grown, the growing conditions, and the specific experimental setup. Further research and experimentation would be needed to determine the exact growth period reduction achievable with rockwool-based plant phenotyping methods for other plants.

Conclusion

In conclusion, both System Dynamics Stella and PlantCV are powerful tools that can be used to enhance plant phenotyping research. System Dynamics Stella is an effective tool for modeling complex systems and predicting outcomes under different scenarios, which can be valuable for plant breeding and crop management. Meanwhile, PlantCV provides a suite of image analysis tools that can automate the extraction of quantitative plant phenotypic traits from images, enabling high-throughput phenotyping and reducing the potential for human error.

When used together, these tools can provide a comprehensive approach to plant phenotyping that combines both modeling and image analysis. For example, Stella can be used to model how different environmental factors affect plant growth and development, while PlantCV can be used to extract quantitative traits from images of plants grown under these different conditions. This integrated approach help researchers better understand the complex interactions between plants and their environment, leading to improved crop yields and plant performance.

Furthermore, the user-friendly interfaces of both System Dynamics Stella and PlantCV make them accessible to researchers with diverse backgrounds and skill sets. As a result, these tools have the potential to democratize plant phenotyping research and enable more researchers to contribute to this important field. Overall, the combination of System Dynamics Stella and PlantCV can provide a powerful and efficient approach to plant phenotyping that can help drive advances in agriculture and plant science.

For our system these two tools have proven that our phenotyping protype is working well and providing the targeted results. This has ensured us to move forward with our research of replacing soil by rockwool and look for the mathematical model of our indoor precision vegetable production system.

Acknowledgements

References

[1] Manuel Vázquez-Arellano, Hans W Griepentrog, David Reiser, and Dimitris S Paraforos. 3-d imaging systems for agricultural applicationsâA˘Ta review. ˘ Sensors, 16(5):618, 2016.

[2] X Zhou, HB Zheng, XQ Xu, JY He, XK Ge, X Yao, T Cheng, Y Zhu, WX Cao, and YC Tian. Predicting grain yield in rice using multi-temporal vegetation indices from uav-based multispectral and digital imagery. ISPRS Journal of Photogrammetry and Remote Sensing, 130:246–255, 2017.

[3] Pradal C, Coupel-Ledru A, Fournier C, Tardieu F. 2019. Genetic and environmental dissection of biomass accumulation in multi-genotype maize canopies. Journal of Experimental Botany 70:2523–2534.

[4] D Yumeina, GK Aji, and T Morimoto. Dynamic optimization of water temperature for maximizing leaf water content of tomato in hydroponics using an intelligent control technique. In V International Symposium on Applications of Modelling as an Innovative Technology in the Horticultural Supply Chain-Model-IT 1154, pages 55–64, 2015.

[5] Dmitrii S, Victor K, Maxim F. 2020. Instance segmentation for assessment of plant growth dynamics in artificial soilless conditions. Plant Methods, 16, 1-11.

[6] Lucas M, Lobet G, Laplaze L, Muller B, Guédon Y. 2018. A new phenotyping pipeline reveals three types of lateral roots and a random branching patern in two cereals. Plant Physiology 177:896–910.

[7] Casadebaig P, Debaeke P, Wallach D. 2020. A new approach to crop model calibration: phenotyping plus post-processing. Crop Science 60:709–720.

[8] Nardi P, Mateo GD, Palahi M, Mugnozza GS. 2016. Structure and evolution of Mediterranean forest research: a science mapping approach. PLoS One 11:e0155016. doi:10.1371/journal. pone.0155016.

[9] Sarathi M Weraduwage, Jin Chen, Fransisca C Anozie, Alejandro Morales, Sean E

[10] Weise, and Thomas D Sharkey. The relationship between leaf area growth and biomass accumulation in arabidopsis thaliana. Frontiers in Plant Science, 6:167, 2015.

Finite element method of frictional sliding contact between pin and disc tribology model

Hailemariam SHEGAWU[1], Gábor KALÁCSKA[2], István OLDAL[2]

[1]Mechanical Engineering Doctoral School (MTDI), Szent István Campus, Gödöllő, MATE
[2]Institute of Technology, Hungarian University of Agriculture and Life Sciences, MATE, Gödöllő

Abstract

Frictional sliding contact occurs when two bodies make surface contact while moving in a relative motion against the resistance of friction. The deformation of the contact surfaces, static and sliding motion, slip traction and stick traction, and compressive and adhesive forces can all be identified during this phenomenon. An ANSYS workbench was used to investigate the frictional contact between the pin and the disc within boundary conditions. In this investigation, aluminum alloys (AL7075) disc material and polyethylene pin material were both employed. The results of equivalent stress (von mise stress), slip traction and stick traction, deformation, and contact pressure values were highlighted using colors, with red denoting the maximum and blue denoting the minimum. We conclude that all values of the aforementioned characteristics, such as contact pressure, deformation, von Mises stress, slip traction, and stick traction, are high on the pin contact surface, which is more vulnerable to failure or wear than the disc.

Keywords

Frictional contact, contact pressure, equivalent stress, ANYSY workbench, polyethylene

1. Introduction

The study of stresses and deformations resulting from the interaction of solid bodies at their surfaces is known as contact mechanics. Because touch is the primary means of applying load to a body, difficulties involving contact interactions are common in engineering applications. In both daily life and industrial production, frictional contact issues between deformable bodies are common. Material loss from surfaces could result from the tribological interactions of interacting substances. The frictional sliding surface contact of a pin on a disc is a significant phenomenon to investigate wear, friction, plastic deformation, frictional heat production, sliding contact fatigue, and too many experimental studies of the pin on the disc to chemical and mechanical characteristics.

126

Solid-solid interfacial phenomena involving sliding friction have received extensive research attention (Jerier & Molinari, 2012). Amontons, Coulomb, and more recently Archard, Greenwood, and Williamson are a few influential authors who laid the theoretical groundwork for normal and frictional contacts(Jerier & Molinari, 2012).

Aluminum alloys are favored engineering materials in the automotive, aerospace, and mineral processing sectors for creating numerous highly-performing components that are used for diverse applications due to their lower weight and superior thermal conductivity features (Kumar et al., 2012). Al7075 is one of many aluminum alloy series that has received extensive research. Al7075 alloy is preferred in the aerospace and automotive industries because of its extremely high strength and increased toughness (Kumar et al., 2012).

Polyethylene engineering material is increasingly widely employed in the packaging industry due to its benefits in terms of flexibility, physical strength, durability, and affordability. It is used to create Tetra packs, candy wafers, shampoo sachets, motor pumps, and other equipment sealing covers and food packaging (Suresh et al., 2011).

Modern technology has found solutions for difficult phenomena like frictional contact surfaces. Researchers have been using the ANSYS Workbench to study frictional contact surfaces. The machine components and tools are a result of material stress and damage to the contact surface when a relative motion occurs (Sardar et al., 2020).

A few of the research articles and works relevant to these issues that were published recently are given below.

In a dry slide braking system made of gray cast iron and low metallic friction materials, Gui et al.(Gui et al., 2016) used a finite element technique to explore the thermal, mechanical, and tribological behaviors of interacting surfaces. There were several different approaches used, such as thermo-mechanical analysis, wear analysis, heat boundary conditions, a hybrid mesh method that combines the benefits of pure Lagrangian and pure Eulerian mesh methods, and fully coupled thermo-mechanical-wear simulation. Numerical simulations, constraints, boundary conditions, contact definitions, contact pressure, wear depth, temperature change, and dynamical stress were all included. They found that non-uniform contact conditions can be changed by material loss and that wear has a significant impact on contact pressure. The study's constraints prevented it from including the impact of slip and wear type identification.

Hua et al. (Hua et al., 2020) examined the dry-sliding properties of a FeCoCrMoCBY bulk metallic glass (BMG) using a couple of experimental and finite-element approaches with a specific application of the combination of abrasion and oxidation. The procedures included dry-sliding in air, at room temperature, and experimental (wear on a ball-on-disk reciprocating mode) ball (Si3N4, Al2O3, and ZrO), sample material Fe41Co7Cr15Mo14C15B6Y2 BMG test conditions. Furthermore, calculations and finite-element modeling (FEM), structural characterization, wear behaviors, the effect of alloy hardness, Young's modulus on wear rates were also included. Contact mechanics of couple pairs are also calculated and simulated using FEM. The wear performance of Fe-based BMG varies greatly

depending on counterpart materials, they conclude. The study's limitations eliminated the effects of temperature, cracks, and surface roughness.

Froelich et al.(Froelich et al., 2014) studied the use of a finite element method to calculate wear, friction, and contact temperature. Employing finite element analysis, the material was used to represent steel shafts and elastomer seal rings. Several methods were used, including model setup, seal configuration, wear simulation, temperature calculation, friction torque, and initial seal system condition, temperature, and friction throughout the operation. They concluded that surface asperities had a microscopic impact on the local distribution of temperature and pressure. The restriction did not apply to crack or corrosive wear.

The purpose of this study, according to Duan et al. (Duan et al., 2017b), was to combine finite elements with smoothed particle hydrodynamics to tackle the mesh distortion problem caused by FEM. Monocrystalline silicon carbide and diamond grits were employed as the materials. Definition of scratching kinds, twice-scratching simulation, experimental validation, material constitutive equation, performance parameter, and analysis of twice-scratching simulation findings was among the methods used. Furthermore, analysis of experimental data, comparison of tests and simulations, material damage distribution, interference mechanism, effect on groove width and depth, and effect on contact force were all included. Figure 1 shows the material damage distribution after scratching (a) section A of the groove, (b) the top view of the groove, (c) the interference region of the lateral fractures, and (d) section B of the groove twice. The length of the lateral cracks and the width of the plastic deformation was used to determine the interference mode. The study's limitations included the absence of cracks, the influence of slip, and the effect of temperature.
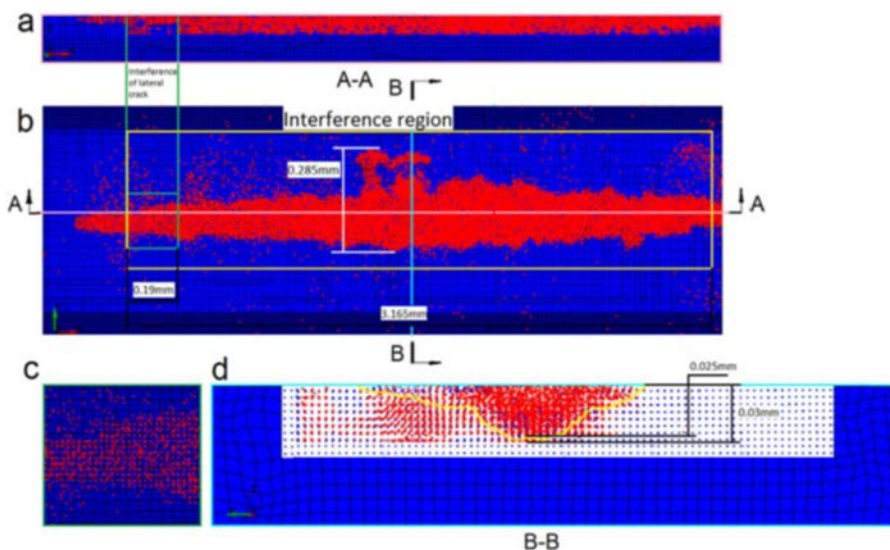

Figure 1. Depicts the material damage distribution following scratching (Duan et al., 2017b).

Yue and Wahab (Yue & Wahab, 2017) considered enhancing the finite element fretting wear model by introducing a time-dependent coefficient of friction. Steel/steel simulation material with a cylinder on a flat contact structure. FE geometry, configuration models, loading histories, wear models, and simulation parameters were a few of the techniques used. The impact of COF on fretting wear in the gross sliding regime, experimental validation of FE results, the partial slip condition, and the gross sliding condition were also discussed. Figure 2 compares the wear scars left by CoF and VCoF models after 3000 and 18,000 cycles with different displacements under gross sliding circumstances. The wear rates of the COF models remained constant as fretting wear continued, and they both agreed on gross sliding and partial slip scenarios. Yet, the evolution of wear rates from VCOF models varied in these two regimes. In this experiment, the effects of temperature and crack were not taken into account.
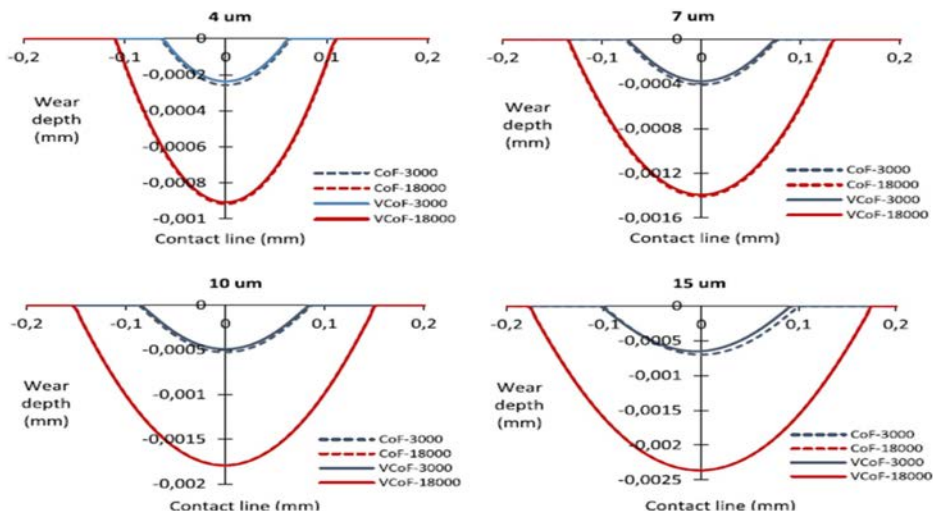
Figure 2. Shows a comparison of wear scars in gross sliding (Yue & Wahab, 2017).

Mukras et al. (Mukras et al., 2009) developed a wear prediction procedure for bodies that face oscillatory contact (such as pin–pivot joints) by the finite element method. The wear model's computational prediction method, simulation procedure (step-update), extrapolation schemes, and parallel computing of cycle- and intermediate cycle-update were among the approaches used. In addition, step-update simulation testing and intermediate cycle-update—parallel processing was available. They concluded that there is a fair approach to forecast wear on bodies that are in oscillatory contact. Temperature and type of wear identification were not considered in this investigation.

The purpose of this study, according to Duan et al.(Duan et al., 2017c), was to combine finite elements with smoothed particle hydrodynamics to tackle the mesh distortion problem caused by FEM. Monocrystalline silicon carbide and

diamond grits were employed as the materials. Definition of scratching kinds, twice-scratching simulation, experimental validation, material constitutive equation, performance parameter, and analysis of twice-scratching simulation findings was among the methods used. Furthermore, analysis of experimental data, comparison of tests and simulations, material damage distribution, interference mechanism, effect on groove width and depth, and effect on contact force were all included. The length of the lateral cracks and the width of the plastic deformation was used to determine the interference mode. The study's limitations included the absence of cracks, the influence of slip, and the effect of temperature.
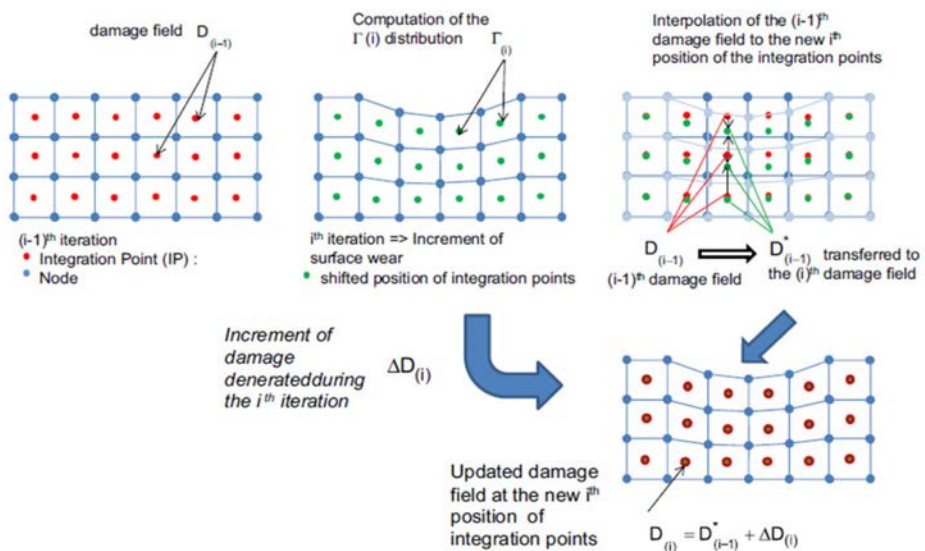
Figure 3. Depicts the fretting-wearing process (Garcin et al., 2015).

Garcin et al.(Garcin et al., 2015) investigated the effect of surface wear on crack formation prediction using a finite element method. The materials utilized for cylinder/plane contact pairings are Ti–6Al–4V/Ti–6Al–4V. Figure 3 depicts the transfer field methods used to calculate the cumulative damage caused by fretting wear in a planar specimen. Plain fretting set-up studies, materials, and contact conditions experiments, fretting scar inspection, fretting wear examination, and fretting crack examination were among the procedures used. In addition, the effect of displacement amplitude on friction and fretting, as well as the determination of energy wear rate damage, quantification of crack nucleation endurance, contact damage modeling of FEM, and modeling of surface wear, as well as a correlation between experimental and simulated fretting were included. FEM crack modeling of the multiaxial fatigue criterion under fretting wear gross slip conditions, determination of the endurance chart, determination of the

cumulative damage law, and influence of surface wear extension on fretting damage distribution were also discussed. Furthermore, the modeling of fretting maps and prediction of partial and extensive slip fracture nucleation displacement amplitudes were included. They concluded that increasing the number of loading cycles increases the probability of cracking in domains with partial and gross slip. Surface roughness and temperature effects were eliminated due to the study's limitations.

Using a finite element model with a smooth particle hydrodynamic mesh, Duan et al.(Duan et al., 2017a) investigated material removal modes in monocrystal Sic scratching by a single diamond. The main purpose of using FEM was to avoid excessive grid distortions and SPH to tackle boundary concerns. Coupling SPH and FE simulations, experiments, and constitutive equations were among the approaches used. SPH and FEM coupled simulation with diamond grit, stress distribution analysis, effect on maximum width, depth of the groove, and contact force were also included. Scratching monocrystal SiC with a single diamond grit resulted in three removal modes: plastic deformation mode, ductile-brittle transition critical mode, and brittle removal mode, according to the report. The study's limitations included monocrystal SiC isotropy, temperature independence of all physical parameters, minimal heat transfer of workpiece material, and slight elastic deformation on grain.

Ding et al.(Ding et al., 2007)investigated the impact of debris on fretting wear by the finite element method. The material used in the research was nitride flat specimens and a cylinder made of diamond. Figure 4 shows a schematic illustration of a fretting contact with worn debris, with arrows indicating the direction of debris particle motion. The method entailed an experimental investigation of debris behavior, a fretting contact model in the presence of debris, as well as a fretting wear simulation that included debris effects. They determined that the inclusion of the debris layer creates a reduced scar width and a slightly higher wear depth, based on modeling data. The study's limitations ignored the effects of temperature and fracture.

Basseville et al.(Basseville et al., 2011) investigated realistic stress and strain fields at the local scale by fretting with finite elements. Figure 5: Schematic representation of the impactor/target surfaces and wear boxes (37–78 debris were found in the contact region according to the case study). Material response fretting map, titanium alloy (Ti6Al4V) cylinder, third body many rectangular particles with diameters of 5μm×1μm, spaced by 2.5μm, and steel plate were among the ways employed. Furthermore, the number of particles was affected by the loading conditions, the entire contact area, third body modeling, FE mesh, boundary conditions, and numerical modeling of the wear process. In addition, criterion wear, impactor and debris wear, geometry updates, third body evolution, contact stress evolution, and fatigue crack start prediction were all included. They found that, in gross and mixed slides, debris was expelled from the contact area due to a variety of stick-slip mechanisms, as demonstrated by simulations. The effects of friction and temperature on the study were limited.
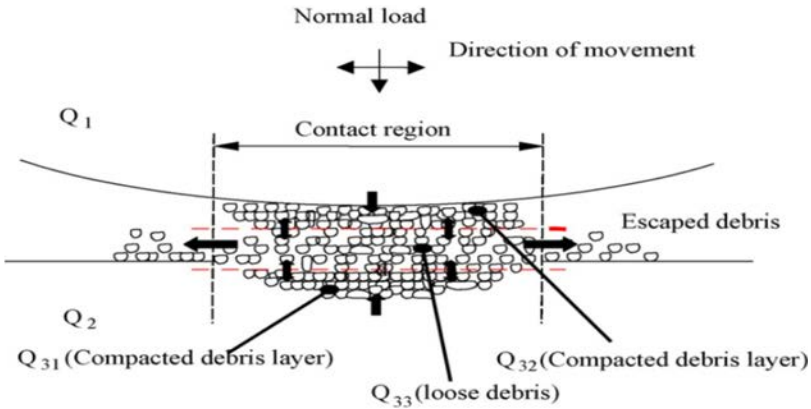
Figure 4. Shows a fretting contact with worn debris present (Ding et al., 2007).
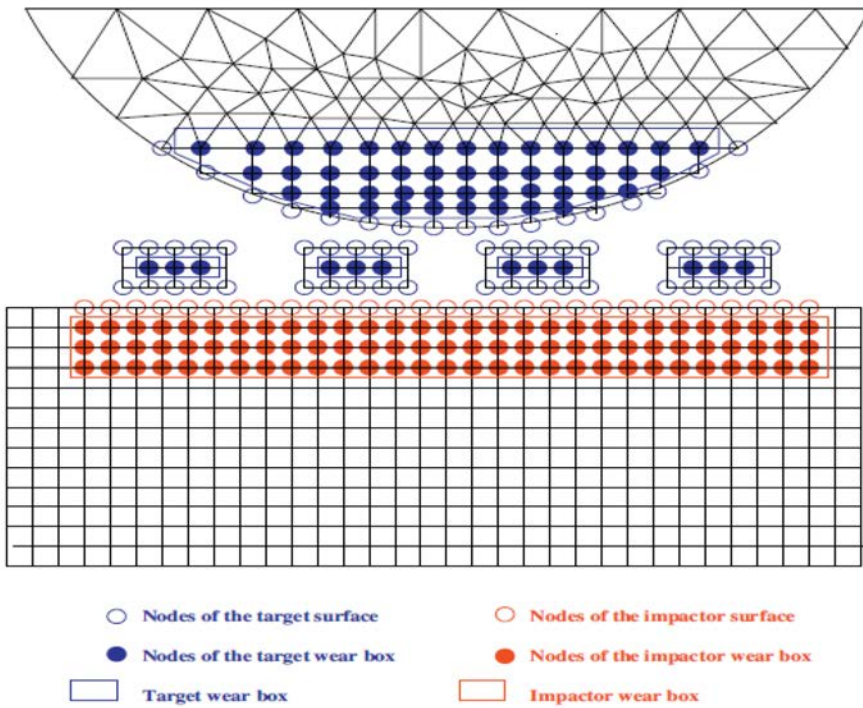
Figure 5. Depicts the impactor/target surfaces and wear boxes (Basseville et al., 2011).

Lengiewicz and Stupkiewicz (Lengiewicz & Stupkiewicz, 2013) focused on the premise that contact conditions were entirely controlled by the wear process and that elastic deflections had no bearing on the solution by using the pin-on-disc test and the finite element method to contact and wear. The use of a wear-controlled quasi-steady-state sliding model, the conforming contact zone's shape,

the quasi-steady-state wear problem, the Archard wear model, a comparison with a 3D finite element model, and a parametric analysis were all taken into consideration. For example, the strategy was easily adaptable to more intricate local wear models by assuming that the wear coefficient was pressure-dependent. The study's flaw was that temperature and fatigue failure was not taken into consideration.

Table 1. Parameters used in the simulation (Lengiewicz & Stupkiewicz, 2013).

Parameter	Load case #1	Load case #2
The radius of the ball, R	3 mm	–
Sliding path length per one cycle, S	20π mm	–
Young's modulus of the ball, Eb	400GPa	–
Young's modulus of the disc, Ed	210GPa	–
Poisson's ratio of the ball, νb	0.3	–
Poisson's ratio of the disc, νd	0.3	–
Friction coefficient, μ	0.3	–
Normal force, F	2 N	20N
Wear coefficient of the disc, kd	2.5_10−8 mm2/N	2.5_10−9 mm2/N

Din et al. (Din et al., 2019) examined a specific application of adhesive wear in a uni-directional (UD) reinforced carbon thermoplastic Polyetherimide (PEI) composite laminate caused by the sliding of a metallic counterpart by FE. (a) Parallel (P), (b) Anti-Parallel (AP), and (c) Normal sliding directions to fibers are shown in Figure 6. (N). Simulation setup and boundary conditions, 3D Puck's theory, parallel and anti-parallel (AP) configurations, damage exposure factors, and damage exposure factors vs specified wear rate were some of the methodologies used. They concluded that orthogonal sliding concerning fiber resulted in higher damage exposure factors and hence a higher subsequent wear rate in terms of tribological performance. Thermal and chemical wear were not included in the restriction.
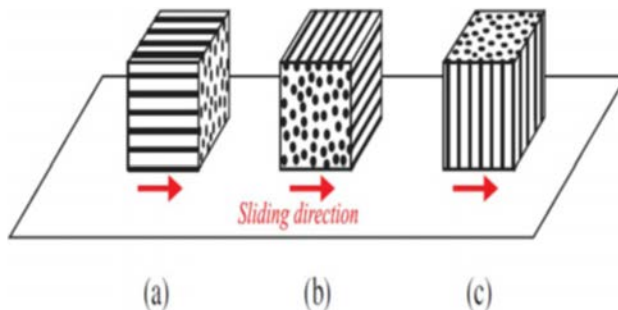
Figure 6. Shows the three main sliding directions with fibers (Din et al., 2019).

The study by Xin et al. (Xin et al., 2014) concentrated on the prediction of seal wear using the finite element method. An illustration of the simulation method for seal wear using a FE model is shown in Figure 7. The techniques included a test rig, a structural finite element model, friction heat analysis, wear rate computation, a worn volume model for the seals, and steel for the chamber and shaft. They also included a rubber-based material for the seals and steel for the chamber and shaft. The findings might be used by engineering designers to determine which kind of seal was needed based on the working circumstances. There were restrictions on the Archard wear law, and the crack effect was eliminated.
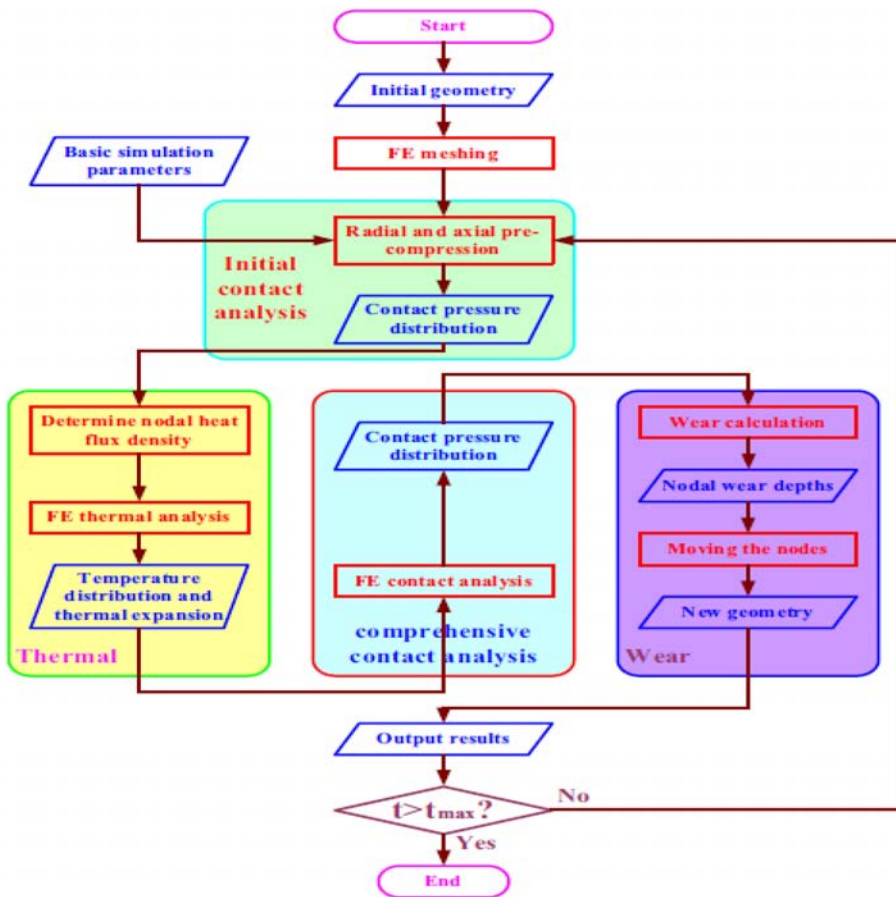
Figure 7. Shows the wear process as a flow chart (Xin et al., 2014).

Arnaud and Fouvry (Arnaud & Fouvry, 2018) concentrated on the growth of the debris layer trapped in the interface, sometimes referred to as the "third body," as discovered by finite element analysis and testing with fretting wear.

The method involved choosing the right material, Ti-6Al-4V/Ti-6Al-4V, by both experimental and FE means, performing a plain fretting test, analyzing the third body layer, and monitoring the progression of wear as well as the impact of sliding amplitude on wear. Examples of finite element models include finite element simulations, numerical applications of energy wear modeling, and FEM third body consideration. Additionally, the third body's elastic properties were taken into account by the FEM model, the wear profile with and without the third body was compared, and the impacts of test length and sliding amplitude were implemented. They found that wear depth extension is preferred to lateral wear extension by the third body debris layer, which serves as a contact pressure concentrator. The limitations of the study disregarded the impact of temperature and cracks.

Using finite element analysis, Yue and Wahab (Yue & Wahab, 2014) investigated the possibility of a stress singularity at a cylinder on flat contact concerning numerous factors, including applied displacement, coefficient friction, and fretting wear cycles. Figure 8 depicts the FE model's measurements. FE model validation of the contact and fretting wear models, the effect of applied displacement, the effect of COF, and the nd effort wear cycles were some of the elements of the approach. Other aspects included the stress singularity signature, energy wear model, Ti-6Al-4V material for the pad and specimen, and Ti-6Al-4V material. After one-fourth of a fretting wear cycle, it was determined that there was no stress singularity in partial slip or gross sliding at lower COF when the applied displacement was greater than 4 m, but it exists at higher COF when the applied displacement is 4 m, in which case the contact interface almost sticks to each other. This experiment did not consider the effects of load and surface roughness.
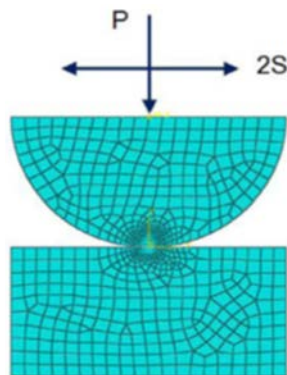

Figure 8. Depicts the dimensions of the FE model
(Yue & Wahab, 2014).

The purpose of our study is to examine equivalent (von-mise) stress, contact stress, stick surface traction, slip surface traction, and deformation resulting from

friction effect during relative motion between pin and disc within an externally applied pressure.

2. Materials and methods

With the aid of the ANSYS Workbench software and the finite element approach, we were able to simulate stick surface traction, slip surface traction, contact pressure, von Mises stress, and deformation using an aluminum alloy (AL7075) material disc.

The chemical makeup of aluminum alloy (AL7075) was listed in Table 2.

The mechanical properties and physical properties of aluminum alloy (AL7075) material used for this paperwork, and Table 3 summarize some of its characteristics.

A pin made up of polyethylene material. Polyethylene is the material that was employed in the project, and Table 4 lists its mechanical characteristics.

Table 2. Chemical composition of AL7075 by percentage (Kumar et al., 2012)

composition	Si	Fe	Cu	Mn	Mg	Cr	Zn	Ti	Al
AL7075	0.4	0.5	1.6	0.3	2.5	0.15	5.5	0.2	88.85

Table 3. Properties of AL7075 (Kumar et al., 2012)

properties	AL7075
Elastic Modulus (GPa)	70-80
Density (g/cc)	2.81
Poisson's ratio	0.33
Hardness (HB500)	60
Tensile strength	220

Table 4. Mechanical properties of polyethylene (De la Torre et al., 2021)

properties	polyethylene
Modulus of elasticity (MPa)	940
Modulus of rigidity (MPa)	332
Poisson's ratio	0.46
Yield strength (MPa)	25
Ultimate strength (MPa)	40

The real disc that was discovered in our lab is depicted in figure 9 below. This real disc is constructed of an alloy of aluminum (AL7075). The actual polyethylene pin was shown in Figure 10 below.
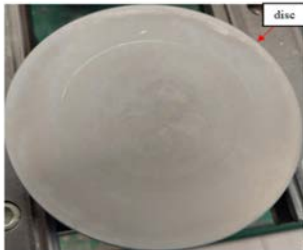
Figure 9. Real disc

Figure 10. Actual pin

We disassembled abrasive wear tester equipment. We were getting measurements of the actual dimensions of a holding, the pin, and the disc from the pin on the disc abrasive wear testing equipment to conduct our analysis of frictional surface contact of the pin on the disc using the ANSYS workbench.

Figure 11 shows the abrasive wear tester device in our tribological laboratory.
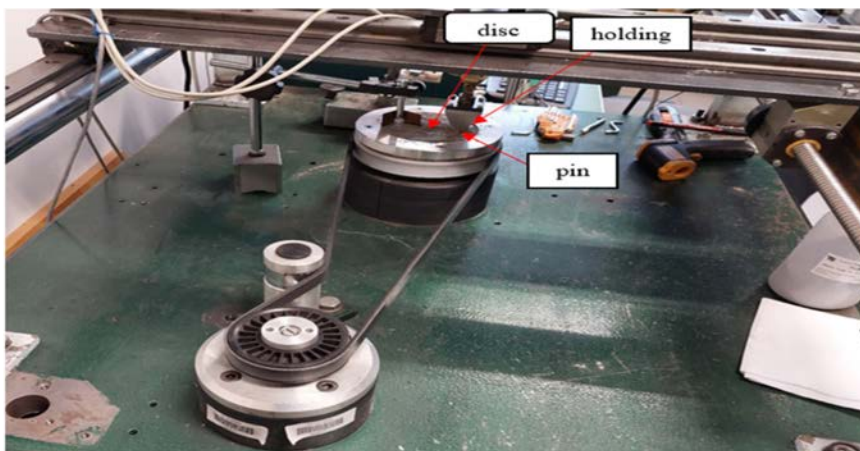
Figure 11. Shows abrasive wear tester machine

Frictional, no separation, bonded, rough, and frictionless contact types are available in ANSYS workbench. Depending on the kind of issue you want to solve, you should choose the right contact type.

Frictional contact is frequently seen in everyday situations and engineering issues. The majority of contact issues seen in practice are nonlinear.

The process of doing a general finite element analysis while in frictional surface contact is depicted in Figure 12.

The pin and the disc parts as well as assembly drawings produced by Ansys Workbench Design Modular.

We avoided holding a portion of the machine in our analysis and instead used displacement constraints to keep things simple and cut down on computation time.
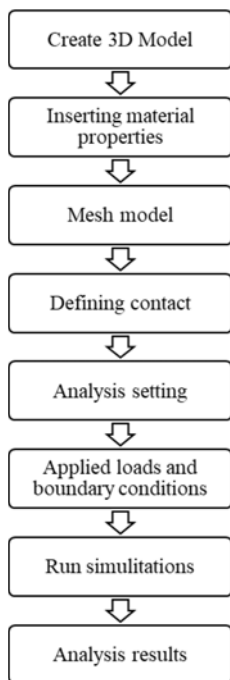
Figure 12. Process in Finite Element Analysis

A 90 mm diameter by 15 mm thick disc and an 8 mm square pin were both employed in this paper. The center of sliding distance was offset by a 35 mm radius from the center of the disc.

To put displacement constraints around them, the pin's four sides were divided into two equal portions.

Figure 13. 3D model of pin and disc

The process of producing connections of contacts between the surfaces of the pin and the surfaces of the disc came next in this examination. For creating, there are four options to avoid element distortion errors.

1. we select the bottom surface of the pin as the target and the top surface of the disc as the contact.
2. We choose to use the disc's top surface as the target and the pin's bottom surface as the contact.
3. we can assign more surfaces of the pin as the contact and more surface of the disc as the target.
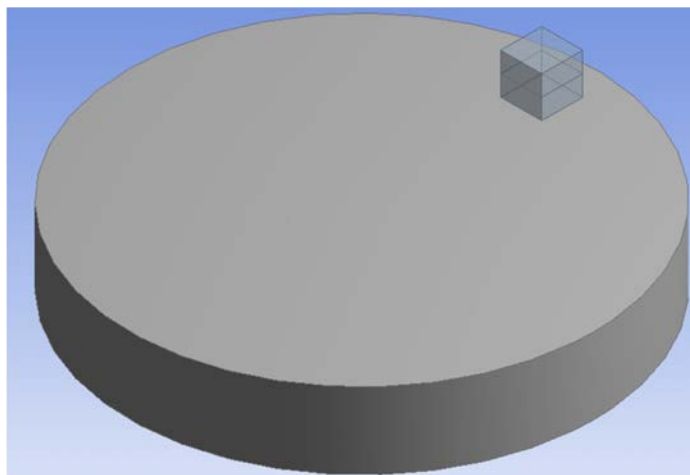4. We can add designate more disc surfaces as the contact and more pin surfaces as the target.

For our investigation, we selected the top surface of the disc to act as the contact and the bottom surface of the pin to act as the target. Finally, we selected frictional types of contact and inserted friction values of the system. Figure 14 illustrates in detail how to configure contact parameters.

Details of "Frictional - disc To pin"	
Scope	
Scoping Method	Geometry Selection
Contact	1 Face
Target	1 Face
Contact Bodies	disc
Target Bodies	pin
Definition	
Type	Frictional
☐ Friction Coefficient	0.15
Scope Mode	Automatic
Behavior	Symmetric
Trim Contact	Program Controlled
Trim Tolerance	3.2335e-004 m
Suppressed	No
Advanced	
Formulation	Program Controlled
Detection Method	Program Controlled
Penetration Tolerance	Program Controlled
Elastic Slip Tolerance	Program Controlled
Normal Stiffness	Program Controlled

Figure 14. Set frictional disc and pin

The solid model must be discretized into a "mesh" made up of several elements, which is a crucial prerequisite of the finite element approach. Tetrahedrons, hexahedrons, and combinations of them are frequently employed in three-dimensional numerical analysis. Tetrahedral element meshes benefit from great efficiency, simplicity of implementation, adaptability for adaptive mesh creation, and simplicity of mesh regeneration. Tetrahedral element meshes'

automatic generation technology is currently completely developed and widely used to handle complex geometry. Yet, in terms of analysis accuracy, element count, distortion resistance, and regeneration durations, hexahedral element meshes are superior to tetrahedron element meshes(Huang et al., 2016). Hexahedra is a desirable option because of this for the numerical study of three-dimensional issues. Many aspects of the solid model, including surface curvatures, the distance between geometric entities, the distribution of field variables, and density windows, all influence the mesh size (Huang et al., 2016). The process of adaptive generation for hexahedral mesh is shown in Figure 15.
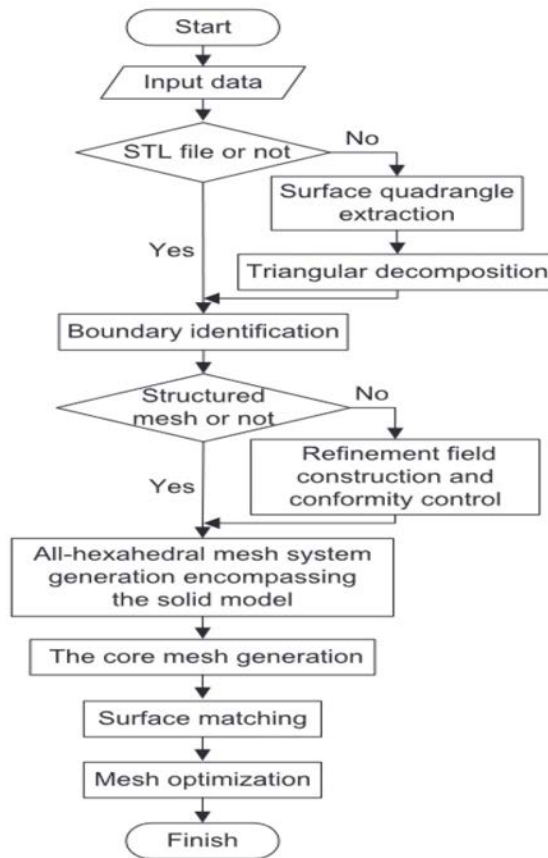
Figure 15. Process of hexahedral mesh(Huang et al., 2016)

We selected hexahedra to mesh to three dimensions of pin-on-disc assembly for our investigation. The local mesh is used in addition to global meshing to increase the number of elements. The pin and the disc finite element geometry is meshed using quadratic elements. The produced geometry meshes with the ANSYS WORKBENCH program using a linear type of quadratic elements. The

assembly drawing of the pin and the disc was meshed using elements with sizes 2 mm for the following stage in this investigation.
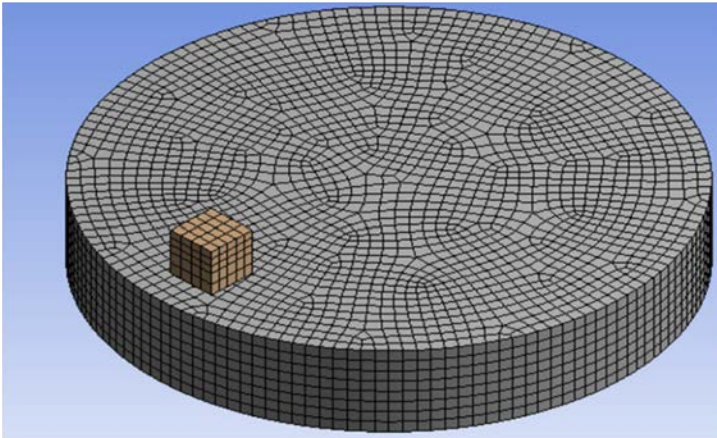
Figure 16. A mesh model of pin and disc

There are two different types of analysis settings for the system's incremental load in transient analysis. These are the ANSYS workbench's analysis of the number of steps and time settings. We decided to choose the number of stages as depicted in figure 17 below.

Details of "Analysis Settings"	
Step Controls	
Number Of Steps	2.
Current Step Number	2.
Step End Time	2. s
Auto Time Stepping	On
Define By	Substeps
Carry Over Time Step	Off
Initial Substeps	50.
Minimum Substeps	20.
Maximum Substeps	1000.
Time Integration	On
Solver Controls	
Solver Type	Program Controlled
Weak Springs	Off
Large Deflection	On
Restart Controls	
Nonlinear Controls	
Output Controls	
Damping Controls	
Analysis Data Management	

Figure 17. Analysis setting

The first step in using ANSYS is choosing the proper analysis method that will be utilized to assess the created FE model. The created FE models were evaluated using two methods, namely static structural analysis and transient dynamic analysis, even though there are many ways to perform the evaluation (Hamim et al., 2018). Static structural analysis can be used to calculate the displacement, stress, strain, and force brought on by imposed loads in a structure or component without taking inertia and damping effects into consideration (Hamim et al., 2018).

By accounting for inertia and damping effects, transient dynamic analysis, sometimes referred to as time-history analysis, is used to ascertain the dynamic response of structures under any broad time-dependent loads. When any combination of static, transient, and harmonic loads is applied, this kind of analysis can be utilized to calculate time-varying displacement, strain, stress, and force (Hamim et al., 2018).

Both linear and nonlinear transient structural analyses are available in ANSYS. A nonlinear transient structural analysis was used in this work.

The pin and disc assembly would then be subjected to all forces and boundary conditions. We set displacement constraints all around the pin's upper portion and exerted 0.2 MPa of pressure on its top surface in the opposite z-axis direction. At the bottom of the disc, we also applied the remote displacement limits and permitted the disc to rotate on the z-axis with a 60-rpm angular velocity. Applying boundary conditions in the ANSYS Workbench module entails choosing the simulation's first mode and setting its physical parameters. The prerequisites for simulation begin with these variables. The borders of each area are established and the following parameters are defined when these have been fixed: Figure 18 depicts all of the loads and boundary conditions that were applied to the pin and disc assembly.
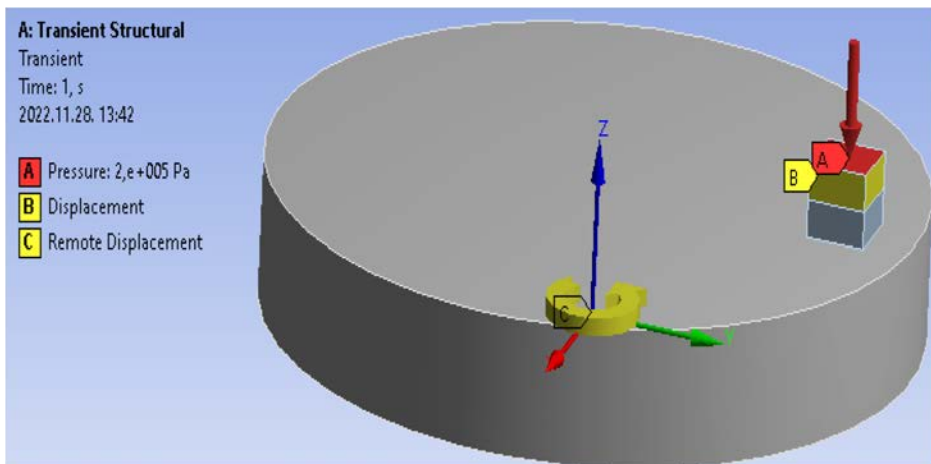
Figure 18. Depicts the loads and boundary conditions

3. Results and discussion

A designer will utilize Von mise stress analysis to determine whether his design structure will fail. When the material's strength is less than the stress's maximum value, failure is unavoidable. Von mise stress in Figure 19 displays the outcomes of the transient analysis. As we examine the von Mises image, we can observe that it is minimum at the top and reaches its maximum at the bottom surface of the pin. The red color at the pin's contact surface denotes the biggest von mise stress, which is $5.6919e^5$ Pa, while the blue color, which is present on the disc and pin, represents the smallest von mise stress, which is 1363.8Pa.
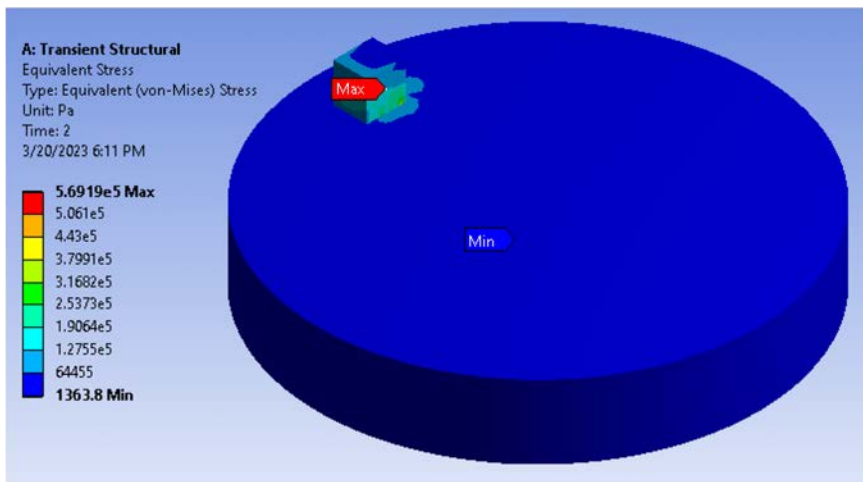
Figure 19. Equivalent (Von-Mises) result
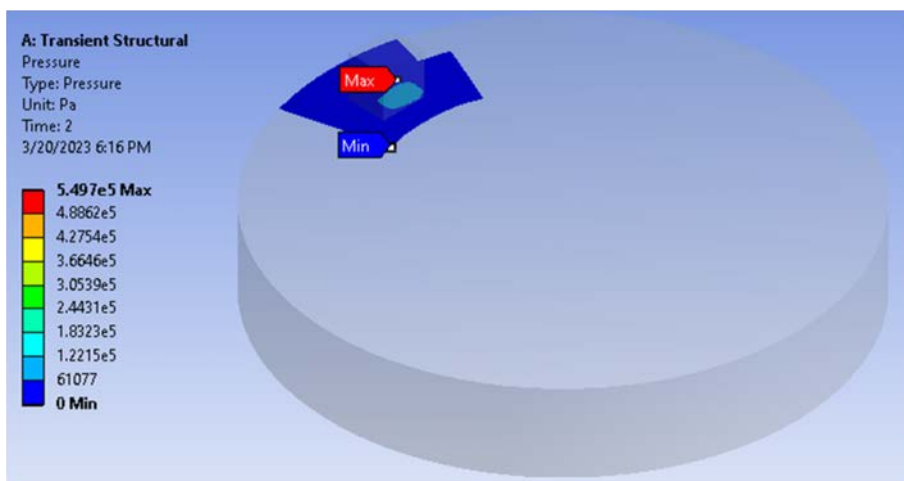
Figure 20. Contact pressure

Due to the application of an outside force to bodies coming into contact at certain moments, which results in three-dimensional tensions. Contact stress is the term used to describe it. Heinrich Hertz, however, made the connection between an externally applied force or pressure and a contact area between two or more bodies in 1881. This is the contact pressure or tension of Hertz. The contact pressure in Figure 20 displays the outcomes of the transient analysis. The red color at the pin's contact surface denotes the biggest contact pressure, which is $5.497e^5$ Pa while the blue color, which is present on the disc and pin, represents the smallest contact tress, which is 0 Pa.

Deformation is when a body is subjected to an external force that causes it to alter from its initial position to a new final position. In general, deformation can be divided into three categories: brittle, ductile, and elastic. There are just two different kinds of choices in the ANSYS workbench environment. Directional deformation and total deformation are the two types. Since total deformation has global implications, we decided to use it in our paper. The results of the transient analysis are shown in time-varying deformation in Figure 21. When we observe the deformation picture, we see that it is minimal at the disc's core, increases as we move across it, and reaches its maximum at the disc's outer surface. Whereas the blue color, which is present on both the disc and the pin, represents the smallest distortion, which is 0m, the red color at the pin's contact surface indicates the largest deformation, which is 0.007844m.
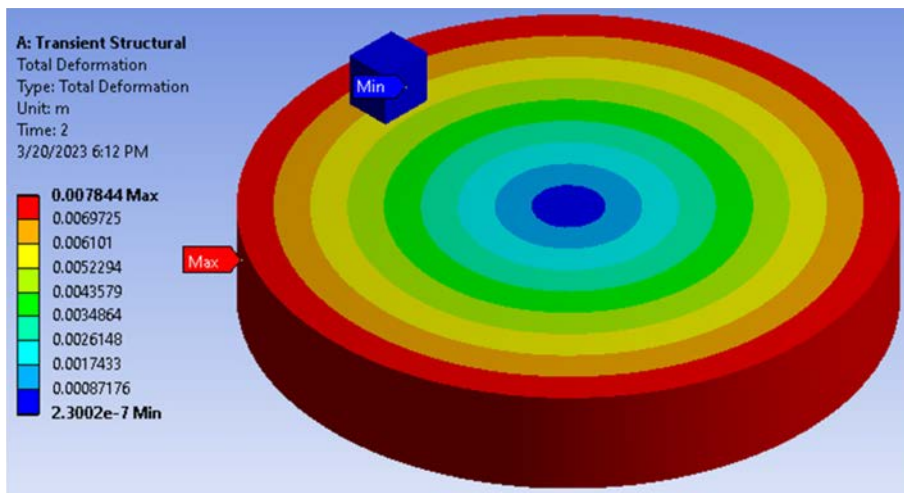
Figure 21. Total deformation

A frictional heat is produced as the pin slides across the disc while under stress and friction. Both the stick and slip conditions are included in this frictional heat value. The maximum is represented by red colors, which are also used to denote the stick condition, and the medium is represented by orange

colors, which are also used to denote the slide condition, as seen in figure 22. In contrast to the stick and slip, they come in a variety of other colors, such as the lemon, blue, and violet in the illustration, but they have less surface traction. The stick traction gradually builds up to its maximum value before beginning to decline. Because the stick traction's maximal value is where slip traction occurs. Then, following a slip, traction gradually decreases until a minimum value is reached. The next stick gradually climbs until it reaches the highest value, after which the cycle repeats.
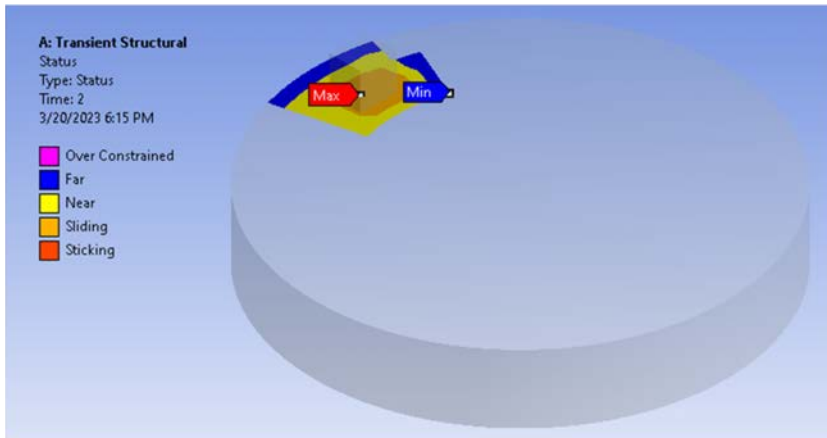
Figure 22. Status

Future plans for abrasive wear: Many studies on abrasive wear have been carried out using pin-on-disc abrasive wear tester machines and a couple of FEM and DEM. For example (Leonard et al., 2013) and (Li et al., 2013) were investigating abrasive wear by a couple of FEM and DEM. In contrast, they did not take into account the temperature, the slide, the size, or the quantity of the particles. For instance, (Penagos et al., 2017) and (Zafar & Sharma, 2016) were examined for abrasive wear using a pin-on-disc abrasive wear tester machine. However, they did not take into account temperature, a significant number of particles, or surface roughness. We can see that practically all of these articles have restrictions. We will use an abrasive wear tester machine along with a couple of FEM and DEM to try to address these restrictions as well as additional issues that weren't covered.

Conclusions

- By using various boundary conditions, the sliding frictional contact was used to simulate the contact stress, contact pressure, von mise stress, and deformation between the pin made of polyethylene material and the disc made of aluminum alloy (AL7075).

- We can summarize based on the above-detailed analysis:
- We utilized the Finite Element Method (FEM) to analyze contact stress, deformation, and von Mises stress.
- To investigate deformation, contact stress, and von Mise stress between the pin on the disc, the ANSYS software workbench was used.
- The polyethylene pin experienced the highest levels of deformation, contact stress, and von Mise stress. These numbers demonstrated to us that failure occurs at the polyethylene pin rather than the aluminum alloy disc.

Acknowledgements

References

[1] Basseville, S., Heripre, E., & Cailletaud, G. (2011). Numerical simulation of the third body in fretting problems. *WEAR*, *270*(11–12), 876–887. https://doi.org/10.1016/j.wear.2011.02.016

[2] De la Torre, B., Barrios, L., De la Torre-Mosquera, J., Bujan, J., Ortega, M. A., & Gonzalez-Bravo, C. (2021). Analysis of the Risk of Wear on Cemented and Uncemented Polyethylene Liners According to Different Variables in Hip Arthroplasty. *MATERIALS*, *14*(23). https://doi.org/10.3390/ma14237243

[3] Din, I. U., Panier, S., Hao, P., Franz, G., Bijwe, J., & Hui, L. (2019). Finite element modeling of indentation and adhesive wear in sliding of carbon fiber reinforced thermoplastic polymer against metallic counterpart. *TRIBOLOGY INTERNATIONAL*, *135*, 200–212.
https://doi.org/10.1016/j.triboint.2019.03.010

[4] Ding, J., McColl, I. R., Leen, S. B., & Shipway, P. H. (2007). A finite element-based approach to simulating the effects of debris on fretting wear. *WEAR*, *263*(1, SI), 481–491. https://doi.org/10.1016/j.wear.2006.12.056

[5] Duan, N., Yu, Y., Wang, W., & Xu, X. (2017a). SPH and FE coupled 3D simulation of monocrystal SiC scratching by single diamond grit. *INTERNATIONAL JOURNAL OF REFRACTORY METALS & HARD MATERIALS*, *64*, 279–293. https://doi.org/10.1016/j.ijrmhm.2016.09.016

[6] Duan, N., Yu, Y., Wang, W., & Xu, X. (2017b). Analysis of grit interference mechanisms for the double scratching of monocrystalline silicon carbide by coupling the FEM and SPH. *INTERNATIONAL JOURNAL OF MACHINE TOOLS & MANUFACTURE*, *120*, 49–60.
https://doi.org/10.1016/j.ijmachtools.2017.04.012

[7] Duan, N., Yu, Y., Wang, W., & Xu, X. (2017c). Analysis of grit interference mechanisms for the double scratching of monocrystalline silicon carbide by

coupling the FEM and SPH. *INTERNATIONAL JOURNAL OF MACHINE TOOLS & MANUFACTURE*, *120*, 49–60. https://doi.org/10.1016/j.ijmachtools.2017.04.012

[8] Froelich, D., Magyar, B., & Sauer, B. (2014). A comprehensive model of wear, friction and contact temperature in radial shaft seals. *WEAR*, *311*(1–2), 71–80. https://doi.org/10.1016/j.wear.2013.12.030

[9] Garcin, S., Fouvry, S., & Heredia, S. (2015). A FEM fretting map modeling: Effect of surface wear on crack nucleation. *WEAR*, *330*(SI), 145–159. https://doi.org/10.1016/j.wear.2015.01.013

[10] Gui, L., Wang, X., Fan, Z., & Zhang, F. (2016). A simulation method of thermo-mechanical and tribological coupled analysis in dry sliding systems. *TRIBOLOGY INTERNATIONAL*, *103*, 121–131. https://doi.org/10.1016/j.triboint.2016.06.021

[11] Hamim, A., Yusoff, N. I. M., Ceylan, H., Rosyidi, S. A. P., & El-Shafie, A. (2018). Comparative study on using static and dynamic finite element models to develop FWD measurement on flexible pavement structures. *CONSTRUCTION AND BUILDING MATERIALS*, *176*, 583–592. https://doi.org/10.1016/j.conbuildmat.2018.05.082

[12] Hua, N., Zhang, X., Liao, Z., Hong, X., Guo, Q., Huang, Y., Ye, X., Chen, W., Zhang, T., Jin, X., Wang, Q., & Liaw, P. K. (2020). Dry wear behavior and mechanism of a Fe-based bulk metallic glass: Description by Hertzian contact calculation and finite-element method simulation. *JOURNAL OF NON-CRYSTALLINE SOLIDS*, *543*. https://doi.org/10.1016/j.jnoncrysol.2020.120065

[13] Huang, L., Zhao, G., Wang, Z., & Zhang, X. (2016). Adaptive hexahedral mesh generation and regeneration using an improved grid-based method. *ADVANCES IN ENGINEERING SOFTWARE*, *102*, 49–70. https://doi.org/10.1016/j.advengsoft.2016.09.004

[14] Jerier, J. F., & Molinari, J. F. (2012). Normal contact between rough surfaces by the Discrete Element Method. *TRIBOLOGY INTERNATIONAL*, *47*, 1–8. https://doi.org/10.1016/j.triboint.2011.08.016

[15] Kumar, G. B. V., Rao, C. S. P., & Selvaraj, N. (2012). Mechanical and dry sliding wear behavior of Al7075 alloy-reinforced with SiC particles. *JOURNAL OF COMPOSITE MATERIALS*, *46*(10), 1201–1209. https://doi.org/10.1177/0021998311414948

[16] Leonard, B. D., Sadeghi, F., Shinde, S., & Mittelbach, M. (2013). Rough surface and damage mechanics wear modeling using the combined finite-discrete element method. *WEAR*, *305*(1–2), 312–321. https://doi.org/10.1016/j.wear.2012.12.034

[17] Li, W., Huang, Y., Fu, B., Cui, Y., & Dong, S. (2013). Fretting damage modeling of liner-bearing interaction by combined finite element – discrete element method. *Tribology International*, *61*, 19–31. https://doi.org/10.1016/j.triboint.2012.11.019

[18] Mukras, S., Kim, N. H., Sawyer, W. G., Jackson, D. B., & Bergquist, L. W. (2009). Numerical integration schemes and parallel computation for wear

prediction using finite element method. *WEAR*, *266*(7–8), 822–831. https://doi.org/10.1016/j.wear.2008.12.016

[19] Penagos, J. J., Pereira, J. I., Machado, P. C., Albertin, E., & Sinatora, A. (2017). Synergetic effect of niobium and molybdenum on abrasion resistance of high chromium cast irons. *WEAR*, *376*(B), 983–992. https://doi.org/10.1016/j.wear.2017.01.103

[20] Sardar, S., Karmakar, S. K., & Das, D. (2020). Identification and modelling of applicable wear conditions for stir cast Al-composite. *FRICTION*, *8*(5), 847–873. https://doi.org/10.1007/s40544-019-0302-6

[21] Suresh, B., Maruthamuthu, S., Khare, A., Palanisamy, N., Muralidharan, V. S., Ragunathan, R., Kannan, M., & Pandiyaraj, K. N. (2011). Influence of thermal oxidation on surface and thermo-mechanical properties of polyethylene. *JOURNAL OF POLYMER RESEARCH*, *18*(6), 2175–2184. https://doi.org/10.1007/s10965-011-9628-0

[22] Yue, T., & Wahab, M. A. (2014). Finite element analysis of stress singularity in partial slip and gross sliding regimes in fretting wear. *WEAR*, *321*, 53–63. https://doi.org/10.1016/j.wear.2014.09.008

[23] Yue, T., & Wahab, M. A. (2017). Finite element analysis of fretting wear under variable coefficient of friction and different contact regimes. *TRIBOLOGY INTERNATIONAL*, *107*, 274–282. https://doi.org/10.1016/j.triboint.2016.11.044

[24] Zafar, S., & Sharma, A. K. (2016). Abrasive and erosive wear behaviour of nanometric WC-12Co microwave clads. *WEAR*, *346*, 29–45. https://doi.org/10.1016/j.wear.2015.11.003

Biodegradable composite material using a 3D printer

Rawabe Fatima FAIDALLAH[1], Zoltán SZAKÁL[2], István OLDAL[2]

[1]Mechanical Engineering Doctoral School (MTDI), Szent István Campus, Gödöllő, MATE
[2]Institute of Technology, Hungarian University of Agriculture and Life Sciences, MATE, Gödöllő

Abstract

Three-dimensional (3D) printing is a flexible technique that has attracted increasing interest in recent years. Powerful biodegradable materials are available for 3D printing and are important for emergencies like COVID-19 and environmental preservation. Several techniques have been employed to improve compatibility for customized and improved material features. Due to their low cost of manufacturing, environmental friendliness, and appropriateness for a wide range of applications, biodegradable polymers, and composites are gaining more and more attention from companies and researchers. The use of natural resources to create fully or partially biodegradable composite materials is one modest step toward safeguarding the environment. PHB (Polyhydroxybutyrates), PLA (Polylactic Acid), HIPS (High Impact Polystyrene), and PHA (Polyhydroxyalkanoates) are a few examples of bioplastics that are created, function similarly to traditional plastics, and are biodegradable. In plastic manufacturing, the currently popular geometry shape tensile tests (ASTM D638, ISO 527-2). In these shapes, the exclusive location of yielding in the material will be in the neck, as the reduced area gives the neck the largest local stress, this problem will create a weak spot near the neck's edge, which is under the most pressure and stress. Researchers suggested solving this weak point by using ASTM D3039 standards to reduce pressure and stress near the neck's edge. Every country desperately needs to develop bioplastic usage and proper waste management for a pollution-free world. This research is expected to provide a general overview of 3D-printed biodegradable polymer fused deposition modeling (FDM) technology. Also, to make a comparative analysis between rectangular shape ASTM D3039 (0°, 15°, 90°) angle (trying to avoid the weak spot at the neck of the specimens) with the different tensile test specimens which are based on ASTM /ISO standards printed with different building orientations (flat and on-edge) of polyethylene terephthalate glycol (PETG) material. Afterward, the two different printing orientations were examined, and the variations in tensile strength value, E modulus, strain, and elongation at break among the tested samples were studied and compared. The experimental result showed the best tensile properties for ASTM D3039-0° with the on-edge building orientation but the best-broken area was to the flat orientation and the lowest tensile properties were for ISO 527-2 through both building orientations. This comparison showed that the rectangle shape improved the tensile properties, the tensile strength of ASTM 90-0° was 17.87%, 21% higher than the ISO 527 geometry shape for Flat, On-Edge orientation, respectively. The lowest

tensile properties were to ISO 527 which the researchers suggest working with this tensile geometry standard shape. More intensified research is needed for the large-scale production and commercialization of bioplastic products to be successful worldwide.

Keywords

FDM, biodegradable material, Sandwiches structure, different tensile geometry shapes, Mechanical properties.

1. Introduction

Review of biodegradable material

Three-dimensional printing is a buzzword in the material manufacturing world of materials manufacturing, and it has lately been the focus of an investigation by materials scientists. This technology has grown rapidly in recent years and is expected to revolutionize manufacturing sectors by enabling the development of next-generation high-performance materials. Additive manufacturing (AM) could be defined as "the process of joining materials to produce parts from 3D model data" Often layer upon layer, as opposed to formative and subtractive manufacturing methods. The AM process fuses cool and solidifies to create 3D geometries without adopting complex molds (Technologies and Terminology 2012).

Polymers have become a very important material in our daily lives. They are used in various fields such as food, industry, medicine, and the automotive industry. Newly, polymers have begun to replace advanced materials due to their superior properties. However, disposable materials account for more than one-third of plastic production, resulting in environmental problems because of waste and plastic emissions (Negrin et al. 2018). A renewed interest in the research of degradable polymers has been inspired by greater awareness of the pollution problem and its effect on the environment. Because of environmental issues, researchers resort to developing materials that do not have a harmful effect and are environmentally friendly. Most biodegradable polymers belong to thermoplastics (poly (lactic acid), poly (vinyl alcohol, poly hydroxyl alkanoate), or plant polymers (e.g., starch and cellulose). Thermoplastics made from polyolefins are not biodegradable, although some of them contain pro-oxidant additives that make them photodegradable and term degradable. The use of non-biodegradable polyethylene films (PE) on green spaces or soils has caused serious problems in Southeast Asia (Calabia et al. 2013). Non-biodegradable polymers such as polypropylene (PP), polyethylene (PE), poly (ethylene terephthalate), polystyrene ethylene vinyl alcohol, expanded polystyrene, polyurethane, polyamides, and poly (vinyl chloride) have become widely used in the packaging industry due to their good physical and mechanical properties.

Polymers are commonly utilized in 3D printing, but the raw materials used for 3D printing nowadays consist of different polymer composites to get the desired qualities of the end product (Boparai and Singh 2018). The time it takes for a printer to manufacture a final product is typically a few hours; however, the period varies on the size of the item to be made and the type of printer used for 3D printing (Mohamed et al. 2017). The mechanical and functional qualities of the products can be improved by choosing feedstock with greater mechanical properties and producing polymer composites by adding reinforcements in the form of particles, fibres, or nanomaterials to the composite polymer matrix (Zhang et al. 2020), (Murawski et al. 2019). Bio-based or natural fillers, which can be made from a variety of agricultural and industrial wastes, have successfully added mechanical strength to base polymers (Mazzanti, Malagutti, and Mollica 2019). Additionally, these fillers enable the items' recycling and biodegradability, reducing their negative environmental effects. To satisfy customers, 3D printing of bio nanocomposites has recently gotten a lot of attention from a wide range of industries.

Additive manufacturing has been advantageous at short design cycles, suitable for manufacturing complex structures, and high material utilization compared to traditional subtractive manufacturing. Therefore, additive manufacturing has been widely used in manufacturing parts and devices for aerospace (Joshi and Sheikh 2015), aviation (Murr 2016), automobiles (Korger et al. 2016), medical devices (Revilla-León and Özcan 2019), construction (Buchanan and Gardner 2019), clothing (Jasminka and Josipa 2018), and so on. This technology creates objects by adding materials to reduce waste while reaching satisfactory geometric accuracy (Levy, Schindel, and Kruth 2003). It is begun with a meshed 3D computer model that could be created by acquired image data or structures built in Solidworks or computer-aided design (CAD) software. An STL (Surface Tessellation Language) file is commonly created, figure 1 the process of 3d printing product. These three technologies combined made possible the printing of three-dimensional objects sent to the 3D printing machine(Cooper 2001, Kruth 1991). Speed, direct data translation, management of complicated geometry, high precision, environmental benefits, and cost-effectiveness are just a few of its features. The 3D printing technology known as stereolithography (SLA) was the first commercial application of additive manufacturing (AM) in 1987 (Wohlers and Gornet 2014). Since then, the AM has evolved very rapidly, particularly in the last decade. There are different methods of this technology object manufacturing (LOM) based on plastic lamination (Ahn et al. 2012), stereolithography apparatus (SLA) based on photopolymerization (Wang et al. 2016), selective laser sintering (SLS) (D. Slavko and K. Matic, 2010), and fused deposition modelling based on the melting of plastic filaments. Figure 1 shows various additive manufacturing techniques related to the polymer's 3D printing.

The FDM (fused deposition modeling) process is worked by extruding thermoplastic material, which has heated up to its melting point through a nozzle, then depositing the extruded layers of materials on top of each other. Currently, FDM considers the most widely used technology of all types of 3DP technology around the globe due to the low cost of the printer device, sim PLA

(Cuiffo et al. 2017), PVA (polyvinyl alcohol) (Ni, Wang, and Zhao 2017), TPU (thermoplastic polyurethane) (Xiao and Gao 2017), nylon (Chunze et al. 2009). It can be considered as one of the most widely used materials in 3D printing technologies, and a variety of cheap filaments (Liu et al. 2019). Platform temperature, nozzle size, layer thickness, printing direction, nozzle head temperature, printing speed, and raster angle are parameters that could be controlled to improve print quality. Other researchers looked at the details of many processing parameters. According to the research, a suitable bed temperature and regulated convective heat transfer conditions can increase the bonding strength of successive layers, improving the mechanical properties of printed objects (Sun et al. 2008).
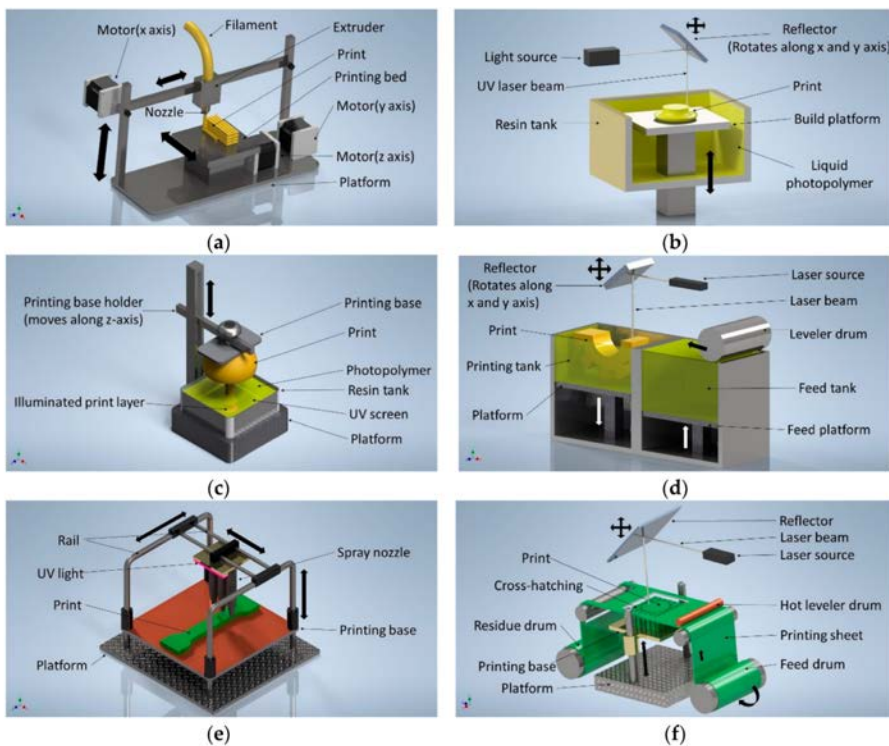
Figure 1. Various techniques for polymer 3D printing (**a**) fused deposition modelling (FDM), (**b**) stereolithography (SLA) technique, (**c**) digital light processing (DLP), (**d**) selective laser sintering (SLS), (**e**) polyjet printing process, (**f**) sheet lamination (LOM) (Nath and Nilufar 2020).

FDM technologies are widely used in different applications like aeronautics, automotive, construction, aerospace, and medicine. Various thermoplastic polymers like acrylonitrile butadiene styrene (ABS), polylactic acid (PLA), and polyimide are used as the material of FDM technologies in the shape of filament. ABS material has better elongation, ductility, and flexural strength compared with PLA material, but it has emitted gas in the printing process. On the other hand, PLA material is a more

environmentally friendly material compared with ABS material because of degrades faster than ABS material and is produced from renewable resources. In addition, it is a biodegradable thermoplastic polymer compound, non-toxic, and ecologically friendly aliphatic polyester made from lactic acid (derived from animals and plants) that is used to make films, textiles, and bottles. PLA has excellent mechanical qualities and, because of its biodegradability, can be used to replace petroleum-based polymers (Ngo et al. 2018).

Fused Deposition Modelling (FDM)

The FDM process is worked by extruding thermoplastic material, which uses thermoplastic filament as feedstock, the filament has heated up to its melting point, then is extruded through a nozzle in the XY plane creating a layer of solid material on the build plate. Creating a model can be done by depositing a layer contour, The material is then extruded in the XY plane by a nozzle, forming a solid layer on the build plate. By depositing a layer contour and then filling the interior with plasticized material with zigzag head movements, a model could be created. The head moves along the Z-axis after manufacturing one layer, starting the build-up of the next layer. We can make various forms using this method with a minimum of the previous step.
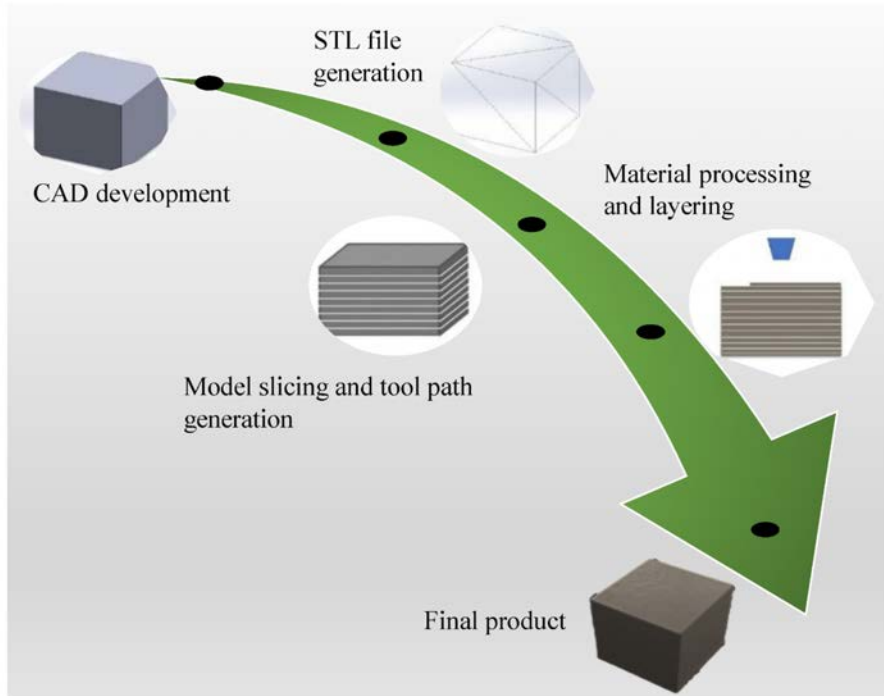

Figure 2. FDM 3D printing procedure (Kafle et al. 2021).

The manufacturing process begins with the creation of a model in a CAD program and then its transfer to software like (Ultra-software) that could control o0f process parameters such as head movement, feed rate, layer thickness, infill, head and table temperatures, slicing, support application, etc. Then the software creates G-code, which can then be transferred to a 3D printer to create an actual model. The model that was taken from the printer may need requires finishing machining to delete the supports and flaws (Bakarich et al. 2014, Dudek 2013). Currently, FDM considers the most widely used technology of all types of 3DP technology around the globe due to its low cost of the printer device, simplicity, and variety of inexpensive filaments. Figure 2 shows a procedure of the 3D printing process g the FDM technology.

With simple designs, it may be relatively straightforward to remove the support materials, but for more complex ones, it may be more difficult. Ultimaker uses a water-soluble support material that does not leave any residue in the supporting components to create transparent parts. Building dynamic structures is made simple by this type of support material. The extruder's motion, the material's temperature, speed, and flow rate during the nozzle all have an impact on how precisely the component was made. The FDM technique (Figure 3) is extensively used to create anatomical models for training in dental and surgical procedures (Mostafa et al. 2009).
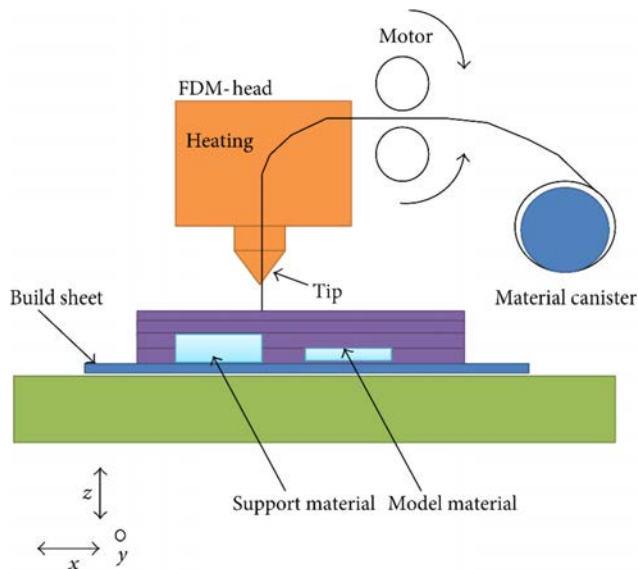

Figure 3. Fusion deposition modelling (FDM) process (Onwubolu and Rayegani 2014).

FDM Feedstock materials using thermoplastics

For common components that are designed to experience low stress, typical thermoplastics like polylactic acid (PLA), acrylonitrile butadiene styrene (ABS),

polyethylene (PE), and polypropylene (PP) are used. However, since they have more wear resistance than typical plastics, engineering polymers like polycarbonate (PC), nylon (PA), and polyethylene terephthalate (PET) is used in structural elements. While this is the case, modern polymers, such as Polyether-ether-ketone (PEEK) and Polyethyleneimine (PEI), are resistant to high temperatures, and chemical.

The next section goes through the most popular thermoplastics for filaments used in 3D printing (PEEK, ABS, PET, and nylon 6).

Polyether Ether Ketone (PEEK)

PEEK is lightweight, chemically and thermally resistant (Wang et al. 2016). Around 340 °C is the printing temperature for PEEK (Xiao and Gao 2017). Around 143 °C is when glass transition occurs in this material. It also has a lot of benefits, including superior mechanical and chemical resistance properties (high resistance to biodegradation and thermal degradation), which allow it to be used in harsh environments that call for high service temperatures or mechanical properties, like piston parts, bone, bearings, cars, and airplanes (Wang et al. 2020). PEEK may be handled similarly to an amorphous polymer, resulting in dimensional stability and strong layer adhesion, making it a good alternative feedstock for FDM.

Acrylonitrile Butadiene Styrene (ABS)

Styrene and acrylonitrile are polymerized with polybutadiene to create ABS, an amorphous material. Because to its greater hardness, resilience, and resistance to corrosive chemicals compared to PLA, ABS is better suited for usage in FDM (Kuo et al. 2016). Yet, because of its propensity to warp and a high shrinkage factor, it is fairly challenging to print on. Chemically sensitive individuals may be harmed by ABS's chemical vapours. ABS typically melts at temperatures between 200 and 250 °C (Rutkowski and Levin 1986). The fabrication of a few useful components has used ABS in the automotive, medical, and aerospace industries (Lee et al. 2017).

Nylon 6

Nylon 6 is known for its impact strength, flexibility, and heat resistance. Both durability and good toughness characteristics are present. It absorbs a lot of moisture, though, because it is a hygroscopic material, which lowers its general quality (Terekhina et al. 2019). Nylon is prone to warping, just as ABS. By maintaining the bed's temperature at roughly 75 °C, the warping impact can be lessened. To retain high-quality products, it should be stored in a cold, dry environment because it is moisture-sensitive (Cho et al. 1996).

Polyethylene Terephthalate (PET)

PET is a semi-crystalline polymer that is a component of the polyester family. Glycol-modified polyethylene terephthalate (PETG), which is less brittle and more convenient to use, is more widely used in 3D printing filament than raw

PET. PETG is easier to print than ABS and may be used to create 3D goods with a smooth surface finish and strong impact resistance, but it also absorbs moisture from the air readily (Kauffman 2010).

Bio-degradable polymer
Depending on their origin, biodegradable polymers are categorized into two categories: natural and synthetic. Synthetic polymers have an advantage over natural polymers in that they are more adaptable, have adjustable mechanical characteristics, and can vary the rate of deterioration as needed. Natural polymers, on the other hand, appear appealing due to their outstanding biocompatibility, but they have not been completely studied due to undesired features including antigenicity and batch fluctuation (Domb, Kumar, and Ezra 2011). Many fascinating uses for biodegradable polymers exist, including drug administration, tissue engineering, gene therapy, regenerative medicine, temporarily implanted devices, implant coatings, etc. (Hacker and Mikos 2009, Luten et al. 2008). The basic criteria for selecting a polymer as a degradable biomaterial are matching the mechanical properties and degradation rate to the application requirements, nontoxic degradation products, biocompatibility, durability/stability, processability, and cost (Domb, Kumar, and Ezra 2011, Gunatillake, Adhikari, and Gadegaard 2003). Mechanical properties should be matched to the application to maintain adequate strength until the surrounding tissue has healed (Gunatillake et al. 2006). There are many biodegradable polymers available for different applications (Figure 4), and the choice of the polymer depends on the requirements placed on a particular biomaterial.
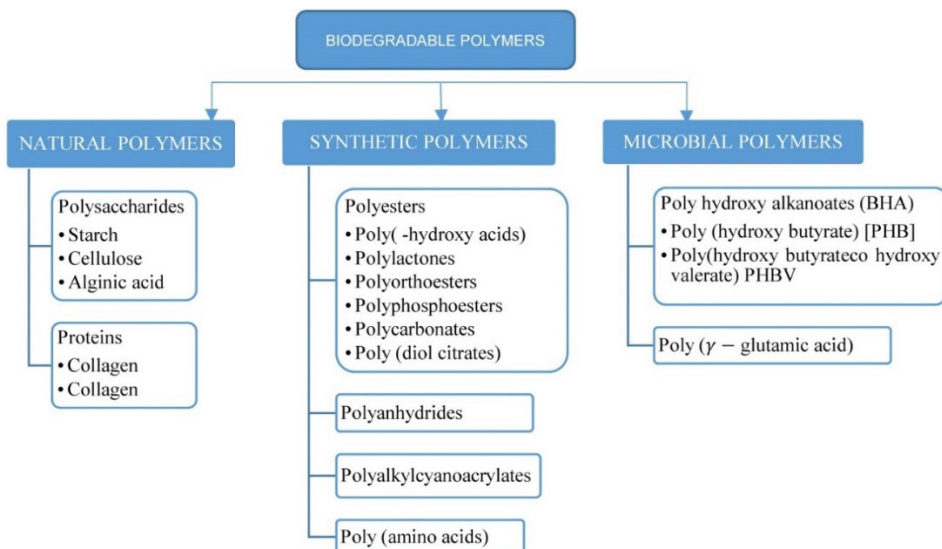

Figure 4. Classification of biodegradable polymers.

PHA can be used as such or in a blend with polylactic acid. PVA is a biodegradable and water-soluble polymer that is used to support construction. Duran et al (Duran et al. 2015) PVA is printed as a support structure for ABS. They found that PVA is printable for up to 45 minutes when dried before it absorbs moisture from the air and becomes unprintable. High-impact polystyrene (HIPS) is similar to ABS with good mechanical properties and extrusion temperature. It is used as a substrate for ABS because it dissolves in limonene, but ABS does not. In biocompatible and medical applications, 3D printing filaments are made from polymers with low melting temperatures.

These materials can be used in the FDM process to fabricate parts that blend into human tissue, such as scaffolds. Chia et al. (Chia and Wu 2015) and Serra et al. (Serra, Planell, and Navarro 2013) list some of these materials. Pietrzak et al. (Pietrzak, Isreb, and Alhnan 2015) and Melocchi et al. (Melocchi et al. 2015) developed capsules for drug delivery systems by using biodegradable 3D-printed hollow hydroxypropyl cellulose (HPC). These capsules are taken orally and the degradation of the capsule in the stomach releases the drugs concealed in it.

Polylactic Acid (PLA)
PLA is a common thermoplastic known for its biodegradability but also known for its sensitivity to humidity over 60 °C. PLA has a relatively low melt point of 145–186 °C and can be easily formed into filament with a temperature over 185–190 °C (Kim et al. 2017). It is also characterized with biocompatibility and good mechanical properties (relatively high strength and modulus). The constructed PLA parts have been observed to have lower distortions while printing than ABS. However, they are less resistant and thermally conductive (Kumar, Singh, and Farina 2018, Rodríguez-Panes, Claver, and Camacho 2018). PLA constructions are most commonly utilized in practical applications that demand a certain level of aesthetics (Dey, Hoffman, and Yodo 2020, Mazzanti, Malagutti, and Mollica 2019). It is extracted from renewable energy sources like maize starch or cane sugar. It may be produced using existing production equipment (the ones created and utilized in the oil and gas industry for materials). As a result, production process is quite inexpensive. PLA, therefore, has the second biggest production capacity of every bioplastic (most usually referred to as polymer protein) (de Ciurana, Serenóa, and Vallès 2013). Polylactic acid has a wide range of applications. Some of the most common applications are eco-friendly medical equipment, disposable films, and containers. PLA is excellent for use as a shrink-wrap sheet because it binds when heated. Furthermore, the ease with which polylactic acid fuses lends itself to some intriguing applications for printing technology (Jerez-Mesa et al. 2017).

Polyhydroxyalkanoates (PHA)
PHA consists of a class of natural-based polyesters synthesized using microbial fermentation of carbon-based feedstock; which are biodegradable and readily compostable thermoplastics (Mckeen 2012). The polymer shows a glass transition temperature in the range of −5 to 20 °C. PHA are both bio-based and

biodegradable, with physical and chemical properties similar to polypropylene, thereby making it a good alternative to PLA in biopolymer system developments. PHA is generally known to be:

– Although resistant to UV radiation, it is weak toward acids and bases.
– Biocompatible and non-toxic, thereby making it suitable for biomedical and food packaging applications (Mckeen 2012).
– Insoluble in water, and relatively resistant to hydrolytic degradation

Its biocompatibility and biodegradability by simple hydrolysis of ester bonds in aerobic conditions and piezoelectric properties make them suitable for drug delivery, tissue engineering, and orthopedic applications.

High impact polystyrene (HIPS)
HIPS is a biodegradable thermoplastic with low strength and good process technology. The excellent flow characteristics, inexpensive cos, and impact resistance of this FDM filament are all benefits (Kumar, Singh, and Farina 2018). However, it is prone to wear and requires a high printing temperature and a hot build platform. HIPS has qualities that are comparable to ABS, however, it is less thick. HIPS is preferable for support structures because it dissolves with chemicals such as limonene (Pakkanen et al. 2017).

High-density polyethylene
Polyolefin thermoplastics such as high-density polyethylene (HDPE) are the world's leading manufacturers of plastics, environmentally friendly polymerization processes, recycling, and sustainability. HDPE is an ethylene monomer material made of thermoplastics. When used as HDPE pipe, it is sometimes called " polyethylene" or "alkathene". Higher-density polyethylene is used to make high-density plastic water bottles, plastic lumber, abrasion resistant containers, and geomembranes. An evaluation of the mechanical reusability of HDPE, a raw material widely used for open additive manufacturing, to assess the feasibility of using this recycled plastic in open 3D additive manufacturing (Singh et al. 2018).

Poly(ε-caprolactone) (PCL)
The most extensively investigated member of this family is poly (caprolactone) (PCL) (Hayashi 1994, Holland and Tighe 1992). Semicrystalline polymer PCL is thought to be non-toxic and tissue-compatible, with a glass transition temperature of about -60°C. The polymer is compatible with a variety of different polymers and has a low melting point (59 to 64 °C). As PCL degrades much more slowly than PLA, it is a useful base polymer for creating long-lasting, implanted drug delivery systems. Chemically, PCL is thought to be non-toxic and tissue-compatible (Kronenthal 1975). Because to PCL's delayed degradation property, it has been researched as a vehicle for the long-term administration of medications/vaccines (Capronor) and cell-based therapy. Levonorgestrel, a

hormone that is present in Capronor, is a long-acting contraceptive [64].(Lee and Kaplan 2006). PCL has a modest tensile strength (about 23 MPa) and a very high elongation at breakage (>700%) (Gunatillake, Mayadunne, and Adhikari 2006). PCL is well suited for fused deposition modelling (3D melt printing) and it has been used to prepare a variety of 3D scaffolds for tissue engineering (Shim et al. 2012).

Cellulose and nanocellulose

Cellulose is a sustainable and non-degradable polymer. Numerous living things generate this very inventive polymeric substance, which is widely used in the food and medicinal industries (Javadzadeh and Hamedeyaz 2014). Its abundance results from the continuous photosynthetic cycles that take place within plant cells, which can manufacture several tons per year (Javadzadeh and Hamedeyaz 2014). Husk fiber, bamboo, wood, and sugar cane bagasse are some examples of plants or agricultural waste from which they can be obtained (Javadzadeh and Hamedeyaz 2014). Cellulose's primary properties are biodegradability, hydrophilicity, chirality, extensive chemical adaptability, and capacity Most significantly, in the context of this review, it has the potential to meet the growing need for lightweight, ecologically friendly products, but, like lignin, it may be constrained by its poor mechanical qualities (Dai et al. 2019). Bio resources like corn, cellulose found in wood, and others can be used to make bio polymers. The general process for producing bio-based polymer composite components using FDM is shown in Figure 5. to form a variety of semicrystalline fiber topologies (Klemm et al. 2005).
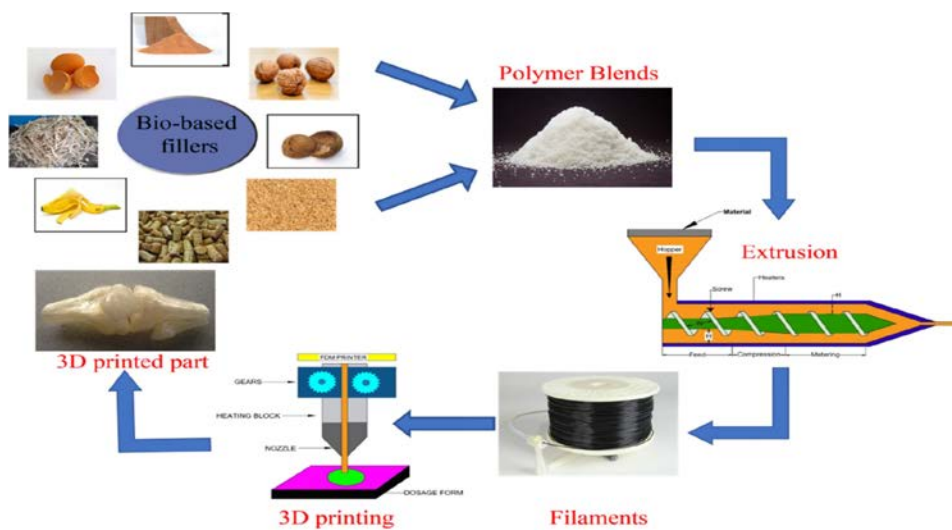

Figure 5. Schematic diagram of the typical 3D printing procedure for bio-based polymer nanocomposites (Mandala et al. 2022).

Comparative with different tensile geometry shapes

These standards are separated into plastics ASTM D638 (ASTM International - Standards Worldwide n.d.), ISO 527-2 (ISO - ISO 527-1:2012 - Plastics — Determination of Tensile Properties — Part 1: General Principles n.d.: 527)) and composites (ASTM D3039 (ASTM International - Standards Worldwide n.d.), ISO 527-4 (ISO 1997, 2009)) based on an analysis of the applicability of existing standards to mechanical testing of polymer additive manufacturing materials and parts. The decision to conduct customized tests rather than standardized ones or even the type of specimen used may be impacted by practical demands in addition to the basic guidelines provided by the standard (Moura et al. 2020). A decision might be taken, for example, to deal with non-standard (most sub size specimens due to the limited supply of feedstock material, particularly if a novel formulation is being tested for research purposes. Due to the destructive nature of tensile testing, smaller samples than those required may also be chosen for expensive materials (Moura et al. 2020). Despite the popularity of dumbbell-shaped samples based on ASTM D638 and ISO 527-2, it is common to observe unacceptable failure outside the narrow section because the dog bone geometry is difficult to print by FDM (Auffray, Gouge, and Hattali 2022, Özen et al. 2021, Tymrak, Kreiger, and Pearce 2014a, Alvarez, Lagos, and Aizpun 2016, Chandran et al. 2021, Miller, Brown, and Warner 2019). In particular, the ample fillet that the narrow section to the grips was originally designed to decrease stress concentration where the cross-sectional area changes in specimens that were shaped or specimens that were manufactured from sheets or plates (which are all continuous solids), but the curvature of this fillet can hardly be reproduced by the raster's printed by FDM. This could lead to structural defects, such as abrupt raster terminations, as material gaps (especially if the part is contoured), or sudden changes in the deposition path, which would then be the cause of an abnormal stress peak and a non-axial stress state at the radii, especially in relatively thin specimens (Özen et al. 2021, Ahn et al. 2002, Montero et al. 2001, Rankouhi et al. 2016).

ASTM D638 and ISO 527-2 (determining the tensile characteristics for molding and extrusion plastics) have been used to evaluate the materials' response, where the researchers (Tymrak, Kreiger, and Pearce 2014b, Ahn et al. 2002, Milosevic, Stoof, and Pickering 2017) discovered that specimens prematurely failed this early failure was due to the stress concentration in the dog bone's radius close to the gauge length.

The end of the filaments in this section of the specimens created an extreme shear. To circumvent these printing difficulties the original dog-bone geometry can be modified with a larger curvature radius (Auffray, Gouge, and Hattali 2022, Özen et al. 2021, Croccolo, De Agostinis, and Olmi 2013). It was proposed that ASTM D3039 (Standard Test Method for determining the Tensile Properties of Polymer Matrix Composite Materials) be used as a remedy (Ahn et al. 2002, Somireddy and Czekanski 2017, International 2007). it is officially dedicated to determining the tensile properties of polymer-matrix composite materials. ASTM D3039 could be applied also to neat polymer parts printed by

FDM due to their resemblance to orthotropic laminae. Miller et al.(Miller, Brown, and Warner 2019) evaluated the tensile behavior of ABS samples printed by FFF and found that rectangular coupons satisfying ASTM D3039 had a larger percentage of samples that met the standard for acceptable failure than ASTM D638 type I and type IV dog bones. Comparing ASTM D638 type I and type IV also showed that type IV dog bones had higher average compliance to the failure criterion than type I dog bones did. Comparing ASTM D638 type I and type IV also showed that type IV dog bones had higher average compliance to the failure criterion than type I dog bones did. The fillet radius was highlighted by the authors as the primary cause of ASTM D638 dog bones' inconsistent failure, with the inclusion of the additional inner radius increasing the performance (failure acceptability) of type IV dog bones in comparison to type I counterparts. Also proved that the elastic modulus was overestimated by the ASTM D638 type IV geometry. For ASTM D3039 test specimens, opposite trends were observed that caused the elastic modulus and tensile strength to be overestimated and underestimated, respectively. In the end, ASTM D638 type I performed equally well for the elastic modulus and strength as ASTM D638 type IV and ASTM D3039 (Miller, Brown, and Warner 2019).

In this study, the test specimen shape and grasping were investigated to determine the tensile performance. It forms part of an investigation into exploring the design freedom of 3D printing. It is necessary to understand the effect of changing the selected design of tensile geometry shape and printing parameters on the tensile properties of the FDM test specimens. As mentioned earlier, the variables selected for this experiment were chosen based on the experience and knowledge of the researchers. Five different geometry shape specimens' configurations have been prepared, (ISO 527, three types of ASTM D3039, and ASTM D638) of PETG polymer. The specimens have been printed in 3D printing with two different building orientations (flat, and on-edge) by using the FDM technique to examine the effects of using different orientations on the tensile strength and elongation at the break.

2. Materials and Method

Manufacturing of 3D printed specimens with different tensile geometry shapes
The test samples were created using a commercial FDM-type 3D printer, the "Geetech A20M". The printer's 255 x 255 x 255 mm work area has made it possible to produce many pieces concurrently. The processing settings of the material could be changed while manufacturing specimens on an FDM printer to fully understand the mechanical properties.

All specimens were layer-by-layer printed using various fillings. The test pieces are fabricated in diverse directions to examine the influence of print orientation (flat and upright orientation). The samples were printed by 0.2mm of layer thickness, 0.24 of initial layer height, printing temperature 230℃, platform temperature 70℃, and infill density of 100%.

Table 1. Specifications regarding preparation.

Model name	Standards	Specification(s)
Tensile test type I specimens	ISO 527-2	150*20*3 mm
Tensile test type II specimens	ASTM D638	165*19*3 mm
Tensile test type III specimens	ASTM D3039	175*20*5 mm
Tensile test type IIV specimens	ASTM D3039-90°	175*20*5 mm
Tensile test type V specimens	ASTM D3039-15°	165*20*2 mm

Poly Ethylene Terephthalate Glycol (PETG) has been used for the manufacturing of specimens. the filament is a black color PETG material branded Filanora and has a diameter of 1.75 mm. The specimens were designed by using Solidworks software the different standards shape are shown in figure .

(a)   (b)   (c)

(d)   (e)
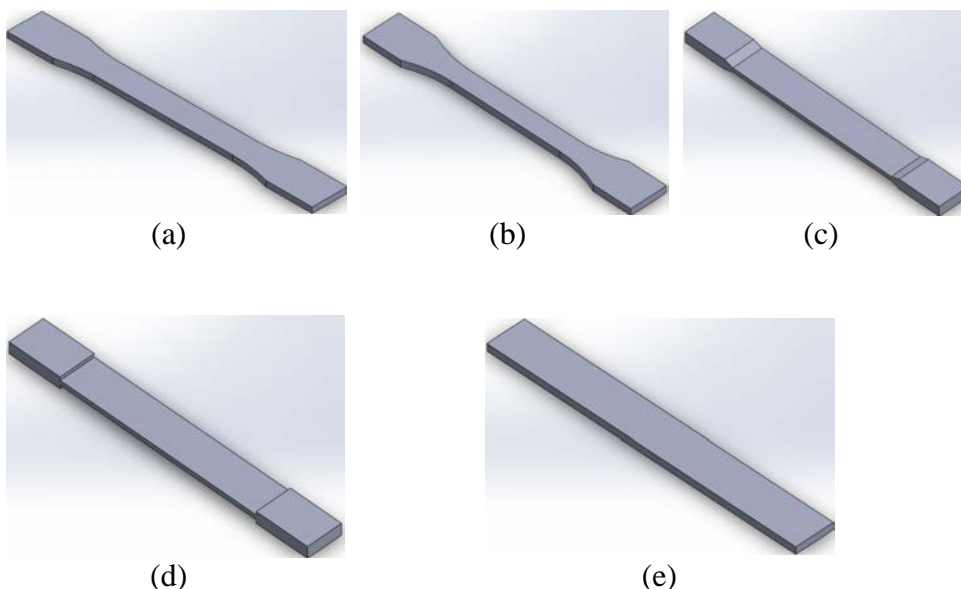
Figure 6. Describe the different geometric shape drawings by Solidworks software: (a) ASTM D638, (b) ISO 527-2, (c) ASTM D3039-15°, (d) ASTM D3039-90°, (e) ASTM D3039-0°

Experimentations

The universal test machine (Zwick / Roell Z100, Germany) was used to test sandwich structure specimens (for compression, tensile, and three-point bending), and (tensile test) for different tensile geometry specimens. Three repeated tests have been accomplished on the samples that were constructed for each configuration of the sandwich structure's core (honeycomb and rhombus) and Three repeated tests have been accomplished with each two different

building orientations (flat, and on-edge) of the different geometry shapes. The following sections clarify the conditions and details of the tests performed.

Specimen dimensions employing the (ASTM D638, ASTM D3039 (0,15,90)°, and ISO 527-2) for tensile testing of PET-G polymer. The tensile behavior determination included the tensile strength, tensile Young's modulus, and the failure form under the specified conditions. The modulus of elasticity determined experimentally within the elastic range by using an extensometer in order to study the strain rate sensitivity (viscoelasticity) (see Figure 7G). Extensometer is an instrument for measuring elongation which is attached to tensile test specimens and helps calculate young's modulus precisely. Each specimen is fixed by the grips as it is seen in Figure 1G, showing a specimen before tensile testing. The specimens were stretched at a steady speed of 3 mm/min along their main axis until they broke.

Specimens printing: The test pieces were manufactured using PETG filaments on a 3D printer. There have been ten different series produced. The total number of samples is 30 samples (Three specimens from each series were printed with the same print settings). The specimens are printed according to printing parameters. Figure 7 shows the group of samples according to different geometry shapes.
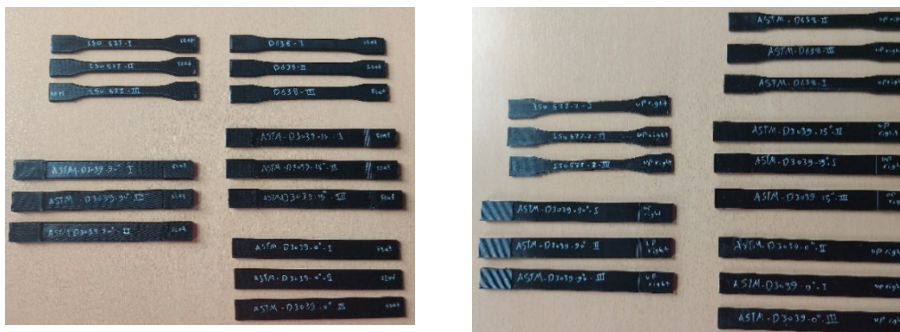
(F)

(G)

Figure 7. Different tensile specimens' geometries before tensile test:
(F) all tensile specimens' geometries, (G) the extensometer measure

3.Result and Discussion

Tensile performance of different geometry standard shape
Different tensile standard-shape specimens were created to determine the effect of build orientation on mechanical properties. Figure 8 summarizes the specimen design orientations used for tensile testing. As can be seen, samples were produced on the base test plate in the two main directions.
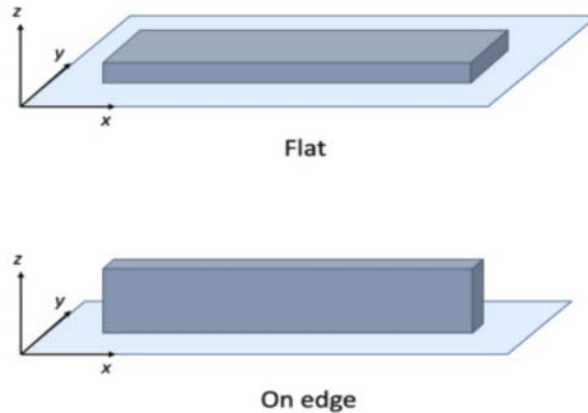

Figure 8. Represent builds orientation: On edge orientation, Flat orientation

Every layer has inner lines and a shell (contour). The direction of the layer contour for the flat sample is parallel to the applied tensile test force. These samples had a greater chance of elongation since the lengthy inner lines were constructed at a 45° angle with a reasonable number of layers (higher strain). The On-Edge workpiece has such a complex structure since its cross-section contains a huge number of layers, a narrow size contour, and short inner lines. This explains how these samples were pulled with a great degree of strength during the test.

The load-displacement curves that were obtained from the tensile test for all examined shape geometry and orientations are shown in figure 9. It is clear that the building orientation of the 3D printing parameter and the shape geometry has a significant impact on the values of force versus elongation. The results were divided into two curves according to the building orientation, and each curve describes different shapes of tensile standards depending on the building orientation. The highest standard force for the different shape geometry was to ASTM D3039-0° (flat and on edge), as shown in fig.9 the highest average of ASTM D3039-0° standard force was at 1693 N, 2632N for flat and on edge orientation, respectively. In the other hand for ASTM D638 the heights standard force was at 1562 N, 1890 N for flat and on edge orientation, respectively.
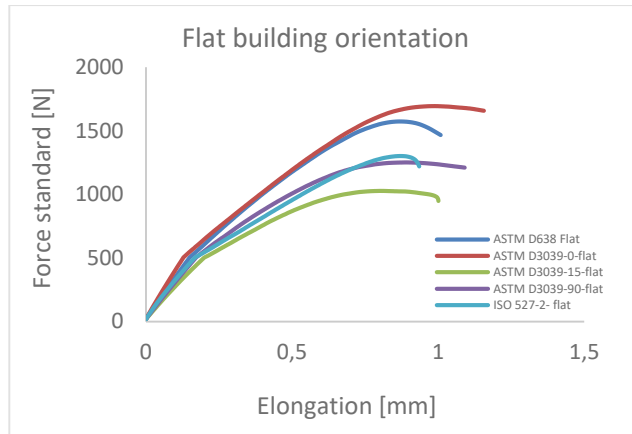
(a)
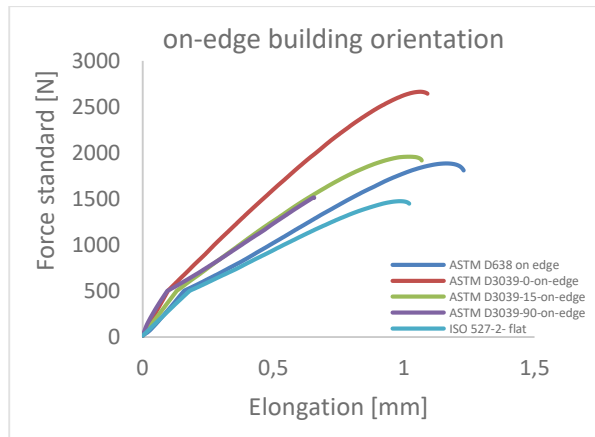
(b)

Figure 9. Load-displacement curves standard Force for: (a) Flat building orientation, (b) on edge orientation.

In terms of the tensile strength flat building orientation, which ranged between 23 and 28.25 MPa, the better values were from ASTM D3039-0°. For the on-Edge building orientation, the stress ranged between 36.45 and 46.71 MPa the better values were also from ASTM D3039-0° in comparative with the lowest value was to the ISO 527 (see figure 10a).. The average of the ASTM D3039-0° tensile strength for On-Edge orientation was 39.52% higher than that of the flat orientation. The increased tensile strength of these specimens is due to their reliable geometry shape. which avoided the weak spot at the neck of the specimens of ADTM D638 and ISO 527. In case of the comparative between ISO 527 and ASTM D638, the average of ASTM D638 specimens was higher than the average of ISO 527 specimens by 13.27%,19.5% for flat/ on edge orientation, respectively. The increased tensile strength of these specimens is

due to their reliable geometry shape. which avoided the weak spot at the neck of the specimens of ADTM D638 and ISO 527. Therefore, the applied load was distributed across a larger area, resulting in higher resistance to failure.

	ASTM D638	ISO 527	ASTM D3039-0°	ASTM D3039-15°	ASTM D3039-90°
flat orientaiton	26,75	23,2	28,25	26,46	25,38
on-edge orientation	45,23	36,45	46,71	48,32	39,9

(a)

	ASTM D638	ISO 527	ASTM D3039-0°	ASTM D3039-15°	ASTM D3039-90°
flat orientation	1382,4	1188,35	1622,12	1478,56	1439
on edge orientation	2112,5	1660	2582,65	2502,58	2773,78
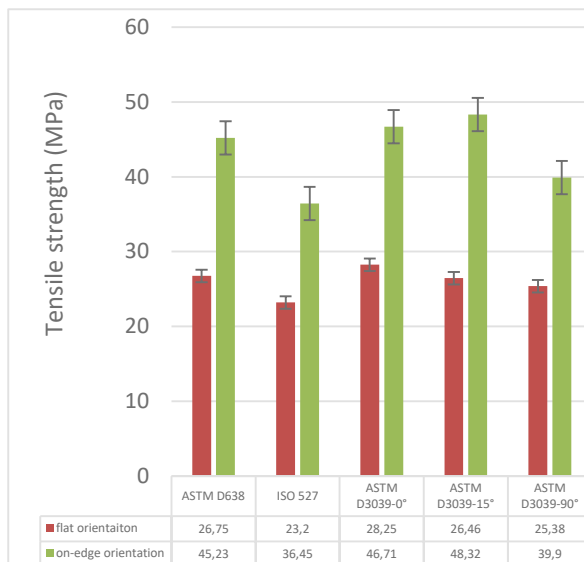
(b)
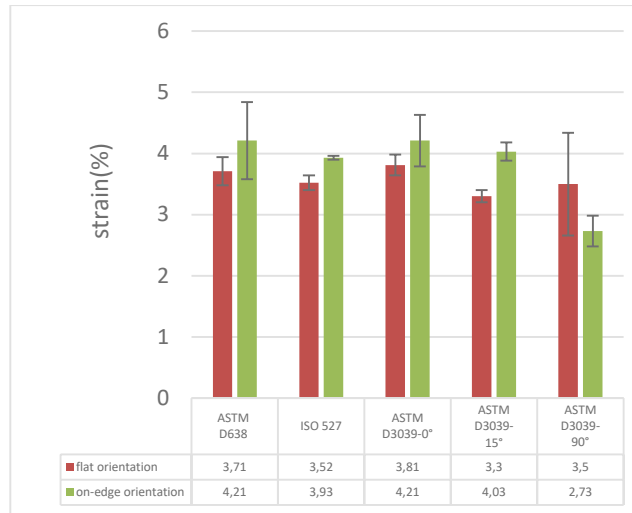
(c)

Figure 10. The result of the different geometry shapes during tensile test: (a) tensile strength for flat/on-edge building orientation, (b) tensile Modulus for flat/on-edge building orientation, (c) tensile strain for flat/on-edge building orientation.

In terms of the tensile modulus flat building orientation were ranged between 1188 and 1622 MPa, the better values were from ASTM 3039-0° (figure 10b), In other hand on-Edge building orientation of the tensile modulus ranged between 1660 and 2773 the better values were from ASTM D3039-90°. In addition, the increased tensile Modulus of ASTM D3039-0° was 26.74%, 40.15% higher than the ISO 527 geometry shape for flat/On-Edge orientation, respectively. In comparative between ASTM D638 and ISO 527 the average of ASTM D638 specimens was 14%, 21% higher than the ISO 527 geometry shape for flat/On-Edge orientation, respectively.

In case of the tensile strain the values were ranged between 2.73%, 4.21% (figure 10c). for the flat orientation the better value was to the ASTM D3039-0° and the lower value was to the ISO 527.

By testing FDM dog bones, Kay credited the lower tensile strengths and a higher degree of scattering to the use of ASTM D638, which is not recommended. He highlighted how failures frequently happened in the neck area of dog bones treated with FDM as a result of stress concentration in the part's transition zones. Improvements were shown when parts were tested according to ASTM D3039, a specification that includes the use of tabs and is intended for the testing of composites (Kay 2014). However, it should be mentioned that D638 is made for testing polymeric bulk materials, whereas these additive manufacturing parts more closely approximate a composite structure as previously described. ASTM 3039 is a geometry shape specifically designed to test composite materials and furthermore, higher values for these parts' ultimate

strength and modulus would be envisaged as a result of a higher percentage of continuous polymeric extruded fibers spanning the gauge length.

Figure 11 shows the specimens after the tensile test. In the case of testing specimens, it must always be taken into account that the break better to be in the middle. It is obvious that the broken area for the on-edge orientation was near the edge and the specimen shape that breaks in the neck part (when gripping) is not recommend. As a general trend, on edge orientation provides higher strength to the samples obtained by FDM according to results for the different standards, but the influence of the orientation shows more important in the case of the ASTM/ISO standards. These observations are in conformity with the results of Aliheidari et al.(Aliheidari et al. 2017), who claimed that the mechanical properties are directly influenced by the layered structure's characteristics, particularly the adhesion between the layers.

| (a) | (b) |

Figure 11. The specimens broken area: (a) flat orientation, (b) on-edge orientation

Conclusions

the available data suggests that rectangular cups with straight edges, such as those in ASTM D3039, should be used preferred to dumbbell-shaped like ones with curved edges, such in ASTM D638 to achieve a higher compliance with the failure criterion. According to experimental results, ASTM D3039 rectangle shape which is supported by the straight edges that reduce abrupt transition zones and reduce early failure brought on by stress concentration.

The best tensile properties were for the rectangle on-edge building orientation but this value can't be considered as the real value for the engineers due to the material does not have the same strength value as in reality. Based on its measurements, it is advisable to use standard test specimens that give the smallest value. For engineering applications, the lowest mechanical standard

which was for ISO 527 geometry shape and in the mechanical application we suggest to work with the lowest tensile properties so it is better to work with ISO 527 tensile shape geometry standard.

Future works

The essential objectives of the research will be achieved by means of performing the next steps.

1. New sandwiches structure core compressive and three-point bending thest will be studied with different thickness face layers and differernt position through the test machine (Horizental and vertical) for compressive test.
2. New composite material will be formed with differernt weight of fiber by using filament maker machine.
3. The mechanical properties will be determined by tests (impact, hardness, tensile, compressive and three-point bending).
4. Analysing the results that have obtained during the experiments and illustrating the necessary drawings (Figures and curves), then the main points are discussed in detail.
5. Finishing the remainder of experiments and research activities.
6. Carrying on writing the PhD dissertation and publishing more papers as well as participating in more conferences.

References

[1] Ahn, D., Kweon, J.-H., Choi, J., and Lee, S. (2012) 'Quantification of Surface Roughness of Parts Processed by Laminated Object Manufacturing'. *Journal of Materials Processing Technology* [online] 212 (2), 339–346. available from <https://linkinghub.elsevier.com/retrieve/pii/S0924013611002391> [27 December 2021]

[2] Ahn, S.-H., Montero, M., Odell, D., Roundy, S., and Wright, P.K. (2002) 'Anisotropic Material Properties of Fused Deposition Modeling ABS'. *Rapid Prototyping Journal*

[3] Aliheidari, N., Tripuraneni, R., Ameli, A., and Nadimpalli, S. (2017) 'Fracture Resistance Measurement of Fused Deposition Modeling 3D Printed Polymers'. *Polymer Testing* [online] 60, 94–101. available from <https://linkinghub.elsevier.com/retrieve/pii/S0142941817300065> [5 December 2022]

[4] Alvarez, K., Lagos, R.F.C., and Aizpun, M. (2016) *Investigating the Influence of Infill Percentage on the Mechanical Properties of Fused Deposition Modelled ABS Parts. Ing e Investig 36: 110–116.*

[5] *ASTM International - Standards Worldwide* (n.d.) available from <https://www.astm.org/> [18 August 2022]

[6] Auffray, L., Gouge, P.-A., and Hattali, L. (2022) 'Design of Experiment Analysis on Tensile Properties of PLA Samples Produced by Fused Filament Fabrication'. *The International Journal of Advanced Manufacturing Technology* 1–15

[7] Bakarich, S.E., Gorkin, R., in het Panhuis, M., and Spinks, G.M. (2014) 'Three-Dimensional Printing Fiber Reinforced Hydrogel Composites'. *ACS Applied Materials & Interfaces* [online] 6 (18), 15998–16006. available from <https://pubs.acs.org/doi/10.1021/am503878d> [12 January 2022]

[8] Boparai, K.S. and Singh, R. (2018) *Thermoplastic Composites for Fused Deposition Modeling Filament: Challenges and Applications*.

[9] Buchanan, C. and Gardner, L. (2019) 'Metal 3D Printing in Construction: A Review of Methods, Research, Applications, Opportunities and Challenges'. *Engineering Structures* [online] 180, 332–348. available from <https://linkinghub.elsevier.com/retrieve/pii/S0141029618307958> [22 January 2022]

[10] Calabia, B., Ninomiya, F., Yagi, H., Oishi, A., Taguchi, K., Kunioka, M., and Funabashi, M. (2013) 'Biodegradable Poly(Butylene Succinate) Composites Reinforced by Cotton Fiber with Silane Coupling Agent'. *Polymers* [online] 5 (1), 128–141. available from <http://www.mdpi.com/2073-4360/5/1/128> [19 March 2022]

[11] Chandran, V., Kalman, J., Fayazbakhsh, K., and Bougherara, H. (2021) 'A Comparative Study of the Tensile Properties of Compression Molded and 3D Printed PLA Specimens in Dry and Water Saturated Conditions'. *Journal of Mechanical Science and Technology* 35, 1977–1985

[12] Chia, H.N. and Wu, B.M. (2015) 'Recent Advances in 3D Printing of Biomaterials'. *Journal of Biological Engineering* [online] 9 (1), 4. available from <http://www.jbioleng.org/content/9/1/4> [20 March 2022]

[13] Cho, B.-G., McCarthy, S.P., Fanucci, J.P., and Nolet, S.C. (1996) 'Fiber Reinforced Nylon-6 Composites Produced by the Reaction Injection Pultrusion Process'. *Polymer Composites* 17 (5), 673–681

[14] Chunze, Y., Yusheng, S., Jinsong, Y., and Jinhui, L. (2009) 'A Nanosilica/Nylon-12 Composite Powder for Selective Laser Sintering'. *Journal of Reinforced Plastics and Composites* [online] 28 (23), 2889–2902. available from <http://journals.sagepub.com/doi/10.1177/0731684408094062> [13 January 2022]

[15] de Ciurana, J., Serenóa, L., and Vallès, È. (2013) 'Selecting Process Parameters in RepRap Additive Manufacturing System for PLA Scaffolds Manufacture'. *Procedia CIRP* [online] 5, 152–157. available from <https://linkinghub.elsevier.com/retrieve/pii/S2212827113000322> [20 March 2022]

[16] Cooper, K. (2001) *Rapid Prototyping Technology* [online] 0 edn. CRC Press. available from <https://www.taylorfrancis.com/books/9780203910795> [27 December 2021]

[17] Croccolo, D., De Agostinis, M., and Olmi, G. (2013) 'Experimental Characterization and Analytical Modelling of the Mechanical Behaviour of Fused Deposition Processed Parts Made of ABS-M30'. *Computational Materials Science* 79, 506–518

[18] Cuiffo, M.A., Snyder, J., Elliott, A.M., Romero, N., Kannan, S., and Halada, G.P. (2017) 'Impact of the Fused Deposition (FDM) Printing Process on Polylactic Acid (PLA) Chemistry and Structure'. *Applied Sciences* [online] 7 (6), 579. available from <http://www.mdpi.com/2076-3417/7/6/579> [21 March 2022]

[19] D. Slavko and K. Matic, (2010) *Selective Laser Sintering of Composite Materials Technologies*. vol. 21. Annals of DAAAM & Proceedings

[20] Dai, L., Cheng, T., Duan, C., Zhao, W., Zhang, W., Zou, X., Aspler, J., and Ni, Y. (2019) '3D Printing Using Plant-Derived Cellulose and Its Derivatives: A Review'. *Carbohydrate Polymers* [online] 203, 71–86. available from <https://linkinghub.elsevier.com/retrieve/pii/S0144861718310919> [20 March 2022]

[21] Dey, A., Hoffman, D., and Yodo, N. (2020) 'Optimizing Multiple Process Parameters in Fused Deposition Modeling with Particle Swarm Optimization'. *International Journal on Interactive Design and Manufacturing (IJIDeM)* 14 (2), 393–405

[22] Domb, A.J., Kumar, N., and Ezra, A. (eds.) (2011) *Biodegradable Polymers in Clinical Use and Clinical Development: Domb/Biodegradable Polymers* [online] Hoboken, NJ, USA: John Wiley & Sons, Inc. available from <http://doi.wiley.com/10.1002/9781118015810> [19 March 2022]

[23] Dudek, P. (2013) 'FDM 3D Printing Technology in Manufacturing Composite Elements'. *Archives of Metallurgy and Materials* [online] 58 (4), 1415–1418. available from <http://journals.pan.pl/dlibra/publication/102133/edition/88150/content> [12 January 2022]

[24] Duran, C., Subbian, V., Giovanetti, M.T., Simkins, J.R., and Beyette Jr, F.R. (2015) 'Experimental Desktop 3D Printing Using Dual Extrusion and Water-Soluble Polyvinyl Alcohol'. *Rapid Prototyping Journal*

[25] Gunatillake, P., Mayadunne, R., and Adhikari, R. (2006) 'Recent Developments in Biodegradable Synthetic Polymers'. in *Biotechnology Annual Review* [online] vol. 12. Elsevier, 301–347. available from <https://linkinghub.elsevier.com/retrieve/pii/S1387265606120098> [21 March 2022]

[26] Gunatillake, P., Mayadunne, R., Adhikari, R., and El-Gewely, M.R. (2006) *Biotechnol Annu Rev*.

[27] Gunatillake, P.A., Adhikari, R., and Gadegaard, N. (2003) 'Biodegradable Synthetic Polymers for Tissue Engineering'. *Eur Cell Mater* 5 (1), 1–16

[28] Hacker, M. and Mikos, A. (2009) *Foundations of Regenerative Medicine: Clinical and Therapeutic Applications*. Academic press, London

[29] Hayashi, T. (1994) 'Biodegradable Polymers for Biomedical Uses'. *Progress in Polymer Science* 19 (4), 663–702

[30] Holland, S.J. and Tighe, B.J. (1992) 'Biodegradable Polymers'. *Advances in Pharmaceutical Science* 6, 101–164

[31] International, A. (2007) *Standard Test Method for Tensile Properties of Polymer Matrix Composite Materials*. ASTM international

[32] *ISO - ISO 527-1:2012 - Plastics — Determination of Tensile Properties — Part 1: General Principles* (n.d.) available from <https://www.iso.org/standard/56045.html> [18 August 2022]

[33] ISO, B. (2009) '527-5. Plastics-Determination of Tensile Properties-Part 5: Test Conditions for Unidirectional Fibre-Reinforced Plastic Composites'. *European Committee for Standardisation*

[34] ISO, E. (1997) '527-4. Plastics-Determination of Tensile Properties-Part 4: Test Conditions for Isotropic and Orthotropic Fibre-Reinforced Plastic Composites'. *International Organization for Standardization (ISO), Geneva, Switzerland*

[35] Jasminka, K. and Josipa, Š. (2018) '3D Print Additive Technology as a Form of Textile Material Substitutein Clothing Design – Interdisciplinary Approach in Designing Corsetsand Fashion Accessories'. *Industria Textila* [online] 69 (03), 190–196. available from <http://www.revistaindustriatextila.ro/images/2018/03/004_JASMINKA%20KONCIC_IndustriaTextila_03_2018.pdf> [22 January 2022]

[36] Javadzadeh, Y. and Hamedeyaz, S. (2014) 'Floating Drug Delivery Systems for Eradication of Helicobacter Pylori in Treatment of Peptic Ulcer Disease'. in *Trends in Helicobacter Pylori Infection* [online] ed. by Roesler, B. InTech. available from <http://www.intechopen.com/books/trends-in-helicobacter-pylori-infection/floating-drug-delivery-systems-for-eradication-of-helicobacter-pylori-in-treatment-of-peptic-ulcer-d> [20 March 2022]

[37] Jerez-Mesa, R., Travieso-Rodriguez, J.A., Llumà-Fuentes, J., Gomez-Gras, G., and Puig, D. (2017) 'Fatigue Lifespan Study of PLA Parts Obtained by Additive Manufacturing'. *Procedia Manufacturing* [online] 13, 872–879. available from <https://linkinghub.elsevier.com/retrieve/pii/S2351978917307837> [20 March 2022]

[38] Joshi, S.C. and Sheikh, A.A. (2015) '3D Printing in Aerospace and Its Long-Term Sustainability'. *Virtual and Physical Prototyping* [online] 10 (4), 175–185. available from <http://www.tandfonline.com/doi/full/10.1080/17452759.2015.1111519> [22 January 2022]

[39] Kafle, A., Luis, E., Silwal, R., Pan, H.M., Shrestha, P.L., and Bastola, A.K. (2021) '3D/4D Printing of Polymers: Fused Deposition Modelling (FDM), Selective Laser Sintering (SLS), and Stereolithography (SLA)'. *Polymers* [online] 13 (18), 3101. available from <https://www.mdpi.com/2073-4360/13/18/3101> [28 December 2022]

[40] Kauffman, G.B. (2010) *Book Review of Polymer Data Handbook*. ACS Publications

[41] Kay, R. (2014) *Effect of Raster Orientation on the Structural Properties of Components Fabricated by Fused Deposition Modeling*. The Ohio State University

[42] Kim, K., Park, J., Suh, J., Kim, M., Jeong, Y., and Park, I. (2017) '3D Printing of Multiaxial Force Sensors Using Carbon Nanotube (CNT)/Thermoplastic Polyurethane (TPU) Filaments'. *Sensors and Actuators A: Physical* 263, 493–500

[43] Klemm, D., Heublein, B., Fink, H.-P., and Bohn, A. (2005) 'Cellulose: Fascinating Biopolymer and Sustainable Raw Material'. *Angewandte Chemie International Edition* [online] 44 (22), 3358–3393. available from <https://onlinelibrary.wiley.com/doi/10.1002/anie.200460587> [20 March 2022]

[44] Korger, M., Bergschneider, J., Lutz, M., Mahltig, B., Finsterbusch, K., and Rabe, M. (2016) 'Possible Applications of 3D Printing Technology on Textile Substrates'. *IOP Conference Series: Materials Science and Engineering* [online] 141, 012011. available from <https://iopscience.iop.org/article/10.1088/1757-899X/141/1/012011> [22 January 2022]

[45] Kronenthal, R.L. (1975) 'Biodegradable Polymers in Medicine and Surgery'. in *Polymers in Medicine and Surgery*. Springer, 119–137

[46] Kruth, J.P. (1991) 'Material Incress Manufacturing by Rapid Prototyping Techniques'. *CIRP Annals* [online] 40 (2), 603–614. available from <https://linkinghub.elsevier.com/retrieve/pii/S0007850607611366> [27 December 2021]

[47] Kumar, R., Singh, R., and Farina, I. (2018) 'On the 3D Printing of Recycled ABS, PLA and HIPS Thermoplastics for Structural Applications'. *PSU Research Review*

[48] Kuo, C.-C., Liu, L.-C., Teng, W.-F., Chang, H.-Y., Chien, F.-M., Liao, S.-J., Kuo, W.-F., and Chen, C.-M. (2016) 'Preparation of Starch/Acrylonitrile-Butadiene-Styrene Copolymers (ABS) Biomass Alloys and Their Feasible Evaluation for 3D Printing Applications'. *Composites Part B: Engineering* 86, 36–39

[49] Lee, H., Lim, C.H.J., Low, M.J., Tham, N., Murukeshan, V.M., and Kim, Y.-J. (2017) 'Lasers in Additive Manufacturing: A Review'. *International Journal of Precision Engineering and Manufacturing-Green Technology* [online] 4 (3), 307–322. available from <http://link.springer.com/10.1007/s40684-017-0037-7> [11 January 2022]

[50] Lee, K. and Kaplan, D. (2006) *Tissue Engineering I: Scaffold Systems for Tissue Engineering*. vol. 102. Springer

[51] Levy, G.N., Schindel, R., and Kruth, J.P. (2003) 'RAPID MANUFACTURING AND RAPID TOOLING WITH LAYER MANUFACTURING (LM) TECHNOLOGIES, STATE OF THE ART AND

FUTURE PERSPECTIVES'. *CIRP Annals* [online] 52 (2), 589–609. available from
<https://linkinghub.elsevier.com/retrieve/pii/S0007850607602066>
[27 December 2021]

[52] Liu, Z., Wang, Y., Wu, B., Cui, C., Guo, Y., and Yan, C. (2019) 'A Critical Review of Fused Deposition Modeling 3D Printing Technology in Manufacturing Polylactic Acid Parts'. *The International Journal of Advanced Manufacturing Technology* [online] 102 (9–12), 2877–2889. available from <http://link.springer.com/10.1007/s00170-019-03332-x> [30 December 2021]

[53] Luten, J., van Nostrum, C.F., De Smedt, S.C., and Hennink, W.E. (2008) 'Biodegradable Polymers as Non-Viral Carriers for Plasmid DNA Delivery'. *Journal of Controlled Release* 126 (2), 97–110

[54] Mandala, R., Bannoth, A.P., Akella, S., Rangari, V.K., and Kodali, D. (2022) 'A Short Review on Fused Deposition Modeling 3D Printing of Bio-based Polymer Nanocomposites'. *Journal of Applied Polymer Science* [online] 139 (14), 51904. available from
<https://onlinelibrary.wiley.com/doi/10.1002/app.51904> [28 December 2022]

[55] Mazzanti, V., Malagutti, L., and Mollica, F. (2019) 'FDM 3D Printing of Polymers Containing Natural Fillers: A Review of Their Mechanical Properties'. *Polymers* 11 (7), 1094

[56] Mckeen, L. (2012) *Renewable Resource and Biodegradable Polymers*. vol. 10. Elsevier, Amsterdam, The Netherlands. DOI

[57] Melocchi, A., Parietti, F., Loreti, G., Maroni, A., Gazzaniga, A., and Zema, L. (2015) '3D Printing by Fused Deposition Modeling (FDM) of a Swellable/Erodible Capsular Device for Oral Pulsatile Release of Drugs'. *Journal of Drug Delivery Science and Technology* 30, 360–367

[58] Miller, A., Brown, C., and Warner, G. (2019) 'Guidance on the Use of Existing ASTM Polymer Testing Standards for ABS Parts Fabricated Using FFF'. *Smart and Sustainable Manufacturing Systems* [online] 3 (1), 20190051. available from
<http://www.astm.org/doiLink.cgi?SSMS20190051> [18 February 2023]

[59] Milosevic, M., Stoof, D., and Pickering, K. (2017) 'Characterizing the Mechanical Properties of Fused Deposition Modelling Natural Fiber Recycled Polypropylene Composites'. *Journal of Composites Science* [online] 1 (1), 7. available from <https://www.mdpi.com/2504-477X/1/1/7> [21 August 2022]

[60] Mohamed, O.A., Masood, S.H., Bhowmik, J.L., and Somers, A.E. (2017) 'Investigation on the Tribological Behavior and Wear Mechanism of Parts Processed by Fused Deposition Additive Manufacturing Process'. *Journal of Manufacturing Processes* 29, 149–159

[61] Montero, M., Roundy, S., Odell, D., Ahn, S.-H., and Wright, P.K. (2001) 'Material Characterization of Fused Deposition Modeling (FDM) ABS by Designed Experiments'. *Society of Manufacturing Engineers* 10 (13552540210441166), 1–21

[62] Mostafa, N., Syed, H.M., Igor, S., and Andrew, G. (2009) 'A Study of Melt Flow Analysis of an ABS-Iron Composite in Fused Deposition Modelling Process'. *Tsinghua Science & Technology* 14, 29–37

[63] Moura, L.S., Vittoria, G.D., Gabriel, A.H., Fonseca, E.B., Gabriel, L.P., Webster, T.J., and Lopes, É.S. (2020) 'A Highly Accurate Methodology for the Prediction and Correlation of Mechanical Properties Based on the Slimness Ratio of Additively Manufactured Tensile Test Specimens'. *Journal of Materials Science* 55 (22), 9578–9596

[64] Murawski, A., Diaz, R., Inglesby, S., Delabar, K., and Quirino, R.L. (2019) 'Synthesis of Bio-Based Polymer Composites: Fabrication, Fillers, Properties, and Challenges'. in *Polymer Nanocomposites in Biomedical Engineering* [online] ed. by Sadasivuni, K.K., Ponnamma, D., Rajan, M., Ahmed, B., and Al-Maadeed, M.A.S.A. Lecture Notes in Bioengineering. Cham: Springer International Publishing, 29–55. available from <http://link.springer.com/10.1007/978-3-030-04741-2_2> [20 December 2022]

[65] Murr, L.E. (2016) 'Frontiers of 3D Printing/Additive Manufacturing: From Human Organs to Aircraft Fabrication†'. *Journal of Materials Science & Technology* [online] 32 (10), 987–995. available from <https://linkinghub.elsevier.com/retrieve/pii/S1005030216301335> [22 January 2022]

[66] Nath, S.D. and Nilufar, S. (2020) 'An Overview of Additive Manufacturing of Polymers and Associated Composites'. *Polymers* [online] 12 (11), 2719. available from <https://www.mdpi.com/2073-4360/12/11/2719> [28 December 2022]

[67] Negrin, M., Macerata, E., Consolati, G., Quasso, F., Genovese, L., Soccio, M., Giola, M., Lotti, N., Munari, A., and Mariani, M. (2018) 'Gamma Radiation Effects on Random Copolymers Based on Poly(Butylene Succinate) for Packaging Applications'. *Radiation Physics and Chemistry* [online] 142, 34–43. available from <https://linkinghub.elsevier.com/retrieve/pii/S0969806X16305850> [19 March 2022]

[68] Ngo, T.D., Kashani, A., Imbalzano, G., Nguyen, K.T.Q., and Hui, D. (2018) 'Additive Manufacturing (3D Printing): A Review of Materials, Methods, Applications and Challenges'. *Composites Part B: Engineering* [online] 143, 172–196. available from <https://linkinghub.elsevier.com/retrieve/pii/S1359836817342944> [30 December 2021]

[69] Ni, F., Wang, G., and Zhao, H. (2017) 'Fabrication of Water-Soluble Poly(Vinyl Alcohol)-Based Composites with Improved Thermal Behavior for Potential Three-Dimensional Printing Application: ARTICLE'. *Journal of Applied Polymer Science* [online] 134 (24). available from <https://onlinelibrary.wiley.com/doi/10.1002/app.44966> [21 March 2022]

[70] Onwubolu, G.C. and Rayegani, F. (2014) 'Characterization and Optimization of Mechanical Properties of ABS Parts Manufactured by the Fused Deposition Modelling Process'. *International Journal of Manufacturing Engineering* 2014

[71] Özen, A., Auhl, D., Völlmecke, C., Kiendl, J., and Abali, B.E. (2021) 'Optimization of Manufacturing Parameters and Tensile Specimen Geometry for Fused Deposition Modeling (FDM) 3D-Printed PETG'. *Materials* 14 (10), 2556

[72] Pakkanen, J., Manfredi, D., Minetola, P., and Iuliano, L. (2017) 'About the Use of Recycled or Biodegradable Filaments for Sustainability of 3D Printing'. in *International Conference on Sustainable Design and Manufacturing*. held 2017. Springer, 776–785

[73] Pietrzak, K., Isreb, A., and Alhnan, M.A. (2015) 'A Flexible-Dose Dispenser for Immediate and Extended Release 3D Printed Tablets'. *European Journal of Pharmaceutics and Biopharmaceutics* [online] 96, 380–387. available from <https://linkinghub.elsevier.com/retrieve/pii/S0939641115003306> [20 March 2022]

[74] Rankouhi, B., Javadpour, S., Delfanian, F., and Letcher, T. (2016) 'Failure Analysis and Mechanical Characterization of 3D Printed ABS with Respect to Layer Thickness and Orientation'. *Journal of Failure Analysis and Prevention* 16, 467–481

[75] Revilla-León, M. and Özcan, M. (2019) 'Additive Manufacturing Technologies Used for Processing Polymers: Current Status and Potential Application in Prosthetic Dentistry: Polymer Additive Manufacturing for Prosthodontics'. *Journal of Prosthodontics* [online] 28 (2), 146–158. available from <https://onlinelibrary.wiley.com/doi/10.1111/jopr.12801> [22 January 2022]

[76] Rodríguez-Panes, A., Claver, J., and Camacho, A.M. (2018) 'The Influence of Manufacturing Parameters on the Mechanical Behaviour of PLA and ABS Pieces Manufactured by FDM: A Comparative Analysis'. *Materials* 11 (8), 1333

[77] Rutkowski, J.V. and Levin, B.C. (1986) 'Acrylonitrile–Butadiene–Styrene Copolymers (ABS): Pyrolysis and Combustion Products and Their Toxicity—a Review of the Literature'. *Fire and Materials* 10 (3-4), 93–105

[78] Serra, T., Planell, J.A., and Navarro, M. (2013) 'High-Resolution PLA-Based Composite Scaffolds via 3-D Printing Technology'. *Acta Biomaterialia* 9 (3), 5521–5530

[79] Shim, J.-H., Lee, J.-S., Kim, J.Y., and Cho, D.-W. (2012) 'Bioprinting of a Mechanically Enhanced Three-Dimensional Dual Cell-Laden Construct for Osteochondral Tissue Engineering Using a Multi-Head Tissue/Organ Building System'. *Journal of Micromechanics and Microengineering* 22 (8), 085014

[80] Singh, A.K., Saltonstall, B., Patil, B., Hoffmann, N., Doddamani, M., and Gupta, N. (2018) 'Additive Manufacturing of Syntactic Foams: Part 2: Specimen Printing and Mechanical Property Characterization'. *JOM* [online] 70 (3), 310–314. available from <http://link.springer.com/10.1007/s11837-017-2731-x> [21 March 2022]

[81] Somireddy, M. and Czekanski, A. (2017) 'Mechanical Characterization of Additively Manufactured Parts by FE Modeling of Mesostructure'. *Journal of Manufacturing and Materials Processing* 1 (2), 18

[82] Sun, Q., Rizvi, G.M., Bellehumeur, C.T., and Gu, P. (2008) 'Effect of Processing Conditions on the Bonding Quality of FDM Polymer Filaments'. *Rapid Prototyping Journal* [online] 14 (2), 72–80. available from <https://www.emerald.com/insight/content/doi/10.1108/13552540810862028/full/html> [21 March 2022]

[83] Technologies, A.C.F. on A.M. and Terminology, A.C.F. on A.M.T.S.F. 91 on (2012) *Standard Terminology for Additive Manufacturing Technologies.* Astm International

[84] Terekhina, S., Skornyakov, I., Tarasova, T., and Egorov, S. (2019) 'Effects of the Infill Density on the Mechanical Properties of Nylon Specimens Made by Filament Fused Fabrication'. *Technologies* 7 (3), 57

[85] Tymrak, B.M., Kreiger, M., and Pearce, J.M. (2014a) 'Mechanical Properties of Components Fabricated with Open-Source 3-D Printers under Realistic Environmental Conditions'. *Materials & Design* [online] 58, 242–246. available from
<https://linkinghub.elsevier.com/retrieve/pii/S0261306914001538>
[30 January 2022]

[86] Tymrak, B.M., Kreiger, M., and Pearce, J.M. (2014b) 'Mechanical Properties of Components Fabricated with Open-Source 3-D Printers under Realistic Environmental Conditions'. *Materials & Design* [online] 58, 242–246. available from
<https://linkinghub.elsevier.com/retrieve/pii/S0261306914001538>
[20 August 2022]

[87] Wang, J., Goyanes, A., Gaisford, S., and Basit, A.W. (2016) 'Stereolithographic (SLA) 3D Printing of Oral Modified-Release Dosage Forms'. *International Journal of Pharmaceutics* [online] 503 (1–2), 207–212. available from
<https://linkinghub.elsevier.com/retrieve/pii/S0378517316302150>
[29 December 2021]

[88] Wang, Q., Ji, C., Sun, L., Sun, J., and Liu, J. (2020) 'Cellulose Nanofibrils Filled Poly(Lactic Acid) Biocomposite Filament for FDM 3D Printing'. *Molecules* [online] 25 (10), 2319. available from
<https://www.mdpi.com/1420-3049/25/10/2319> [21 March 2022]

[89] Wohlers, T. and Gornet, T. (2014) 'History of Additive Manufacturing'. *Wohlers Report* 24 (2014), 118

[90] Xiao, J. and Gao, Y. (2017) 'The Manufacture of 3D Printing of Medical Grade TPU'. *Progress in Additive Manufacturing* [online] 2 (3), 117–123. available from <http://link.springer.com/10.1007/s40964-017-0023-1> [21 March 2022]

[91] Zhang, P., Wang, Z., Li, J., Li, X., and Cheng, L. (2020) 'From Materials to Devices Using Fused Deposition Modeling: A State-of-Art Review'. *Nanotechnology Reviews* [online] 9 (1), 1594–1609. available from <https://www.degruyter.com/document/doi/10.1515/ntrev-2020-0101/html> [20 December 2022]

Reactions on the typical temperatures of the diesel aftertreatment system

Dániel SZŐLLŐSI[1,2], Péter KISS[3]

[1]Exhaust System Evaluation, IBIDEN Hungary Technical Center,
IBIDEN Hungary Kft., Dunavarsány
[2]Mechanical Engineering Doctoral School (MTDI), Szent István Campus, Gödöllő, MATE
[3]Institute of Technology, Hungarian University of Agriculture and Life Sciences, MATE, Gödöllő

Abstract

The temperature of the exhaust gas has a direct impact on the reactions that occur in the emission after-treatment system, which is part of the vehicle's exhaust system. There are reactions that only occur considerably above or below a particular temperature, and some beneficial chemical reactions only occur in a specific temperature range. Certain reactions take place more rapidly at lower temperatures when catalysts are present. Examples of this in the exhaust gas aftertreatment system include artificially bringing precious metals into touch with exhaust gas (3-way catalyst, diesel oxidation catalyst - DOC), or even other components of exhaust gas can catalyze the desired reactions.

The temperature of the exhaust gas at each individual measurement point is crucial since it enables to quantify and characterize the reactions going to take place and the results can be understood more easily. Accordingly, additional literature research conducted in this area and described the processes occurring at specific temperatures for the three exhaust system elements (DOC, diesel particulate filter - DPF, selective catalytic reducer - SCR). The typical temperatures of diesel exhaust checked in the range of ~150-700 °C. To list the outcomes of this research, a summary table created.

Keywords

Exhaust gas, temperature, reaction, DOC, DPF, SCR

1. Introduction

Diesel engine emission and their reduction tendencies
As a result of the diesel engine combustion a lot of harmful and less harmful materials emitted. Now, only those components that are significant from a legislative standpoint and, more specifically, from the perspective of NO_x and particulate removal, are considered.
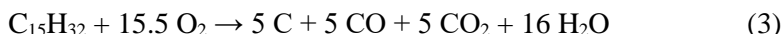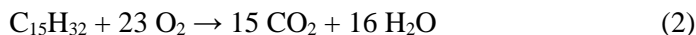
The cause of hydrocarbon (HC) emissions is unburned fuel. It develops in the combustion chamber's lower-temperature areas as a result of inadequately high

temperatures. In addition to the original components, their breakdown products, and oxygen-containing derivatives (volatile organic compounds, or VOCs, such as alcohols, aldehydes, and ketones), they may contain partially or entirely non-oxidized hydrocarbons (alkanes, alkenes, hydrocarbons containing carbon double triple bonds, aromatic polycyclic carcinogenic mutagenic substances, etc.).

The reaction for complete combustion can be written like following:

$$C_xH_y + (x+y/4)\ O_2 \rightarrow x\ CO_2 + (y/2)\ H_2O \tag{1}$$
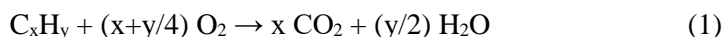
Diesel oil does not burn entirely under conditions where there is not enough air or oxygen present, which results in incomplete combustion. During this process, hydrogen and carbon oxidized to generate water and carbon monoxide, respectively. Hence, carbon monoxide, carbon, and water are the products of incomplete combustion. Below we can see as an example the complete and incomplete combustion of pentadecane as tipical diesel fuel component:

$$C_{15}H_{32} + 23\ O_2 \rightarrow 15\ CO_2 + 16\ H_2O \tag{2}$$

$$C_{15}H_{32} + 15.5\ O_2 \rightarrow 5\ C + 5\ CO + 5\ CO_2 + 16\ H_2O \tag{3}$$

Because diesel engines have a significant air surplus, the creation of CO (carbon monoxide), is limited. At the high combustion temperature of around 2,000 degrees Celsius, the combustion mainly leads to the formation of CO, not CO_2. In this case, the balance has been tipped in favor of CO formation (1-4). It only shifts in the direction of CO_2 generation during the expansion phase and when it cools down during going through the exhaust (Kalló 2000).

$$CO + \tfrac{1}{2}\ O_2 \leftrightarrow CO_2 \tag{4}$$

Particulate matter (PM) from diesel engines is also significant since it results from improper combustion. They are created by the aggregation of different particles along the exhaust system. It contains carbon, partially burnt fuel, partially burnt lubricating oil, ash from fuel and lubricating oil, water, metal particles (Agarval 2007)(figure 1.).

The particles are highly complex since they including a variety of elements. The aforementioned components are often adsorbed onto a central carbon core to form agglomerates that are typically 15 to 40 nm in size, with 90% of them being smaller than 1 μm (Burtscher 2005). Nucleation is the first step in the production of particulates, and the nucleation particles are then agglomerated. By homogeneous and heterogeneous nucleation mechanisms, the nucleation takes place in the engine cylinder (carbon, ash) and the exhaust system (hydrocarbons, sulfuric acid, water). Most writers categorize ambient particulate matter into the following groups based on its aerodynamic diameter, which is determined by measuring the diameter of a sphere with a density of 1 g/cm^3 and an air velocity equal to that of the observed particle:
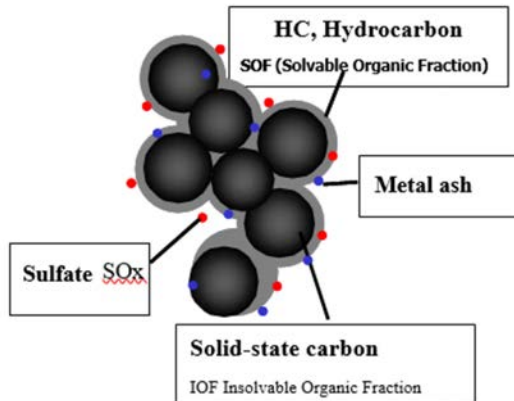
Figure 1. Structure of the Soot particles

- Coarse particles or PM_{10}—particulates of an aerodynamic diameter ≤ 10 µm
- Fine particles or $PM_{2.5}$—particles with a diameter ≤ 2.5 µm
- Ultrafine particles of diameters below 0.1 µm or 100 nm
- Nanoparticles, characterized by diameters of less than 50 nm (Dieselnet 2002).
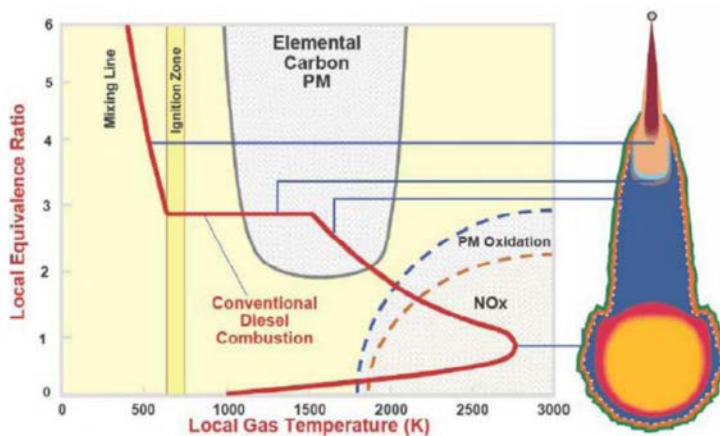

Figure 2. Structure of the Soot particles (Charlton 2007)

In a typical combustion, airborne nitrogen does not interact with oxygen. Yet, with a starting temperature of 1600 °C, nitrogen already combines with oxygen to produce NO_x emissions due to the inhomogeneous combustion characteristic of diesel engines. The NO and NO_2 are the two primary elements of NO_x emissions.

The in-cylinder zones shown in Figure 2. are determined by local temperature and equivalency ratios, which are calculated by dividing the actual fuel-to-air ratio by the stoichiometric fuel-to-air ratio. The conventional diesel combustion occupy operational points in areas where nitric oxide (NO) and heavy soot are also produced.

There are three primary methods by which NO is produced during diesel combustion. In the quick (or Fenimore) mechanism NO rapidly produced in the flame zone of the laminar premixed flames before the thermal mechanism can take place (Fenimore 1972):

$$CH + N_2 \leftrightarrow HCN + N \tag{5}$$

$$C + N_2 \leftrightarrow CN + N \tag{6}$$

$$HCN + O \leftrightarrow NCO + H \tag{7}$$

$$NCO + H \leftrightarrow NH + CO \tag{8}$$

$$NH + H \leftrightarrow N + H_2 \tag{9}$$

$$N + OH \leftrightarrow NO + H \tag{10}$$

In case of the nitrous oxide mechanism, oxygen radicals (O) and volatile nitrogen species like hydrogen cyanide or nitrous oxide oxidized during combustion nitrogen interacts to create intermediaries like N_2O and is oxidized into NO. Low temperature and lean fuel (0.8) are the conditions that this mechanism operates in. The main steps in this mechanism (Turns 2000):

$$O + N_2 \rightarrow N_2O \tag{11}$$

$$H + N_2O \rightarrow NO + NH \tag{12}$$

$$O + N_2O \rightarrow NO + NO \tag{13}$$

The thermal (or Zeldovich) mechanism is the third and most significant mechanism. Take place significantly above 1300 °C. It originally consists of the two reactions Zeldovich outlined, but eventually adds a third process (Rente 2004):

$$N + O_2 \leftrightarrow NO + O \tag{14}$$

$$O + N_2 \leftrightarrow NO + N \tag{15}$$

$$N + OH \leftrightarrow NO + H \tag{16}$$

Under typical air circumstances, NO, which predominates in NO_x inside the combustion chamber, slowly oxidizes to NO_2.

Emission aftertreatment

Nowadays, there are several well-functioning exhaust gas treatment technologies for diesel engines. The most significant ones are the following:

PM reduction technologies:

- – - diesel oxidation catalyst (DOC),
- – - diesel particulate filter (DPF),
- – - closed crankcase ventilation (CCV).

NO_x emission control technologies:

- – - exhaust gas recirculation (EGR),
- – - selective catalytic reduction (SCR),
- – - NO_x catalyst (LNC),
- – - NO_x trap (LNT).

Currently, the DPF (Diesel Particulate Filter) is the safest technology in terms of particle emissions (PN - Particle Number). From NO_x emission point of view the most widely used technology is Selective Catalytic Reduction (SCR). In order to meet current and future emission standards, diesel engines need to use additional NO_x and PN reduction options (Pischinger 2008).

Oxidation catalysts continue to be crucial in diesel engines as well, just as they were in early gasoline engines for the oxidation of hydrocarbons and CO. They have demonstrated their efficiency in lowering particle emissions as well, which can reach up to 20-50% (total particle weight), despite being initially created to reduce gas emissions (MECA 2007).

Diesel particulate filters also a tested technique. They are honeycomb-shaped, and the opposing side of each cell is always closed. Therefore, filtering occurs through the cell wall's pores. The two most often used raw materials for the ceramic body of the particle filter are silicon carbide (SiC) and cordierite ($2MgO-2Al_2O_3-5SiO_2$). Modern Cordierite or SiC particle filters can remove 99.9% of engine particulate emissions.

NO_x has evolved into the main target of efforts to reduce emissions due to its smog and ozone-forming characteristics. This was lessened by using exhaust gas recirculation (EGR), which can reduce the nitrogen oxide level of the exhaust gas by as much as 50%. (Szőllősi 2022).

With the addition of urea, selective catalytic reduction (SCR) may eliminate nitrogen oxides even more effectively. A considerable 80% reduction in hydrocarbon emissions can be attained through this procedure, in addition to NO_x removal (up to 75–90% efficiency) (Bíró 2020), and solid particle emissions can also be decreased by an additional 20–30%. (MECA 2007, Kalló 2000).

2. Experimental

Operation conditions of the diesel engine
The exhaust temperature can vary with load, engine, exhaust components used, exhaust layout, lengths, volumes of aftertreatment parts. Because of this we should check temperature ranges along the whole exhaust system. Our test setup containing a DOC a DPF and a SCR system. We would like to check the temperatures at a normal emission cycle like NEDC, and also we should consider the temperature range during soot regeneration. Temperature also checked even in severe condition when uncontrolled burning of the accumulated soot happening (Drop to idle test - DTI).

With that we can confirm the temperatures for our specific test layout on each exhaust component. With understanding our layout temperatures we can estimate the chemical reactions take place along the exhaust system.

Emission cycles
Emission cycles were made to represent regular car use and to simulate it for test bench usage. As a result of the tightening emission regulations, more and more official test cycles are being established. The emission cycle varies depending on whether HD or PC vehicles are involved, as well as where in the world it is in use. There is also a difference for on road and off road applications. These cycles include information on engine conditions like load, engine speed, etc. to ensure repeatability and comparability. In our tests we using simple NEDC cycle what is created for European passenger car legislations. It contains urban and extra urban parts also.
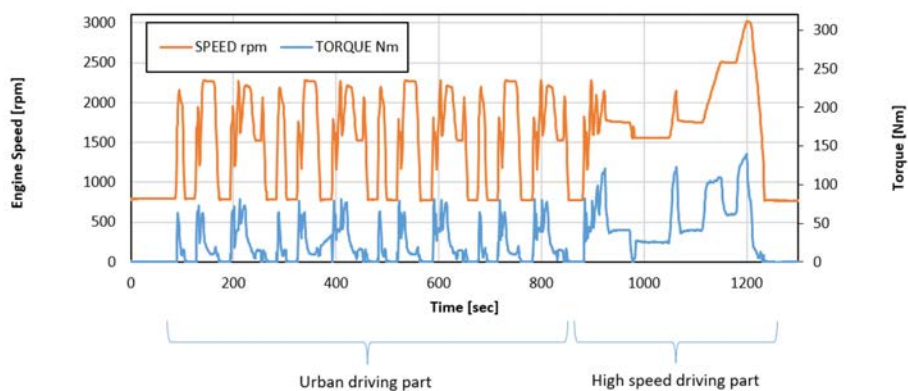

Figure 3. Diesel passenger car engine out temperatures

Regeneration
During the engine operation, soot continuously accumulate in the particulate filter. When the DPF collect the PM, the pressure loss increases due to the

resistance generated when the exhaust gas passes through the PM layer. It negatively affect back to the engine and causing performance loss and fuel consumption increase also. Because of it, we need to remove it by oxidizing the soot built up in the filter. This procedure called regeneration. For the complete regeneration at least above 550 °C temperature necessary (Konstandopoulos 2000).
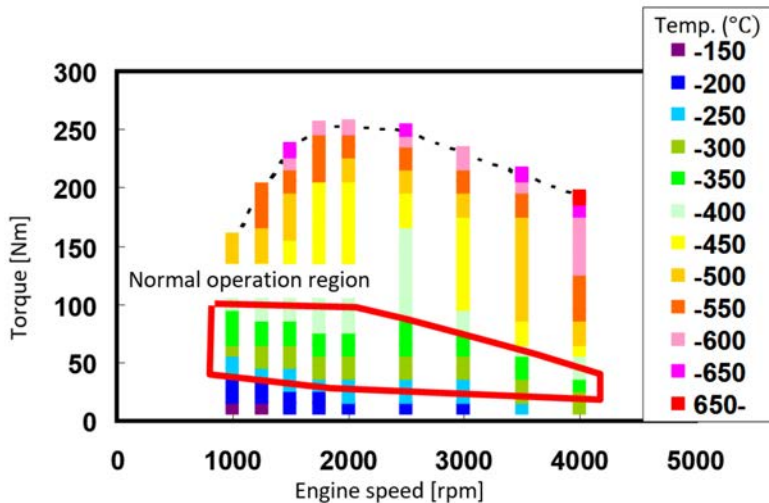

Figure 4. Diesel passenger car engine out temperatures

The exhaust gas temperature for each, engine operating range is shown in Figure 4. While a DPF-equipped vehicle is driven, there is a significant difference between the PM regeneration temperature and real exhaust gas temperature.

The main regeneration strategies to reach this temperature, is the passive and active regeneration. A passive method regenerates the PM constantly at a lower temperature by lowering the activation energy of the oxidation and combustion of the PM with a catalyst. To catalyze the oxidation two general approach exist. One of the system use fuel additives like CeO_2, FeO, or other excellent OSC (oxygen storage capacity) compounds are used as constituent metallic elements in organic complexes (Ce and Fe).

Catalyst support filter is a method to directly support the catalyst on the DPF. Systems with the device have an even simpler configuration than the fuel-originated catalyst, as no addition device required. The regeneration of the PM utilizes the heat from the oxidation and combustion of hydrocarbon (HC) and carbon monoxide (CO) (the gaseous contents in the exhaust gas) or SOF (unburned fuel in the PM) with noble metals such as Pt (Bisett 1985)(Koltsakis 1996).

It is exceedingly challenging to provide enough energy to reach the combustion temperature needed for PM (600 °C or greater), and the techniques used to do so complicate and enlarge the system. While continuous regeneration by catalytic action is desirable, it can only be accomplished under specific operating circumstances since the regeneration temperature is higher than the typical temperature of diesel exhaust gases.

In our measurement layout we will use catalyst support filter along with active regeneration. In the active system, the energy required for the regeneration of the soot reached from the engine's intra-cylindrical temperature, what is exceeds 2200 °C. We can efficiently employ this amount of heat by using a "post-injection" regeneration technique with a multi-stage injection into the engine's combustion cylinder. After achieving the necessary torque to operate a vehicle, through main injection, for milliseconds, extra gasoline "post-injected" into the cylinder.

With this two technique, the necessary oxidation temperature can be reached.

Severe regeneration

This method for determining regeneration limits simulates the worst possible regeneration that could occur to a vehicle. O_2 concentration is low and exhaust temperature rises while a car is moving uphill at high speed and in low gear. The outcome is the ignition of the soot inside the particle filter. After reaching the summit, the car begins to descend with engine brake (figure 5.). Fresh air with a sudden rise in O_2 concentration was delivered to the filter, and it cause rapid excess burning. The burning will be more intense the more soot there is. (Ohno 2008)
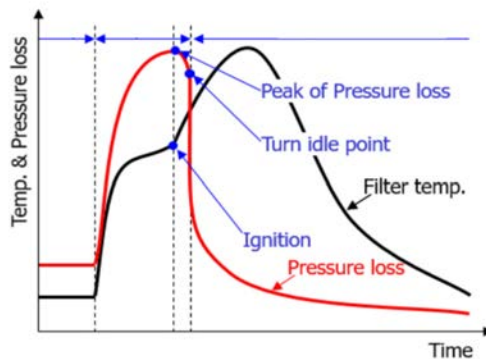

Figure 5. Schematics of uncontrolled regeneration

It should also be taken into account as the most worst-case situation with regard to temperature.

Test equipment

For our tests we used a 2.0L, inline, 4-cylinder Turbocharged DW10 engine with EURO 5 emission specification. It has a direct injection fuel system, a DOHC 16 valve aluminium alloy cylinder head with 103 kW peak power and 340 Nm torque. It has an an original EGR system.

The engine installed in a AVL test rig with controlled conditioner systems for engine oil, coolant, combustion air, charged air and fuel. It is a certified motorcycle brake bench that includes the latest emission (NEDC, WLTC, WHTC, WHSC) cycles and is also capable of simulating rolling resistance.
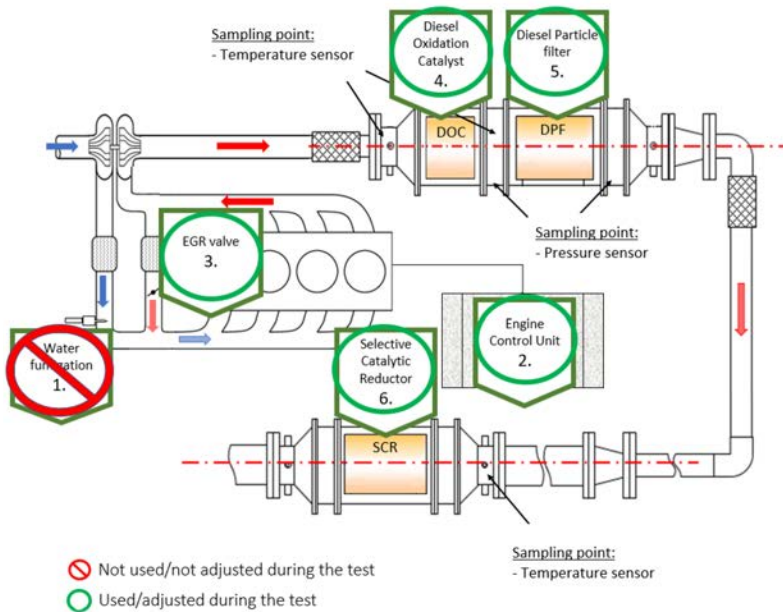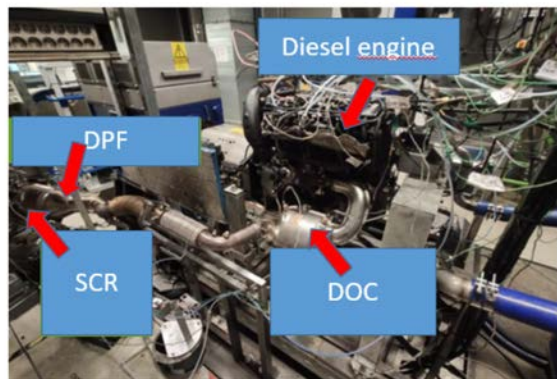

Figure 6. Test cell outline

Figure 7. Test cell layout

The emission aftertreatment system consist of a diesel oxidation catalyst, a catalyzed particulate filter and an SCR system. For the temperature measurements we are using 3.5mm K-type thermocouples in the exhaust system and also a pressure measuring device with analog digital signal converter.

Test method

In the three conditions already mentioned, we want to take the temperature before the DOC, DPF, and SCR. During these measurements, we follow a set test protocol and maintain constant values for the following variables: water, oil, combustion air, fuel, cell temperature, and humidity. The exhaust temperatures at these three positions will be our output parameter in these tests. These results serves as the starting point for our reaction model.

During the emission measurement, first we should make sure that the filter not containing any remained soot therefore we started with a soot burning in a furnace at 650 °C, and then we measured the filter weight at 150 °C to avoid any water vapor effect. We leave the system to cool down, till oil temperature reached room temperature (Toil≤25 °C). Then we ran a NEDC cycle with cold start. The cycle 10.9 km and 19.7 minute. At the end we measured the weight also. With the weight measurements we can identify any abnormal engine operation, accumulated weight during all the 3 repetition should be within ±1 gram. We repeated this procedure 3 times.

For soot regeneration, we went through the following procedure. We burned out the filter at 650 °C and then we measured weight. We continued with soot loading and filled 25g into the particulate filter. For this test, we used pressure sensors before and after the particle filter to be able to monitor the pressure changes related to soot accumulation and burning. With post injection we increased the temperature to ~ 600 °C and we continue to inject till the pressure drop on the filter became stable, as all the soot is burned out from the ceramic monolith. Then we started from the beginning and perform it two more times. For soot regeneration we used fixed heavy load along the whole cycle.

To simulate the severe condition of an uncontrolled regeneration, first we also burned out the filter at 650 °C and then we measured weight. We loaded 40g soot into the filter and we ran the procedure showed in figure 4. We ran the filter on heavy load and when we saw that the pressure loss on the filter started to decrease (soot ignited and started to consume), we dropped the engine to idling causing uncontrolled burning in the filter. We also repeated this test 3 times.

3. Results and discussion

Layout temperature results

During the cold start NEDC test, we can see the exhaust temperatures increasing from room temperature. During the urban cycle part, the temperature along the exhaust system, not even reach 200 °C. At the high-speed part of the cycle it is increasing to a maximum 291 °C temperature before the DOC. Before the DPF,

the mean temperature increasing minimal, but during the high-speed part we can see same maximum DPF in temperature (291 °C) as a result of DOC light off temperature reached and start the optimal operation. Before the SCR, we can see also increasing temperatures, at the end of the cycle we can reach 259 °C.
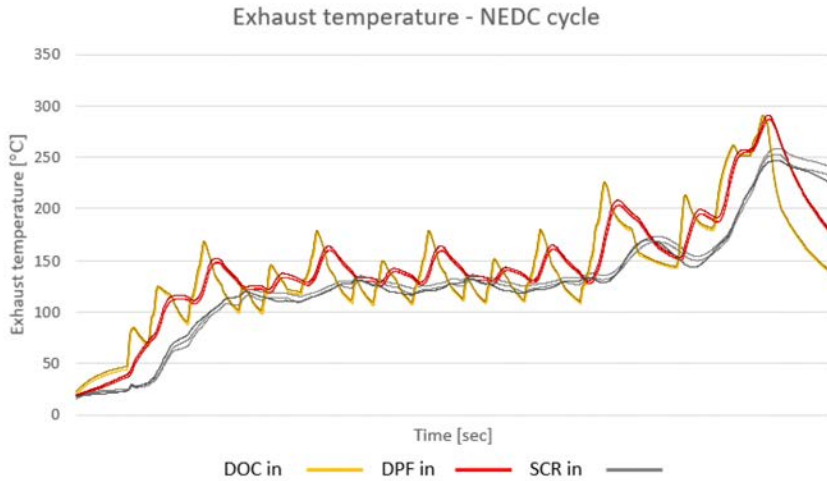

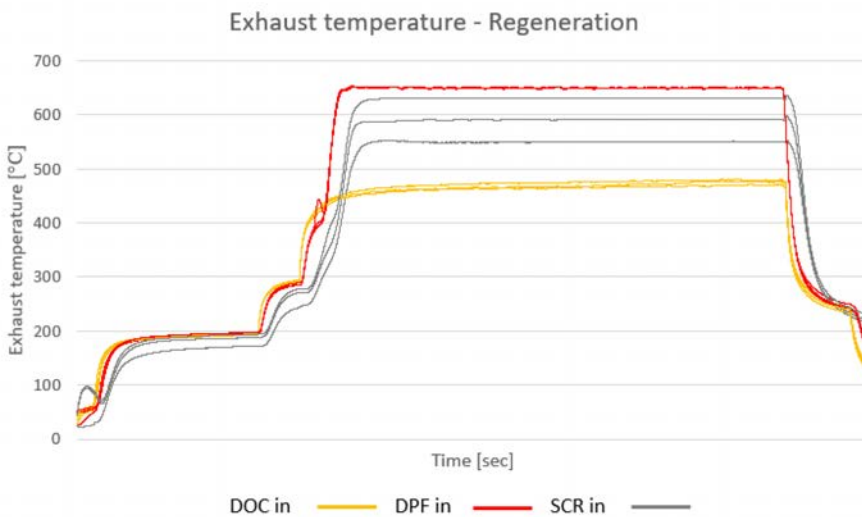*Figure 8.* Exhaust temperature during NEDC cycle

Figure 9. Exhaust temperature during particle filter regeneration procedure

During the soot regeneration, with post injection we increased the engine out temperature (max. 481 °C DOC in temperature), and on the DOC the unburned

hydrocarbon increased further the temperature to above 600 °C temperature at the inlet of the DPF (with a maximum 653 °C). As a result, complete burning out of the filter will takes place increasing the SCR temperature well above 500 °C also (max. 637 °C).

During the uncontrolled regeneration, the DOC inlet temperature increased till the maximum 459 °C when we go to idle. DOC increasing the temperature further till 579 °C maximum till the dropping to idling. After that fresh cold arrive to the exhaust decreasing the temperature both before DOC and DPF. But because of the oxygen rich air we can rapid temperature increasing before the SCR as a result of the excess uncontrolled burning. The maximum temperature before the SCR is 684 °C.
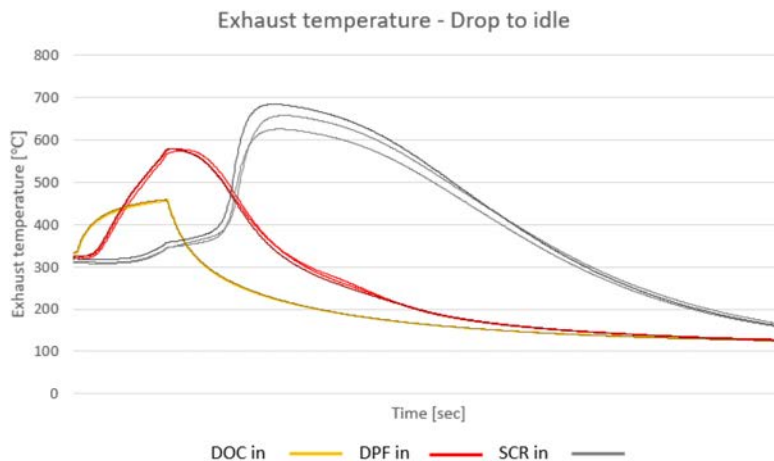

Figure 10. Exhaust temperature during uncontrolled regeneration

Excluding abnormal engine operation (because of possible engine failures) we can see exhaust temperatures from around 150 °C to about 700 °C on operation temperature engine. If we would like to break it down to the 3 examined exhaust part, we can see the following:
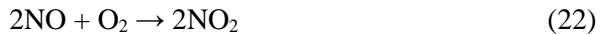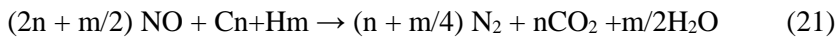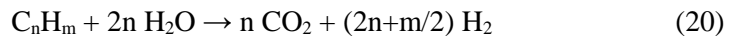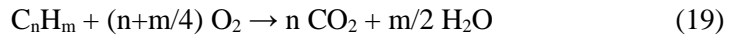- for DOC inlet from ~ 150 °C to 481 °C
- for DPF inlet from ~ 150 °C to 653 °C
- for SCR inlet from ~ 150 °C to 684 °C

Even though we are moving away from the engine, the maximum temperature figures are rising due to the catalyst effect.

Reaction model
As a result of our measurement, reactions collected in the temperature range 150-700 °C. It promotes the oxidation of several exhaust gas constituents by

oxygen, which is abundant in diesel exhaust gas. The DOC cannot reduce NO_x because of the presence of oxygen. On the catalyst, the following main reactions takes place (Kalló 2000):

$$CO + \tfrac{1}{2} O_2 \rightarrow CO_2 \tag{17}$$

$$CO + H_2O \rightarrow CO_2 + H_2 \tag{18}$$

$$C_nH_m + (n+m/4) O_2 \rightarrow n\, CO_2 + m/2\, H_2O \tag{19}$$

$$C_nH_m + 2n\, H_2O \rightarrow n\, CO_2 + (2n+m/2)\, H_2 \tag{20}$$

$$(2n + m/2)\, NO + C_nH_m \rightarrow (n + m/4)\, N_2 + nCO_2 + m/2H_2O \tag{21}$$

$$2NO + O_2 \rightarrow 2NO_2 \tag{22}$$

The catalyst's light-off temperature is when the given reaction reaction passes 50% conversion. For the above reactions in the DOC it is around 250 °C.
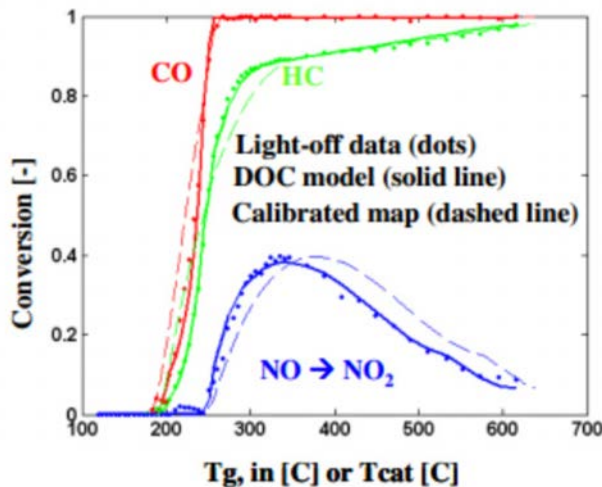
Figure 11. Conversion curves in the DOC (Katare 2014)

The oxidation of NO to NO_2 is essential for the operation of modern diesel emission reduction systems. Nitrogen dioxide is needed to increase the performance of various types of SCR catalysts and to promote the passive regeneration of diesel particulate filters (DPFs). DOCs used in DPF/SCR applications are generally optimized for high NO_2 production.

As previously discussed, the regeneration of the DPF is significant above 550°C as follows;

$$Soot + O_2 \rightarrow CO_2 + H_2O \tag{23}$$

If a catalytic layer on the filter's inlet side applied, it triggers the oxidation of soot particles at a temperature of 250–300 °C. With NO_2, the oxidation can happen on even lower temperature (200-500 C°)(Strzelec 2016). You can see the detailed test steps below with intermediate products (Mataresse 2017):

$$(C\text{-}C + NO_2 \rightarrow C\text{-}C(NO_2) \rightarrow C\text{-}C(O) + NO \tag{24}$$

$$(C\text{-}C(O) \rightarrow NO_2 \rightarrow C\text{-}C(NO_3) \rightarrow C(O)C(O) + NO \tag{25}$$

$$(C(O)C(O) + NO_2 \rightarrow CO_2 + CO + NO \tag{26}$$

$$(C\text{-}C(O) + 1/2 O_2 \rightarrow C(O)C(O) \tag{27}$$

$$(C(O)C(O) + 1/2O_2 \rightarrow CO_2 + CO \tag{28}$$

$$NO_2 + C \rightarrow NO + CO \tag{29}$$

$$2NO_2 + C \rightarrow 2NO + CO_2 \tag{30}$$
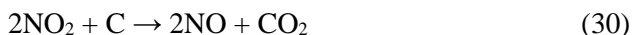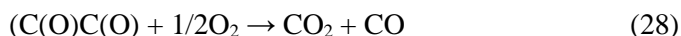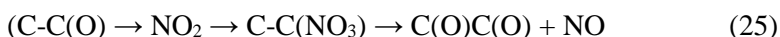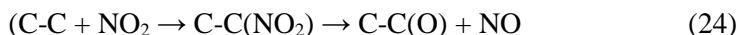
Two fundamentally different catalytic ways of reducing NO_x emissions are possible depending on the stoichiometric composition of the gas mixture entering the catalyst bed.
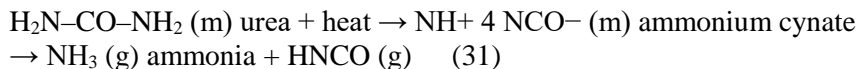
If there are equivalent or excess amounts of reducing substances compared to oxidizing substances in the gas, NO_x can be catalytically reduced with the non-oxidized components (CO, H_2, CH) (non-selective catalytic reduction).

If, on the other hand, there is more oxygen in the gas than is necessary for the complete oxidation of the reducing components present, the reduction of nitrogen oxides with the latter can only be achieved with a selective catalyst.

Ammonia (NH_4) is used for reduction. Ammonia is a highly toxic gas, the storage of which in the vehicle would pose an unacceptable risk. Ammonia is thus created by thermal decomposition by injecting it into the hot exhaust gases at the point of use. For this, a 32.5% mixture of urea ($[NH_2]2CO$) in demineralized water is used (Tischer 2019) (Schaber 2004).

H_2N–CO–NH_2 (m) urea + heat $\rightarrow$ NH+ 4 NCO− (m) ammonium cynate
$\rightarrow NH_3$ (g) ammonia + HNCO (g)   (31)

This decomposes into ammonia at 132 °C, but we have to reach a much higher temperature before we can start the injection. This is important because explosive NH_4NO_3 can be formed during the process below 200 °C, so this cannot be ignored when controlling the system.

$$2NH_3 + 2NO_2 + H_2O \rightarrow NH4NO_3 + NH_4NO_2 \qquad (32)$$

A platinum-based catalyst is used at low temperatures. The minimum temperature should not exceed 200 °C and the maximum 225 °C, so that the NH_3 does not oxidize. (Ramis 1990) (Kalló 2000) (Koebel 2000, 2001, 2002)

$$4\ NO + 4NH_3 + O_2 \rightarrow 4N_2 + 6H_2O \text{ (standard)} \qquad (33)$$

$$2\ NO + 2NO_2 + 4NH_3 \rightarrow 4N_2 + 6H_2O \text{ (fast)} \qquad (34)$$

$$6\ NO_2 + 8HN_3 \rightarrow 7N_2 + 12H_2O \qquad (35)$$

$$6NO + 4NH_3 \rightarrow 5N_2 + 6H_2O \qquad (36)$$

$$2NO_2 + 4NH_3 + O_2 \rightarrow 3N_2 + 6H_2O \qquad (37)$$

$$6\ NO_2 + 8HN_3 \rightarrow 7N_2 + 12H_2O \qquad (38)$$
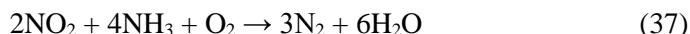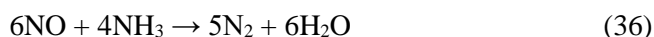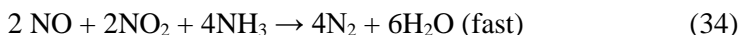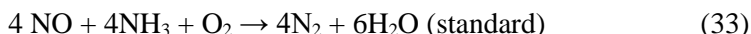
If NO_2 exceeds NO concentration the reaction pathway as follows;

$$8\ NO_2 + 6\ NH_3 \rightarrow 7\ N_2O + 9\ H_2O \qquad (39)$$

$$4\ NO_2 + 4\ NH3 + O_2 \rightarrow 4\ N_2O + 6\ H_2O \qquad (40)$$

Also several secondary reactions occur along with the main reactions;
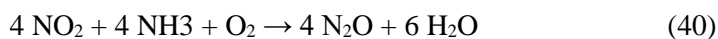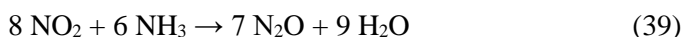
$$2NH_3 + 2O_2 \rightarrow N_2O + 3H_2O \qquad (41)$$

$$4NH_3 + 3O_2 \rightarrow 2N_2 + 6H_2O \qquad (42)$$

$$4NH_3 + 5O_2 \rightarrow 4NO + 6H_2O \qquad (43)$$
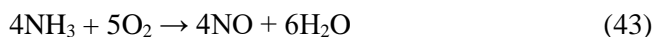
For higher temperature applications (250-500°C), V_2O_5 and zeolite catalysts are used. The reaction steps with intermediates (Ramis 1990) (Kalló 2000) (Koebel 2000, 2001, 2002):

$$6NO + 4NH_3 \rightarrow 5N_2 + 6H_2O \qquad (44)$$

$$(VO^{2+} + NH_3 \rightarrow [HO\text{-}V\text{-}NH_2]^{2+}) \qquad (45)$$

$$(NO + [HO\text{-}V\text{-}NH_2]^{2+} \rightarrow [HO\text{-}V\text{-}NH_2\text{-}NO]^{2+}) \qquad (46)$$

$$([HO\text{-}V\text{-}NH2\text{-}NO]^{2+} \rightarrow N_2 + H_2O + [VOH]^{2+}) \qquad (47)$$

$$([VOH]^{2+} + 1/4\ O_2 \rightarrow VO^{2+} + 1/2\ H_2O) \qquad (48)$$

$$(NH_3 + NO + 1/4\ O_2 \rightarrow N_2 + 6/4\ H_2O) \tag{49}$$

$$4\ NO + 4NH_3 + O_2 \rightarrow 4N_2 + 6H_2O\ \text{(standard)} \tag{50}$$

$$(V^{+5}=O + NH_3 \rightarrow HO\text{-}V^{+4}\text{-}N\ H_2) \tag{51}$$

$$(HO\text{-}V^{+4}\text{-}N\ H_2 + NO \rightarrow HO\text{-}V^{+4}\text{-}(NH_2)\text{-}NO) \tag{52}$$

$$(HO\text{-}V^{+4}\text{-}(NH_2)\text{-}NO \rightarrow HO\text{-}V^{+4} + N_2 + H_2O) \tag{53}$$

$$(2\ HO\text{-}V^{+4} + NO_2 \rightarrow 2\ V^{+5}=O + NO' + H_2O) \tag{54}$$

$$2\ NO + 2NO_2 + 4NH_3 \rightarrow 4N_2 + 6H_2O\ \text{(fast)} \tag{55}$$
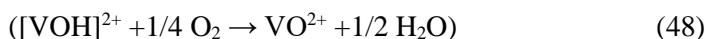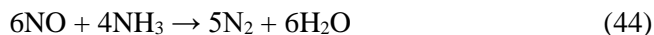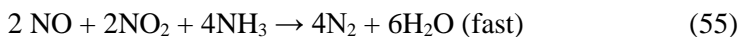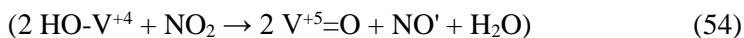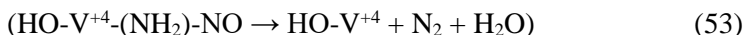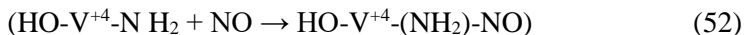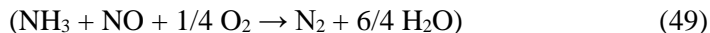
If NO:NO$_2$ ratio1:1, below 300 °C, the ttt will happen:

$$2NO_2 + 4NH_3 + O_2 \rightarrow 3N_2 + 6H_2O \tag{56}$$

$$6\ NO_2 + 8HN_3 \rightarrow 7N_2 + 12H_2O \tag{57}$$
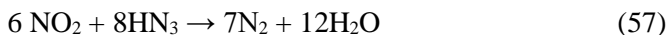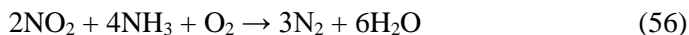
If the NO$_2$ exceeds a NO concentration the following reactions takes place;

$$8\ NO_2 + 6\ NH_3 \rightarrow 7\ N_2O + 9\ H_2O \tag{58}$$

$$4\ NO_2 + 4\ NH_3 + O_2 \rightarrow 4\ N_2O + 6\ H_2O \tag{59}$$

Also the side reactions;

$$2NH_3 + 2O_2 \rightarrow N_2O + 3H_2O \tag{60}$$

$$4NH_3 + 3O_2 \rightarrow 2N_2 + 6H_2O \tag{61}$$

$$4NH3 + 5O_2 \rightarrow 4NO + 6H_2O \tag{62}$$
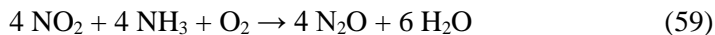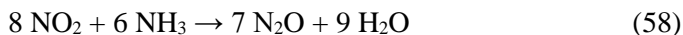
For an easy overview, we included all of these reactions into one summary table (Figure 12). In the table, temperature levels can be seen from 150°C to 700°C. The three exhaust part separated into 3 columns.
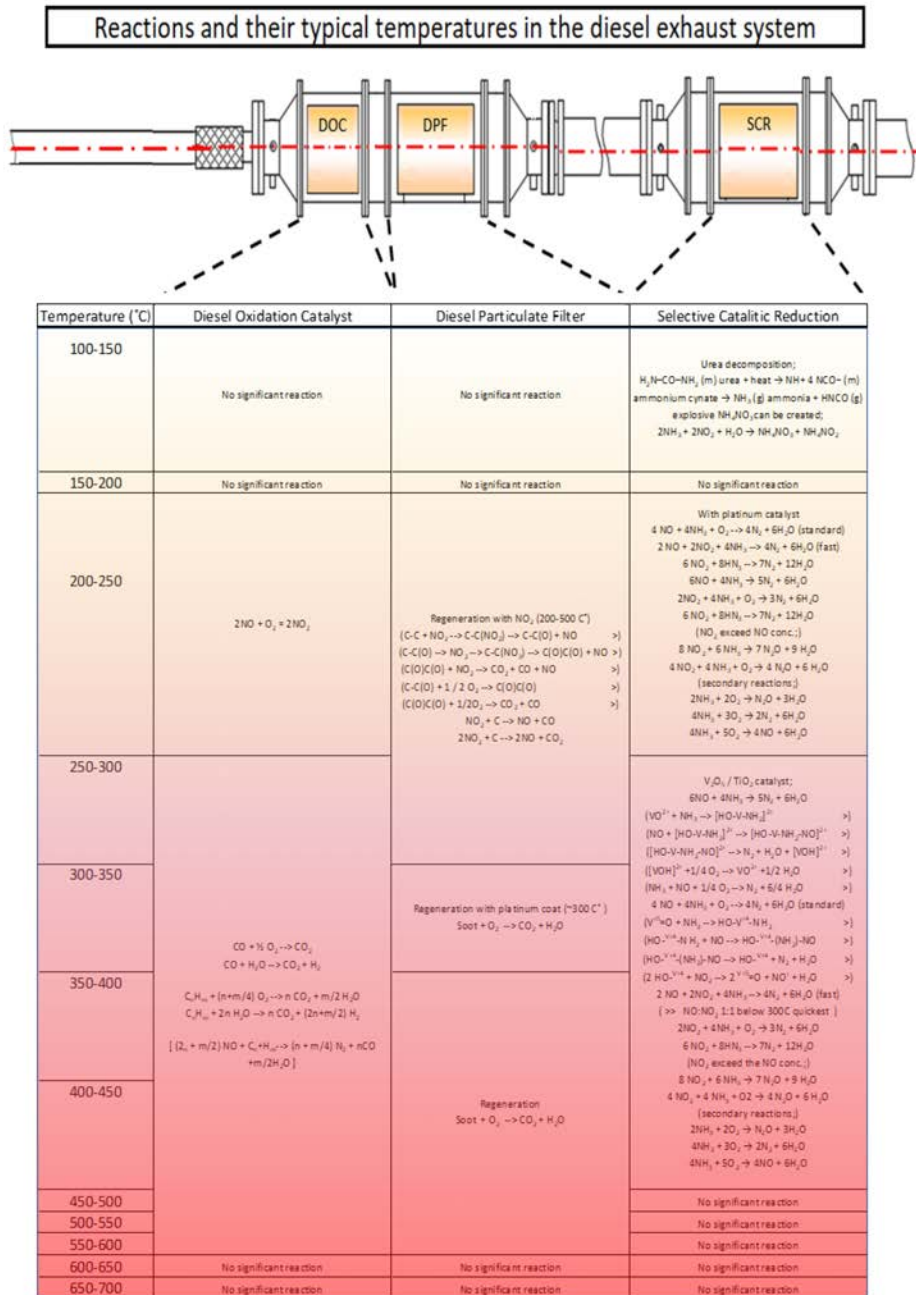
Figure 12. Reaction model

Conclusions

From emission aftertreatment point of view, most of the desirable reactions occurring in the exhaust system are exotherms and catalysts promoting these reactions. From our test, we can see how effectively these systems working and raising the temperatures in the DOC and DPF. Even though we are moving away from the engine along the exhaust, during several operation condition the maximum temperature figures are rising due to the catalyst effect of the system elements, DOC, DPF and SCR.

To create more precise temperature model, for the future, we can establish tests where we measure filter/catalyst inside temperatures. In case of, for example the DOC, typically the inlet side of the ceramic monolith coated (applied catalytic material), therefore probably we can collect more precise temperature data if we can sample the internal temperature of the monolith.

Considering the temperature range during emission cycle (~130-250 °C), the platinum type SCR favorable for our further testing with its low temperature operation range. But care should be necessary taken, we should cut off urea dosing above 225 °C to avoid the oxidation of NH_3.

During literature survey, in many publications (Fenimore 1972) (Turns 2000) we can see the strong catalyst effect of the water, so in our further testing when the water injection will be added to the system, we should count with possible new reaction pathways also.

Acknowledgements

References

[1] Jánosi L. and P. Kiss (1988) Belsőégésű motorok nitrogénoxid kibocsátásának követése más motorjellemzőkből, Agrár-Műszaki Bizottság kutatási és fejlesztési tanácskozás Gödöllő, MÉM Műszaki Intézet, 34-36.
[2] Ohno K. (2006) A Study on Performance of Particulate Filters Using R-SiC Porous Materials for Diesel Vehicles
[3] Bíró N. (2020) Egyedi Adblue befecskendező rendszer tervezése és tesztelése, Master's Thesis, Szent István University
[4] Manufacturers of Emission Controls Association (MECA) (2007) Emission Control Technologies for Diesel-Powered Vehicles
[5] Prasad R, and VR. Bella (2011) A review on diesel soot emission, its effect and control, Bulletin of Chemical Reaction Engineering & Catalysis vol. 5, 69–86.

[6] Khair MK. and WA Majewski (2006) Diesel emissions and their control. SAE International

[7] Agarwal AK. (2007) Biofuels (alcohols and biodiesel) applications as fuels for internal combustion engines. Progress in Energy and Combustion Science vol. 33, 233–271.

[8] Burtscher H. (2005) Physical characterization of particulate emissions from diesel engines: a review. Journal of Aerosol Science vol. 36, 896–932.

[9] Lee T, Park J, Kwon S., Lee J., Kim J. (2013) Variability in operation based NO_x emission factors with different test routes and its effects on the real-driving emissions of light diesel vehicles, The Science of the Total Environment, 461–462:377–385.

[10] Kalló D. (2000) Katalitikus eljárások a környezetvédelemben, University of Veszprém

[11] Turns SR. (2000) An Introduction to Combustion, McGraw-Hill (Second edition), 168-171

[12] Charlton S. (2007) Heavy-Duty Diesel Emission Control Symposium, presentation, 2007

[13] Pischinger S., Körfer T., Wiartalla, et al. (2007) Combined Particulate Matter and NOx Aftertreatment Systems for Stringent Emission Standards, Diesel Exhaust Aftertreatment 2000-2007 SAE books, April 2008, pp. 105-118

[14] Konstandopoulos A.G., Kostoglou M. (2000) Reciprocating flow regeneration of soot filters Combust Flame, Volume 121, pp. 488-500

[15] Rente T. (2004) Injection strategies for Heavy Duty DI Diesel Engines. Doctoral thesis, Chalmers University of Technology

[16] Fenimore C.P. (1971) Formation of nitric oxide in premixed hydrocarbon, Symposium (International) on Combustion Volume 13, Issue 1, Pages 373-380

[17] Szőllősi D., Kiss P. (2022) Soot accumulation in the diesel particulate filter and its effect on the filtration efficiency, Mechanical Engineering Letters, Volume 22, pp 61-69

[18] Teng H., McCandless J.C., Schneyer J.B. (2003) Compression ignition delay (phisical+chemical) of dimethyl ether – an alternative fuel for compression–ignition engines, SAE Technical Paper

[19] Konstandopoulos A.G., Kostoglou M., (2000) Reciprocating flow regeneration of soot filters Combust Flame 121, pp. 488-500

[20] Bissett, E.J, Shadman F. (1985) Thermal regeneration of diesel-particulate filters, AIChE Journal 31, pp. 753-758

[21] Koltsakis G.C., Stamatelos A.M. (1996) Modeling thermal regeneration of diesel particulate traps, AIChE Journal, 42, pp. 1662-1672

[22] Ohno K. (2008) New Technology with Porous Materials: Progress in the Development of the Diesel Vehicle Business Kazushige Ohno, Ceramic Engineering and Science Proceedings, Advances in Bioceramics and Porous Ceramics: Ceramic Engineering and Science Proceedings, Volume 29, Issue 7, pp. 313-325

[23] Katare S. (2006) "Robust Parameter Estimation Algorithms for Nonlinear Aftertreatment Models." SAE Technical Paper, Diesel Exhaust Emission Control Modeling, Transactions Journal of Fuels and Lubricants-V115-4, pp. 17

[24] Strzelec A., Vander Wal R.L., Thompson T.N., Toops T.J., Daw C.S. (2016) NO_2 oxidation reactivity and burning mode of diesel particulates, Springer, Journal Volume: 59; Journal Issue: 8-9

[25] R. Matarrese R., Castoldi L., Lietti L. (2017) Oxidation of model soot by NO_2 and O_2 in the presence of water vapour, Dipartimento di Energia, Laboratory of Catalysis and Catalytic Processes and NEMAS, Centre of Excellence, Politecnico di Milano, Elsevier, Chemical Engineering Science 173, 560-569

[26] Diesel Exhaust Particle Size (2002) Dieselnet Technology Guide, Revision 2002.11c https://dieselnet.com/tech/dpm_size.php

[27] Tischer S., Börnhorst M., Amsler, Schoch G., Deutschmann O. (2019) Thermodynamics and reaction mechanism of urea decomposition, Physical Chemistry Chemical Physics 21, pp. 16785-16797

[28] Schaber P.M., Colson J., Higgins S., Thielen D., Anspach B., Brauer J. (2004) Thermal decomposition (pyrolysis) of urea in an open reaction vessel, Elsevier, Thermochimica Acta 424, pp. 131–142

[29] Koebel M., Elsener M., Kleemann M. (2000) Urea-SCR: a promising technique to reduce NOx emissions from automotive diesel engines, Catalysis Today, Volume 59, Issues 3–4, pp. 335-345

[30] Koebel M., Elsener M., Madia G. (2001) Reaction Pathways in the Selective Catalytic Reduction Process with NO and NO2 at Low Temperatures, Industrial Engineering Chemistry Research 40, pp. 52–59

[31] Koebel M., Madia G., Raimondi F., Wokaun A. (2002) Enhanced Reoxidation of Vanadia by NO2 in the Fast SCR Reaction, Journal of Catalysis, Volume 209, Issue 1, Pages 159-165

[32] Ramis G., Busca G., Bregani F., Forzatti P. (1990) Fourier Transform-Infrared Study of the Adsorption and Coadsorption of Nitric Oxide, Nitrogen Dioxide and Ammonia on Vanadia-Titania and Mechanism of Selective Catalytic Reduction, Elsevier Applied Catalysis 64, pp. 259-278

Large-scale photovoltaics integration

Teklebrhan NEGASH[1], István SERES[2], István FARKAS[3]

[1]Mechanical Engineering Doctoral School (MTDI), Szent István Campus, Gödöllő, MATE

[2]Institute of Mathematics and Basic Science, Hungarian University of Agriculture and Life Sciences, MATE, Gödöllő

[3]Institute of Technology, Hungarian University of Agriculture and Life Sciences, MATE, Gödöllő

Abstract

Researchers and institutions are focusing on large-scale PV integration to achieve the ambitious renewable energy targets. Decarbonization of the energy system is being studied in many regions and found to be feasible. This work studied the integration of large-scale solar PV with enabling technologies, with a focus on power quality issues. A MATLAB-Simulink model was developed to filter ripples and harmonics of the power generated by solar PV systems, based on maximum power point tracking controller found in many inverters. Complementarity was discussed, and geographically dispersed resources were utilized for spatial and temporal complementarity analysis. Storage and curtailment were investigated for integrating large-scale PV, and new concepts such as vehicle-to-grid technologies and grid flexibility were discussed. Grid flexibility scenarios were proposed, including the no dump condition.

Keywords

Solar PV, wind, complementarity, storage, grid flexibility

Introduction

The United Nations General Assembly (UNGA) adopted sustainable development goals in 2015 with a strong framework centred on international cooperation to achieve a sustainable future. Collectively the goals and targets are aimed to terminate poverty, fight inequality and injustice and protect the environment. Securing sustainable energy is the main pillar to achieve all these goals and targets. Achieving modern, affordable and reliable energy for all is the main pilar of sustainable development goals. Among the many initiatives taken to achieve the 2030 agenda increasing the share of renewable energy in the global energy mix is the among the priorities. Moreover, it is highlighted that increasing the share of solar photovoltaics and wind energy and improving energy efficiency play a great role in achieving sustainable development goal by 2030 (UNDP, 2015). This draws the attention of significant number of researchers.

Globally utilization and deployment of large-scale solar Photovoltaics (PV) is growing rapidly and the capacity addition of photovoltaics power plants are expected to grow faster in the near future. Solar PV technologies convert direct sun light to electricity using semiconductor materials have both advantage and disadvantage in their utilization. Even though the lack of moving parts in PV technologies is a big advantage in reducing mechanical related failures but the absence of inertia (unlike the conventional generators) is a concern in their large-scale integration. The dynamic behaviour of PV technology is mostly dominated by working principle and characteristics of inverters. Therefore, its increased integration needs a treatment to minimize the impacts that can be created from its intrinsic behaviour (Liu et al., 2010). Moreover, proper understanding of system requirements is required to effectively integrate large scale PV to the grid either as PV only or in hybrid (PV + wind) form.

Usually, the PV systems are divided into standalone and grid connected PV systems. Standalone systems are not connected to the main grid due to different reasons such as placing in remote area or in isolated locations (such as islands) due to some natural barrier or if it is not cost effective to extend the transmission to the location. This type of PV technology can provide about 14% of world's population to those who have no access to electricity. Grid connected PV systems are systems which are connected to the main grid and represents about 95% of the total installed capacity in 2018. Grid connected PV plants can be categorized in three divisions namely residential (rooftop) of few kW range, commercial industrial (rage from ten to hundreds of kW range) and utility scale megawatt (MW) range and beyond. The first two types are intended to satisfy the local load demand and to inject the remaining capacity to the grid. In the other hand utility scale solar PV are otherwise called solar farms and they directly connected and integrated to the main grid (Gandhi et al., 2020).

Both rooftop and utility scale PV technologies are increasing the share of photovoltaic in the global energy mix. Rooftop PV technology have numerous advantages comparing to utility scale PV installation. Because rooftop PV technologies do not require useful land for installation and energy is consumed at the spot of production. For that reason, the expansion of rooftop PV technologies is supported and encouraged by policy makers to increase PV penetration. However, expanding distributed PV systems needs appropriate platform for financing and should further comply and satisfy grid standards and requirements in order to securely integrate to the grid. Despite its demand for useful land, ground mounted large scale utility PV is much easier to deploy, and the current installed PV capacity is dominated by these types(Solomon, 2019). In addition to the obvious advantage of solar PV on the environment deployment of large-scale distributed solar PV technology has benefits from economic and electrical point of view. The concept of distributed generation has benefits associated with transmission loses as electricity is consumed at spot of production. Moreover, replacing the conventional centralized generation units by such environmentally friendly generating units can eliminate CO_2 emission (Gandhi et al., 2020).

Technically grid connected solar PV has the potential to cover significant portion of the global electrical demand. The power output of solar PV is

proportional to the potential of solar radiation and the fluctuating nature of solar radiation creates numerous technical challenges upon integrating in large scale. This means there must be a significant amount dispatchable generating units in order to balance the fluctuating nature of PV generation. Moreover, in order to integrate large amount of solar PV a more flexible grid system is required which can ramp up and down rapidly (Lai et al., 2017). The most notable challenges worth mentioning during integration of large-scale PV system are grid matching ability, uncertainty and variability. To improve and overcome these challenges several solutions were proposed by different researchers such as demand response, energy storage, resource complementarity, increased grid flexibility, curtailment and others (Solomon, 2019). Though solar PV is not naturally dispatchable (output cannot be controlled as it varies with solar radiation) and cannot be schedule as in conventional power plants like coal and gas power plants, but it can have significant match with load demand in certain time of the day particularly in summer where air conditioning is needed for cooling purposes (Denholm and Margolis, 2006).

With all its advantages solar PV integration to the grid comes with issues related to power quality particularly during large scale integration. The most noted power quality issues are reliability, voltage stability and harmonics. Moreover, large scale integration of solar PV to utility grid raises concerns in frequency control and allocation of reserves. The intermittent nature of solar PV is the main reason for the voltage and current unbalance in utility grids when PV penetration is high. It also causes power quality problems such as voltage disturbance, harmonics distortion, poor power factor and flicker (Mahela et al., 2021).

With the ambitious national and international renewable energy development goals several power quality issues or concerns need to be addressed ahead of time to realize the proposed targets. Fluctuation and intermittency of solar PV due to passing clouds and diurnal pattern influences the utility grid negatively. Several studies are conducted in power quality issues and their mitigation approaches for grid connected large scale PV systems. But there are power quality issues that challenges the energy transition concept which are not yet thoroughly investigated. Energy transition concept aims to decarbonize the global energy system by achieving 100% renewable energy penetration. The major objective of this work is therefore to analyse the major power quality issues in large scale grid connected PV system and to deal with possible mitigation approaches. The study starts by studying and investigating major software programs and their capability in designing and simulating efficient PV system. The need of enabling technologies such as storage and complementarity of resources in smoothing, balancing of the mismatch, and increasing the penetration is comprehensively studied.

The role of simulation tools in smoothing and balancing PV system performance
The simplest solar PV system is composed of solar panel, inverter and connection cables. The power produced from PV system is directly feed to the grid network via inverter. The intermittency caused due to fast passing clouds is

the main reason to limit higher PV penetration. The variability caused due to such phenomenon is the reason for voltage fluctuation. Time series measurements from ground station can be used to assess and estimate the AC power generated from PV system to the utility grid. However, there are some mismatch and non-synchronizing profiles between these time series. A more advanced models and accurate estimation is therefore required to assess the performance of the PV system under different conditions. MATLAB/Simulink tool is a premier in designing ad simulating PV performance under different condition and transient clouds (Benaissa et al., 2017).

The performance of PV system though varies from system to system but in most commercial PV systems the efficiency varies between 8-15%. The other components like the maximum power point tracking algorithm (MPPT) and inverter have their own efficiency around 98% and 95-98% respectively.

MATLAB and Simulink tools are the most viable options in designing and optimizing MPPT algorithms for improving the performance of PV systems. However, the performance improvement cannot be only achieved using such tools for PV panels. The performance PV panels mainly depends on the technology and on the materials they fabricated. And there are other direction of research focusing on material and technical improvements of these devices in dedicated laboratories and research institutions.
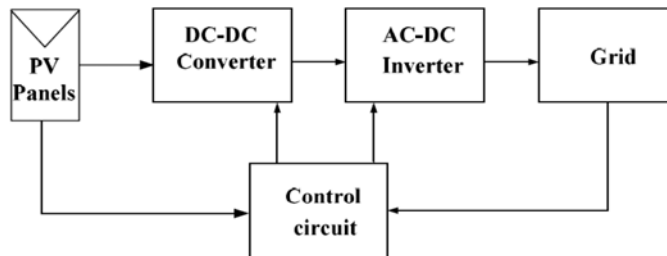
Figure 1. Schematic representation of grid-connected PV system (Soham and Bhasme, 2017)

The performance improvement of PV inverters can however be done using MATLAB Simulink modelling tools. The performance enhancement can be done even for plants that are already in use by updating their MPPT control algorithms. This can increase the PV performance by increasing the PV power generation and ultimately decreases the cost per kilowatt of generation. The non-linear characteristics of the voltage and current output makes the MPPT control algorithms more important. Because the relation between current and voltage it cannot easily defined manually. The point at which the power output of a PV system (Voltage x current) is maximum depends on different environmental factors like irradiance and temperature. These parameters are continuously varying in different time scales in minutes, hours, days and even seasons. Thus, the MPPT is dedicated to follow all the changes so as to track the maximum

point under all operating conditions. The MPPT algorithms balances and smooths the inverter power output by keeping the DC-bus voltage constant. The generated power is always varying due to environmental condition, but the controller keeps the voltage constant and balances the AC output regardless of the DC-power generated. There are different MPPT algorithms for tracking the maximum power point such as Fuzzy Logic Control (FLC), Perturb and Observe Incremental Conductance and Artificial Neural Network (ANN) (Jain et al., 2015).

Matching large scale PV generation to grid requirement
Secure and reliable power system needs to satisfy the constant varying load demand and should provide operating reserves for any unforeseen circumstances. To achieve this goal power plant operators, utilize a mix of different types of power plants to satisfy the demand. Most of the time baseload plants are deployed to meet the minimum constant load demand while intermediate load plants are used to satisfy the daily changing load demand. Another type of plants may require responding the peak load demand. The above plants can satisfy the predictable variability of load ranging from days to seasons, however, utilities require to reserve additional power plants for unpredictable increase in demand such loss of conventional power plants and transmissionism lines and other contingencies. These plants are called operating reserves and are responsible for frequency regulation and load-perdition errors and contingencies for unpredictable line outage (Denholm and Hand, 2011).

Power system operators utilize their collective power plants to satisfy the varying load demand based on their characteristics and ramping capabilities. Different power plants cannot have the same characteristics for example, coal power plants may operate as baseload plants while gas power plants can be employed as peak load plants for their fast-ramping capabilities. The plants that are utilized for operating reserves has fast ramping capabilities it means they can turn on and off rapidly to satisfy the fluctuating load demand. Here, we can note that power output of solar PV is not controllable rather it depends on the environmental conditions. Thus, due to their uncontrollable characteristics PV power plants cannot be used or contributed to baseload plants (Solomon et al., 2010). For example, in a clear sky day around the noon solar irradiance can raise significantly and this gives more PV generation which leads to power overloads and over voltage which leads to grid disturbances.

An important aspect worth mentioning is grid system flexibility, it is the ability of the aggregated generators to satisfy and respond the variable and unpredictable loads. For example, if we have large PV generation at a specific time of the day a flexible grid system reduces the baseload and operating reserves to their minimum level to accommodate the PV generation while maintaining system reliability. Therefore, it is crucial to have a very high flexibility power system to integrate high penetration of non-dispatchable generators like solar PV and wind power generators. The more the power system flexibility is the more the variable renewable integrated. If the difference

between the maximum and minimum generation of a baseload plant is low the system cannot add more variable generators. Therefore, it does not allow higher renewable penetration. For that reason, both the baseload and operation reserve generators must be flexible enough to realize high penetration of renewables. If the aggregate power systems (baseload and operating reserve and peak load plants) are not flexible enough large quantity of variable renewable generation will be curtailed or dumped which leads to economic downturn. A power system which is dominated by the more flexible power plants like gas turbine power plants are more flexible than that of dominated by coal and nuclear powerplants (Denholm and Hand, 2011).
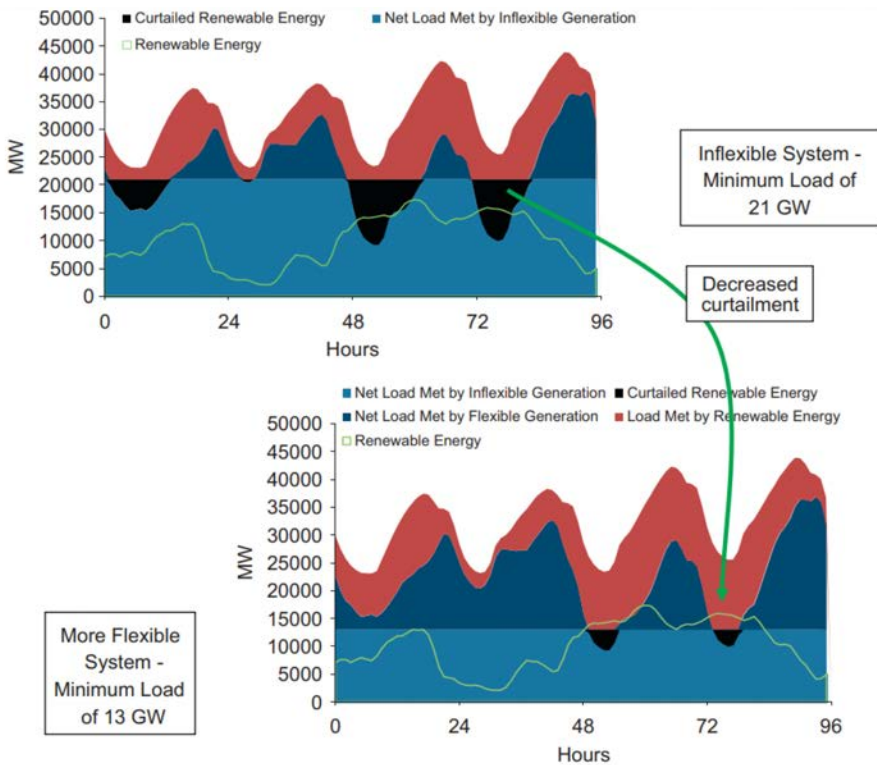
Figure 2. Impact of system flexibility on curtailed or dumped renewable generation
(Denholm and Hand, 2011)

From Fig. 2 we can demonstrate that more system flexibility can allow more renewable energy penetration. In the inflexible system where the baseload minimum value is 21 GW more renewable energy is wasted while in the lower graph where the minimum value of 13 GW very less variable renewable generation is wasted. Therefore, the ability power system to ramp up and down rapidly determines how much renewable generation to integrate to grid. If the

system is inflexible and not fast enough to react the PV fluctuation due to fast passing clouds no saving in fuel and more of the generated PV power will be wasted or curtailed unless some storage device is utilized.

Resource complementarity as a smoothing mechanism
Due to their dependence on environmental conditions solar and wind resources are variable and intermittent both temporally and spatially. This intermittent nature of solar and wind is the main challenge for power operators in their integration to the utility grid. However, their variation may not be the same pattern and sometimes their characteristics may be anti-correlated. The anti-corelated behaviour of solar and wind characteristics can be an advantage for utilizing them in hybrid form to partially smoothen the power output. When anti-correlated solar and wind are deployed together extreme variations can be cancelled each other to generate steady total generation that can be adopted as primary source. However, such smoothing effect can only be achieved if and only if solar and wind are compensating each other. For example, when wind availability is significant enough at night to compensate the shortfall of power from solar PV. However, not only compensating characteristics of combined solar PV and wind power output helps to deploy them as primary source but also the generation should match the particular hour load profile otherwise the generated power will be curtailed or wasted (Weschenfelder et al., 2020).

The ability of two energy generating sources to work together by complementing their generation at reduced operational challenges and need of enabling technologies can be termed as energetic complementarity. Energetic complementarity of two or more energy resources can be temporal, spatial or combined of both (both in time and space together). Spatial complementarity can be seen between one or more energy resource. In this category energy generating resources can complement each other in different places. For example, geographically distributed wind resources can complement each other similarly wind and solar resources locating in different regions can complement each other. It means the deficit of one energy source in one region is complemented by similar or different resource in different region at the same time. Geographically distributed renewable resources complement each other to smooth the variability. The correlation in power generation of renewable resources decreases as the distance between them increases. Temporal complementarity is seen between two or more renewable energy resources located in the same place. Two or more resources exhibits complementing characteristics in time. For example, solar and wind have different characteristics and pattern in different season of the year. If we take Hungary as an example solar availability is very less in winter but winds are available, in the other hand in summer the reverse happens solar availability reaches its peak value while winds are low. Complementarity can also be defined both in space and time called spatio-temporal complementarity. It is when complementarity of one or more renewable energy resources is studied simultaneously in time and space domain (Jurasz et al., 2020).

   To access the feasibility and uncertainty of resource complementarity most studies use hourly time series data sets. In renewable assessment at least one hour resolution time series is required to capture the variation. In complementarity analysis the optimal mix is important aspect if the optimal quantity of each resource is properly determined the unnecessary wastage and curtailment of resources is partially solved. During complementarity analysis different objective functions may be defined based on the need and priorities of the study. The benefits of complementarity can be best maximized by properly determining the optimum mix resources (da Luz and Moura, 2019). In large scale grid connected PV systems the weather dependent irradiance variability causes substantial fluctuation in the generated power.
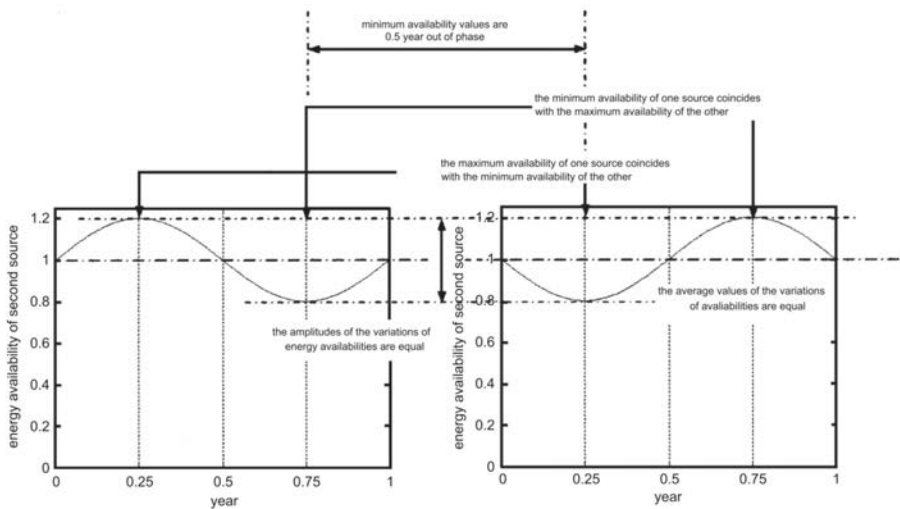
Figure 3. Sine function illustrating complementarity between two renewable resources
(Beluco et al., 2019)

   As mentioned in previous sections when the penetration of PV increases in the utility network it negatively affects the power quality. Particularly short-term fluctuations affect the grid by causing frequency fluctuation and results in power quality disturbances. The authors in (Barkhouse et al., 2015) investigates the smoothing effect of geographically distributed large scale PV plants. They found that the higher the number PV plants grouped together and the further the plants are and strongest the smoothing effect will be. The authors investigated the smoothing effect as a function distance between plants in different time scales. The smoothing effect with distance separation was more pronounced in wind power than solar PV. Winds vary considerably with distance and significant smoothing effect is observed in geographically distributed wind farms.
   Comparing to standalone PV or wind systems combination(hybrid) of PV and wind substantially increases renewable penetration without or at reduced storage

size. But the increase in penetration may be limited due to mismatch between generation and load profile. To reach high renewable penetration other enabling technologies such as energy storage devices are required. It is reported that wind-solar PV complementarity increase renewable penetration up to 20% in relative to wind or solar PV alone. Benefits of complementarity can be further boosted by coupling enabling technologies like curtailment and storage. Moreover, solar PV/wind complementarity can reduce ramping need while improving system reliability (Solomon et al., 2020).

There are different statistical metrics and indices to evaluate complementarity. The most common metrics used in solar PV-wind complementarity are Pearson correlation coefficient (PCC), standard deviation and indices such as time complementarity index and load tracking index. Pearson correlation coefficient is the most widely used metrics to assess solar-wind complementarity. Sites with negative correlation coefficient can complement each other it means the deficit one resource is compensated by the availability of the other resource. Positively corelated resources cannot benefit from their combination.

The role of energy storage for large scale PV integration
Energy system always suffers from variability and uncertainty moreover supply and demand always varies over time. To address these challenges and to provide reliable power to consumers a flexible power system is required. With ambitious renewable energy development goals future power system is expected to be dominated by intermittent and variable renewable resources which requires a high level of flexibility to balance. Providing secure and reliable power to customers without any burden on the society should be the priority of power suppliers. Energy storage devices are one option in future energy system to balance the power generation. These technologies are considered as the essential components of power system that adds flexibility to power system by bridging the gap between supply and demand in space and time. Geographic gabs can be satisfied if and only if energy storage is portable or stored energy is capable of transmitted or transported (Child and Breyer, 2016).

Supply and demand of power system should always need to be balanced. The balancing challenge is more demanding when large scale of PV power is integrated to utility grid. In such cases there must be sufficient reserve capacity to secure the supply. The reserve capacity can be a fast-ramping power plants like gas or storage unit. Energy storage are designed to store energy when there is excess generation form renewable resources and give back when there is deficit in the renewable generation. Such dynamics reduces energy curtailment and increase renewable penetration (Weitemeyer et al., 2015). Energy Storage has double flexibility both in charging and discharging, that is storing energy when there is surplus generation and feeding back the grid when there is deficit in renewable generation.

Energy storage is the main element to integrate large scale PV technology by reducing curtailment, here the main task is to identify the time duration of the energy storage capacity. Large scale storage facilities like pumped hydro have

fairly long duration hours of around 8 hours or more, other small scale storage device like batteries most often have time scale duration of 4 hours or less. These small-scale storage devices may deploy in places where they work sufficiently in satisfying the peak demand. So, the selection of storage duration depends on the resource potential and pattern of the generation (Denholm and Mai, 2019). Moreover, storage deployment is more efficient when using with optimal solar PV - wind mix. Storage capacity is defined by its energy capacity and power capacity. The number of hours a storage can be taken for charging or discharging is the energy capacity divide by power capacity. The capacity of energy storage device is measured in kilo watt hour (kWh) while power capacity normally is a power described by kilowatts (kW) or megawatts (MW). The storage duration is the time duration when the storage is discharging at its power capacity before reaching its minimum value. There are times when the battery or other storage devices are not discharged completely to avoid degrading of the storage device.

Rapid and random fluctuation of photovoltaic power generation due to passing clouds creates several problems in the grid. A short term storge device is therefore necessary to cope such fluctuation to regulate the frequency of the power system on a regular basis. Complementing renewables at dispersed geographic locations can also cancel these small fluctuations (Denholm and Mai, 2019).

In this study we will analyse how storage increase renewable penetration while reducing curtailment and balancing needs. In our analyses we are aimed to increase the share of solar PV by deploying different enabling technologies such storage, curtailment and balancing capacity.

Electric vehicles as storage
The decarbonization of electric system requires higher penetration of renewables and the electric vehicles can play a significant role in this transition. The deployment of electric vehicles has showing sharp increase in recent years and charging the grid network using electric vehicles will no more be a new concept. In addition to their contribution to road transport electric vehicles have benefits in avoiding environmental pollution and also acts as an electrical energy storage. Electric vehicles are seen as a new technology employed for balancing the grid by charging and discharging the battery whenever needed (Sharma et al., 2020).

Batteries in electric vehicles store excess energy from renewables and provide or feed the power grid when needed. The fluctuating nature of renewables is always a burrier for utilizing renewables at its maximum capacity but storages such as electric vehicles' batteries can be employed to realize their higher integration by providing stored energy when winds are weak or when the sun is not available. Electric vehicles' batteries can be used either by vehicle-to-grid (V2G) approach or when end of vehicle life. End of vehicle life is when the battery is no more suitable for the transport vehicle but can be used in low demand grid network as storage. When the capacity or performance of a battery decreases to 70-80% of its original capacity such a battery will not be

appropriate in transport vehicles. Such retired batteries however, can have a significant contribution in less demanding stationary energy storage applications for many years. "Smart vehicle-to-grid charging can facilitate dynamic electric vehicle charging and load shifting, and electric vehicles can also be used to store electricity and deliver it back to the grid at peak times". By 2050 the projected vehicle to grid battery capacity is expected to exceed the grid demand. By 20250 the expected aggregate sum of both V2G and end of vehicle life capacity is 32 to 62 terawatt-hour. But by this year the expected grid demand for a short-term storage is on the range of 3.4 to 19.2 terawatt-hour which much less than the projected V2G capacity(Xu et al., 2023).

Electric vehicles can also be used in connection to local renewable generation units without connecting to the utility grid. Such usage has many advantages as generation is always excess and the price is always fixed (Dang et al., 2021).

Analysis methodology

In this section data handling and methodological analysis were discussed. All methods including analytical and graphical illustrations were presented. The first section of this report deals about power quality simulation and was performed on MATLAB computing environment and Simulink user interface.
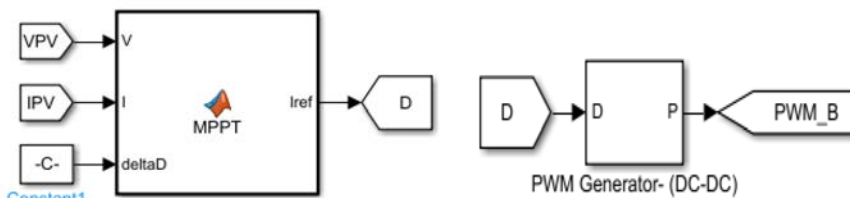

Figure 4. Maximum power point tracker with pulse width modulator
of DC-DC converter

Site selection

Table 1. Geographical information of solar sites

Site	location	Altitude above sea level (m)
Areza	14.9N, 38.6E	1949
Dekemhare	15.1N, 39.1E	2015
Kerkebet	16.3N, 37.4E	384

The resources complementarity study and the subsequent storage analysis were carried out based on data collected from selected sites in Eritrea. The potential sites were selected based on previous literature and an assessment of online database. The geographical information for the selected sites is given in Table 1.

Table 2. Geographical information of wind sites

Site	location	Altitude above sea level (m)
Assab	13N, 42.7E	Sea port
Dbarwa	15.1N, 38.7E	2340
Teseney	15.4N, 36.7E	1412

Solar and Wind data collection methodology
Time series data for solar PV generation and wind speed was obtained from PVGIS an open and free data base. PVGIS is an online and open-source database that provides customers with datasets for PV generation, solar radiation, wind speed and temperature for most parts of the globe. From PVGIS user can download comma separated value (.csv) files for varying time scales. The current versions of PVGIS can evaluate the performance of different PV technologies for fixed and tracking grid connected PV systems. The system evaluates the performance of different PV technologies considering different effects such temperature and shadow. The system considers overall system loses of 14%. The solar PV generation for selected sites are then downloaded as .csv file and processed to import for further analysis.
The wind speed obtained from PVGIS is however a little bit underestimated and was not comparable in magnitude with the actual ground measurements. The pattern/variation of the normalized values are however similar to original ground-based measurements. Therefore, the magnitude was scaled by more reliable data source Global Wind Atlas (GWA).

The scaled wind speed (v_{th}) is then extrapolated to turbine hub heigh by log law equation:

$$v_{th} = v_r \frac{ln(^z/_{z_o})}{ln(^{z_r}/_{z_o})}, \qquad (1)$$

where, v_r is the wind speed at reference height z_r and z_o is the roughness length. The unit of speed (v_{th}) is m/s.
The roughness length z_o was estimated from google map and visual inspection of the sites. For the proximate sites a combination of visual inspection and google map was used for estimating the roughness length but for some of the farthest sites only google map is utilized to estimate the roughness length.

Wind speed is then corrected to their respective local air density. The local density (ρ) of each site is a function of temperature and altitude and is given by

$$\rho = 3.4837 \frac{101.29 - z \cdot 0.011837 + z^2 \cdot 4.793 \cdot 10^{-7}}{T}, \tag{2}$$

where T is temperature in kelvin and z is altitude above sea level in meters

The standard power curve wind speed given by the manufacturer is then corrected (v_{site}) to match the local air density by Eq (3):

$$v_{site} = v_{std} \left(\frac{\rho_o}{\rho}\right)^{\frac{1}{3}}, \tag{3}$$

where ρ_o is standard air density (ρ_o=1.225 kg/m³) and v_{std} is the standard wind speed of the turbine power curve at turbine height.

Linear interpolation technique is then used to compute the power output $p(v)$ of the selected wind turbine:

$$p_{site}(v) = interp1(v_{site}, p_{std}, v_{std}), \tag{4}$$

where p_{site} represent the power generation of the corrected power curve and v_{th} is the wind speed at turbine heigh, where $p(v)$ is given in kW unit.

One hour resolution of time series load demand (*load*) for one year was used in this analysis.

The analyses aimed to obtain optimum combination of solar PV and wind speed to reduce curtailment and increase penetration. The combined power (P_{rew}) of solar PV and wind was then computed using PV ratio (r) and wind ratio of ($1 - r$).

The different mix of solar PV and wind generated power can be computed as:

$$P_{rew}(t) = k\left(r\big(Pv(t)\big) + (1 - r)\big(wind(t)\big)\right), \tag{5}$$

where k is scaling factor.

Similarly, the residual load (P_{mix}) can be computed from the following equation:

$$P_{mix}(t) = k\left(r\big(Pv(t)\big) + (1 - r)\big(wind(t)\big)\right) - load(t). \tag{6}$$

Optimization of storage, curtailment and balancing power
The need for storage is more pronounced when integrating large scale of renewables. In this analysis a storage system is designed to decrease both curtailment and balancing needs. By decreasing curtailment, the penetration rate of renewables increases significantly. In the other hand a small increase in storage capacity shows significant increase in renewable energy penetration.

The system parameters like storage maximum capacity, efficiency (eta) and initial condition are clearly stated at the beginning of the analysis. Then the useful energy and penetration of renewables is easily computed from the flowchart given in Fig. 4.
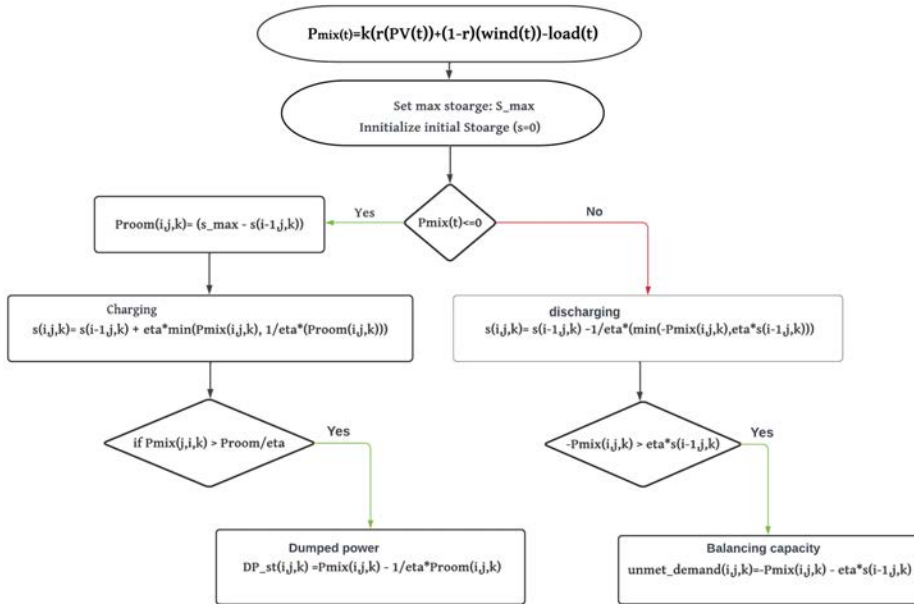

Figure 5. Flow chart of storage analysis

The useful renewable energy (U_E) utilized can be determined by subtracting dumped power (DE) from the renewable generation:

$$U_E(t) = P_{rew}(t) - DE(t). \tag{7}$$

Penetration (P) which is the annual energy covered by renewables is determined:

$$P = \frac{\sum_{t=1}^{8760} U_E(t)}{\sum_{t=1}^{8760} load(t)}. \tag{8}$$

Grid flexibility
Grid flexibility is an important aspect of grid system. The more the grid flexibility is the higher it can accommodate variable renewable generation. The power generation from solar PV is intermittent and uncontrollable. Such plants cannot contribute to the base-load part of the system however they can contribute to the variable part of the plants. Grid flexibility can be computed by (Solomon et al., 2010)

$$ff = 1 - \frac{l_{min}}{l_{max}}, \tag{9}$$

where l_{max} and l_{min} are the maximum and minimum hourly generation of the power system (grid).

The minimum generation (l_{min}) that the grid can generate at any time of the year can be computed.

$$l_b(t) = (1 - ff)\, l_{max}, \tag{10}$$

where l_b is the base load plant generation at hour t, this can be otherwise called base load capacity:

The remaining power capacity of the grid depends on variable generation units including renewables. The variable solar PV can contribute to this variable demand. The share of the variable part of the grid at any hour t can be computed as:

$$l_{var}(t) = l(t) - (1 - ff)\, l_{max}, \tag{11}$$

where l_{var} is the variable generation of the grid and l is the hourly generation of the grid.

The no dump concept is important to adopt, so the following relationship is defined to determine the no dump PV power output. Let *R=PVgen/load*, where *PVgen* and *load* are normalized to their maximum MWh capacity.

Then the no dump capacity of the grid can be determined by

$$No\_Dump = \frac{1}{\max(R)}. \tag{12}$$

The time series of the hourly power generated ($P_{hourly-}ND$) for the dump scenario can be determined:

$$P_{hourly-}ND = No_{Dump}\, PV_{gen}, \tag{13}$$

where PV_{gen} the hourly power generated from PV system in kW.

Results and discussion

Power quality analysis
The Power output of the PV panel is connected to the grid through a series of components like DC-DC converter, filters and inverter. The DC-DC boost converter has high switching frequency and is used to maximize the array voltage to required level depending on system requirement. The MMPT algorithm varies the duty cycle to generate an appropriate signal for extracting

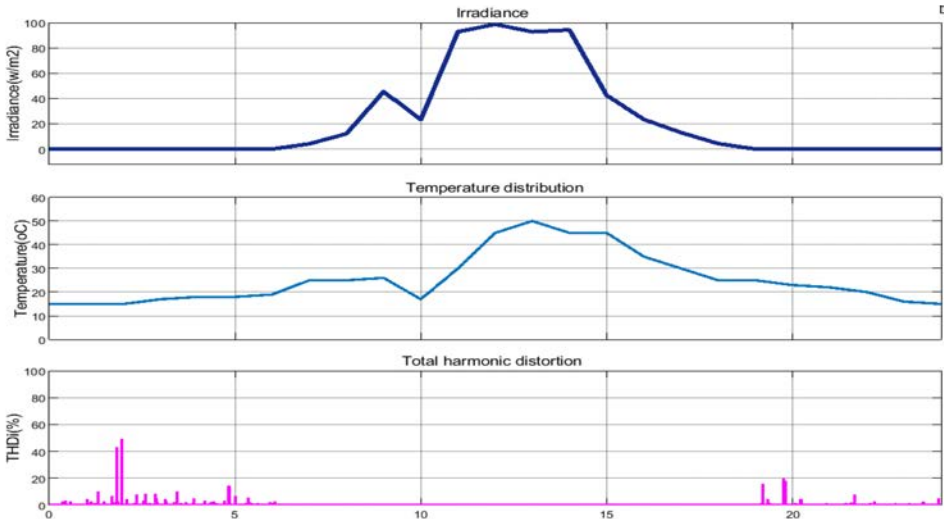maximum power. Current harmonics and ripples in the generated voltage are filtered using low bypass filters.

Figure 6. Total harmonic distortion under different working conditions of irradiance and temperature

In this section a representative artificial solar data was taken by authors to describe the different conditions of a day. The data were selected in such a way to enable us to investigate the different working conditions of a PV system under varying environmental condition such as passing clouds and transients. The solar and temperature profiles of the input variables are given in Fig. 6.
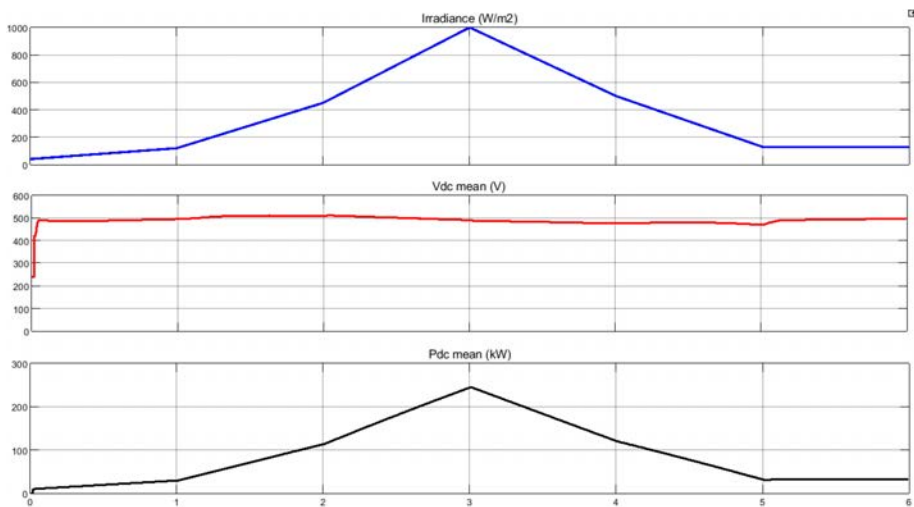

Figure 7. The relation between DC-link voltage and power generated from PV system

As shown in Fig. 6 the effect of environmental parameters such irradiation and temperature on active power generated is significant. The total harmonic distortion was found to be maximum during low irradiance hours.

Regulating the DC-link voltage is the main function of the MPPT algorithm. If the DC-link voltage is maintained constant as shown in Fig. 7, the system is balanced, and the power is a function of the generated current.

Analysis of enablers

In this section the complementarity, storage and curtailment issues are discussed. The penetration of renewable energy resources can be better achieved by employing different enabling technologies. Deploying different renewable resources in geographically dispersed regions can help compensate the deficit one by the excess generation of the other in the same location or different. Solar PV and wind are the most suitable resources for combined use. Solar PV and wind power complementarity analysis was carried out in this work with the ultimate goal to increase penetration of PV power. Fig. 8 shows how solar PV, wind power and load varies throughout the year. All-time series datasets were normalized to their mean value.

a) hourly profiles   b) daily profiles
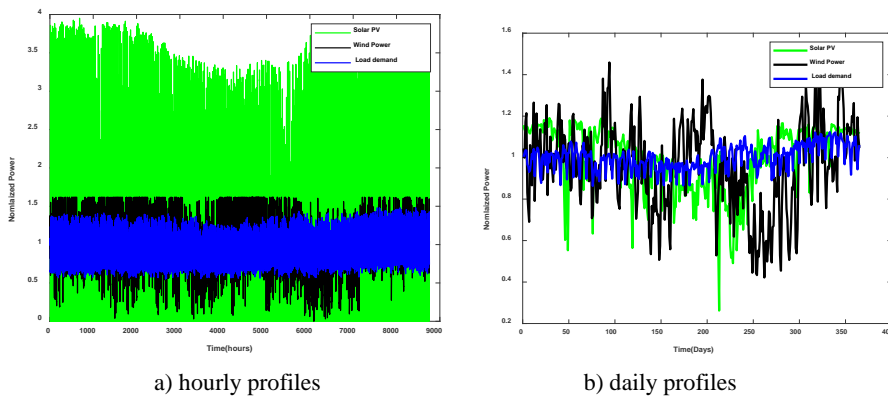
Figure 8. Solar PV, wind power and load demand

As shown in Fig. 8(a) the hourly (normalized) PV generation is dispersed from the mean value and reaches as much as four times the mean. This is due to the significant variation between day and night pattern of the solar radiation. However as seen in Fig. 8(b) the fluctuation significantly reduced when the time resolution is changed to daily scale. The correlation coefficient for all three data sets for the hourly and daily time scales was computed. Table 3 give an indication how solar PV, wind generation and load correlate each other on both hourly and daily time scales.

Table 3. Pearson correlation coefficients between PV, wind and load

Energy resource- 1	Energy resource- 1	Hourly PCC	Daily PCC
PV	Wind	0.2328	0.1342
wind	load	0.2821	0.1346
PV	load	0.4745	0.1600
Load	PV + wind	0.5038	0.1904

The PCC values for aggregate solar PV and wind generation units were compared for hourly and daily time scales and the complementarity was found to be more suitable in the daily time scales. Resources with lower correlation coefficient are effective to complement each other. Moreover, sites with negative correlation coefficient can better work together in complementarity mode. The correlation coefficient between load and the combined Solar PV and wind generation is higher in both hourly and daily time scale. This implies that the generation and demand have the same pattern, i.e., when the demand is high there is also high PV plus wind generation which is good match.
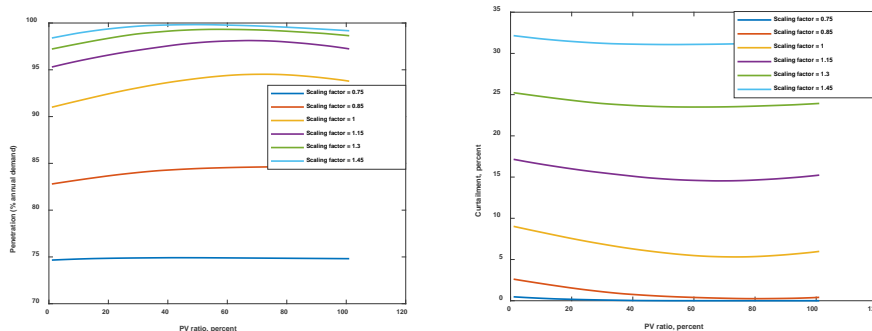

Figure 9. Penetration and curtailment vs PV ratio

From Fig. 9 one can easily visualize the amount of total renewable energy dumped to reach high penetration of renewables. To reach like 100% renewable (PV-wind combination) approximately 30% of the generated energy has to be curtailed. This means more energy is needed to be generated in order to cover the loses as well. For this reason, a scaling factor is introduced to increase the generation of renewables. Without curtailment however, we cannot reach high level of renewable penetration. For scaling factor of one the penetration can reach around 93 % at 65% PV ratio. This high level of penetration is achieved by utilizing different enabling technologies such as storage, curtailment and

balancing capacity. Since solar radiation is almost constant throughout the year in countries like Eritrea the contribution of energy from solar PV is significant. The balancing need at PV ratio of 49% and scaling factor of 1.15 is given in Fig. 10(a). Only few days of the year the balancing capacity need to be operated otherwise the renewable generation can satisfy the demand. As shown in the figure the balancing capacity is high when there is no energy left on storage. By increasing the capacity of the energy storage, we can significantly decrease the balancing capacity.
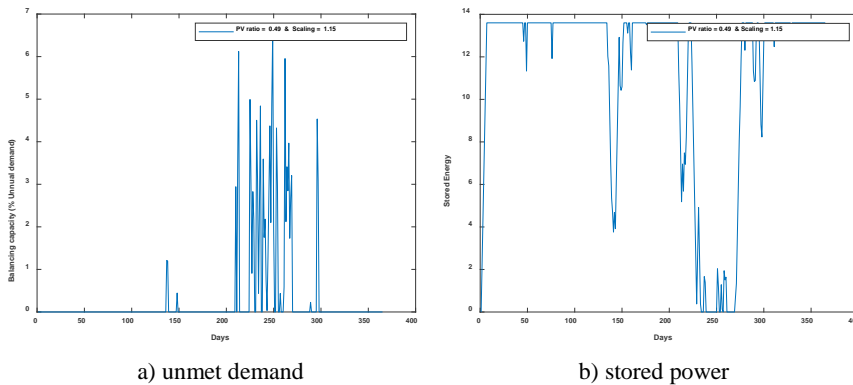
a) unmet demand   b) stored power
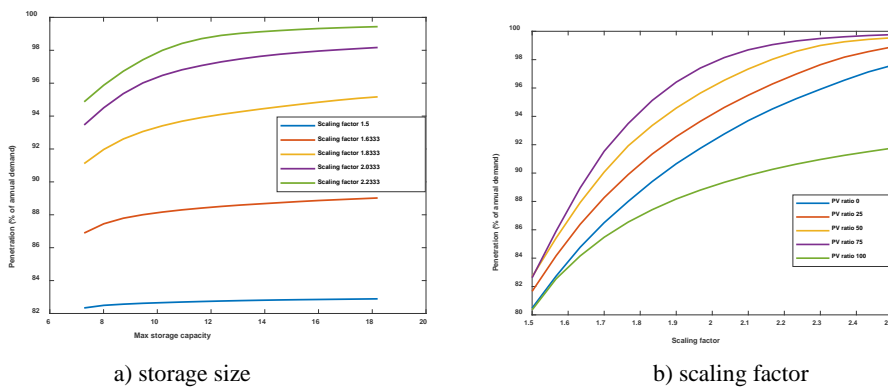
Figure 10. The effects on penetration

Both the balancing needs and storage are used as enabling technologies for achieving high penetration of renewables. The optimal share of PV - wind ratio to achieve high penetration varies with storage capacity size and the scaling factor.

a) storage size   b) scaling factor

Figure 11. The effects on penetration

As shown in Fig. 11(a) the penetration progressively increases with storage capacity. The optimum storage size where the penetration is maximum can be found using additional optimization techniques. On the current work the effect of increasing storage capacity on penetration was investigated. Based on the non-economic model adopted in this study the penetration is observed to increase significantly by storge capacity. Similarly higher penetration can be achieved by over sizing the PV/wind generation by multiplying by some factor as shown in Fig. 11(b). However, while increasing the renewable generation the economic aspect needs to be considered as weather to increase the size of the renewable generation or to have some balancing capacity instead. From Fig. 11(b) we can see that the penetration is maximum at PV ratio 75% for all penetration levels. While PV only scenario (100% PV) has always the lowest penetration regardless of the scaling factor.

Grid flexibility
In previous sections we analysed the smoothing effect of combined solar PV and wind power generation in geographically dispersed sites. It demonstrates that the combined value has many advantages such reliability, smoothing effect and grid matching capability. Here in this section, we will consider only solar PV integration. The effect of grid flexibility is crucial for integrating fluctuating and intermittent renewable resources. A grid with high capability to ramp up and down rapidly to cope up with fluctuating renewable generation and load demand is advantageous.
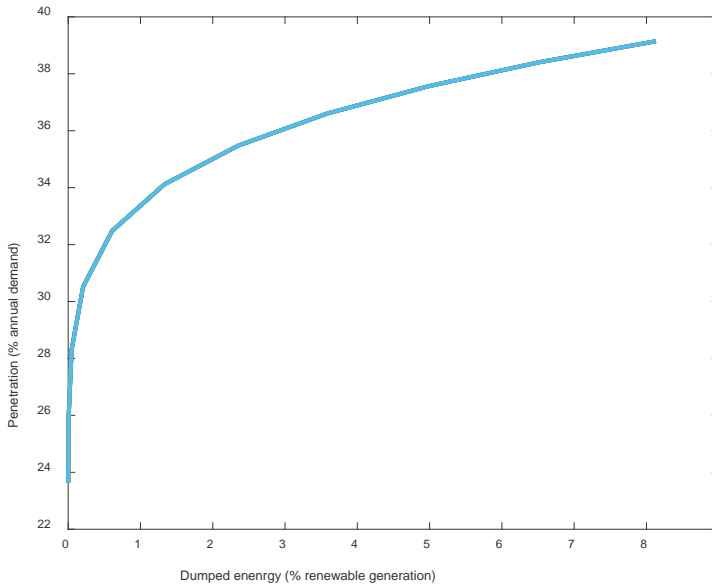

Figure 12. The penetration and curtailment (grid flexibility=1)

The first attempt was to design a PV system that never dumps any part of its generation. Though dumping and curtailment are important to achieve high penetration of renewables but considering the economic point of view it is also good to produce what you can utilize. Thus, the no dump concept is employed to efficiently integrate the generated PV to the utility grid. The no dump power is the power generated by PV at each hour that never being wasted or dumped. The power output of the PV system is normalized to 1 MW. Fig. 12. shows how the penetration and dumped power varies with small increment of the no dump size. Here we discussed only for ideal power plants with a grid flexibly of 1 but in later works the real situation of power plants with varying grid flexibility will be addressed.

Fig. 12 shows the penetration versus curtailment graph. As seen from the figure both the penetration and curtailment increase together until it reaches 4% of curtailment but later with further increase in curtailment the slope of the penetration curve slows down and gradually becomes flat. This shows that the penetration increases as the no dump capacity increases but when it reaches some point the penetration remains constant and all the added generation is wasted.

Future plans

Large scale PV integration is the focus of many researchers and high-level studies were conducted in different areas of PV system. There are however, many areas of research which is not yet thoroughly investigated. The coming semester is therefore planned for conducting cutting edge researches in the area of power quality improvement techniques and large-scale PV integration. The priorities for the upcoming works can be arranged as follows:

a) Maximizing the penetration of PV ratio in PV/wind hybrid system. This hybrid system has advantage from both the smoothing effect and capability of integrating large scale renewables. Most of the time simple design of hybrid systems are dominated by wind power, here our objective is to maximize the PV ratio in the hybrid system by employing different enabling technologies.

b) The effect of storage, curtailment and balancing needs on integrating large scale PV generation will be thoroughly studied.

c) Experimental data collection and its associated data cleaning and processing will be conducted.

d) Artificial intelligence and machine learning based power quality analysis will be conducted in fifth semester.

e) The role of grid flexibility for integrating high penetration of PV generation by considering different working scenarios will be conducted.

Conclusions

The ultimate goal of this study is to integrate large scale PV power to the utility grid by minimizing the power quality issues while maintaining the system

reliability. The power quality issues are among the main barriers for integrating large scale of renewables. To minimize their impacts different methodologies were developed by researchers. In this work MATLAB-Simulink based model was developed to suppress the harmonics and regulate the voltage fluctuation. Along with these other alternative solutions were also examined to supplement the model in smoothing the generations. Resource complementarity particularly for PV/wind was analysed for a dispersed of geographical sites. To increase the smoothing effect geographical dispersed sites were selected. The farthest the distance between the sites the most complementing the generations is. A suitable model was developed to find the optimal mix of these resources. The optimal mix is the ratio where PV and wind generation are perfectly matched for higher penetration by smoothing their fluctuation. Other enabling technologies such as storage and curtailment were also analysed for different PV ratio and scaling factors. The PV and wind ratio was found to be reasonable and optimal for balanced utilization of the resources. Based on the daily time series, a PV ratio of 65% and wind ratio of 35% was found to be the most optimal with no storage requirement. The generation can be further increased by increasing the scale factor to reach higher penetration. Though curtailment is wastage of energy but sometimes it acts as a tool to increase the penetration higher. By curtailing some energy, we can substantially increase the penetration level of renewables. The effect of storage size in smoothing and increasing penetration is clearly demonstrated. A small increase in storage capacity size yields a significant increase in penetration with decreased curtailment. But it is necessary to determine how far the storage can increase while its economic and energy benefits are not compromised. To achieve higher penetration of around 100% renewables some means of balancing capacity are needed. These are required to achieve high PV-wind penetration by providing the required energy to the grid when renewable generation is less, and storage is empty. The importance of grid flexibility in integrating large scale of renewables is presented with specific scenario. In depth discussion will be given in the following publications for different grid flexibilities.

Acknowledgements

References

[1] Barkhouse, D.A.R., Gunawan, O., Gokmen, T., Todorov, T.K. and Mitzi, D.B. (2015). Yield predictions for photovoltaic power plants: empirical validation,recent advances and remaining uncertainties. *Progress in*

Photovoltaics: Research and Applications, *20*(1), 6–11. https://doi.org/10.1002/pip

[2] Beluco, A., Risso, A. and Canales, F.A. (2019). Simplified evaluation of energetic complementarity based on monthly average data. *MethodsX*, *6*(May), 1194–1198. https://doi.org/10.1016/j.mex.2019.05.019

[3] Benaissa, O.M., Hadjeri, S. and Zidi, S.A. (2017). Modeling and simulation of grid connected PV generation system using matlab/simulink. *International Journal of Power Electronics and Drive Systems*, *8*(1), 392–401. https://doi.org/10.11591/ijpeds.v8i1. pp. 392-401.

[4] Child, M. and Breyer, C. (2016). The Role of energy storage solutions in a 100% renewable Finnish Energy System. *Energy Procedia*, *99*(March), 25–34. https://doi.org/10.1016/j.egypro.2016.10.094

[5] da Luz, T. and Moura, P. (2019). Power generation expansion planning with complementarity between renewable sources and regions for 100% renewable energy systems. *International Transactions on Electrical Energy Systems*, *29*(7), 1–19. https://doi.org/10.1002/2050-7038.2817

[6] Dang, Q., Wu, D. and Boulet, B. (2021). Electric vehicle battery as energy storage unit consider renewable power uncertainty. *2021 IEEE Energy Conversion Congress and Exposition, ECCE 2021 - Proceedings*, 668–673. https://doi.org/10.1109/ECCE47101.2021.9595375

[7] Denholm, P. and Hand, M. (2011). Grid flexibility and storage required to achieve very high penetration of variable renewable electricity. *Energy Policy*, *39*(3), 1817–1830. https://doi.org/10.1016/j.enpol.2011.01.019

[8] Denholm, P. and Mai, T. (2019). *Timescales of energy storage needed for reducing renewable energy curtailment*. *130*, 388–399. https://doi.org/10.1016/j.renene.2018.06.079

[9] Denholm, P. and Margolis, R.M. (2006). Very large-scale deployment of grid-connected solar photovoltaics in the United States: Challenges and opportunities. *American Solar Energy Society - Solar 2006: 35th ASES Annual Conf., 31st ASES National Passive Solar Conf., 1st ASES Policy and Marketing Conf., ASME Solar Energy Division Int. Solar Energy Conference*, *1*(April), 302–306.

[10] Gandhi, O., Kumar, D.S., Rodríguez-Gallegos, C D. and Srinivasan, D. (2020). Review of power system impacts at high PV penetration Part I: Factors limiting PV penetration. *Solar Energy*, *210*(May), 181–201. https://doi.org/10.1016/j.solener.2020.06.097

[11] Jain, S., Vaibhav, A. and Goyal, L. (2015). *Comparative analysis of MPPT techniques for PV in domestic applications*. 1–6. https://doi.org/10.1109/poweri.2014.7117636

[12] Jurasz, J., Canales, F.A., Kies, A., Guezgouz, M. and Beluco, A. (2020). A review on the complementarity of renewable energy sources: Concept, metrics, application and future research directions. In *Solar Energy* (Vol. 195, pp. 703–724). Elsevier Ltd. https://doi.org/10.1016/j.solener.2019.11.087

[13] Lai, C. S., Jia, Y., Lai, L. L., Xu, Z., McCulloch, M. D. and Wong, K. P. (2017). A comprehensive review on large-scale photovoltaic system with applications of electrical energy storage. *Renewable and Sustainable Energy Reviews*, *78*(November 2016), 439–451. https://doi.org/10.1016/j.rser.2017.04.078

[] Liu, H., Jin, L., Le, D. and Chowdhury, A. A. (2010). Impact of high penetration of solar photovoltaic generation on power system small signal stability. *2010 International Conference on Power System Technology: Technological Innovations Making Power Grid Smarter, POWERCON2010*. https://doi.org/10.1109/POWERCON.2010.5666627

[14] Mahela, O.P., Khan, B., Alhelou, H.H., Tanwar, S. and Padmanaban, S. (2021). Harmonic mitigation and power quality improvement in utility grid with solar energy penetration using distribution static compensator. *IET Power Electronics*, *14*(5), 912–922. https://doi.org/10.1049/pel2.12074

[15] Sharma, S., Panwar, A.K. and Tripathi, M.M. (2020). Storage technologies for electric vehicles. *Journal of Traffic and Transportation Engineering (English Edition)*, *7*(3), 340–361. https://doi.org/10.1016/j.jtte.2020.04.004

[16] Soham, D. and Dr. N.R. Bhasme. (2017). A Review of Topologies of Inverter for Grid Connected PV Systems. *International Conference on Innovations in Power and Advanced Computing Technologies*.

[17] Solomon, A.A. (2019). Large scale photovoltaics and the future energy system requirement. *AIMS Energy*, *7*(5), 600–618. https://doi.org/10.3934/energy.2019.5.600

[18] Solomon, A.A., Child, M., Caldera, U. and Breyer, C. (2020). Exploiting wind-solar resource complementarity to reduce energy storage need. *AIMS Energy*, *8*(5), 749–770. https://doi.org/10.3934/ENERGY.2020.5.749

[19] Solomon, A.A., Faiman, D. and Meron, G. (2010). An energy-based evaluation of the matching possibilities of very large photovoltaic plants to the electricity grid: Israel as a case study. *Energy Policy*, *38*(10), 5457–5468. https://doi.org/10.1016/j.enpol.2009.12.024

[20] UNDP. (2015). *AFFORDABLE AND CLEAN ENERGY*. https://www.undp.org/sustainable-development-goals

[21] Weitemeyer, S., Kleinhans, D., Vogt, T. and Agert, C. (2015). Integration of Renewable Energy Sources in future power systems: The role of storage. *Renewable Energy*, *75*, 14–20. https://doi.org/10.1016/j.renene.2014.09.028

[22] Weschenfelder, F., de Novaes Pires Leite, G., Araújo da Costa, A.C., de Castro Vilela, O., Ribeiro, C.M., Villa Ochoa, A.A. and Araújo, A.M. (2020). A review on the complementarity between grid-connected solar and wind power systems. *Journal of Cleaner Production*, *257*. https://doi.org/10.1016/j.jclepro.2020.120617

[23] Xu, C., Behrens, P., Gasper, P., Smith, K., Hu, M., Tukker, A. and Steubing, B. (2023). Electric vehicle batteries alone could satisfy short-term grid storage demand by as early as 2030. *Nature Communications*, *14*(1). https://doi.org/10.1038/s41467-022-35393-0

Effect of ageing of thermosetting polymers on wear resistance

Tamás SÁRKÁNY[1], Róbert KERESZTES[2], Gábor KALÁCSKA[2]

[1] Department of Innovative Vehicles and Materials,
GAMF Faculty of Engineering and Computer Science, John von Neumann University
[2] Institute of Technology, Hungarian University of Agriculture and Life
Sciences, MATE, Gödöllő

Abstract

With the proliferation and increasing use of composite structures, many of the issues that were already well defined for metallic structures have been raised by users. One such question might be, for example, what is the expected lifetime of a composite component. These questions have not yet been answered exactly. Many factors can damage the structure of a material. Prominent among these are abrasion and degradation, i.e. ageing, caused by UV radiation. There are many applications where these components are exposed to intense sunlight. Although we are able to protect ourselves against these effects, it is advisable to find the links. In my research, I want to find out how fast the matrix of fibre-reinforced composite structures can age and how this ageing affects wear resistance.

Keywords

 composite, wear, polymer ageing

Introduction

A polymeric material may degrade due to chemical changes resulting from reaction with a component in the environment. In principle, most pure organic synthetic polymers do not absorb wavelengths longer than 300 nanometres due to their ideal structure and can therefore be damaged by sunlight. However, polymers can also undergo photo-oxidation, which in chemical terms means oxidation by light. The polymer reacts very slowly with oxygen at normal temperatures, so oxidation only becomes apparent after a long time. When UV radiation is irradiated on the polymer under the same conditions for 12 days, a strong band appears in the spectrum. In this case, the polymer free radicals are generated by the synergistic effect of factors such as electromagnetic radiation and thermal energy during the oxidation process (Mahzan at al., 2017).

The effects of ultraviolet radiation on composite materials have been investigated in several previous literatures, with a special focus on natural fibre composites reinforced with polymer matrix. From the reviewed reports, it is clear that UV plays a significant role in material strength degradation. The authors of these papers have found that the tensile strength of reinforcement fibres decreased with UV exposure time (Kumar at al., 2002).

Experimental setup

The used materials

Three types of resin were investigated in the research. All 3 types are widely used in the industry. The specific types are MGS RIMR426 epoxy resin, POLYNT 2662 IA polyester resin and Distitron 370N3 vinylester resin. The resins were moulded into 1 mm thick sheets, from which the test specimens were milled using a CNC milling machine.

The way of ageing

The matrices of the test specimens were subjected one by one to an aging test. In order to characterise the effect of the physical ageing of the polymers on the wear resistance, I used the equipment available in the department to carry out the ageing tests on the resin. The machine used is a product of the American manufacturer Atlas, whose UV tester is an instrument for fluorescent UV and condensation weathering tests. The instrument emits radiation at different wavelengths using UVA-340, UVB-313 and UVA-351 fluorescent tubes.

Table 1 shows the maximum intensity of ultraviolet radiation averaged over a whole year in Hungary. The highest average irradiance in Hungary is in Szeged. With this data, it is possible to calculate how many days 1 hour of irradiation corresponds to in the UV testing machine. In the experimental design, 50 and 150 hour cycles were used (B. Judit at al., 2013).

Table 1. Correlation of experimental UV radiation in Hungary

Intensity	Irradiation time of UV equipment		Irradiated energy	Radiation in Hungary	
fix	50 hour	180000 sec	110 kJ/m^2	0.09 year	33 day
fix	150 hour	540000 sec	540 kJ/m^2	0.27 day	98 day

The examination method

The experiments were carried out using a standardized method designed by Taber Industries for testing different types of materials. This standard (American Society for Testing and Materials) was published as ASTM D4060-10. Wear resistance is determined by measuring the mass lost after each wear period. The more material lost, the lower the wear resistance. Figure 2 shows this mechanical movement, where one abrasive stone rubs the sample outwards

towards the edge and the other inwards towards the centre, while a vacuum removes loose debris during the test. The stones make a full circle on the sample surface, causing abrasion at all angles to the weave or grain of the material. The resulting wear marks form a pattern of intersecting arcs in a circular band that can cover an area of about 30 cm2 .(Sárkány, 2023)
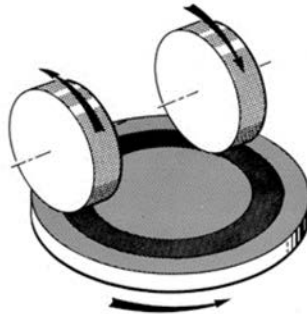

Figure 1. Schematic draw of the test apparatus (Deli, A. at al., 2018)

The standard specifies the exact thickness of the grinding stones, with a lower and upper tolerance of 12.76 +/- 0.3 millimetres, and an outer diameter of 51.96 +/- 0.5 millimetres when new, and never less than 44.4 millimetres. The test specimens may be circular or square bodies with a hole of 6,5 mm in the centre. The dimensions of the test pieces are 100 millimetres in diameter or 100 x 100 millimetres square. The thickness of the test pieces shall not exceed 6,3 millimetres. Adjustment of the grinding stones is mandatory before each test piece and every 600 cycles during the process. The S-11 regulating disc shall be rotated on the rotary table for a minimum of 25 cycles, the maximum value according to the standard being 50 cycles, after which the regulating disc shall be discarded and a new one used. Under no circumstances should the freshly regulated stones be rubbed or touched, as this will impair the efficiency of the measurement by introducing various impurities. During the testing of each specimen, five intermediate mass measurements were taken every 200 cycles to investigate the nature of the mass loss, so that eventually a specimen was subjected to 1000 cycles. The mass measurements of the specimens were carried out using the ABT 120-5DM precision balance, which can display the results in grams to five decimal places. The measurements were carried out in a constant place, at a temperature of around 20°C and constant humidity. The CS-10 grinding stones and the 750 g load weight were kept constant between tests. The total load of 1 kilogram per arm consisted of the arm's own weight, which was 250 grams, and the load weight, which was 750 grams. The abrasive used in the experiment was alumina (Sárkány, 2023). The weight reduction can be used to infer the wear rate.

Results and discussion

The Results of the wear tests

Of the three types of resin tested, the picture shows the wear curve of the vinylester. Two measurements were made for each type of test specimen. Thus, the diagram shows the wear curves of the 2 unaged specimens, the 2 specimens aged 50 hours and the 2 specimens aged 150 hours. The curves show that the surface of the resin was damaged by the ageing process, so that there was a significant loss of mass after the first 200-hour measurement, but the slope of the curves did not change significantly.
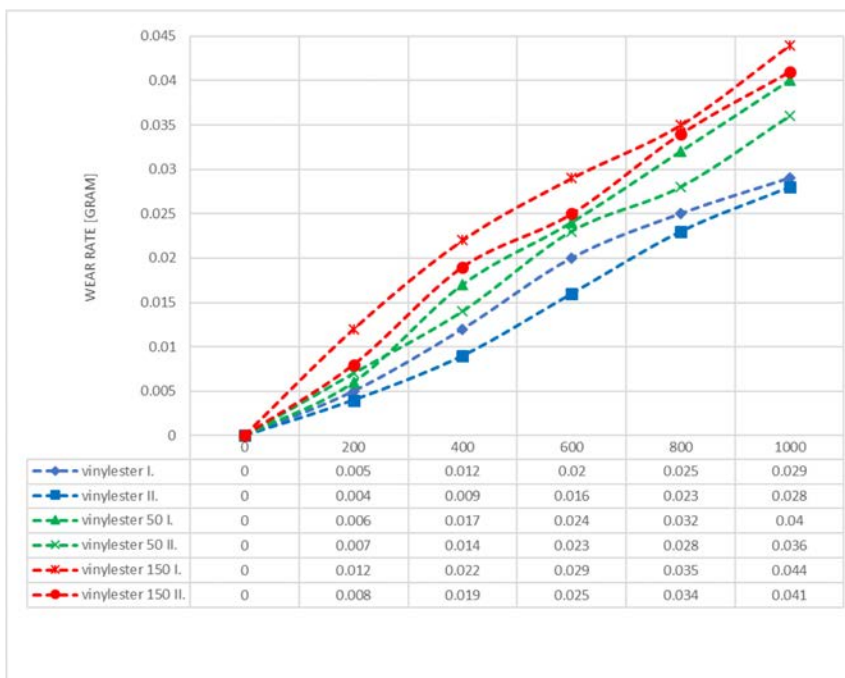

	0	200	400	600	800	1000
vinylester I.	0	0.005	0.012	0.02	0.025	0.029
vinylester II.	0	0.004	0.009	0.016	0.023	0.028
vinylester 50 I.	0	0.006	0.017	0.024	0.032	0.04
vinylester 50 II.	0	0.007	0.014	0.023	0.028	0.036
vinylester 150 I.	0	0.012	0.022	0.029	0.035	0.044
vinylester 150 II.	0	0.008	0.019	0.025	0.034	0.041

Figure 2. Effect of ageing on the wear curve of vinylester

The curing diagram shows the epoxy wear curves. The characteristics are similar to those of vinyl ester. The lower two parallel curves are those of the unaged specimen. The middle two curves are for the 50 hour aged specimen and finally the top two are for the 150 hour aged specimen. Here again, it is observed that the first 200 cycles of abrasion wear faster on the aged specimens, after which the rate of wear becomes the same as on the unaged specimen.
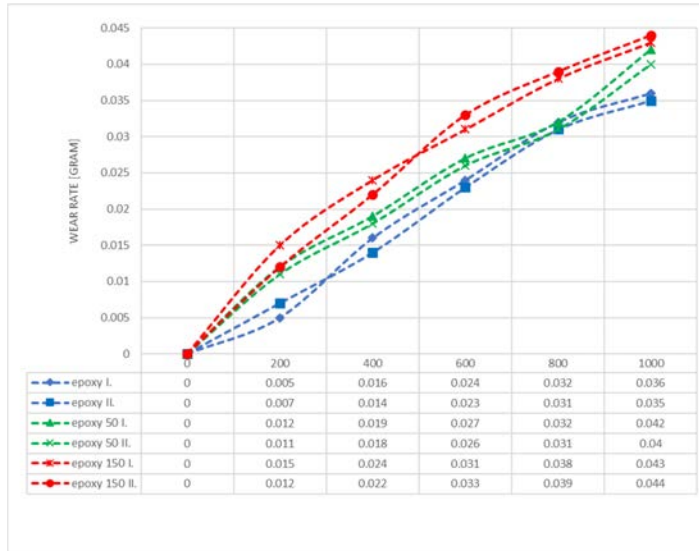
	0	200	400	600	800	1000
epoxy I.	0	0.005	0.016	0.024	0.032	0.036
epoxy II.	0	0.007	0.014	0.023	0.031	0.035
epoxy 50 I.	0	0.012	0.019	0.027	0.032	0.042
epoxy 50 II.	0	0.011	0.018	0.026	0.031	0.04
epoxy 150 I.	0	0.015	0.024	0.031	0.038	0.043
epoxy 150 II.	0	0.012	0.022	0.033	0.039	0.044

Figure 3. Effect of ageing on the wear curve of epoxy

The following figure shows the wear curve of polyester. The same phenomena can be observed here as for the previous two materials. The wear resistance of these materials is almost identical. The vinyl ester matrix was found to be the most wear resistant in the non-aged condition, but vinyl ester also showed the best deterioration after ageing based on visual observations.
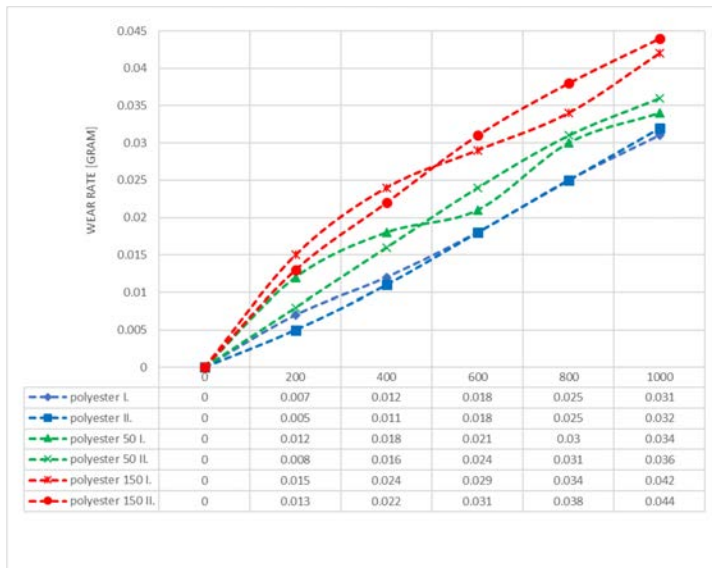

	0	200	400	600	800	1000
polyester I.	0	0.007	0.012	0.018	0.025	0.031
polyester II.	0	0.005	0.011	0.018	0.025	0.032
polyester 50 I.	0	0.012	0.018	0.021	0.03	0.034
polyester 50 II.	0	0.008	0.016	0.024	0.031	0.036
polyester 150 I.	0	0.015	0.024	0.029	0.034	0.042
polyester 150 II.	0	0.013	0.022	0.031	0.038	0.044

Figure 4. Effect of ageing on the wear curve of polyester

The Results of the hardness measurement

In order to find a correlation between the hardness of the polymer and its wear resistance, hardness measurements were also carried out. The ultraviolet irradiated specimens were subjected to Shore-D hardness measurements three times. One specimen was measured five times in succession and the results were averaged. The results of the measurements taken were plotted on the curves shown in the following figure. Here it can be clearly seen that the hardness of all three matrices increased with ultraviolet irradiation. So, despite the increase in hardness, the wear resistance decreased due to structural damage of the material.
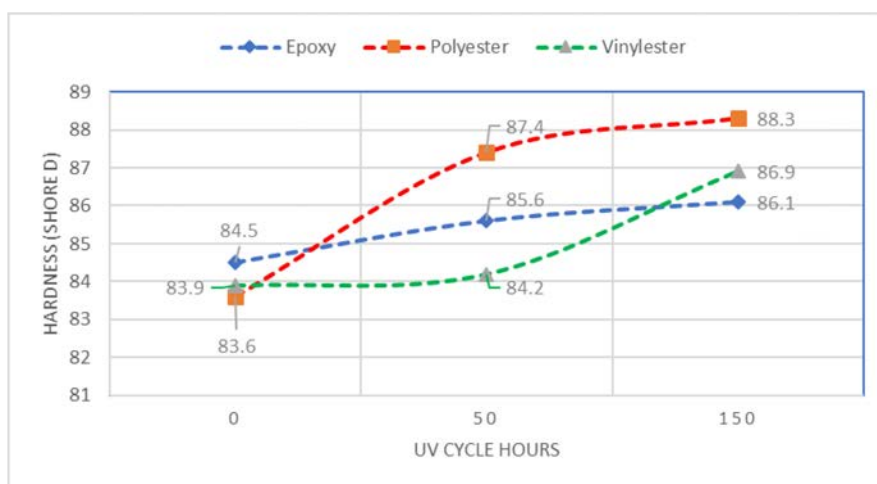

Figure 5. Shore-D hardness results following UV irradiation

Future plans for research

The ageing time could be increased so that the effect could be measured over a wider field. Abraded surfaces could be examined by SEM microscopy. This would shed light on what exactly increased the material abrasion. Existing research suggests that delamination during degradation weakens the structure of the matrix. (Talreja, R. at al., 1987) But whether the wear phenomenon on the aged specimens is abrasive or adhesive can only be determined by microscopic measurements. There are also plans for future reinforcement of the test specimens. The test equipment used now produces abrasive wear. It is also necessary to perform later some kind of adhesion wear test, such as pin-on-disk or blocs-on-ring tests.

Conclusion

- Ageing causes severe coloring
- The hardness of the raw material increases with ageing
- Wear resistance decreases with ageing
- As hardness increases, wear resistance decreases. In any case, the abrasive wear rate decreased due to the increase in hardness, but the adhesive wear rate increased due to structural damage of the material.
- First surface layers wear away rapidly with ageing, then the rate of wear is nearly the same as in the unaged test specimen.
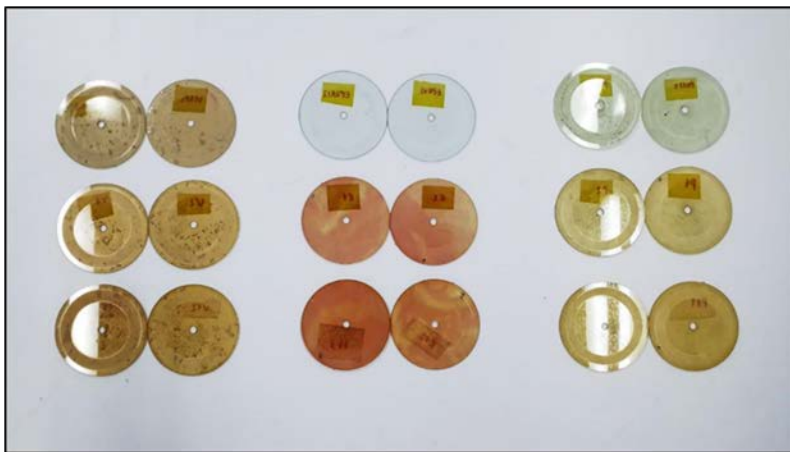

Figure 6. The matrices after 0; 50 and 150 hours of UV exposure

Acknowledgement

References

[1] Kumar, B. G., Singh, R. P., & Nakamura, T. (2002). Degradation of carbon fiber-reinforced epoxy composites by ultraviolet radiation and condensation. Journal of Composite materials, 36(24), 2713-2733.

[2] Mahzan, S., Fitri, M., & Zaleha, M. (2017). UV radiation effect towards mechanical properties of Natural Fibre Reinforced Composite material: A

Review. In IOP conference series: materials science and engineering (Vol. 165, No. 1, p. 012021). IOP Publishing.

[3] B. Judit, M. Róbert, G. István, M. István, P. Rita és W. Tamás, Meteorológiai alapismeretek, Eötvös Loránd Tudományegyetem, 2013.

[4] Deli, A. A., Jármai, K., & Kovacs, G. (2018). Small and full scale testing of container production for ships and airplanes, a review

[5] Sárkány Tamás (2023) Wear testing of composite material combinations in agricultural utility vehicles.

[6[] Talreja, R., & Talreja, R. (1987). Fatigue of composite materials (p. 49). Lancaster, PA: Technomic.